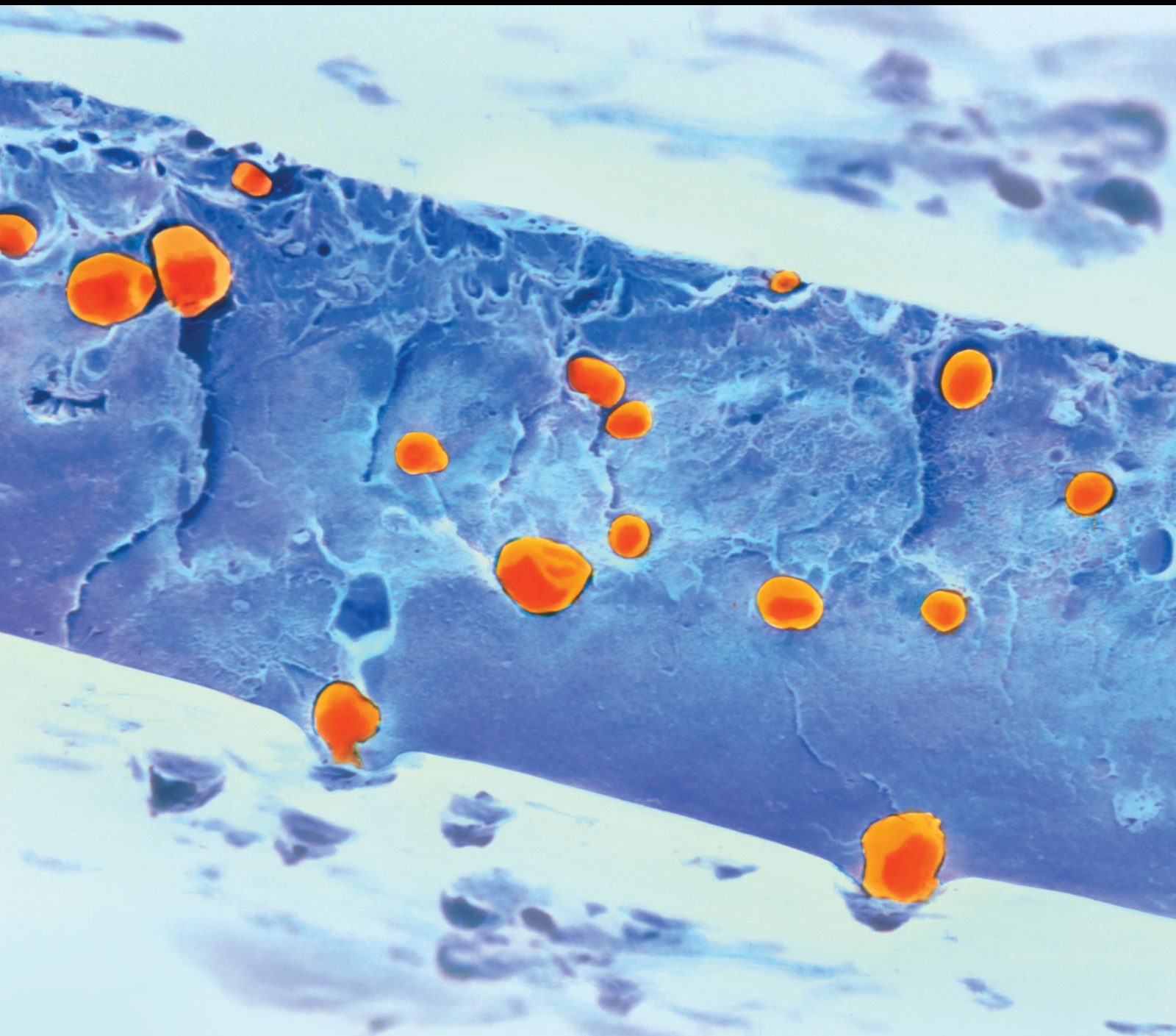


International Journal of Polymer Science

Civil Engineering Applications of Polymer Composites

Guest Editors: Gonzalo Martínez-Barrera, Osman Gencel, and João M. L. Reis





Civil Engineering Applications of Polymer Composites

International Journal of Polymer Science

Civil Engineering Applications of Polymer Composites

Guest Editors: Gonzalo Martínez-Barrera, Osman Gencel,
and João M. L. Reis



Copyright © 2016 Hindawi Publishing Corporation. All rights reserved.

This is a special issue published in "International Journal of Polymer Science." All articles are open access articles distributed under the Creative Commons Attribution License, which permits unrestricted use, distribution, and reproduction in any medium, provided the original work is properly cited.

Editorial Board

Domenico Acierno, Italy
Sharif Ahmad, India
Mats R. Andersson, Australia
Luc Averous, France
Massimiliano Barletta, Italy
Christopher Batich, USA
Giuseppe Battaglia, UK
Marc Behl, Germany
Laurent Billon, France
David G. Bucknall, USA
Andrea Camposeo, Italy
Wen Shyang Chow, Malaysia
J. d. Christiansen, Denmark
Yoshiki Chujo, Japan
Angel Concheiro, Spain
Marek Cypryk, Poland
Li Ming Dai, USA
Yulin Deng, USA
Maria Laura Di Lorenzo, Italy
Eliane Espuche, France
Antonio Facchetti, USA
Marta Fernández-García, Spain
Benny Dean Freeman, USA
Jean-François Gérard, France
Peng He, USA
Jan-Chan Huang, USA
Wei Huang, China
Nabil Ibrahim, Egypt
Tadashi Inoue, Japan
Avraam I. Isayev, USA

Koji Ishizu, Japan
Tadahisa Iwata, Japan
Patric Jannasch, Sweden
Nobuhiro Kawatsuki, Japan
J.M. Kenny, Italy
Mubarak A. Khan, Bangladesh
Ruhul A. Khan, Canada
Saad Khan, USA
Jui-Yang Lai, Taiwan
Jose Ramon Leiza, Spain
Guiping Ma, China
Evangelos Manias, USA
Ulrich Maschke, France
Jani Matisons, Australia
Geoffrey R. Mitchell, UK
Subrata Mondal, India
Christian B. Nielsen, UK
Toribio F. Otero, Spain
Qinmin Pan, Canada
Alessandro Pegoretti, Italy
"Onder Pekcan, Turkey
Zhonghua Peng, USA
Beng T. Poh, Malaysia
Antje Potthast, Austria
Debora Puglia, Italy
Miriam Rafailovich, USA
Arthur J. Ragauskas, USA
Subramaniam Ramesh, Malaysia
Bernabé Luis Rivas, Chile
Juan Rodriguez-Hernandez, Spain

Hossein Roghani-Mamaqani, Iran
Pietro Russo, Italy
Jean-Marc Saiter, France
Mehdi Salami-Kalajahi, Iran
Erol Sancaktar, USA
Albert P. H. J. Schenning, Netherlands
Matthias Schnabelrauch, Germany
Shu Seki, Japan
Vitor Sencadas, Australia
Robert A Shanks, Australia
Mikhail Shtilman, Russia
Basavarajaiah Siddaramaiah, India
Dennis W. Smith Jr., USA
Atsushi Sudo, Japan
Kohji Tashiro, Japan
Hideto Tsuji, Japan
Masaki Tsuji, Japan
Stefano Turri, Italy
Hiroshi Uyama, Japan
Cornelia Vasile, Romania
Alenka Vesel, Slovenia
Yakov S. Vygodskii, Russia
De-Yi Wang, Spain
Qinglin Wu, USA
Frederik Wurm, Germany
Huining Xiao, Canada
Yiqi Yang, USA
Long Yu, Australia
Philippe Zinck, France

Contents

Civil Engineering Applications of Polymer Composites

Gonzalo Martínez-Barrera, Osman Gencel, and João M. L. Reis

Volume 2016, Article ID 3941504, 2 pages

Environmental Impacts on the Strength Parameters of Mineral-Acrylic (PMMA/ATH) Facade Panels

Aleksander Byrdy and Michał Kołaczowski

Volume 2015, Article ID 134714, 5 pages

Shrinkage Behaviour of Fibre Reinforced Concrete with Recycled Tyre Polymer Fibres

Marijana Serdar, Ana Baričević, Marija Jelčić Rukavina, Martina Pezer,

Dubravka Bjegović, and Nina Štirmer

Volume 2015, Article ID 145918, 9 pages

Feasibility of Using High-Performance Steel Fibre Reinforced Concrete for Simplifying Reinforcement Details of Critical Members

Seok-Joon Jang, Dae-Hyun Kang, Kyung-Lim Ahn, Wan-Shin Park, Sun-Woong Kim, and Hyun-Do Yun

Volume 2015, Article ID 850562, 12 pages

Shear Strength of Unreinforced Masonry Wall Retrofitted with Fiber Reinforced Polymer and Hybrid Sheet

Yun-Cheul Choi, Hyun-Ki Choi, Dongkeun Lee, and Chang Sik Choi

Volume 2015, Article ID 863057, 13 pages

Prediction of Flexural Capacity of RC Beams Strengthened in Flexure with FRP Fabric and Cementitious Matrix

Kyusan Jung, Kinam Hong, Sanghoon Han, Jaekyu Park, and Jaehyun Kim

Volume 2015, Article ID 868541, 11 pages

Waste Materials from Tetra Pak Packages as Reinforcement of Polymer Concrete

Miguel Martínez-López, Gonzalo Martínez-Barrera, Carlos Barrera-Díaz, Fernando Ureña-Núñez, and Witold Brostow

Volume 2015, Article ID 763917, 8 pages

Shear Behavior of Concrete Beams Reinforced with GFRP Shear Reinforcement

Heecheul Kim, Min Sook Kim, Myung Joon Ko, and Young Hak Lee

Volume 2015, Article ID 213583, 8 pages

Experimental Assessment on the Flexural Bonding Performance of Concrete Beam with GFRP Reinforcing Bar under Repeated Loading

Minkwan Ju and Hongseob Oh

Volume 2015, Article ID 367528, 11 pages

Recovery and Modification of Waste Tire Particles and Their Use as Reinforcements of Concrete

Eduardo Sadot Herrera-Sosa, Gonzalo Martínez-Barrera, Carlos Barrera-Díaz, Epifanio Cruz-Zaragoza, and Fernando Ureña-Núñez

Volume 2015, Article ID 234690, 8 pages

An Experimental Investigation on the Failure Behavior of a Notched Concrete Beam Strengthened with Carbon Fiber-Reinforced Polymer

Xia Huang, Jian Wang, Feng Zhang, Song-shan Niu, and Jun Ding

Volume 2015, Article ID 729320, 17 pages

Behavior of Full-Scale Porous GFRP Barrier under Blast Loads

D. Asprone, A. Prota, G. Manfredi, and A. Nanni

Volume 2015, Article ID 349310, 11 pages

Bond Characteristics of Macro Polypropylene Fiber in Cementitious Composites Containing Nanosilica and Styrene Butadiene Latex Polymer

Jae-Woong Han, Ji-Hong Jeon, and Chan-Gi Park

Volume 2015, Article ID 207456, 9 pages

Inverse Emulsion Polymerization for the Synthesis of High Molecular Weight Polyacrylamide and Its Application as Sand Stabilizer

Mahmoud A. Mohsin and Nuha F. Attia

Volume 2015, Article ID 436583, 10 pages

Interface Bond Characterization between Fiber and Cementitious Matrix

Won-Chang Choi, Seok-Joon Jang, and Hyun-Do Yun

Volume 2015, Article ID 616949, 11 pages

Behavior and Performance of GFRP Reinforced Concrete Columns with Various Types of Stirrups

Woraphot Prachasaree, Sitthichai Piriyaakootorn, Athawit Sangsrijun, and Suchart Limkatanyu

Volume 2015, Article ID 237231, 9 pages

Effects of Elevated Temperatures on the Compressive Strength Capacity of Concrete Cylinders Confined with FRP Sheets: An Experimental Investigation

Sherif El-Gamal, Khalifa Al-Jabri, Ahmed Al-Mahri, and Saud Al-Mahrouqi

Volume 2015, Article ID 549187, 10 pages

Editorial

Civil Engineering Applications of Polymer Composites

Gonzalo Martínez-Barrera,¹ Osman Gencel,² and João M. L. Reis³

¹Laboratorio de Investigación y Desarrollo de Materiales Avanzados (LIDMA), Facultad de Química, Universidad Autónoma del Estado de México, Km 12 de la Carretera Toluca-Atlacomulco, 50200 San Cayetano, MEX, Mexico

²Civil Engineering Department, Faculty of Engineering, Bartın University, 74100 Bartın, Turkey

³Theoretical and Applied Mechanics Laboratory (LMTA), Universidade Federal Fluminense, 24220 Niterói, RJ, Brazil

Correspondence should be addressed to Gonzalo Martínez-Barrera; gonzomartinez02@yahoo.com.mx

Received 28 December 2015; Accepted 29 December 2015

Copyright © 2016 Gonzalo Martínez-Barrera et al. This is an open access article distributed under the Creative Commons Attribution License, which permits unrestricted use, distribution, and reproduction in any medium, provided the original work is properly cited.

Researches have been done in order to improve performance of concrete and structures. As we know, polymers provide huge opportunities for the advancement of materials research, the improvement of material property, and the strengthening of structures damaged. In this respect, recent developments about polymer composites and their technological developments in civil engineering are aimed in this issue.

Topics include recovery and modification of waste and recycled tire polymer fibers and their use as reinforcements of concrete. A novel proposal based on the modification of the physicochemical properties of the waste automotive tire particles, by using gamma irradiation, shows that improvements on the mechanical properties depend of gamma irradiation as well as concentration and size of waste tire particles. Another study shows that PP fibers can be substituted with higher amount of recycled tire polymer fibers obtaining concrete with similar shrinkage behavior. Such applications would contribute to solving the problem of waste tire disposal. Waste materials from Tetra Pak packages have been used as reinforcement of polymer concrete elaborated with unsaturated polyester resin and silica sand and submitted to gamma irradiation. The results show improvements on both compressive strength and flexural strength, as well as modulus of elasticity when polymer concrete is irradiated.

Other studies are concerned with latex polymer cementitious composites (LCCs), for example, polypropylene fibers used in cementitious composites containing nanosilica and styrene butadiene latex polymer, where the addition of nanosilica significantly affected the bond strength and interfacial toughness between macro-PP fiber and cementitious

composites. Synthesis of polymers for stabilization of minerals, for example, synthesis of high molecular weight polyacrylamide (PAM) and its application as sand stabilizer: the results showed that the use of high molecular weight polymer gave excellent mechanical and thermal stability to the polymer-sand composite. Other applications of acrylic resins can be found in the paper about environmental impacts on the strength parameters of mineral-acrylic facade panels, elaborated with natural minerals produced from bauxite (aluminium hydroxides, ATH) and from acrylic resin (poly-methyl methacrylate, PMMA) and subjected to aging process in conditions of high temperature, high relative humidity, freeze-thaw cycles, and UV radiation.

Studies have been carried out by using fiber reinforced polymer (FRP) materials; as we know, FRP materials have advantages such as corrosion resistance, light weight, machinability, workability, and high strength. The shear capacities of concrete beams reinforced with glass fiber reinforced polymer (GFRP) plates as shear reinforcement have been studied. Also experimental assessment on the flexural bonding performance of concrete beam with GFRP reinforces bar under repeated loading. Moreover, structural behavior of concrete columns internally reinforced with glass fiber reinforced plastic (GFRP) rebars shows that the amount of GFRP longitudinal and lateral reinforcement slightly affects the column strength. another study is focused on the behavior of full-scale porous GFRP barrier under blast loads; a discontinuous (porous) barrier composed by precast concrete reinforced with GFRP bars was studied to take advantage of electromagnetic and mechanical properties as well as mitigating blast shock waves.

The use of high performance composite fibers allows for the improvement of the mechanical properties of cement composites, which are determined predominantly by the interface properties between the fiber and cementitious matrix. Studies on the interface bond between fiber and cementitious matrix are discussed. The results show improvement on the compressive strength according to the embedment length of the fibers; moreover, chemical bond strength was independent of the water-to-binder ratio. Other studies cover experimental and analytical research results for predicting the flexural capacity of reinforced concrete (RC) beams strengthened in flexure with fabric reinforced cementitious matrix (FRCM). It was confirmed that the slippage between the FRP fabric and matrix occurs at a high strain level.

Unreinforced masonry (URM) structures represent a significant portion of existing historical structures around the world. Recent earthquakes have shown the need for seismic retrofitting for URM structures. A strengthening technique using externally bonded (EB) fiber-reinforced polymer (FRP) composites has attracted engineers since enhancing the shear strength of URM walls with negligible change to cross-sectional area and weight of the walls. Results show that FRP composites were effective to increase shear strength. Confining of damaged or corroded concrete columns with FRP sheets is always interesting for researches. However, the performance of this strengthening system at elevated temperature is still questionable. The effects of elevated temperatures on the compressive strength capacity of carbon and glass FRP-confined concrete cylinders are shown.

Experimental investigation on failure behavior of the notched concrete beam strengthened with carbon fiber reinforced polymer (CFRP) is studied, including the influences of the length, thickness, and methods of bonding of CFRP laminate on the ultimate bearing capacity and the failure modes of the reinforced beam. A comparison between a theoretical analysis and the experimental observation shows that the failure modes observed in the experimental study are in agreement with the analytically predicted failure modes. Another research is concerned with the effects of hooked-end steel fiber contents on the mechanical properties of high performance concrete (HPC) and investigates the feasibility of utilizing steel fibers to simplify the complicated reinforcement detailing of critical HPC members under high shear stress. It is also recommended that both stirrups and steel fiber should be used for fully confining the diagonal bar groups of coupling beams to achieve the ductile behavior.

*Gonzalo Martínez-Barrera
Osman Gencel
João M. L. Reis*

Research Article

Environmental Impacts on the Strength Parameters of Mineral-Acrylic (PMMA/ATH) Facade Panels

Aleksander Byrdy and Michał Kołaczkowski

Building and Structure Physics Division, Institute of Building Materials and Structures, Faculty of Civil Engineering, Cracow University of Technology, 31-155 Cracow, Poland

Correspondence should be addressed to Aleksander Byrdy; abyrdy@pk.edu.pl

Received 6 August 2015; Revised 15 November 2015; Accepted 17 November 2015

Academic Editor: Gonzalo Martínez-Barrera

Copyright © 2015 A. Byrdy and M. Kołaczkowski. This is an open access article distributed under the Creative Commons Attribution License, which permits unrestricted use, distribution, and reproduction in any medium, provided the original work is properly cited.

Composite mineral-acrylic panels consist in 80% of natural minerals produced from bauxite (aluminium hydroxides (ATH)) and in 20% from acrylic resin (polymethyl methacrylate (PMMA)). This material due to high usability is widely used in interior finishes. Recently, the mineral-acrylic panels have been used as external claddings of buildings. So far, there are several dozen elevations realized worldwide. Due to the variability of the strength parameters of PMMA acrylic resins depending on the environmental influence, a number of tests on samples of mineral-acrylic panels to verify their suitability for use in climate conditions in Central Europe were performed. The studies determined the change of the material parameters after being subjected to aging process in conditions of high temperature, high relative humidity, freeze-thaw cycles, and UV radiation. In the studies parameters such as flexural strength and modulus of elasticity were measured at a reference temperature of 23°C. In raised and lowered temperatures only the tensile strength tests were conducted. Due to the lack of information in the available literature, the authors carried out tests of the temperature influence on the PMMA/ATH composite modulus of elasticity and flexural strength which is crucial in designing process.

1. Introduction

In modern architecture, for use on facades, materials with a wide functional range of designs, high strength, and durability are sought. One of such materials is composite mineral-acrylic panels (PMMA/ATH), which consist in 80% of natural minerals, produced from bauxite (aluminium hydroxides (ATH)) and in 20% from acrylic resin (polymethyl methacrylate (PMMA)). These panels have a uniform, nonporous, homogeneous structure and are produced in a wide range of colors. They are easy to cut and stick together, and after suitable thermal treatment, they can be easily formed into various shapes. Because of these properties the PMMA/ATH panels represent a very attractive finishing material and for about 40 years have been commonly used as interior design elements. The use of mineral-acrylic panels on facades of buildings is subject to the development of modern techniques of cladding assembly. So far, there are several dozen mineral-acrylic panels elevations realized worldwide. Modern ventilated facades are made of panels of large size,

fixed to a support substrate by means of a steel or aluminum understructure. Facade panels are nodal supported with mechanical undercut anchors deposited on the rear face of the panel (Figure 1).

An example of such a cladding may be that realized in 2014 from Corian panels, on the “Afrykanarium” building in Wrocław. It has an area of over 6000 m² and it consists of black panels, Corian Deep Nocturne, of the largest size used so far, that is, up to 5,2 × 3,5 m². In the first year of use of the cladding some damages were observed, like out of plane deformations in the summer and cracking in the winter (see Figure 2). In order to explain the causes of the damages, the authors examined the changes in durability of the panels in extreme climate conditions occurring in Central Europe.

2. Materials and Methods

2.1. Physicomechanical Parameters of the PMMA/ATH Panels. To implement modern ventilated PMMA/ATH claddings,

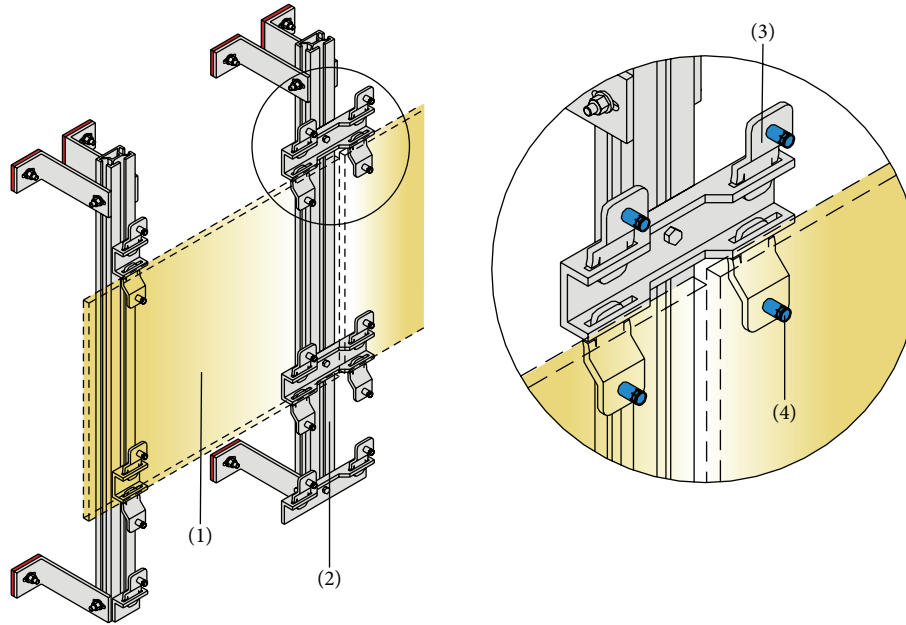


FIGURE 1: Example of understructure for fixing ventilated facade claddings. Designations: (1) facade panel, (2) steel-aluminum understructure, (3) holder fixing the facade panel, and (4) undercut fixing.



FIGURE 2: Damages of the Corian panels of “Afrykanarium” building in Wrocław: (a) cracking in the winter and (b) deformations of panel edges in the summer.

TABLE 1: Basic physicochemical parameters of the acrylic-mineral (PMMA/ATH) panels.

Feature	Declared value
Volume density (kg/m^3)	1680–1175
Water absorption by weight (%)	0–1
Flexural strength (MPa)	57,1–74,0
Modulus of elasticity (MPa)	8040–9220
Coefficient of thermal expansion ($1/\text{K}$)	$2,0\text{--}3,7 \cdot 10^{-5}$

very thin panels with a thickness up to 2 cm are used. Due to the significant environmental loads, facade panels must meet high requirements for physicochemical characteristics. The range of the basic physicochemical parameters of the panels from different manufacturers is shown in Table 1.

2.2. Environmental Loads Acting on Facade Panels. One of the major loads acting on the facade panels is a thermal load. Changes in temperature of cladding panels depend on ambient temperature, solar radiation, solar radiation absorption coefficient of the material, geographic location, exposure of an elevation relative to the world sides, and layering of a wall on which the panels are attached. Dark-coloured panels, directed to the south and south-west, are subjected to a high sunlight absorption and are heated to much higher temperatures than the ambient temperature. Sample record of temperature changes on the surface of the black Corian Deep Nocturne panels measured by the authors is shown in Figure 3.

Based on the studies of the facade with a ventilated gap, it was found that the temperature of the plates from the side of the air gap is lower by 7–12°C than the sunlit

TABLE 2: The average strength characteristics resulting from aging tests of Corian (PMMA/ATH) panels [4].

Method of testing	Flexural strength (MPa)	Modulus of elasticity (MPa)
Preliminary parameters	69,4	9253
Aging by the influence of constant temperature (65 ± 3)°C and a relative humidity close to 100% for 28 days	50,7	8360
Aging for 3×1000 hours, in 40°C and 50% relative humidity, UV 550 W/m ² , water pouring every 100 minutes for 18 minutes	65,0	9543
Cycles of freezing and thawing, 100 cycles	70,2	8833

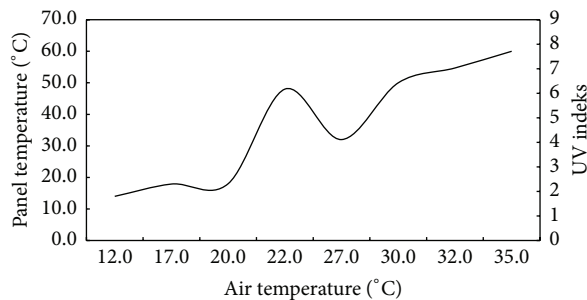


FIGURE 3: Temperature of the outer surface of Corian Deep Noc-turne (PMMA/ATH) black facade panels mounted on the southern wall, read between 27.07.13 and 20.09.13 in Wrocław.

surface temperature. In Central Europe the most vulnerable to thermal load are horizontal claddings and facades oriented towards the south and south-west. On the basis of the calculation model of Mackey and Wright [1] as well as local meteorological data, it was determined that the maximum temperature that can be reached by PMMA/ATH facade panels located in Central Europe is 82.6°C. Such a high temperature can cause not only significant thermal deformation of a cladding but also effects in changes of the strength characteristics of the mineral-acrylic panels [2, 3].

Facade panels are also subject to various other environmental factors such as high moisture and UV radiation and the most important factor, wind load. Bending stress caused by wind load is crucial in designing process and therefore the most important parameter of the material is its flexural strength.

As the plate material is characterized by high thermal expansion, the use of panels of this material requires the installation of sliding supports. Disabling of a free expanding and shrinking of panels subjected to temperature changes might cause very high longitudinal forces leading to distortion of a cladding look. Sliding mount of cladding panels makes the longitudinal forces resulting only from the self-weight of panels and thus being of little importance in the design process. Due to the low effort caused by tensile stress creeping of the material is of secondary importance when sizing plates.

Practically used supports, however, do not provide total freedom of move, because of the occurrence of frictional forces. Those supports fulfill their role because their susceptibility to move is substantial in comparison with the rigidity of the supported element. In the case of the cladding of

the Wrocław “Afrykanarium,” it was questioned if due to environmental condition changes the material’s modulus of elasticity has not been so seriously decreased that the panels rigidity turned out to be too low, in comparison to resistance caused by the frictional forces in the supports. This could result in lack of free move and deformation of the panels, expanding under heating.

The authors performed the studies of Corian samples in order to determine the modulus of elasticity in different climate conditions and to determine if the observed cladding deformations might occur due to decrease of rigidity in the elevated temperature, despite fixing in accordance with the engineering design.

Variation of flexural strength of Corian samples under different environmental conditions was examined in order to determine the actual bearing capacity of panels under wind load in different conditions as well as verification of the safety of the “Afrykanarium” cladding.

The calculations should also be base for drawing practical conclusions about designing of new elevations using PMMA/ATH panels.

3. Results and Discussion

3.1. Results of Studies Described in Available Literature. In order to check the influence of environment on Corian (PMMA/ATH) panels strength parameters, several aging studies verifying their suitability for use on exterior facades were performed, CSTB Report [4]. Components with dimensions of $260 \times 20 \times 13$ mm were selected for the study. The reference trial included 10 samples, whereas each ageing test included 5 samples. The samples were aged at a constant, elevated temperature about 65°C and under a constant, high relative humidity close to saturation for a period of 28 days. The next test consisted in subjecting the panels to a UV radiation of 550 W intensity at 40°C and 50% relative humidity. Total run time of the test was 3000 hours, during which water was poured over the plate periodically (every 100 minutes for 18 minutes). In order to test the effect of freezing and thawing on the strength properties of Corian panels a total of 100 cycles of freezing and thawing of the samples were carried out according to the procedure described in European Standard EN ISO 10545-12:1997 [5]. Verification of the effect of the environment on the material consisted in testing the changes in flexural strength and modulus of elasticity upon bending. The studies whose results are shown in Table 2 ended with strength tests performed at 23°C for

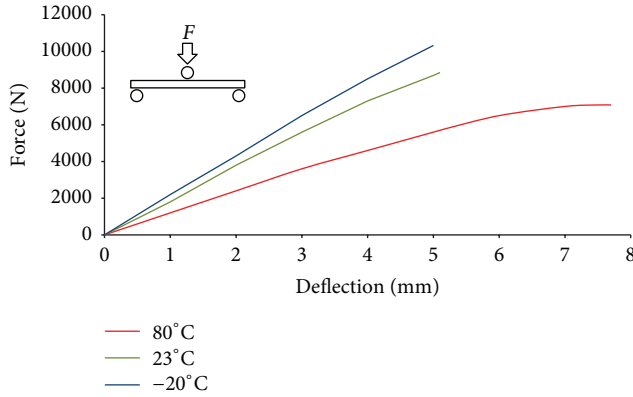


FIGURE 4: Plot of the average load-deflection relationships for Corian (PMMA/ATH) panels subjected to concentrated-load bending at various ambient temperatures.

comparison with the results of the preliminary studies of the material.

It should be emphasized that there are no studies described in the available literature that include PMMA/ATH panels flexural strength measurement at raised temperatures. Temperature changes have a significant impact on the strength parameters of acrylic-mineral panels. A study of tensile strength of PMMA/ATH panels carried out by Nie et al. [6] demonstrated a significant decrease in tensile strength of heated samples of the material. At a temperature of 90°C, nearly 70% lower tensile strength than at 25°C was recorded. Together with tensile strength decrease at elevated temperature there was a decrease of modulus of elasticity of the material.

3.2. Results of Studies Carried out by Authors. According to a study of Marshall and Evans [7] permissible strains determined in the bending and stretching test may be different and therefore the authors decided to determine the effect of temperature changes on the PMMA/ATH panel flexural strength. In order to verify the effect of temperature on strength parameters, panels were subjected to concentrated-load bending tests at temperatures of -20°C , 23°C , and 80°C . Tests were carried out in testing machine for bending test with climate chamber. For each series of tests, 10 samples with dimensions $250 \times 250 \times 12$ mm were used. Samples were supported by hinged linear supports in the spacing of 200 mm (see static scheme on Figure 4). Studies were performed on the Corian Deep Nocturne panels. The resistance to bending tests was carried out using the rate of change of panel's deflection set to 5 mm/min. Samples for testing at reduced or elevated temperature were conditioned for 2 hours before the test in order to reach the right temperature throughout the entire cross section of the sample. Conditioning time of the samples was adopted on the basis of earlier measurements of changes in the internal temperature of the samples with a thermocouple mounted in an opening formed in the sample. The average test results are shown in Table 3 and in Figure 4.

TABLE 3: The average results of the strength test of the Corian (PMMA/ATH) panels at different temperatures.

Method of testing	Flexural strength (MPa)	Modulus of elasticity (MPa)
Parameters at 23°C	82,05	8010
Parameters at -20°C	83,3	9886
Parameters at $+80^{\circ}\text{C}$	57,7	5793

3.3. Studies Results Summary. On the basis of the test results shown in Tables 2 and 3, the following changes in flexural strength of PMMA/ATH Corian panels were determined:

- (i) panels aged for 28 days in 65°C and under the saturated vapor—26,9% decrease,
- (ii) panels subjected to aging by UV radiation—6,3% decrease,
- (iii) panels with temperature of -20°C —1,5% increase,
- (iv) panels with temperature of 80°C —29,7% decrease.

Studies of Corian panels in cycles of freezing and thawing did not show changes in the strength characteristics of the material.

Changes in elastic modulus were observed mainly as a result of temperature changes. Changes in the elastic modulus were measured for 30% of the effort of the element and were as follows:

- (i) panels aged for 28 days in 65°C and under the saturated vapor—9,6% decrease,
- (ii) panels with temperature of -20°C —23,4% increase,
- (iii) panels with temperature of 80°C —27,7% decrease.

4. Conclusion

The results of the tests carried out by the authors showed a significant reduction in the flexural strength of the material under the influence of the raised temperature. The reduction was relatively lower than in the case of tensile strength measured by Nie et al. [6], nonetheless it was significant which is of a high practical importance. Another important factor to reduce the bending strength is aging at elevated temperature and humidity, which was described in [4].

In the case of the analyzed facade, even under significantly reduced bending strength, the calculated resistance of the panels to bending by the wind proved to be sufficient.

The performed studies of the Corian panels allowed us to conclude that, in the case of the described elevation, the recorded changes of strength parameters of the cladding panels were not the direct cause of their damage.

Based on the computational analysis, it was found that if the support was performed according to the design, even the panels under reduced modulus of elasticity would be provided with the correct sliding support. The observed deformations of the panels during the summer were caused by blockage of move due to the implementation of the supports in a manner inconsistent with the project. The

observed cracking of panels joints during the winter was caused by inadequate technology of gluing edges of the panels.

The size of changes of strength characteristics of PMMA/ATH panels resulting from environmental influences depends on the composition and structure of the material [8]. For this reason, the basis for the use of mineral-acrylic panels of particular manufacturer on external facades should be broad studies of the impact of the environment on their mechanical properties. The results of the tests described in the available literature concern PMMA/ATH mechanical properties changes only at elevated temperatures. Bending tests carried out by the authors on Corian samples at -20°C showed improvement in the strength parameters of the material in lowered temperature (Table 3) and a ductile form of the material destruction as in the case of higher temperatures.

To obtain strength characteristics of the PMMA/ATH panels, being the most useful for the design process, aging tests should be performed with the final measurement of the material properties at 80°C . Strength values obtained this way best reflect actual properties of the panels needed to model their work while using the facade. As a result of these studies, a partial factor for the strength properties of mineral-acrylic panels intended for a use on exterior facades should be developed.

Further studies of PMMA/ATH panels should be based on observation of their strength properties in natural conditions. The results of these studies may be the basis for the development of predicted properties changes in time, analogously to the proposal for their modeling published by Santos et al. [8].

Conflict of Interests

The authors declare that there is no conflict of interests regarding the publication of this paper.

Acknowledgment

This work was partially funded by Project L-1/271/DS/2014.

References

- [1] C. Mackey and L. Wright, "Periodic heat flow-composite walls or roofs," *Transactions of the American Society of Heating and Ventilating Engineers*, vol. 52, pp. 283–296, 1946.
- [2] C. Basaran, S. Nie, and C. S. Hutchins, "Time dependent behavior of a particle filled composite PMMA/ATH at elevated temperatures," *Journal of Composite Materials*, vol. 42, no. 19, pp. 2003–2025, 2008.
- [3] E. Gunel and C. Basaran, "Influence of filler content and interphase properties on large deformation micromechanics of particle filled acrylics," *Mechanics of Materials*, vol. 57, pp. 134–146, 2013.
- [4] Centre Scientifique et Technique du Bâtiment (CSTB), "Marne-la-Vallée," Rapport d'Essais CLC 09-26016148/26022557, Centre Scientifique et Technique du Bâtiment (CSTB), 2010.
- [5] International Organization for Standardization, "Ceramic tiles. Determination of frost resistance," EN ISO 10545-12:1997, International Organization for Standardization, 1997.
- [6] S. Nie, C. Basaran, C. S. Hutchins, and H. Ergun, "Failure mechanisms in PMMA/ATH acrylic casting dispersion," *Journal of the Mechanical Behavior of Materials*, vol. 17, no. 2, pp. 79–96, 2006.
- [7] D. B. Marshall and A. G. Evans, "Failure mechanisms in ceramic-fiber/ceramic-matrix composites," *Journal of the American Ceramic Society*, vol. 68, no. 5, pp. 225–231, 1985.
- [8] R. M. Santos, G. L. Botelho, C. Cramez, and A. V. Machado, "Outdoor and accelerated weathering of acrylonitrile-butadiene-styrene: a correlation study," *Polymer Degradation and Stability*, vol. 98, no. 10, pp. 2111–2115, 2013.

Research Article

Shrinkage Behaviour of Fibre Reinforced Concrete with Recycled Tyre Polymer Fibres

Marijana Serdar, Ana Baričević, Marija Jelčić Rukavina, Martina Pezer, Dubravka Bjegović, and Nina Štirmer

Department of Materials, University of Zagreb Faculty of Civil Engineering, Fra Andrije Kacica Miosica 26, 10000 Zagreb, Croatia

Correspondence should be addressed to Ana Baričević; abaricevic@grad.hr

Received 7 August 2015; Revised 7 October 2015; Accepted 11 October 2015

Academic Editor: Gonzalo Martínez-Barrera

Copyright © 2015 Marijana Serdar et al. This is an open access article distributed under the Creative Commons Attribution License, which permits unrestricted use, distribution, and reproduction in any medium, provided the original work is properly cited.

Different types of fibres are often used in concrete to prevent microcracking due to shrinkage, and polypropylene fibres are among the most often used ones. If not prevented, microcracks can lead to the development of larger cracks as drying shrinkage occurs, enabling penetration of aggressive substances from the environment and reducing durability of concrete structures. The hypothesis of the present research is that polypropylene fibres, used in concrete for controlling formation of microcracks due to shrinkage, can be replaced with recycled polymer fibres obtained from end-of-life tyres. To test the hypothesis, concrete mixtures containing polypropylene fibres and recycled tyre polymer fibres were prepared and tested. Experimental programme focused on autogenous, free, and restrained shrinkage. It was shown that PP fibres can be substituted with higher amount of recycled tyre polymer fibres obtaining concrete with similar shrinkage behaviour. The results indicate promising possibilities of using recycled tyre polymer fibres in concrete products. At the same time, such applications would contribute to solving the problem of waste tyre disposal.

1. Introduction

Deformation due to shrinkage of concrete is one of the main reasons for occurrence of cracks, especially for concrete elements such as slabs, pavements, and concrete overlays with large exposed surfaces [1]. When used in structures susceptible to shrinkage and/or exposed to specific loading conditions, cement-based composites are often improved with polypropylene (PP) fibres. The main contribution of PP fibres is reduced deformation of cementitious composites caused by autogenous, plastic, and restrained shrinkage, additional to the increased resistance of composites to spalling during fire [2–5]. Presence of micropolymer fibres reduces the appearance of cracks during shrinkage in the early age of concrete, during first 12 hours, by increasing strength and strain capacity of cement paste [6]. If not controlled, microcracks formed due to the drying shrinkage lead to the development of larger cracks. By reducing the crack width, the penetration of aggressive substances from the environment is reduced [7]. It is well known that cracking

control is essential for the development of more durable and long-lasting structures [8].

Plastic shrinkage results from self-desiccation and external drying of concrete from fresh state to early hardening. Two most important parameters for plastic shrinkage control are the volume fraction of PP fibres and their diameter [3, 7–9]; by controlling them, an adequate control of plastic cracks is achieved. If an appropriate volume fraction (0.2%) and diameter of fibres are used, it is possible to reduce the total amount of plastic shrinkage cracking to 10% of control [2]. Thinner and longer fibres are more streamlined than thicker and shorter ones, while more effective control is achieved with fibrillated rather than monofilament fibres [10]. By combining different lengths (6–20 mm) of multifilament fibres compared to mixes with only one fibre length, additional improvement of plastic shrinkage behaviour of fibre reinforced concrete (FRC) is achieved [9]. PP fibres also have a positive influence on the values of autogenous shrinkage [3, 11]. The autogenous shrinkage is due to the self-desiccation as the hydration of cement goes on and the

cement paste starts hardening. Investigation on influence of different PP fibres volumes show that for 0.25, 0.5, and 0.75% of fibres autogenous shrinkage decreases progressively for 5, 15, and 26%, respectively, in relation to the plain concrete after 24 hours [3]. Additional decrease of deformation due to the early autogenous shrinkage can be achieved with usage of premoistened PP fibres and corresponding reduction of added water [11]. Beneficial effect of polypropylene fibres on reducing the crack width is positively reflected on the value of restrained shrinkage [2]. Multiple cracking displayed by hardened composites with 2% PP fibres by volume during restrained shrinkage tests indicates their ability to distribute induced strains on larger area [5, 12]. The value of their contribution depends on type, diameter, and shape of used fibres. For comparison, according to [13], cracks in plain concrete appear after 36 days, in concrete with sinusoidal fibres appear after 202 days, and in concrete with monofilament fibres did not show cracking even after 600 days. Achieved behaviour is result of better anchoring ability of monofilament fibres, which results in better stress distribution [13]. Up to date experimental results indicate that there is no unambiguous relationship between addition of PP fibres and drying shrinkage of concrete. Some studies did show potential beneficial effect on drying shrinkage when 0.1% of PP fibres by volume were added in the mix but, at the same time, with the increasing addition of fibres the effect was adverse [14, 15].

With the development of environmental awareness, there is a growing interest to find more efficient paths for waste management. Waste tyres present a specific type of waste whose removal from the environment is mandatory due to the health issues, accidental fires, and so forth. Each year in the EU, more than 3.5 million tons of tyres reaches the end of their lives. Tyres comprise roughly 80% rubber granules, reinforced with 15% steel and 5% polymer fibre reinforcement. One of the innovative solutions is to utilize these products obtained by waste tyre recycling in concrete [16–18]. Main challenge regarding recycled tyre polymer fibres (RTPF) is storage; due to their low weight, they are easily carried by the wind and are extremely flammable. Currently, they are mainly landfilled or valorized as an alternative fuel during cement production. Research presented hereafter is part of a large FP7 project, Anagennisi [16, 17], where the aim of the project is to identify suitable applications for RTPF in concrete and to put an end to the current practice of landfilling this material. Based on the limited literature data [18–21], RTPF do not induce negative effects on concrete mechanical properties and could potentially have beneficial effect on controlling cracking of concrete due to different early age deformation.

In the framework of this initial pilot study, RTPF are used for the first time for production of FRC mixes with enhanced resistance to cracking due to shrinkage deformation. Five different mixes were prepared and tested. Two of them were prepared as reference mixes, plain concrete without fibres, and mix with 1 kg/m^3 polypropylene fibres. Since the analysis of RTPF showed that their size (length and diameter) is much smaller compared to polypropylene fibres, it was decided to prepare three mixes with a higher amount of RTPF

substituting 1 kg/m^3 of PP. Therefore, in these three mixes, the amount of the recycled textile fibres was 5, 10, and 15 kg/m^3 .

2. Materials and Methods

2.1. Materials and Mix Design. Geometrical characterization of RTPF fibres was performed by microscopic examination using Olympus BX 51 [17, 22]. The width was determined on a randomly taken sample of fibres, in total consisting of 315 single fibres, measured in longitudinal view of a single thread. Three different types of fibres were determined with average diameters of 10, 20, and $30 \mu\text{m}$ (Table 1, Figure 1). For determination of length, 600 samples were tested. Obtained length distribution is presented in Figure 1. It can be observed that more than 80% of fibres have length shorter than 12 mm. Geometrical characteristics are consequence of various types of waste tyres used during recycling process, that is, car, truck, and other types of tyres from heavy weight vehicles. Besides, polymer fibres are extracted from different manufacturing cycles and then mix together. According to heats of fusion and crystallization determined by differential scanning calorimetry (DSC), the sample consists of 60% of PET (polyesters poly(ethylene terephthalate)), 25% of PA 66 (polyamide 66), and 15% of PBT (poly(butylene terephthalate)) with small contribution of steel and rubber particles [23]. Melting of crystalline part of polymers comprising analysed textile fibre occurs in the temperature range from 210°C to 260°C .

To determine the wettability of a surface of polymer fibres, contact goniometry was used. The contact angle was determined on prepared specimens and averagely was up to 140 degree. This indicates that polymer fibres are hydrophobic but, when immersed in water, they partially submerge indicating presence of different polymers inside of the specimen. Further investigation in this field is currently undertaken.

Concrete mixes were prepared with cement CEM II/B-M (S, V) 42.5 N, crushed limestone as an aggregate, and polycarboxylic ether hyperplasticiser. Aggregate grading curves are presented in Figure 2. Main constituents of cement, in accordance with EN 197-1:2002, are clinker, in proportion of 65–79%, and a mix of slag (S) and fly ash (V), both in proportion of 21–35% [24].

A reference concrete mix was reinforced with polypropylene fibres 19 mm long (Table 2). Those fibres were selected as the most used polypropylene fibres on Croatian market for this specific purpose.

The concrete mix designs are shown in Table 3. All materials were kept for 24 hours in the laboratory at a temperature of $20 \pm 2^\circ\text{C}$. The aggregates and the RTPF were mixed together to ensure a good dispersion of fibres. Mixing was then proceeded for two minutes after adding half of the water. To allow the aggregates to absorb the needed amount of water, the mixing was stopped for about two minutes. Cement was then added and mixing started again with continuous addition of the residual water and superplasticiser. After the insertion of all materials, the mixing continued for another two minutes.

2.2. Methods. Fresh concrete properties (density, slump test, and air content) were tested according to the following

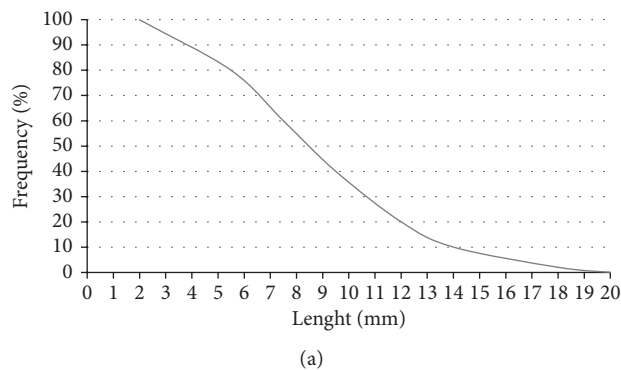


FIGURE 1: (a) Distribution of length of RTPF. (b) Recycled tyre polymer fibres.

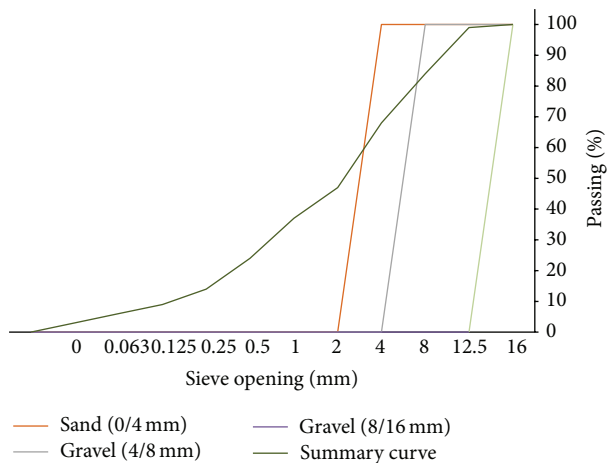


FIGURE 2: Aggregate grading curves.

standards: EN 12350-6:2009, EN 12350-2:2009, and EN 12350-7:2009 [25–27]. Compressive strength was tested after 28 days according to EN 12390-3:2009 [28].

Volume deformations were determined through measurements of autogenous, total, and restrained deformations. Autogenous deformations were measured for each mix on three specimens. End plates of each mould have holes bored at the centre for the insertion of shrinkage measurement pins. One side of the measuring pin is embedded into the concrete after filling the mould in a way that it can freely move together with the specimen. The other side of the pin is connected to the displacement transducer. Each mould was equipped with two digital indicators placed on opposite sides and connected to a computer where the displacement was logged every 5 minutes. The length change of the test specimen was equal to the sum of displacements measured by the two digital indicators. During measurement, all specimens were stored in a chamber at $19 \pm 2^\circ\text{C}$. As autogenous shrinkage is affected by the thermal expansion and contraction caused by the

temperature change in concrete due to the hydration reaction, the temperature in the centre of the specimens was measured by thermocouples [29], Figure 3.

For total shrinkage measurements, specimens were stored in special chamber at 20°C and with relative humidity of 60%. The measurements were carried out at the age of 1, 3, 7, 14, 28, 42, 56, and 90 days using the mobile displacement transducer, with an accuracy of $1\ \mu\text{m}$, Figure 4(a).

The testing setup for restrained shrinkage measurement was implemented according to the method proposed in [30], Figure 4(b). The thickness of the inner steel ring was 8 mm, whilst the outer radius and inner radius were 161.5 mm and 153.5 mm, respectively. The outer steel ring which served as a mould for the concrete was 6 mm thick, with outer diameter of 403 mm. The thickness of the concrete ring was 34 mm, whilst the outer radius and the inner radius were 195.5 mm and 161.5 mm, respectively. The height of each ring was 80 mm. Specimens were equipped with 3 three strain gauges placed at midheight on the inner circumference of the steel ring at an angle of 120° .

3. Results and Discussion

3.1. Fresh State and Mechanical Properties. All tested mixes were designed to achieve S4 consistency class (slump values 160–210 mm) [25]. Apart from plain concrete mix with slump value of 215 mm, all other tested mixes can be classified into targeted consistency class. It can be observed that there is a slight decrease of slump values with the addition of fibres and increasing RTPF content, since part of the added water is used to moist the fibres, which is in accordance with research on premoistened fibres [11]. Higher volumes of fibres require modification of the mix proportions to accommodate the increased surface area of the fibres and to prevent negative effects on workability and air content [9, 31, 32]. This was confirmed by the higher added amount of superplasticiser ($0.86\ \text{L/m}^3$ of concrete) during mixing for 15RTPF (as shown in Table 3) in order to achieve the target consistency class.

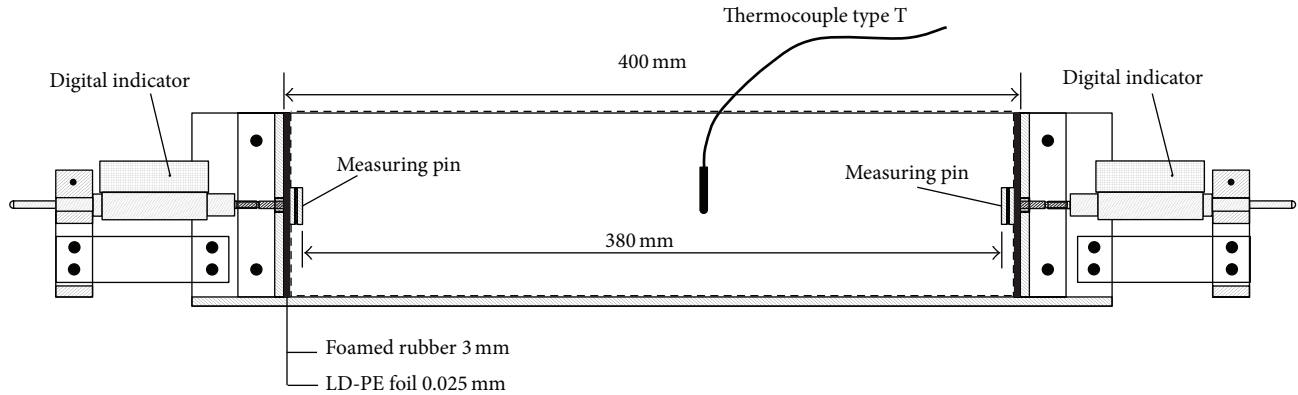


FIGURE 3: Schematic of experimental setup for measuring autogenous shrinkage [29].

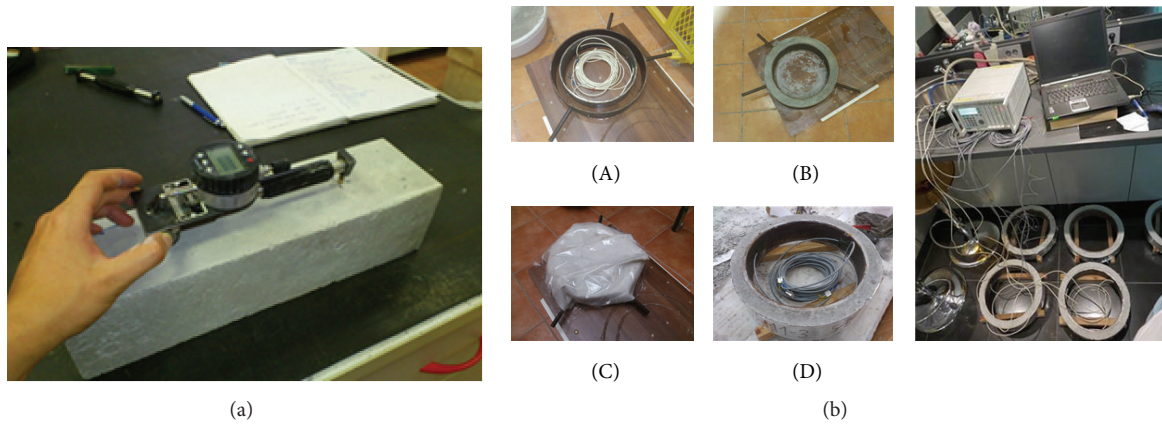


FIGURE 4: (a) Measurement of total shrinkage by mobile displacement transducer. (b) Test setup for restrained shrinkage.

TABLE 1: Properties of RTPF.

Length, mm	Diameter, μm	Melting point, $^{\circ}\text{C}$
8.4 ± 3.8	Type 1	30.93 ± 2.46
	Type 2	20.67 ± 1.75
	Type 3	13.15 ± 1.82

However, obtained decrease is not endangering compaction of concrete and no balling or sedimentation was observed. Results were in good correlation with the results obtained previously and presented in [20, 33].

RTPF have a low specific gravity and if added in the amount of $5\text{--}15\text{ kg/m}^3$, they represent replacement for a maximum of 1% aggregates by weight. Therefore, this replacement cannot affect the density of concrete mix, which is confirmed by results (Table 4). Fibre reinforced concrete mixes had higher air content values (1.65–2.0%) compared to plain concrete (PC) (1.30%).

Compressive strength values obtained at 28 days and shown in Table 4 were similar for all tested mixes ranging from 50.0 MPa (PP mix) to 51.8 MPa (PC mix). Maximum difference in values of particular mixes is within obtained standard deviation values (maximum standard deviation is 3.4 MPa and maximum difference between values obtained

for different mixes is 1.8 MPa), thus leading to the conclusion that studied amounts of fibres do not significantly affect the compressive strength of concrete. The main reason for this is that mechanical properties of concrete mainly depend on the quality of the matrix and on the pore structure. Since the addition of RTPF did not induce significant changes in air content, the influence on mechanical properties was also absent. This is in line with previous research on influence of different volumes of PP fibres on the values of compressive strength, where it was shown that increase in PP fibre volume has minor effect on the compressive strength values [12, 15, 31, 34–36].

3.2. Autogenous Shrinkage. Average results of the autogenous shrinkage measurements (together with temperature profiles) for each tested mix are shown in Figure 5. The results were analysed starting from the moment when swelling of each mix was observed. Initial swelling of concrete is a common phenomenon for the beginning of autogenous shrinkage. Namely, after the compaction of concrete in moulds, due to the settlement, bleeding on surface is present. After settlement is finished and no drying of concrete is allowed, excess water needed for the reaction with cement can often be obtained by reabsorption of bleeding water. In some cases autogenous shrinkage can be eliminated or swelling can

TABLE 2: Properties of polypropylene fibres.

Length, mm	Density, g/cm ³	Tensile strength, GPa	Modulus of elasticity, GPa	Melting point, °C
19 mm	0.915	400–100	2.1–3.5	160–170

TABLE 3: Concrete mix design, per m³.

Components	PC	PP	5RTPF	10RTPF	15RTPF
Cement (kg)	370	370	370	370	370
Water (L)	170	170	170	170	170
Superplasticizer (kg)	2.22	2.22	2.22	2.22	3.08
w/c	0.46	0.46	0.46	0.46	0.46
PP fibres,	—	1	—	—	—
RTPF	—	—	5	10	15
Sand (0/4 mm)	821.9	841.8	815.83	809.88	800.93
Gravel (4/8 mm)	383.1	364.7	380.31	377.50	366.30
Gravel (8/16 mm)	680.0	637.4	675.00	670.00	644.52

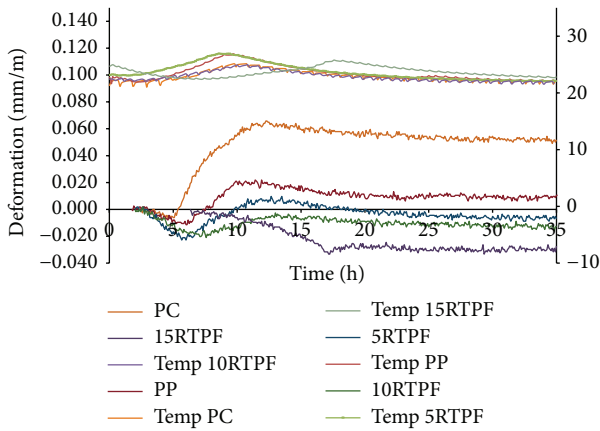


FIGURE 5: Average results of the autogenous shrinkage measurements starting from the appearance of swelling.

be detected rather than shrinkage [37]. This phenomenon occurs in mixes with excess of water and, depending on the amount, may last until the end of binding [38]. Here presented results indicate the potential ability of RTPF to act as self-healing agent. One can observe that swelling increases with the increase of the RTPF content in mix, Figure 5. This could be caused by the ability of RTPF to block a certain amount of free water during mixing which is then slowly released during the time. However, to confirm this observation, further testing will be performed.

To compare only deformation caused by autogenous shrinkage, all curves were normalised at the peak of swelling and at the moment temperature starts to increase, indicating the beginning of cement hydration, as shown in Figure 6. Autogenous shrinkage first starts for ordinary concrete, PC, five hours after the casting. The same process for other mixes starts after 6 hours for mix PP, 6.5 hours for mix 5RTPF, 7.3 hours for mix 10RTPF, and 17.3 hours for mix 15RTPF. Mixes with RTPF showed delayed hydration compared to the ordinary concrete and PP mix.

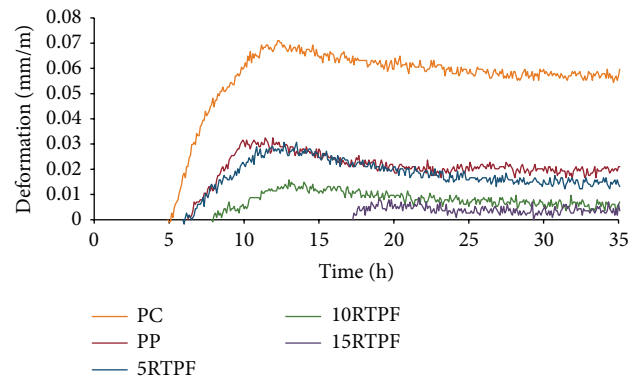


FIGURE 6: Average autogenous shrinkage for all mixes.

Compared to the reference mix, the deformation of RTPF mixes caused by shrinkage is lower. A sudden increase in the value of shrinkage in the case of PC compared to the mixes with RTPF indicates a restraining ability of RTPF. Modulus of elasticity of polymer fibres has similar value as the modulus of elasticity of young concrete; this is why the presence of those fibres has positive influence on stress distribution and lower shrinkage strains. When higher fibre contents are present (10 and 15 kg per m³), water absorbed during mixing is not all released during swelling, and thus additional amount of water is available in fibres even in the later age. This water is crucial for reduction of self-desiccation, the process largely responsible for the autogenous shrinkage of cement-based materials [39].

At the end of the last stage, autogenous deformation of ordinary concrete is 0.0596 mm/m and for concrete with polypropylene fibres 0.0210 mm/m, while for mixes with RTPF the same deformation amounts to 0.0140 mm/m, 0.0061 mm/m, and 0.0061 mm/m (Figure 6). From these results, it can be concluded that the total autogenous shrinkage of mixes with RTPF was lower compared to the autogenous shrinkage of ordinary concrete. These results were in accordance with the literature data, where an increase of

TABLE 4: Fresh concrete properties and compressive strength.

Concrete mix	Slump (mm)	Density (kg/dm ³)	Air content (%)	Compressive strength (MPa)	
				Average	Standard deviation
PC	215	2.41	1.30	51.8	1.9
PP	190	2.39	1.80	50.0	3.4
5RTPF	185	2.38	2.00	51.2	1.3
10RTPF	160	2.38	1.60	51.4	0.2
15RTPF	185	2.36	1.65	50.7	1.6

polypropylene fibre content in concrete is associated with decrease of autogenous shrinkage [3, 11].

3.3. Restrained Shrinkage. Restrained shrinkage was measured by using strain gauges placed around the steel ring. Presented results are gathered on one specimen for each mix. The time histories of the restrained shrinkage for concrete with polypropylene fibres and mix 15RTPF are shown in Figures 7(a) and 7(b).

Results of testing according to ring test method indicate that with the addition of PP fibres stresses that concrete can withstand, which are formed due to restraining of shrinkage, were much higher than that of plain concrete. Substituting PP with 15 kg/m³ of RTPF additionally improved concrete behaviour, increasing tensile stresses that concrete can withstand prior to the crack. At the moment of appearance of first big crack tensile stress for ordinary concrete was 2.2 MPa, 3.3 MPa for concrete with polypropylene fibres, and 4.7 MPa for concrete with RTPF (Figure 7(a)).

Both PP and 15RTPF mixes showed similar behaviour up to the 25th day when the rate of deformations slows down for concrete with polypropylene fibres. This occurs due to the increased tensile stress within the concrete and all pronounced influence of creep, causing the stress relaxation in concrete and steel ring. From 25th day after casting onwards, curves representing the restrained deformation for both mixes are splitting, while deformations of concrete with RTPF fibres are constantly increasing up to the 59th day. The average value of deformation was 90 $\mu\text{m/m}$ for mix 15RTPF, while deformation of mix PP remained unchanged compared to the 25th day, at 60 $\mu\text{m/m}$.

Cracking occurred at the age of 44 days for mix PP and 58 days after casting for mix 15RTPF. Ordinary concrete obtained a visible macrocrack after 65 days from casting. Although this was later than cracks occurred for FRC, deformations that PC can withstand are much lower, which leads to conclusion that crack formed before they became visible. This is clear from detailed analysis of presented graphs on Figure 7 where a decrease of measured stress is present, starting from 13th day, which indicates certain changes within the microstructure. It is evident that an increase in fibre content improved bridging of existing cracks by preventing their further opening. With the action of shrinkage, fibres transmit forces through the crack and thus create tensile stresses along the ring [40]. For composite containing small amount or no fibres, the loads transmitted to fibres are low

and second crack does not form. At the same time, increased proportion of fibres causes development of more cracks with smaller widths. This explains why mix 15RTPF has obtained a macrocrack at later age and has a higher deformation of the steel ring.

Visual inspection on specimens made from concrete with polypropylene fibres, PP, 5RTPF, and 10RTPF mix shows similar results (Figure 8). Cracks determined by visual inspections were bigger and with larger widths compared to those detected by strain gauges. Detection of such small crack is impossible without methods such as acoustic emission or similar ones. Crack width of concrete with polypropylene fibres was the same as that for the concrete with 10 kg/m³ of RTPF and equals 0.15 mm. For mix 5RTPF, crack width was 0.25 mm indicating that due to its geometrical characteristic 5 kg of RTPF per m³ is too small replacement for 1 kg of used polypropylene fibres (length 19 mm).

3.4. Total Shrinkage. Total shrinkage as measured and presented here is actually combined of all aforementioned deformations, since none of the other deformations was subtracted. Therefore, following diagram and values present total shrinkage of a certain mix. Results of testing total shrinkage of concrete with RTPF, as well as of the plain concrete and concrete with polypropylene fibres, are shown in Figure 9. The results represent the mean value obtained from three samples.

During the first part of the measuring period, until the 15th day after casting, all mixes had similar shrinkage rates. In the following period, from 15th day up until 42nd day, a small difference between the mixes started to appear. From 42nd day after casting onwards, up until the end of the measurement period, the total shrinkage of referent mix PC started to increase significantly, while deformation of other mixes was stable. Comparison between mixes PP, 10RTPF, and 15RTPF showed similar behaviour although a slight increase in shrinkage was present with increase of RTPF in concrete. The results had a different trend compared to the ones obtained from autogenous shrinkage but were in accordance with previous research in this field [13, 18].

4. Conclusions

From the presented results of testing fresh state properties and mechanical properties, it can be concluded that the addition of RTPF does not induce negative changes of

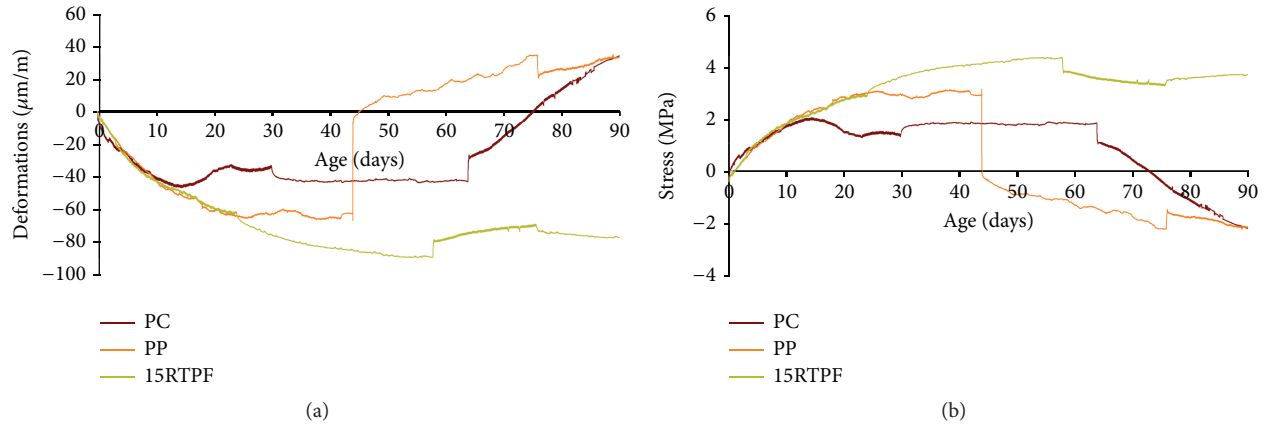


FIGURE 7: Restrained shrinkage: (a) stress and (b) deformations for ring specimens.

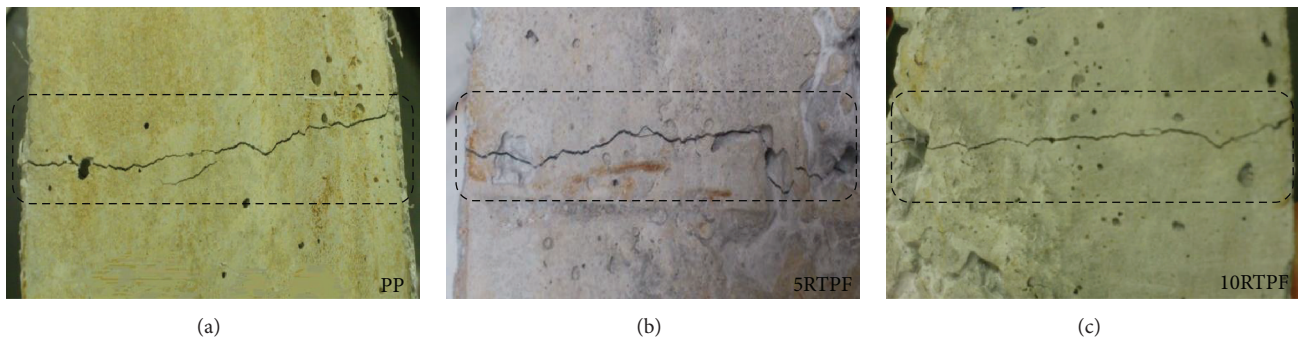


FIGURE 8: Crack width obtained by visual inspection for mixes: (a) PP, (b) 5RTPF, and (c) 10RTPF.

workability and compressive strength of concrete. The main expected influence of the addition of RTPF was on early deformation properties. Following properties were tested: autogenous, restrained and total shrinkage.

Deformation due to autogenous shrinkage is significantly decreased when 1 kg/m^3 of PP is added to concrete mix and further decreases when 5, 10, and 15 kg/m^3 are added (decrease of 63, 72, 89, and 92%, resp., compared to plain concrete at age of 90 days). From the results of deformation due to total shrinkage during drying, no strong and unanimous conclusion can be withdrawn. All concrete mixes exhibit faster deformation during the first days of drying, followed by a slower and constant increase in deformation during later days. The difference is within standard deviation of the measured values. Even though the addition of fibres did not cause detectable changes in total shrinkage, restrained shrinkage was significantly influenced. Ring test method used in the present study indicates that, compared to plain concrete, concrete with the addition of PP fibres and RTPF can withstand higher stresses formed due to restraining of shrinkage. Substituting PP with 15 kg/m^3 of RTPF additionally improved concrete behaviour, increasing tensile stresses that concrete can withstand prior to the crack for up to 53% compared to plain concrete and 30% compared to concrete with 1 kg/m^3 of PP fibres.

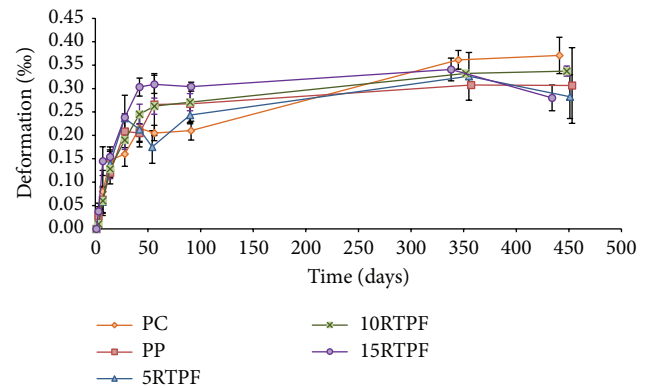


FIGURE 9: Total shrinkage of the concrete mixes with RTPF, polypropylene fibre, and comparable plain.

Based on the performed tests and obtained results in the present study, it can be concluded that RTPF can be used as substitution of PP fibres, since they do not induce negative effects on concrete mechanical properties but do enhance concrete behaviour during shrinkage. The addition of 5 kg/m^3 was found to be a sufficient amount of fibres, in order to reach the same properties as with 1 kg/m^3 PP

fibres. Furthermore, if we want to obtain further decreases of deformation, additional amount of RTPF could be used without compromising other concrete properties (tested in this study). The next step of the research is to evaluate durability properties of mixes with the addition of RTPF, as well as behaviour during exposure to high temperatures.

Conflict of Interests

The authors declare that there is no conflict of interests regarding the publication of this paper.

Acknowledgments

The researches presented in this paper are conducted within the project “Anagennisi: Innovative Reuse of all Tyre Components in Concrete” funded by the European Commission under the 7th Framework Programme Environment topic. Authors would like to thank Irena Pucic, Ph.D., Ruder Boskovic Institute, Division of Material Chemistry, for her contribution for qualitative and semiquantitative analysis of a sample of RTPF fibres. Authors would also like to thank Associate Professor Edita Vujasinovic, Ph.D., and Marijana Pavunc Samarzija, mag. ing. techn. text, University of Zagreb, Faculty of textile technology, Department of Materials, Fibres and Textile Testing, Centre for Development and Transfer of Textile and Clothing Technologies and Fashion Design, for their contribution for preliminary geometrical characterization of RTPF fibres. Authors would like to thank Professor Mirela Leskovic, Ph.D., University of Zagreb, Faculty of Chemical Engineering and Technology for her contribution in determination of RTPF contact angle. Authors would like to thank GUMIIMPEX for their support and student Andrija Šokman for his contribution during experimental work.

References

- [1] R. I. Gilbert, “Shrinkage, cracking and deflection—the serviceability of concrete structures,” *Electronic Journal of Structural Engineering*, vol. 1, pp. 15–37, 2001.
- [2] American Concrete Institute, “Report on the physical properties and durability of fiber-reinforced concrete,” ACI 544.5R-10, 2010.
- [3] D. Saje, B. Bandelj, J. Šušteršič, J. Lopatič, and F. Saje, “Autogenous and drying shrinkage of fibre reinforced high-performance concrete,” *Journal of Advanced Concrete Technology*, vol. 10, no. 2, pp. 59–73, 2012.
- [4] K. Smith and T. Atkinson, “PP fibres to resist fire induced concrete spalling,” *Tunneltalk*, 2010, <http://www.tunneltalk.com/Polypropylene-fibres-Nov10-Resistance-to-concrete-spalling-under-fire.php>.
- [5] R. N. Swamy and H. Stavrides, “Influence of fiber reinforcement on restrained shrinkage and cracking,” *ACI Journal Proceedings*, vol. 76, no. 3, pp. 443–460, 1979.
- [6] J. Ideker and J. Banuelos, “The use of synthetic blended fibers to reduce cracking risk in high performance concrete,” Final Report, Oregon Department of Transportation, Salem, Ore, USA, 2014.
- [7] M. A. Sanjuán and A. Moragues, “Polypropylene-fibre-reinforced mortar mixes: optimization to control plastic shrinkage,” *Composites Science and Technology*, vol. 57, no. 6, pp. 655–660, 1997.
- [8] A. E. Naaman, T. Wongtanakitcharoen, and G. Hauser, “Influence of different fibers on plastic shrinkage cracking of concrete,” *ACI Materials Journal*, vol. 102, no. 1, pp. 49–58, 2005.
- [9] D. Myers, T. H. Kang, and C. Ramseyer, “Early-age properties of polymer fiber-reinforced concrete,” *ACI Materials Journal*, vol. 2, no. 1, pp. 9–14, 2008.
- [10] N. Banthia and R. Gupta, “Influence of polypropylene fiber geometry on plastic shrinkage cracking in concrete,” *Cement and Concrete Research*, vol. 36, no. 7, pp. 1263–1267, 2006.
- [11] D. Saje, B. Bandelj, J. Šušteršič, J. Lopatič, and F. Saje, “Shrinkage of polypropylene fibre reinforced high performance concrete,” *Journal of Materials in Civil Engineering*, vol. 23, no. 7, pp. 941–952, 2011.
- [12] ACI 544.1R-96, “Report on fiber reinforced concrete,” Reported by ACI Committee 544.1 R-96, 2009.
- [13] K. Folliard, C. Smith, G. Sellers, M. Brown, and J. E. Breen, “Evaluation of alternative materials to control drying shrinkage cracking in concrete bridges,” Research Report FHWA/TX-04/0-4098-4, The University of Texas at Austin, 2004.
- [14] T. Aly, J. G. Sanjayan, and F. Collins, “Effect of polypropylene fibers on shrinkage and cracking of concretes,” *Materials and Structures*, vol. 41, no. 10, pp. 1741–1753, 2008.
- [15] A. Sadrmomtazi and A. Fasihi, “Influence of polypropylene fibers on the performance of nano-SiO₂-incorporated mortar,” *Iranian Journal of Science and Technology Transactions of Civil Engineering*, vol. 34, no. 4, pp. 385–395, 2010.
- [16] M. Serdar, A. Baričević, M. Jelčić Rukavina, D. Bjegović, and M. Pezer, “D4.1: RTPF reinforced concrete,” FP7 Project: Innovative Reuse of All Tyre Components in Concrete, 2014.
- [17] A. Baričević, D. Bjegović, N. Štirmer, and M. Pezer, “D4.2: RTPF sprayed concrete,” FP7 Project: Innovative Reuse of all Tyre Components in Concrete, 2014.
- [18] M. Serdar, A. Baricevic, S. Lakusic, and D. Bjegovic, “Special purpose concrete products from waste tyre recyclates,” *Građevinar—Journal of the Croatian Association of Civil Engineers*, vol. 65, pp. 793–801, 2013.
- [19] D. Bjegović, A. Baričević, S. Lakušić, D. Damjanović, and I. Duvnjak, “Positive interaction of industrial and recycled steel fibres in fibre reinforced concrete,” *Journal of Civil Engineering and Management*, vol. 19, no. 1, pp. S50–S60, 2013.
- [20] S. Mavridou and N. Oikonomou, “Utilization of textile fibres from worn automobile tires in cement based mortars,” *Global Nest Journal*, vol. 13, no. 2, pp. 176–181, 2011.
- [21] M. Serdar, A. Baričević, D. Bjegović, and S. Lakušić, “Possibilities of use of products from waste tyre recycling in concrete industry,” *Journal of Applied Engineering Science*, vol. 12, no. 1, pp. 89–93, 2014.
- [22] E. Vujasinović and M. Pavunc Samarzija, *Geometrical Characterization of RTPF Fibres*, Faculty of Textile Technology, Department of Materials, Fibres and Textile Testing, Centre for Development and Transfer of Textile and Clothing Technologies and Fashion Design, 2015.
- [23] I. Pucić, *Analysis of Textile Fibres for Anagennisi Project*, Ruder Bošković Institute, Zagreb, Croatia, 2014.
- [24] Holcim, 2015, <http://www.holcim.hr/fileadmin/templates/HR/doc/Razno/Holcim.Majstor.i.Holcim.Ekspert.cement.uvrecani.brosura.05.2009.pdf>.
- [25] CEN Testing fresh concrete—Part 6: Density (EN 12350-6:2009), Brussels, 2009.

- [26] CEN Testing fresh concrete—Part 2: Slump-test (EN 12350-2:2009), Brussels, 2009.
- [27] CEN Testing fresh concrete—Part 7: Air content—pressure methods (EN 12350-7:2009), Brussels, 2009.
- [28] CEN Testing hardened concrete—Part 3: Compressive strength of test specimens (EN 12390-3:2009), Brussels, Belgium, 2009.
- [29] I. Gabrijel, M. Jelcic Rukavina, and D. Bjegovic, “Autogenous deformations of dolomite based self-compacting concretes with different mineral,” in *Proceedings of the RILEM International Workshop on Performance-Based Specification and Control of Concrete Durability*, D. Bjegovic, H. Beushausen, and M. Serdar, Eds., pp. 507–514, RILEM Publications S.A.R.L., Zagreb, Croatia, June 2014.
- [30] H. R. Shah and J. Weiss, “Quantifying shrinkage cracking in fiber reinforced concrete using the ring test,” *Materials and Structures*, vol. 39, no. 293, pp. 887–899, 2006.
- [31] Z. Bayasi and J. Zeng, “Properties of polypropylene fiber reinforced concrete,” *ACI Materials Journal*, vol. 90, no. 6, pp. 605–610, 1993.
- [32] Committee E-701, “Reinforcement for concrete—materials and applications,” ACI Education Bulletin E2-00, Materials for Concrete Construction, 2006.
- [33] M. Iveković, *Fire resistance of concrete with waste materials [M.Sc. thesis]*, Faculty of Civil Engineering, University of Zagreb, Zagreb, Croatia, 2013.
- [34] E. Seferovic, “Polypropylene fibers in the support work for the Sveti Rok tunnel,” *Gradjevinar—Journal of the Croatian Association of Civil Engineers*, vol. 54, no. 9, pp. 535–539, 2002.
- [35] M. Skazlic, *Hybrid high performance fibre-reinforced concrete [M.Sc. thesis]*, Faculty of Civil Engineering, University of Zagreb, Zagreb, Croatia, 2003.
- [36] R. Kumar, P. Goel, and R. Mathur, “Suitability of concrete reinforced with synthetic fiber for the construction of pavements,” in *Proceedings of the 3rd International Conference on Sustainable Construction Materials and Technologies*, Kyoto, Japan, August 2013.
- [37] E. E. Holt, *Early Age Autogenous Shrinkage of Concrete. Espoo 2001. Technical Research*, VTT Publications no. 446, Centre of Finland, 2001.
- [38] E. Marušić, *Predicting shrinkage deformation of high strength concrete [Ph.D. thesis]*, University of Zagreb Faculty of Civil Engineering, 2012.
- [39] D. P. Bentz, “A review of early-age properties of cement-based materials,” *Cement and Concrete Research*, vol. 38, no. 2, pp. 196–204, 2008.
- [40] H. A. Mesbah and F. Buyle-Bodin, “Efficiency of polypropylene and metallic fibres on control of shrinkage and cracking of recycled aggregate mortars,” *Construction and Building Materials*, vol. 13, no. 8, pp. 439–447, 1999.

Research Article

Feasibility of Using High-Performance Steel Fibre Reinforced Concrete for Simplifying Reinforcement Details of Critical Members

Seok-Joon Jang,¹ Dae-Hyun Kang,¹ Kyung-Lim Ahn,¹ Wan-Shin Park,²
Sun-Woong Kim,² and Hyun-Do Yun¹

¹Department of Architectural Engineering, Chungnam National University, Daejeon 305-764, Republic of Korea

²Department of Construction Engineering Education, Chungnam National University, Daejeon 305-764, Republic of Korea

Correspondence should be addressed to Hyun-Do Yun; wiseroad@cnu.ac.kr

Received 26 July 2015; Accepted 27 September 2015

Academic Editor: João M. L. Dos Reis

Copyright © 2015 Seok-Joon Jang et al. This is an open access article distributed under the Creative Commons Attribution License, which permits unrestricted use, distribution, and reproduction in any medium, provided the original work is properly cited.

This paper addresses the effects of hooked-end steel fibre contents on the mechanical properties of high-performance concrete (HPC) and investigates the feasibility of utilizing steel fibres to simplify the complicated reinforcement detailing of critical HPC members under high shear stress. Mechanical properties of HPCs with specified compressive strength of 60 and 100 MPa include the flow, air content, compressive strength, and flexural strength. The effectiveness of 1.50% steel fibre content on the shear behaviour of diagonally reinforced concrete coupling beam without additional transverse reinforcement was investigated to alleviate complex reinforcing details for the full section confinement of diagonal bar groups. The test results revealed the incorporation of steel fibres significantly affected the mechanical properties of the HPCs. For diagonally reinforced coupling beam (SFRCCB) without additional transverse reinforcement, the addition of 1.5% steel fibre content into 60 MPa HPC coupling beam provides similar cracking and structural behaviours compared to those of diagonally reinforced coupling beam (CCB) with full section confinement details. However, the ductility of SFRCCB was less than that of CCB. It is recommended that both stirrups and steel fibre should be used for fully confining the diagonal bar groups of coupling beams to achieve the ductile behaviour.

1. Introduction

Steel fibrous concrete is a composite material that contains randomly distributed steel fibres in the conventional concrete with the brittle nature. The inclusion of steel fibres significantly improves the tensile strength, postcracking characteristics, and toughness of concrete due to the crack-bridging of added steel fibres. Over the last 40 years, extensive efforts have been devoted to investigate the effects of the incorporation of steel fibres on the mechanical properties of normal-strength concrete [1] as well as the effectiveness of steel fibres as shear reinforcement in the structural elements [2–4].

To investigate the effect of steel fibres on the shear behaviour of reinforced concrete (RC) beams, Narayanan and Darwish [2] carried out 33 shear tests on simply supported rectangular beams with crimped steel fibres as web reinforcement. It was reported that the crack patterns of

steel fibre reinforced concrete (SFRC) beams were similar to those shown in the RC beams with conventional stirrups; the ultimate shear strength of RC beam with 1% crimped steel fibres also exhibited equivalent strengths obtained from RC beam with shear stirrups due to the improvement in dowel action and arch action resulting from the inclusion of steel fibres. Even after their study, in order to improve the shear performance of shear-dominant RC beam, the enhancement of brittle behaviour of conventional concrete in diagonal tension by adding steel fibres has been proposed and investigated over the last decades [5–11].

The replacement of transverse reinforcement with steel fibres in the RC beams was first tried at the early 1970s. Then, a dozen studies have been presented [3, 4, 9, 12–18]. Batson et al. [12] reported first that steel fibres were feasible to replace transverse reinforcements in conventional RC beams. Swamy and Bahia [13] showed that steel fibres control

the dowel cracking, deflection, strains, and rotation due to shear loads. The effectiveness of both steel and synthetic fibres of various kinds was investigated by Li et al. [9]. Their work demonstrated that the improvement of tensile performance in the concrete through fibre reinforcements can be translated into shear performance enhancement. The results obtained by Casanova and Rossi [3] showed that the replacement of transverse reinforcements in 90 MPa high-strength concrete (HSC) beams with 1.25% steel fibres could obtain equivalent performances of HSC beams with 1.1% conventional transverse reinforcements. Cucchiara et al. [4] conducted experimental tests on the hooked-end SFRC beams with different amount of shear reinforcement, shear-to-span ratio, and fibre volume fraction. Their test results indicated that the addition of hooked-end steel fibres in the shear-dominant RC beams can transform the brittle behaviour characterized by shear failure into a ductile one by flexural failure. These results confirmed the feasibility of using steel fibres instead of increasing the amount of shear reinforcement for 40 MPa normal-strength concrete (NSC) beams. The use of steel fibres as shear as well as torsional reinforcement was also studied to examine the effectiveness of fibres as a potential replacement of conventional stirrups [14]. It is reported that the fibrous concrete beams exhibited improved torsional performance compared with the corresponding conventional concrete beams. Recently, Minelli and Plizzari [16] showed that a relatively low amount, less than 0.7%, of steel fibres could remarkably improve the shear strength and ductility of concrete beams without transverse reinforcement. Chalioris [19] investigated the effect of steel fibres in shear-dominant reinforced concrete beams under cyclic loadings. His tests indicated that not only do steel fibres inhibit the development of cracking (crack propagation and crack width grow) but they also prevent cracks from closing during the reversal loading. Further, SFRC proved to be capable of supporting cyclic loading conditions exhibiting greater energy dissipation capacities with respect to the plain concrete.

Despite extensive laboratory demonstrations on usefulness of fibres in various structural applications, the practical application of fibres in construction industries is limited. Limited information on the design methods and specifications makes it difficult for the engineers to use SFRC for structural elements in the buildings and infrastructures. If the required shear force of a reinforced concrete beam is not greater than half of design shear strength provided by concrete, the replacement of the conventional shear reinforcement with deformed steel fibres was allowed in the ACI 318-08 [20]. The addition of deformed steel fibre should be more than 0.75% at fibre volume fraction and compressive strength of SFRC does not exceed 42 MPa. SFRC shall be satisfied with the flexural performance criteria as described in ACI 318-08 S5.6.6. Jain and Singh [18] investigated the validity of flexural performance criteria in the SFRC recommended in the ACI 318-08 for replacing minimum shear reinforcement with deformed steel fibres. They reported that an allowable shear stress value of $0.3\sqrt{f'_c}$ MPa is for being reinforced with the deformed steel fibres instead of transverse reinforcement in the NSC and HSC beams.

The large amount of experimental studies conducted in this sector has been concentrated on shear strength and crack patterns of fibrous NSC beams subjected to monotonic loading. A limited amount of research has focused on the hysteretic behaviours of shear-dominant RC beams incorporating steel fibres instead of conventional transverse reinforcements under reversed cyclic loading.

Recently, social needs for high-rise buildings and large infrastructures lead to an urgent development for higher performance engineering materials possessing high strength, toughness, energy dissipation capacity, durability, and so forth. High-performance steel fibre reinforced concrete (HP-SFRC) is a kind of HPC which has made noticeable advances during last decades. However, very limited research work on mechanical performances and applications of HP-SFRC with different fibre volume fractions and compressive strengths has been conducted so far.

In this study, the influence of steel fibre contents on the mechanical properties of high-performance concrete (HPC) is first experimentally investigated. The flexural performance of high-performance steel fibre reinforced concrete (HP-SFRC) with different fibre volume fractions was evaluated in accordance with ASTM C 1609. The experimental programme also includes the tests on shear-dominant diagonally reinforced concrete coupling beams with and without transverse reinforcement specified in the ACI 318-11 Section 21. The use of hooked-end steel fibres as replacement of transverse reinforcement in the short coupling beam with diagonal reinforcement is investigated herein, in an attempt to simplify the placement of reinforcing bars and reduce congestion without sacrificing shear strength, ductility, and energy absorption capacity under reversed cyclic loading.

2. Mechanical Properties of High-Performance Steel Fibre Reinforced Concretes (HP-SFRCs)

The influence of steel fibres on the mechanical properties of high-performance concretes (HPCs) with specific compressive strengths of 60 and 100 MPa was investigated in this study. This section describes the experimental programme, such as materials used, mix proportion and mixing, test method, and fresh and hardened properties, carried out to examine the effect of adding steel fibres on the mechanical properties of HPC.

2.1. Materials. In this study, HP-SFRCs were mixed using hooked-end steel fibres, fine aggregate, coarse aggregate, and cement paste. The cement paste consists of ordinary Portland cement (OPC), water, superplasticizer, and silica fume. Ordinary Portland cement conforming to Korean Industrial Standard (KS), KS L 5201, was used for the cement pastes. Silica fume was a commercially available product and was used for only 100 MPa high-performance concrete mixtures. A polycarbonate based superplasticizer was added to improve the workability of concretes. River sand with a fineness modulus of 3.1 and crushed aggregate of 13 mm maximum size were used and obtained from a local supplier. Steel fibres

TABLE 1: Mixture proportions of HPCs used in the study.

Mix notation	f'_c (MPa)	V_f (%)	Unit weight (kg/m ³)								
			Cement	Water	Aggregate	Sand	FA	SF	Fibres	SP	AE
06-SFRC00	60	0.0	662	199	537	894	0	0	0	3.97	1.32
06-SFRC05		0.5							39		
06-SFRC10		1.0							79		
06-SFRC15		1.5							118		
10-SFRC00	100	0.0	583	150	816	570	183	67	0	10.46	0
10-SFRC05		0.5							39		
10-SFRC10		1.0							79		
10-SFRC15		1.5							118		

f'_c is a specific compressive strength of HPC; V_f is steel fibre volume fraction; FA is fly ash; SF is silica fume; SP is superplasticizer; AE is air entraining reagent.

TABLE 2: Mechanical properties of HPCs used in the study.

Mix notation	Air content (%)	Slump (mm)	Compressive strength (MPa)		Flexural strength (MPa)	
			28 days (mean \pm SD)	90 days (mean \pm SD)	28 days (mean \pm SD)	90 days (mean \pm SD)
06-SFRC00	2.5	270	67.0 \pm 0.6	73.1 \pm 0.6	11.1 \pm 0.5	—
06-SFRC05	2.7	240	64.7 \pm 0.4	72.5 \pm 2.0	11.0 \pm 0.7	—
06-SFRC10	3.5	225	64.2 \pm 0.1	73.7 \pm 2.3	11.2 \pm 0.2	—
06-SFRC15	3.8	185	64.3 \pm 0.2	71.4 \pm 0.9	15.8 \pm 0.4	—
10-SFRC00	1.1	500	79.1 \pm 3.6	111.9 \pm 1.1	—	14.0 \pm 0.8
10-SFRC05	1.2	205	82.5 \pm 0.0	107.8 \pm 0.9	—	15.1 \pm 0.3
10-SFRC10	1.7	175	88.5 \pm 2.5	110.0 \pm 0.1	—	15.9 \pm 1.6
10-SFRC15	2.0	150	87.1 \pm 4.7	108.7 \pm 2.6	—	18.2 \pm 1.0

Each strength is an average of strengths from three specimens; SD is standard deviation.

used in this investigation were hooked-end bundled fibres with aspect ratio (l/d ; length over diameter ratio) of 60. The average fibre length is 30 mm, the nominal diameter is 0.5 mm, and the tensile strength is 1,100 MPa.

2.2. Mix Proportion and Mixing. The matrix compositions for HPCs were presented in Table 1 in this experiment. Each mixture was chosen to cover the parameters discussed in the experimental programme. The volume fractions of steel fibre in the HPC mixes with specific compressive strength of 60 and 100 MPa were 0, 0.5, 1.0, and 1.5%, respectively. In order to obtain the desired workability, only the superplasticizer dosage was varied. As described above, silica fume and fly ash were used for only 100 MPa HPC.

For the production of HP-SFRCs, the cementitious constituents, such as coarse aggregate, river sand, cement, and silica fume, were initially mixed dry in twin shaft mixer of 1 m³/h capacity. The superplasticizer was then diluted with the mixing water and added to the mixer. Fibres were dispersed by hand in small amounts into cement paste to avoid fibre balling and to achieve a uniform material consistency and good workability. For mixes with 1.5% fibre content, extra time was required for mixing and finishing the specimen surfaces. Fresh HP-SFRCs were cast into 100 \times 200 mm cylindrical moulds for a compressive strength test and into 100 \times 100 \times 400 mm prismatic moulds for flexural strength test. The specimens were demoulded after 24 h and

cured in a water tank until the age of testing. And then a strength test was carried out.

2.3. Test Methods. The workability of fresh HP-SFRC was assessed by using slump test according to KS F 2402. Air content was measured by using the pressure method in accordance with KS F 2409.

The compressive strength tests for cylindrical specimens at the curing age of 3, 7, and 28 days were carried out with a universal testing machine of capacity of 1,000 kN at a loading rate of 0.3 MPa/s. The flexural strength (modulus of rupture, MOR) tests were performed using prismatic specimens under four-point loading. The average mid-span deflection was measured with two transducers placed at the centre of the prismatic specimens. The compressive and flexural strength tests were conducted in accordance with KS F 2405 and KS F 2407, respectively.

2.4. Fresh Properties of HP-SFRC. Slump value workability and entrapped air content measurement were carried out on the fresh high-performance steel fibre reinforced concrete. The results are presented in Table 2. The results showed that air contents of 60 MPa HP-SFRCs decreased gradually with the increase of steel fibre content. The randomly distributed hooked-end steel fibre could possibly form air bubbles thus increasing the percentage of entrapped air. On the other hand, the air contents of 100 MPa HP-SFRCs with different amount

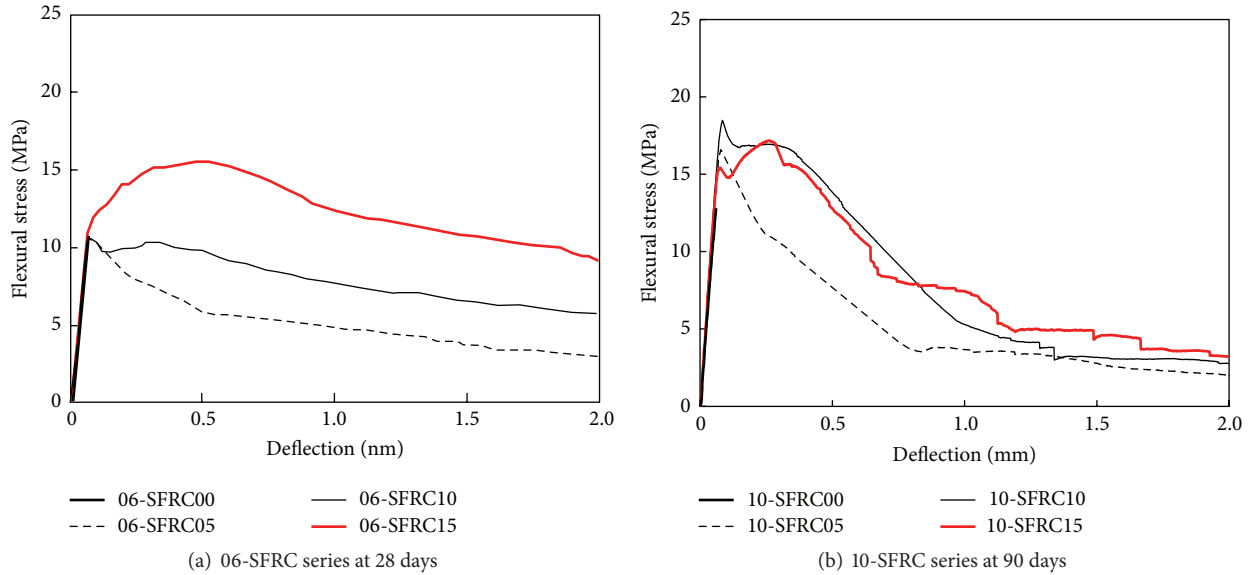


FIGURE 1: Typical load-deflection curves of HP-SFRC prisms.

of SP were in the range from 1.1% to 2.0% and did not show a clear trend like that of 60 MPa SFRC. The air contents of 60 MPa SFRCs were higher than those of 100 MPa SFRCs due to the AE admixture added to only 60 MPa SFRCs.

To estimate the workability of the fresh HP-SFRC according to steel fibre volume fraction, slump values for all the HP-SFRC mixtures were measured. In both 60 and 100 MPa SFRCs, as steel fibre volume percentage increases, the slump values decrease in all HP-SFRC mixtures as reported by existing studies [21–24]. In plain concrete mix with specific compressive strength of 100 MPa, the highest slump value was obtained because the incorporation of fly ash with spherical shape as cement replacement leads to the ball bearing effects in fresh concrete [22]. However, as the steel fibre volume fraction increases, the slump value in the 100 MPa HP-SFRC mixes reduced more remarkably than that in the 60 MPa HP-SFRCs.

2.5. Hardened Properties of HP-SFRC. The results for the compressive and flexural strength of all mixture at curing ages of 28 and 90 days are presented in Table 2. From the results for compressive strength, it is evident that the compressive strength of plain concrete with 60 and 100 MPa mixed in this study exceeded that obtained from varying volume percentage of hooked-end steel fibres. Similar result was reported also by other researchers [22]. Table 2 provided that, for HP-SFRC mixes with specific compressive strength of 60 MPa, the target compressive strengths could be gained at curing age of 28 days while the target strength for 100 MPa HP-SFRCs could be reached at curing age of 90 days.

The flexural strength and performance were evaluated according to ASTM C 1609 procedure. The measured load versus mid-span deflection curves of the 60 MPa HP-SFRC prisms at 28 days and 100 MPa HP-SFRC prisms at 90 days are shown in Figures 1(a) and 1(b), respectively. Figure 1(a) indicates that the incorporation of steel fibre volume ranging

from 0.0% to 1.0% in the 60 MPa SFRCs (06-SFRC00, 05 and 10) had little effect on the modulus of rupture of the prism specimens but significantly improved the postcracking behaviour. The load-deflection curve of 60 MPa SFRC (06-SFRC15) prisms with 1.5% fibre volume fraction showed a plateau before the applied load started to decrease. As shown in Figure 1(b), the flexural strength of 10-SFRC mix series improved with increasing of the fibre volume fraction. The enhancement of flexural strength started from 7.9% at 0.5% fraction and expanded to 30% at 2.0% fraction. The postcracking behaviours of 10-SFRC10 and 10-SFRC15 prisms are similar.

To evaluate the flexural toughness of hooked-end steel fibre reinforced concretes with different fibre volume fractions, the flexural toughness was calculated according to ASTM C 1609. As shown in Figure 2, flexural toughness (T_{150}^D) is measured with the total area under the load-deflection curve up to a specified deflection, 1/150 of the span length. Therefore, the equivalent flexural strength ratio ($R_{T,150}^D$) for evaluating the flexural performance is obtained from the following equation, using first-peak strength (f_1).

Figure 3 shows the flexural performance criteria as described in ACI 318-08 S5.6.6 and fibre volume fraction relationship. Shade area in Figure 3 is the condition satisfying the flexural performance criteria in ACI 318-08 S5.6.6. From Figure 3, it can be recognized that about 1.2% and 1.5% hooked-end steel fibre volume fraction for 60 MPa and 100 MPa SFRCs are the replacement level of minimum shear reinforcement, respectively.

3. Feasibility of Using HP-SFRC as Transverse Reinforcements in Short Coupling Beams

The seismic design provisions of the current ACI 318-11 prescribe extensive requirements for the design and details

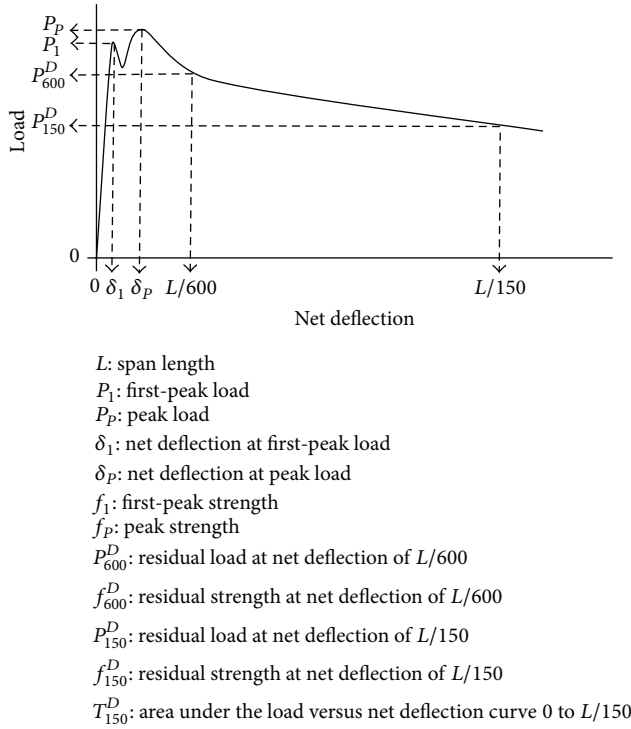


FIGURE 2: Flexural toughness defined by ASTM C1609. $R_{T,150}^D = 150T_{150}^D / f_1 b d^2 \times 100\%$, where b is the width (mm) of the specimen and d is the height (mm) of the specimen.

of coupling beams in the special reinforced concrete coupled shear wall system. Diagonal reinforcement groups are required for coupling beams having a net span-to-depth ratio (l_n/h) less than 2 and a factored shear stress on the gross concrete section exceeding $0.33\sqrt{f_c'} \text{ MPa}$.

It is assumed that the diagonal bar group elements form a truss, with one group acting as the tension member and the other as the compression member for an applied shear load [25]. To suppress premature buckling of the diagonal bar groups, the bars should be confined by transverse reinforcement across the span of the beam to satisfy the same confinement requirements used for tied column. Because these reinforcing details are complex and difficult, ACI 318-08 introduced an alternative detailing option, where transverse reinforcement is placed around the beam cross-section to provide confinement and suppress buckling without transverse bars around the diagonal bar groups. In alternative details of diagonally reinforced coupling beams, stirrup and additional transverse reinforcement such as crosstie and leg bars should be placed closely at spacing not exceeding the smaller of 150 mm and six times the diameter of diagonal bar [20]. Providing additional transverse reinforcement around the entire cross-section also presents significant difficulties with regard to constructability. The utilization of steel fibre or spiral reinforcement as an alternative of the commonly used stirrup and additional transverse reinforcement can be considered to improve the constructability of short reinforced concrete coupling beams.

In this study, the replacement of the stirrup and additional transverse reinforcement with hooked-end steel fibres is also examined to reduce the construction time and cost for diagonally reinforced concrete coupling beams. The experimental programme includes two short coupling beam tests under reversed cyclic loading. One diagonally reinforced coupling beam (CCB) was manufactured with conventional concrete and alternative details as reference beam. The other beam (SFRCCB) was constructed using 60 MPa HP-SFRC with a fibre volume fraction of 1.5%.

3.1. Test Specimens. To investigate the feasibility of replacing stirrup and additional transverse reinforcement with hooked-end steel fibres for the shear-dominant short coupling beams, two specimens were designed, constructed, and tested up to failure. Two diagonally reinforced concrete coupling beam specimens with l_n/h of 2.0 have the same configuration and cross-sectional properties and differ in the layouts of the transverse reinforcement. The characteristics of the beams are shown in Figure 4. As shown in Figure 4, the cross-section of all coupling beams was equal to 200 mm width \times 300 mm depth. At each end of a coupling beam specimen, a rectangular end block with dimensions of 500 mm wide \times 350 mm deep \times 1,270 mm long was used to simulate the surrounding walls and apply the required loading histories.

Conventional concrete coupling beam (CCB) specimen was constructed in accordance with the full section confinement option for diagonally reinforced coupling beams specified in the seismic design provisions of ACI 318-08. Each diagonal bar group consists of eight 10 mm diameter deformed steel bars. The stirrup and additional transverse reinforcement were placed at 50 mm spacing of 6 mm diameter deformed bars around the entire cross-section to satisfy the full section confinement option for CCB specimen. High-performance steel fibre reinforced concrete coupling beam specimen (SFRCCB) is used for a direct comparison with CCB to evaluate the feasibility of replacing transverse crossties and hoop legs with steel fibres. The SFRCCB specimen differs from CCB specimen in that SFRCCB is made with only 60 MPa HP-SFRC instead of stirrup and additional transverse reinforcement in the CCB specimen.

3.2. Testing Setup and Loading Procedure. As shown in Figure 5, diagonally reinforced short coupling beams were tested in a vertical plane with end blocks simulating wall boundary zones at each end. The specimens were subjected to cyclic shear displacement through specially designed strong frame with four pin joints. The strong frame consisted of two steel columns pin-connected with upper loading beam and lower reaction beam. Both end blocks of coupling beam specimen were fully fixed to the upper and lower steel beams of strong frame. Displacements were induced to upper end block of coupling beam by means of an actuator with 1,000 kN capacity connected to the upper steel beam.

Loading histories for coupling beam specimen consist of load-controlled and displacement-controlled cycles. Load control was conducted at 50, 100, 150, and 200 kN. After 200 kN, displacement control used increments of percent chord rotation, defined as the relative lateral displacement

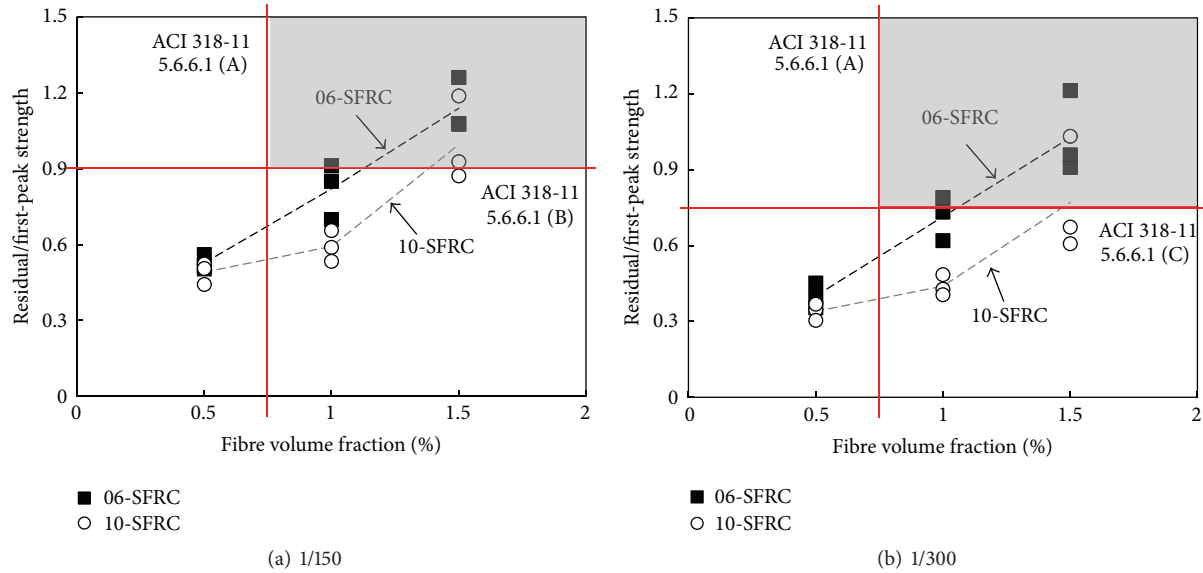


FIGURE 3: Flexural performance of HP-SFRC prisms in accordance with ASTM C 1609.

over the clear span of the coupling beam divided by the beam clear span. Two full cycles were performed at each level of chord rotation up to 5%.

To monitor the external deformations of the coupling beams throughout the test, nine displacement transducers (DTs) were fixed to the surface of specimens. To record the strains developed in the reinforcing steel, strain gauges were mounted on the diagonal, longitudinal, and transverse reinforcement.

3.3. Damage Progress. The cracking process and failure mode of the diagonally reinforced coupling beams differed in accordance with the details of transverse reinforcement. At the beginning of the tests, all the coupling beams showed similar cracking patterns. Cracking patterns at each final cycle of 0.5%, 1.0%, and 2.5% chord rotations for both CCB and SFRCCB beams are shown in Figure 6.

Under the shear load of about 100 kN at load-controlled stage, initial flexural cracks were observed at 100 mm above the coupling beam-wall joint of CCB specimen. Up to chord rotation of 1.0%, flexure-shear cracks occurred extensively through the beam span. Then, horizontal cracks at the tension edge of interface between beam and wall element appeared and as the chord rotation increased, the horizontal crack propagated into the centre of beam without new cracks on the beam span. The main crack formation had occurred by the end of 2.0% chord rotation cycle and it consisted of two or three major shear cracks in each loading direction and some flexural cracks at near joints between beam and wall elements. At the chord rotation of 2.5%, the crushing of cover concrete at the edge of compressive region was started. As the loading cycles progressed, the existing flexural cracks widened and cover concrete spalled. At chord rotation of 3.0% in the negative loading direction, the diagonal reinforcements in compression were buckled and damage was concentrated in the lower region of joint between beam and walls. The CCB

specimen failed in concrete spalling at flexure-compressive region.

In SFRCCB specimen, initial cracks occurred at the same loading stage as the CCB specimen. Several flexural cracks were noted at the entire span of the SFRCCB. Up to the chord rotation of 1.0% as shown in Figure 6, flexural and shear cracks with small width and narrow spacing compared to CCB were observed in the SFRCCB specimen, as the hooked-end steel fibres were effective in bridging these cracks. However, as the applied chord rotation increased up to 1.5%, diagonal cracks widened abruptly. During the second cycle leading to a chord rotation of 2.0%, the SFRCCB specimen experienced a sudden reduction in the lateral load-resisting capacity with increasing significantly the width of diagonal cracks under both direction loadings. This shows that hooked-end steel fibres with length of 30 mm no longer bridge diagonal cracks at more than 1.5% chord rotation. In contrast with the flexural-compressive failure of CCB, the failure of SFRCCB was due to the formation of major diagonal cracks, indicating the shear failure. The replacement of transverse reinforcement for full confinement of entire section with hooked-end steel fibres in the shear-dominant coupling beam is effective at less than 1.5% chord rotation while under the large deformation of more than 1.5% chord rotation the incorporation of steel fibres cannot entirely replace transverse reinforcement due to the deterioration of fibres' bridging cracks. Similar results in the SFRC beams tested under monotonic loading were reported [2, 4].

3.4. Hysteretic Behaviour. The shear force versus chord rotation responses for CCB and SFRCCB specimens are shown in Figure 6. As shown in Figure 6(a), the CCB with diagonal reinforcements confined fully at the entire cross-section exhibited a large postyield ductile behavior with very limited strength degradation up to a chord rotation of 4.0% and 2.5% in the positive and negative loading directions,

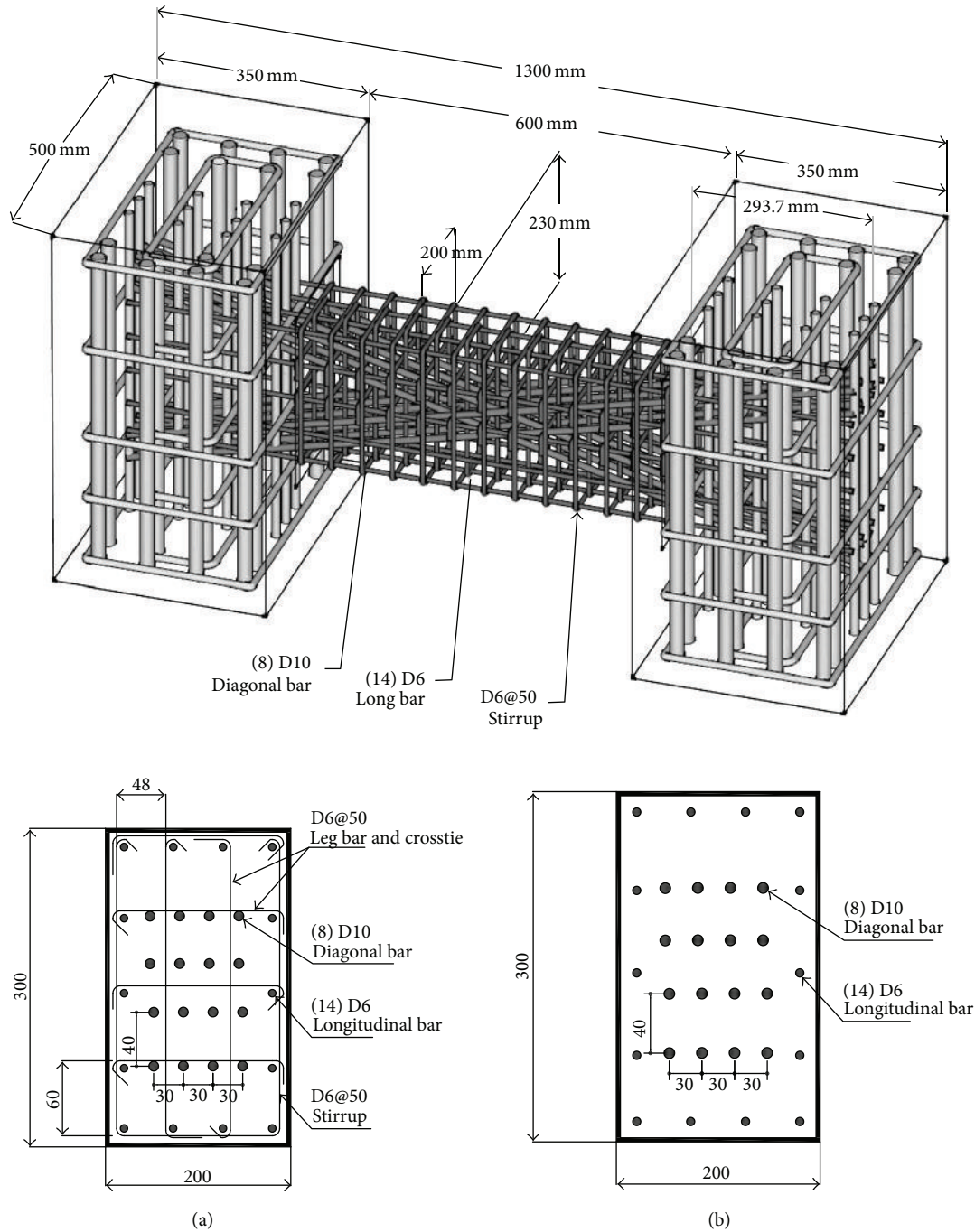


FIGURE 4: Details of diagonally reinforced coupling beams. (a) CCB specimen. (b) SFRCCB specimen.

respectively. The transverse reinforcement for confining the entire beam cross-section of diagonally reinforced concrete coupling beam as detailed in ACI 318-08, Section S21.9.7, was effective to delay the buckling of diagonal bar bundles in compression up to more than average chord rotation of 3.0%. Naish [26] reported that the hysteretic behaviours of both diagonally reinforced concrete coupling beams with full section confinement and diagonal confinement details were very similar over the full range of applied chord rotations. Through their test results, they concluded that, for diagonally

reinforced concrete coupling beams with l_n/h of greater than 2.0, the full section confinement provided equivalent performance compared to diagonal confinement.

It is also clear from Figure 6 that SFRCCB shows a reasonably stable response up to 2.0% chord rotation in both positive and negative loading directions. The SFRCCB specimen exhibited abruptly strength degradation after reaching the peak shear stress at a chord rotation of 2.0%. These results demonstrated that even though the fibre volume fractions satisfying the flexural performance criteria of SFRC in ACI

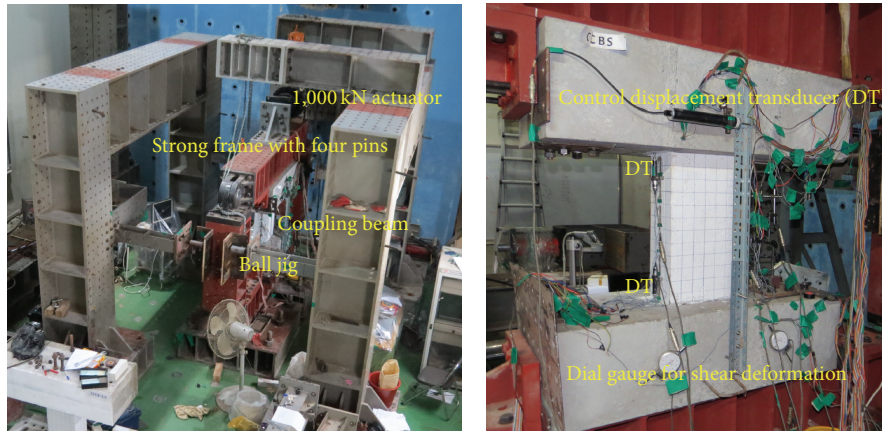


FIGURE 5: Test setup for coupling beams.

318-08 S5.6.6 were effective in controlling cracking opening and confining the diagonal group bars in the diagonally reinforced coupling beams up to a chord rotation of 2.0%, the steel fibre incorporation in the diagonally reinforced coupling beams without transverse reinforcement could not provide appreciable resistance against diagonal shear cracks and buckling of diagonal group bars under large deformation beyond 2.0% chord rotation. This result is similar to Narayanan and Darwish's conclusion that the steel fibres cannot entirely replace the conventional shear reinforcement when the structural elements are under very high shear stress.

Both CCB and SFRCCB specimens were designed to resist approximately $0.32\sqrt{f_{ck}}$ MPa. The average maximum applied shear stress in CCB and SFRCCB was $0.84\sqrt{f_{cu}}$ MPa and $0.82\sqrt{f_{cu}}$ MPa, respectively. Even though the transverse reinforcement detailed at entire beam cross-section for confining diagonal bar groups was completely eliminated in the SFRCCB specimen, the shear strength was equivalent to that of the corresponding CCB with conventional transverse reinforcements for diagonal bars. The similar trends in the SFRC beams without shear reinforcement under monotonic loading also were observed and reported [4, 27].

3.5. Average Shear Strains. The average shear strain in the coupling beam specimens was measured using two diagonal dial gauges over coupling beams. Figure 7(a) shows the average shear stress versus shear strain responses for CCB and SFRCCB specimen. Both specimens did not exhibit pinching due to diagonal reinforcement.

Figure 7(b) indicates the average shear strain and chord rotation relationship of conventional concrete and HP-SFRC coupling beams. As shown in Figure 7(b), it is clear that the rate of average shear strain increase in the SFRCCB was less than that in the CCB specimen. Shear strain in excess of 0.015 and 0.030 rad was recorded in SFRCCB and CCB specimen, respectively. Shear related damage started at shear strain larger than 0.010 and 0.025 rad in the SFRCCB and CCB, respectively. These shear strains can be considered as the shear distortion capacity of the coupling beams with different transverse reinforcing method for diagonal reinforcement group, only hooked-end steel fibre without stirrup

and conventional transverse reinforcements. As shown in Figure 6, more fine cracks in the SFRCCB were observed and the crack width was well controlled compared with CCB specimen up to 1.5% chord rotation due to fibre-bridging action. Up to 1.5% chord rotation, the steel fibres' bridging diagonal cracks in the SFRCCB specimen contributed to the reduction of the shear distortion. At more than 1.5% chord rotation in the SFRCCB without transverse reinforcements, the pullout and breaking of fibres bridging diagonal cracks led to abrupt strength reduction and diagonal shear failure.

3.6. Strain in the Diagonal Reinforcements. Figures 8(a) and 8(b) show the strain-chord rotation histories obtained from strain gauges placed on the diagonal reinforcement and located at the centre of CCB and SFRCCB specimens, respectively. There was substantial difference in the strain histories for diagonal bar in the CCB specimen with full section confinement compared with SFRCCB specimen incorporating hooked-end steel fibres instead of transverse confining reinforcement.

In CCB specimen, tensile strains in the diagonal bars increased as the test progressed while compressive strains did not increase and remained at about half of yielding strain to failure. The diagonal reinforcement in the CCB specimen yielded in tension during 1.5% chord rotation. Even after the tensile yielding of diagonal reinforcements, CCB specimen could exhibit a stable behaviour without the deterioration in strength because transverse reinforcement for full section confinement was effective to delay the buckling of diagonal bars.

In SFRCCB specimen, diagonal reinforcements in tension yielded during the loading of 1.0% chord rotation. Then tensile strains increased up to failure. Compressive strains in diagonal bars increased sharply as opposite to compressive strains in the CCB specimen. At 2.0% chord rotation, diagonal reinforcements in compression were buckled. From these results, it is shown that steel fibre volume, which satisfied the flexural performance criteria stipulated in ACI 318-08 S5.6.6, is not enough to confine the diagonal reinforcement in the short coupling beams with l_n/h of less than 2.0.

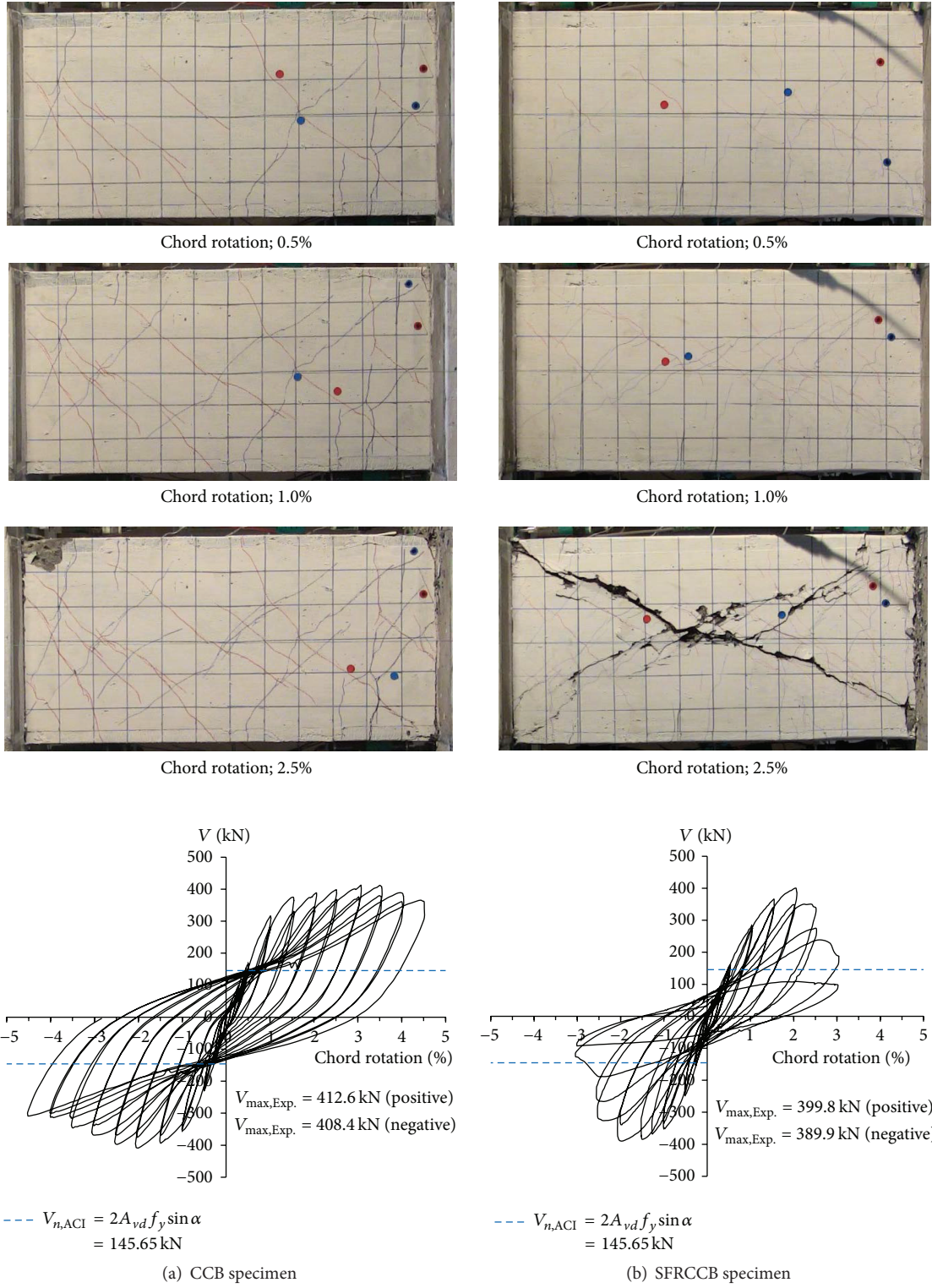


FIGURE 6: Cracking procedure and hysteretic behaviour of coupling beam specimens.

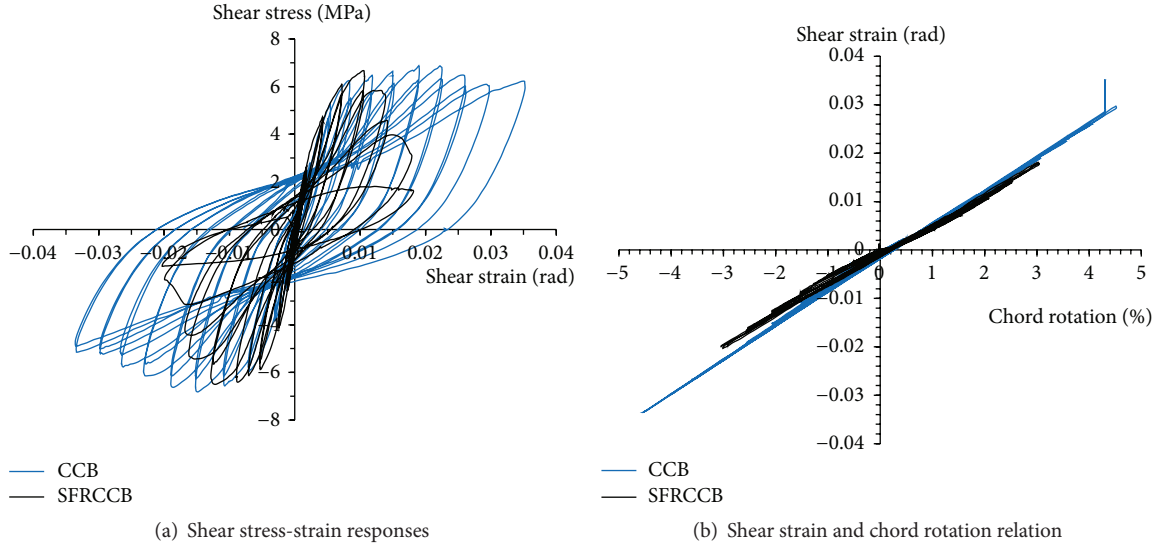


FIGURE 7: Average shear stress versus shear strain responses for coupling beam specimens.

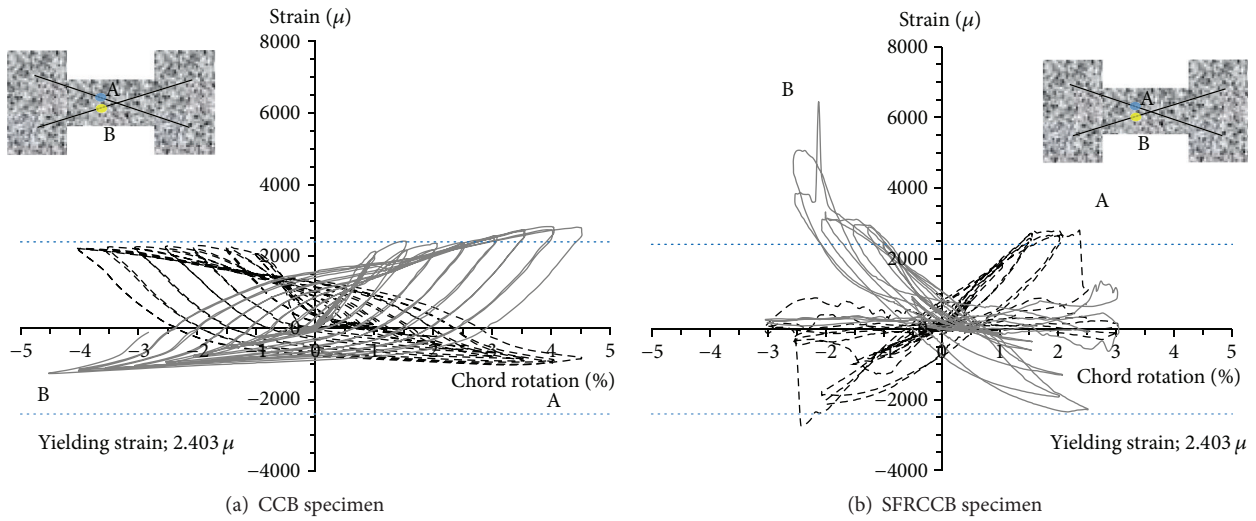


FIGURE 8: Strain behaviours of diagonal reinforcements in the coupling beams.

3.7. Stiffness Degradation and Energy Dissipation Characteristics. The stiffness of both coupling beams was evaluated in terms of the secant stiffness values obtained from peak-to-peak displacement for each hysteretic loop. As can be seen from load versus chord rotation loops, the stiffness decreased with an increase in the chord rotation. The stiffness degradation decreased as the chord rotation increased. The secant stiffness was normalised with respect to the initial secant stiffness to evaluate the stiffness retention capacity of the coupling beam specimens. The energy dissipation capacity of the coupling beam was defined as the area enclosed by the load versus chord rotation loops.

Figures 9(a) and 9(b) show the stiffness decay and cumulative energy dissipation capacity versus chord rotation for both coupling beam specimens, respectively. In Figure 8, it can be seen that up to 2.0% chord rotation, the stiffness

retention and energy dissipation capacities of SFRCCB specimen showed a similar trend compared with those of CCB specimen. Based on these results, it can be concluded that the addition of 1.5% steel fibre content into diagonally reinforced short coupling beams instead of transverse reinforcement for full section confinement was equivalently effective to retain stiffness and improve the energy dissipation capacity up to 2.0% chord rotation.

4. Summary and Conclusions

Based on the test results of high-performance steel fibre reinforced concrete (HP-SFRC) prismatic specimens, conventional concrete, and HP-SFRC short coupling beams with diagonal reinforcements, the following conclusions can be drawn:

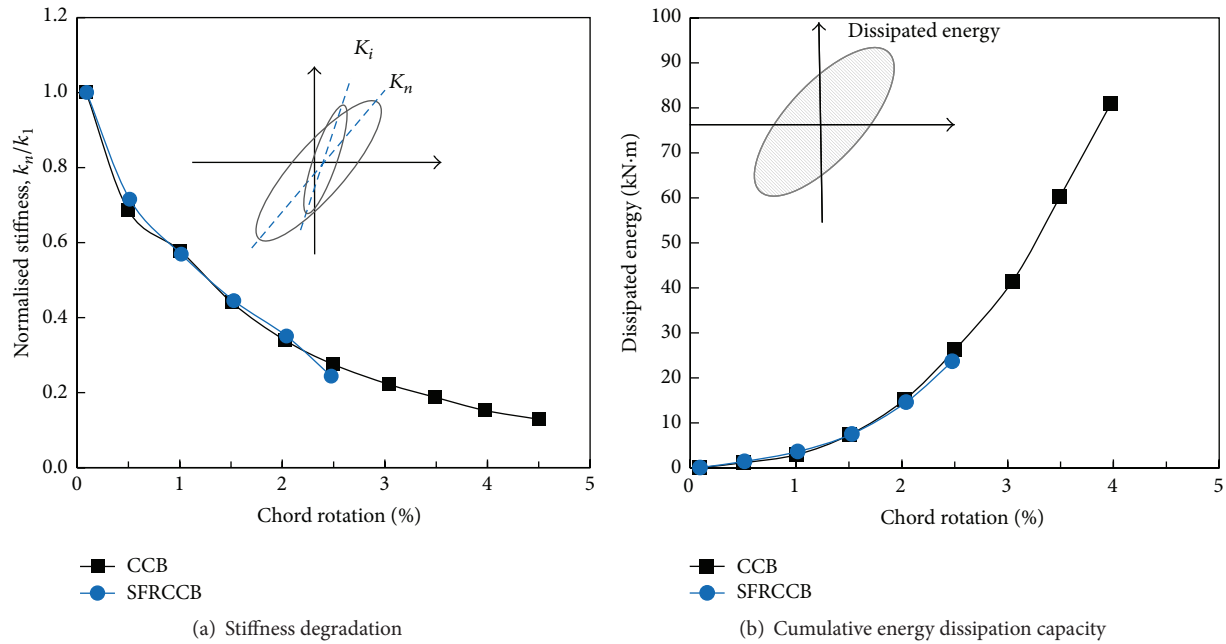


FIGURE 9: Stiffness retention and energy dissipation characteristics.

- (1) For all HP-SFRC mixtures mixed in this study, there was no problem in mixing and casting up to hooked-end steel fibre volume fraction of 1.5%. Fibres were distributed uniformly in the concrete matrix. However, increasing fibre content increased the amount of entrapped air and reduced the slump values of the fresh HP-SFRC.
- (2) The presence of hooked-end steel fibres had little effect on the compressive strength of HP-SFRC with specific compressive strength of 60 and 100 MPa. The modulus of rupture in the HP-SFRC slightly improved with increasing fibre volume fractions. The addition of 1.5% steel fibres to the 60 MPa and 100 MPa HPC caused a maximum increase of 42.3% and 30.0% compared with the modulus of rupture of HPC without steel fibres, respectively.
- (3) The postpeak behaviour of HPC was very improved with the incorporation of hooked-end steel fibre. For HP-SFRCs, the flexural toughness values calculated in accordance with the ASTM C 1609 procedure increased as steel fibre volume fraction increased. Hooked-end steel fibre volume fractions of 1.2% and 1.5% in the 60 and 100 MPa HPCs mixed in this study are sufficient to satisfy the flexural performance criteria specified in the ACI 318-08 S5.6.6 allowing the replacement of minimum shear reinforcement with deformed steel fibres.
- (4) The pattern and width of cracks developed in diagonally reinforced concrete coupling beam replaced all the transverse reinforcements with 1.5% hooked-end steel fibres under cyclic shear loadings, similar to those of the corresponding nonfibrous coupling beam with transverse reinforcements up to 1.5% chord rotation.
- (5) Due to crack-bridging action by steel fibre, more fine cracks distributed over the SFRC coupling beam. Fine cracks lead to the reduction of shear distortion. Steel fibre in the short coupling beam with aspect ratio of 2.0 is effective to inhibit the crack development and decrease the increasing rate of shear strain.
- (6) The presence of 1.5% fibre content in the 60 MPa high-strength concrete coupling beam with diagonal bar groups without transverse reinforcements specified in the seismic design provisions for coupling beams in the ACI 318-08 is sufficient to develop the equivalent shear resistance of conventional coupling beams with diagonal reinforcement groups confined transversely. To achieve a comparable level of ductility prior to shear failure of the diagonally reinforced short coupling beams, partial replacement of transverse reinforcements with steel fibre is necessary.

Conflict of Interests

The authors declare that there is no conflict of interests regarding the publication of this paper.

Acknowledgments

This research was supported by a grant (13SCIPA02) from Smart Civil Infrastructure Research Program funded by Ministry of Land, Infrastructure, and Transport (MOLIT) of Korea government and Korea Agency for Infrastructure Technology Advancement (KAIA).

References

- [1] P. R. Tadepalli, Y. L. Mo, and T. T. C. Hsu, "Mechanical properties of steel fibre concrete," *Magazine of Concrete Research*, vol. 65, no. 8, pp. 462–474, 2013.
- [2] R. Narayanan and I. Y. S. Darwish, "Use of steel fibers as shear reinforcement," *ACI Structural Journal*, vol. 84, no. 3, pp. 216–227, 1987.
- [3] P. Casanova and P. Rossi, "Can steel fibers replace transverse reinforcements in reinforced concrete beams?" *ACI Materials Journal*, vol. 94, no. 5, pp. 341–351, 1997.
- [4] C. Cucchiara, L. La Mendola, and M. Papia, "Effectiveness of stirrups and steel fibres as shear reinforcement," *Cement and Concrete Composites*, vol. 26, no. 7, pp. 777–786, 2004.
- [5] S. A. Ashour, G. S. Hasanain, and F. F. Wafa, "Shear behavior of high-strength fiber reinforced concrete beams," *ACI Structural Journal*, vol. 89, no. 2, pp. 176–184, 1992.
- [6] K. H. Tan, K. Murugappan, and P. Paramasivam, "Shear behavior of steel fiber reinforced concrete beams," *ACI Structural Journal*, vol. 90, no. 1, pp. 3–11, 1993.
- [7] R. N. Swamy, R. Jones, and A. T. P. Chiam, "Influence of steel fibers on the shear resistance of lightweight concrete I-beams," *ACI Structural Journal*, vol. 90, no. 1, pp. 103–114, 1993.
- [8] Y. K. Kwak, M. O. Eberhard, W. S. Kim, and J. Kim, "Shear strength of steel fiber reinforced concrete beams without stirrups," *ACI Structural Journal*, vol. 99, no. 4, pp. 530–538, 2002.
- [9] V. C. Li, R. Ward, and A. M. Hamza, "Steel and synthetic fibers as shear reinforcement," *ACI Materials Journal*, vol. 89, no. 5, pp. 499–508, 1992.
- [10] S. Furlan Jr. and J. B. de Hanai, "Shear behaviour of fiber reinforced concrete beams," *Cement and Concrete Composites*, vol. 19, no. 4, pp. 359–366, 1997.
- [11] D. H. Lim and B. H. Oh, "Experimental and theoretical investigation on the shear of steel fibre reinforced concrete beams," *Engineering Structures*, vol. 21, no. 10, pp. 937–944, 1999.
- [12] G. Batson, C. Ball, L. Bailey, E. Landers, and J. Hooks, "Flexural fatigue strength of steel fiber reinforced concrete beams," *ACI Journal Proceedings*, vol. 69, no. 11, pp. 673–677, 1972.
- [13] R. N. Swamy and H. M. Bahia, "The effectiveness of steel fibers as shear reinforcement," *Concrete International*, vol. 7, no. 3, pp. 35–40, 1985.
- [14] C. E. Chalioris and C. G. Karayannis, "Effectiveness of the use of steel fibres on the torsional behaviour of flanged concrete beams," *Cement and Concrete Composites*, vol. 31, no. 5, pp. 331–341, 2009.
- [15] Z. You, Y. Ding, and C. Niederegger, "Replacing stirrups of self-compacting concrete beams with steel fibers," *Transactions of Tianjin University*, vol. 16, no. 6, pp. 411–416, 2010.
- [16] F. Minelli and G. A. Plizzari, "On the effectiveness of steel fibers as shear reinforcement," *ACI Structural Journal*, vol. 110, no. 3, pp. 379–390, 2013.
- [17] K. Jain and B. Singh, "Steel fibres as minimum shear reinforcement in reinforced concrete beams," *Magazine of Concrete Research*, vol. 65, no. 7, pp. 430–440, 2013.
- [18] K. Jain and B. Singh, "Deformed steel fibres as minimum shear reinforcement comparative appraisal," *Magazine of Concrete Research*, vol. 66, no. 22, pp. 1170–1182, 2014.
- [19] C. E. Chalioris, "Steel fibrous RC beams subjected to cyclic deformations under predominant shear," *Engineering Structures*, vol. 49, pp. 104–118, 2013.
- [20] ACI Committee 318, *Building Code Requirements for Structural Concrete (ACI 318-08) and Commentary*, American Concrete Institute, Farmington Hills, Mich, USA, 2008.
- [21] M. Z. Bayasi and P. Soroushian, "Effect of steel fiber reinforcement on fresh mix properties of concrete," *ACI Materials Journal*, vol. 89, no. 4, pp. 369–374, 1992.
- [22] Ö. Eren and T. Çelik, "Effect of silica fume and steel fibers on some properties of high-strength concrete," *Construction and Building Materials*, vol. 11, no. 7–8, pp. 373–382, 1997.
- [23] P. Balaguru and H. Najm, "High-performance fiber-reinforced concrete mixture proportions with high fiber volume fractions," *ACI Materials Journal*, vol. 101, no. 4, pp. 281–286, 2004.
- [24] I. Mehdipour, N. A. Libre, M. Shekarchi, and M. Khanjani, "Effect of workability characteristics on the hardened performance of FRSCCMs," *Construction and Building Materials*, vol. 40, pp. 611–621, 2013.
- [25] T. Paulay, "Coupling beams of reinforced concrete shear walls," *Journal of the Structural Division*, vol. 97, no. 3, pp. 843–862, 1971.
- [26] D. Naish, *Testing and modeling of reinforced concrete coupling beams [Ph.D. thesis]*, University of California, Los Angeles, Los Angeles, Calif, USA, 2010.
- [27] D. R. Sahoo and A. Sharma, "Effect of steel fiber content on behavior of concrete beams with and without stirrups," *ACI Structural Journal*, vol. 111, no. 5, pp. 1157–1166, 2014.

Research Article

Shear Strength of Unreinforced Masonry Wall Retrofitted with Fiber Reinforced Polymer and Hybrid Sheet

Yun-Cheul Choi,¹ Hyun-Ki Choi,² Dongkeun Lee,³ and Chang Sik Choi⁴

¹*Department of Building Equipment and Fire Protection System, Chungwoon University, Chungnam 350-701, Republic of Korea*

²*Department of Fire and Disaster Prevention Engineering, Kyungnam University, Gyeongsangnam-do 631-701, Republic of Korea*

³*Department of Civil Engineering, Antalya International University, 07190 Antalya, Turkey*

⁴*Department of Architectural Engineering, Hanyang University, Seoul 133-791, Republic of Korea*

Correspondence should be addressed to Dongkeun Lee; dongkeun.lee@antalya.edu.tr

Received 14 June 2015; Revised 14 September 2015; Accepted 16 September 2015

Academic Editor: Gonzalo Martínez-Barrera

Copyright © 2015 Yun-Cheul Choi et al. This is an open access article distributed under the Creative Commons Attribution License, which permits unrestricted use, distribution, and reproduction in any medium, provided the original work is properly cited.

Unreinforced masonry (URM) structures represent a significant portion of existing historical structures around the world. Recent earthquakes have shown the need for seismic retrofitting for URM structures. Various types of strengthening methods have been used for URM structures. In particular, a strengthening technique using externally bonded (EB) fiber reinforced polymer (FRP) composites has attracted engineers since EB FRP materials effectively enhance the shear strength of URM walls with negligible change to cross-sectional area and weight of the walls. Research has been extensively conducted to determine characteristics of URM walls strengthened with EB FRP materials. However, it is still difficult to determine an appropriate retrofitting level due to the complexity of mechanical behavior of strengthened URM walls. In this study, in-plane behavior under lateral loading was, therefore, investigated on a full-scale nonstrengthened URM wall and URM walls retrofitted with two different FRP materials: carbon (CFRP) and hybrid (HFRP) sheets. The test results indicated that both FRP composites were effective in increasing shear strength in comparison with the control specimen. However, better performance was obtained with HFRP compared to CFRP. In addition, an equation for estimating effective strain was proposed, and the theoretical results were in good agreement with the experimental ones.

1. Introduction

In general, masonry structures are considered to be optimal for low-rise structures in many countries due to easy and fast construction, abundant material, and no special technique for construction. Although masonry structures are strong enough to resist large compressive stress, these structures have poor ductility and thus are vulnerable under dynamic loading such as earthquake. For instance, unreinforced masonry (URM) structures have been prohibited for public structures including schools since the Long Beach earthquake, of 1993, in California, USA. Even though structures were constructed to meet the high level seismic requirements of New Zealand, many of those were severely damaged and collapsed due to consecutive earthquakes, in 2010 and 2011. This resulted in a great deal of humans and property losses [1–3].

Recently, the risk of earthquake events has increased in many countries that have a low probability of earthquake occurrences. For example, the number of earthquakes in South Korea increased by 54.3% in the recent three years. As with many countries, there are many masonry structures constructed without meeting current seismic requirements and strengthening, especially in South Korea where there is even an obvious probability of earthquake. More specifically, low-rise masonry structures in South Korea are 30% of all domestic structures, over 40% of all domestic houses, and substantially vulnerable to earthquake [3, 4].

Due to the aforementioned reasons, research on strengthening URM walls has been extremely conducted. FEMA 356 suggests design guidelines of URM walls to resist lateral force and evaluation of existing structures on the basis of existing research results. In addition, FEMA 356 [5] indicates how to assess structures with damage or loss of capacity

for strengthening and suggests various methods such as shotcrete, coating, reinforced core, and prestressed core for URM walls.

In particular, research on URM walls retrofitted with externally bonded (EB) fiber reinforced polymer (FRP) composite materials has been substantially conducted due to the well-known advantages of FRP materials (i.e., good corrosion resistance, light weight, ease of installation, and high specific stiffness and strength). In terms of the material properties of FRP composites, substantial research has been conducted. For instance, research on the effect of temperature has been carried out [6–10]. One of the serious issues on temperature is glass transition temperature (T_g). T_g of resin generally varies from 60 to 82°C. T_g of glass fiber, carbon fiber, and aramid fiber is 275, 1000, and 175°C, respectively. The mechanical properties of polymer adhesives are significantly reduced when the temperature is close to T_g . The time-dependent behavior of FRP composites is also a vital issue. It was reported that creep and relaxation of carbon fiber are practically zero [11]. Research has been also conducted to know the fatigue behavior of FRP composites [12, 13]. Sun and Chan [13] reported that the fatigue life of FRP composites was extended by increasing load frequency. From the standpoint of compressive behavior, the compressive strength of FRP composites is generally lower than tensile strength. For example, 78, 55, and 20% of the tensile strengths of carbon FRP (CFRP), glass FRP (GFRP), and aramid FRP (AFRP) were reported as the compressive strengths, respectively [14].

In addition to research at the material level, the structural behavior of URM walls strengthened with FRP composites has been considerably investigated. The common failure modes of URM walls strengthened in shear are the debonding of EB FRP composites, the rupture of FRP composites, or the failure of URM wall. In many tests, the debonding of EB FRP composites was observed [15–17]. It was reported that thicker and stiffer FRP composites were more susceptible to debonding. EB FRP sheets are prone to buckling under compression stress, causing debonding failure. This buckling of EB FRP sheets occurred during the tests [15]. The shear performance of URM walls strengthened with CFRP laminates was investigated [18]. It was reported that both strength and displacement were improved by using CFRP laminates. Research on the behavior of damaged URM walls strengthened with CFRP laminates was carried out by Gergely and Young [19]. ElGawady et al. [20] carried out experimental studies on shear strength of URM walls strengthened with FRP composites such as GFRP and AFRP composites. They suggested a model to predict shear strength of URM walls retrofitted with FRP composites. ElGawady et al. [21] recommended full surface cover strengthening for predamaged masonry walls rather than X-type configuration. They also reported that the walls strengthened with FRP sheets in the X-type configuration were affected by the existing cracks in the predamaged walls. Two different types of FRP material (CFRP versus GFRP) were compared [17]. They found that GFRP laminates were superior to CFRP laminates when it comes to shear capacity. The in-plane behavior of URM walls strengthened with a GFRP reinforced

mortar coating was investigated [22]. Various mortars were used for the coating. It was reported that both strength and ductility were considerably increased. Two composite materials, ferrocement and GFRP, were used to strengthen confined masonry walls under vertical and lateral cyclic loading [23]. The wall specimens were retrofitted with three different FRP configurations of X-type, corner, and full coverage. It was found that the two composites were effective in improving the ductility and energy absorption significantly. However, lateral drift was slightly improved. Eight specimens were examined to investigate the in-plane behavior of URM walls strengthened with basalt FRP (BFRP) composites [24]. They reported that the failure mode of strengthened walls was different by using BFRP composites in comparison with the control wall. Furthermore, a design model for URM walls strengthened with BFRP composites was proposed in the study.

Although EB FRP composites do not reach their ultimate states, structures can fail by the debonding of composites from concrete substrate due to shear or flexural palling at the end of composite materials. Similarly, the deformation of composites is caused after concrete substrate deforms since EB FRP composites are bonded to the substrate, which is called passive strengthening technique [25]. Although there are various bonding methods to improve bond capacity between composites and concrete substrate in terms of the passive strengthening technique, methods using epoxy or polyester resins are generally used. In this study, epoxy resin was used. As mentioned previously, when epoxy is used, special care should be taken for the change of mechanical characteristics due to temperature. Thermal characteristics of FRP composites are influenced by the T_g of epoxy rather than that of fiber. It was reported that the spalling area of matrix increased and the mechanical properties of matrix decreased under high temperature such as 130°C. However, the tensile strength and stiffness of matrix tended to increase under low temperature such as –40°C due to the shrinkage of matrix [6–8, 26, 27]. Therefore, temperature can be an essential factor with respect to T_g . However, the effect of the environment on FRP composites is out of the scope of this study on the basis of the following reasons. Firstly, there are few factors influencing the mechanical properties of materials in the civil engineering environment excluding fire in comparison with aerospace and defense industry. Secondly, it is rare that FRP reinforcement under tensile stress will fail prior to the failure of masonry substrate since the tensile capacity of FRP reinforcement is generally superior to that of the substrate. Lastly, the URM walls examined in this study are interior curtain walls hardly affected by extraordinary environmental conditions. Therefore, it was assumed that FRP composites with epoxy resin were not affected by the environment in this study.

As mentioned above, considerable research has been conducted on URM walls strengthened with various FRP composites such as CFRP, GFRP, AFRP, and BFRP composites. However, research on the in-plane behavior of URM walls retrofitted with hybrid FRP (HFRP) is significantly limited. Therefore, the objective of this study is to investigate the in-plane behavior of URM walls strengthened with CFRP

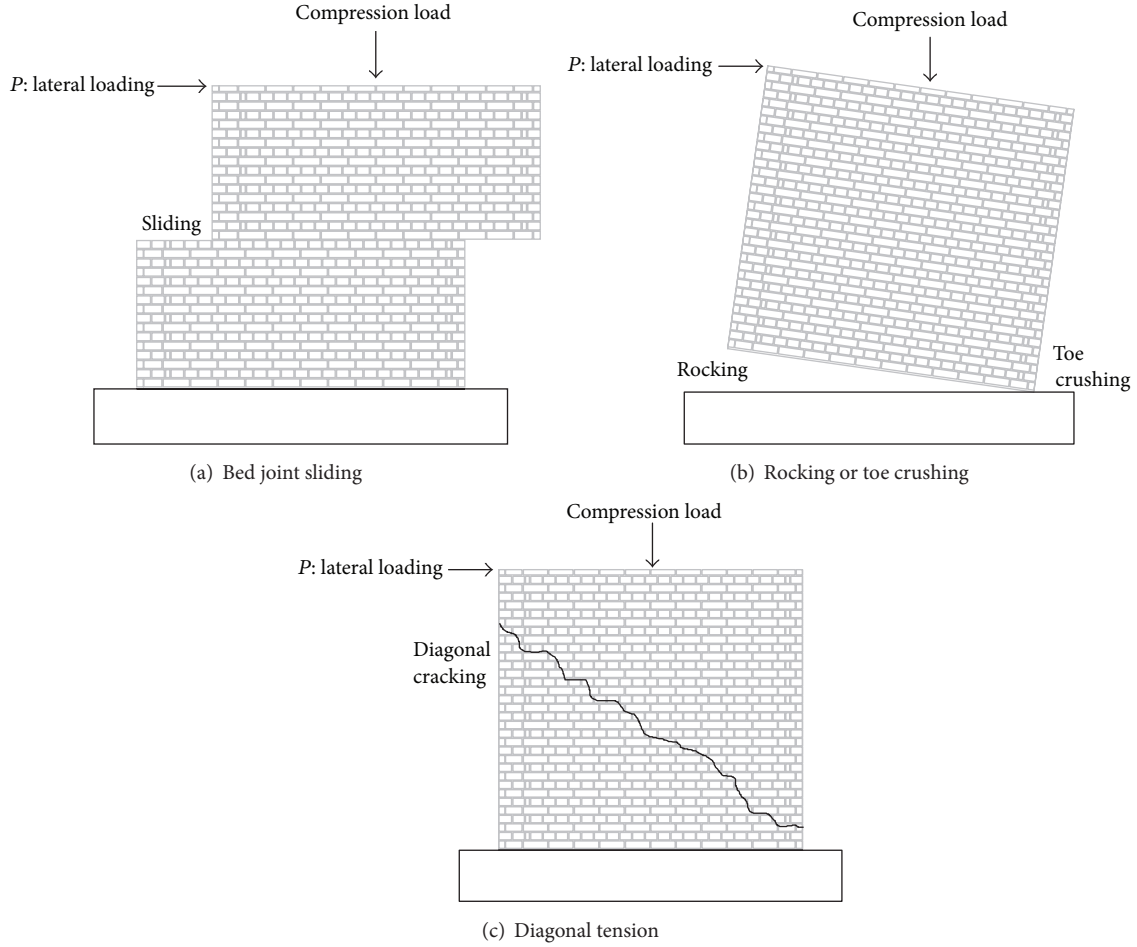


FIGURE 1: Failure mode of unreinforced masonry wall.

and HFRP (GFRP plus AFRP) sheets under cyclic loading. Furthermore, an equation is proposed to estimate accurate effective strain and thus the shear strength of URM walls retrofitted with EB FRP composite materials.

2. Performance Appraisal of Nonreinforced and Reinforced Masonry Walls

Behavior of URM walls is quite different from that of reinforced masonry walls. In particular, failure modes of URM walls are substantially crucial since strengthening material FRP sheets have their own directional natures. Moreover, it is essential to know the strength of existing URM walls for determining the proper strengthening level. Thus, failure modes of URM walls have been divided into four categories in this study. Strength capacity of URM walls in each category was estimated in accordance with FEMA 356 [5].

2.1. Failure Mode and Related Strength of URM Walls. Failure modes of URM walls can be divided into shear and flexure categories, and then each category can be subdivided into deformation and force controlled actions. Failure modes can be determined depending on the length-to-height ratio (L/h)

TABLE 1: Failure mode of unreinforced masonry wall by aspect ratio.

	Deformation controlled action	Force controlled action
$L/h < 1.0$	Rocking	Toe crushing
$L/h > 1.5$	Bed joint sliding	Diagonal tension

and the amount of compressive stress. Failure modes are summarized in Figure 1 and Table 1.

Shear strength of URM walls can be predicted using the estimation equations by FEMA 356 [5] as follows:

$$\begin{aligned}
 Q_{CE} &= V_{bjs} = v_{me} A_n, \\
 Q_{CE} &= V_r = 0.9 \alpha P_E \left(\frac{L}{h_{eff}} \right), \\
 Q_{CE} &= V_{tc} = \alpha P_E \left(\frac{L}{h_{eff}} \right) \left(1 - \frac{f_a}{0.7 f'_m} \right), \\
 Q_{CE} &= V_{dt} = f_{dt} A_n \left(\frac{L}{h_{eff}} \right) \left(1 + \frac{f_a}{f_{dt}} \right),
 \end{aligned} \tag{1}$$

where Q_{CE} is shear strength of URM wall, V_{bjs} , V_r , V_{tc} , and V_{dt} are shear strength in case of bed joint sliding, rocking, toe crushing, and diagonal tension, respectively, v_{me} is shear stress in case of bed joint sliding, A_n is bonding area of mortar, L is wall length, h_{eff} is wall height, α is boundary condition constant (0.5 and 1.0 for cantilever and both fixed ends, resp.), P_E is expected axial compressive force on wall, f_a is axial compressive stress (axial compressive force/area of wall), f'_m is compressive strength of masonry, and f_{dt} is diagonal tension stress.

2.2. Strength of URM Walls Retrofitted with FRP Sheet. Studies were conducted to predict the shear strength of URM walls strengthened with FRP composite materials. For instance, ElGawady [28] conducted research on the shear strength of URM walls retrofitted with FRP sheets using the shear strength estimation model suggested by Triantafillou [29]. The model by Triantafillou was derived to predict the shear

strength of reinforced concrete (RC) beams strengthened with FRP sheets. In the model, the effective strain of the FRP sheet was used instead of ultimate strain as follows:

$$\begin{aligned} P &= F_m + F_{FRP}, \\ F_{FRP} &= \rho_h E_{FRP} \epsilon_{eff} t L, \\ \rho_h &= \frac{A_{FRP}}{L t}, \end{aligned} \quad (2)$$

where F_m is strength of URM walls, F_{FRP} is effective strength of FRP material, ρ_h is strengthening ratio in horizontal direction, E_{FRP} is elastic modulus of FRP, ϵ_{eff} is effective strain of FRP, t is wall thickness, L is wall length, and A_{FRP} is cross-sectional area of FRP. Effective strain of the FRP sheet was derived using existing experimental data and is expressed as follows:

$$\epsilon_{eff} = \begin{cases} 0.0119 - 0.0205 (\rho_h E_{FRP}) + 0.0104 (\rho_h E_{FRP})^2 & \text{when } 0 \leq \rho_h E_{FRP} \leq 1 \text{ GPa} \\ 0.0024 - 0.00065 (\rho_h E_{FRP}) & \text{when } \rho_h E_{FRP} \geq 1 \text{ GPa.} \end{cases} \quad (3)$$

AC 125 [30] model is the guideline suggested by the International Code Council (ICC). In accordance with AC 125 [30], lateral resistance of the FRP sheet applied to one side of URM or RC walls can be estimated using the following equations:

$$\begin{aligned} F_{FRP} &= 0.75 \rho_h f_j t L, \\ f_j &= 0.004 E_{FRP} < 0.75 f_{FRP,u}, \end{aligned} \quad (4)$$

where $f_{FRP,u}$ is ultimate tensile strength of FRP sheet and f_j is axial force of FRP sheet.

3. Specimens and Test Plan

In this study, the in-plane behavior of URM walls strengthened with unidirectional FRP sheet applied to one side of the walls was investigated to quantify the strengthening effectiveness of FRP composites. To achieve the purpose, three full-scale specimens were designed. One (URM-0.92) was nonstrengthened to serve as a control specimen and the other two (RTM-CFS-SF and RTM-HBRD-SF) were strengthened with CFRP and HFRP sheets, respectively. The aspect ratio (L/h) of the specimens was designed to be close to 1 for expressing rocking phenomenon under low axial force.

3.1. Material Properties. As mentioned above, two types of FRP composites were used. One is CFRP, a widely used strengthening material, and the other is HFRP, newly developed. HFRP was made of GFRP and AFRP to introduce advantages of the two FRP composites. The mechanical properties of the CFRP and HFRP composites were obtained experimentally in the laboratory and are provided in Table 2.

The values provided in Table 2 are the average values of the three specimens tested. The values are not rounded off. The HFRP composite shows higher ultimate strain but lower tensile strength and elastic modulus than the CFRP composite. Both FRP composites are expected to improve deformability of URM walls from the standpoint of the ultimate strain of the FRP composites as listed in Table 2. The stress-strain relationships of both FRP composites are depicted in Figure 2.

Since the masonry wall specimens were full scale, commercially available cement bricks with dimensions of $190 \times 90 \times 57$ mm were used. Bed joints of 10 mm and 1.0 B thickness were chosen. The average compressive strength of the bricks was obtained as 15.7 MPa following the test method per KS F 4004 (Table 3) [31]. Ordinary mortar was applied and 1:1 ratio was used for mixing cement and sand. The average compressive strength of the mortar was recorded as 8.4 MPa using specimens with dimensions of $50 \times 50 \times 50$ mm.

3.2. Strengthening URM Walls Using FRP Sheet. The parts between the walls and their bases were strengthened with FRP composites in the vertical direction to avoid early flexural failure due to low axial force and aspect ratio. The strengthening amount to resist flexure was determined following the sectional analysis used for RC walls as depicted in Figure 3. The bricks and FRP sheets were assumed to resist compressive and tensile stresses only, respectively. The compressive stress block was assumed in accordance with ACI 318 [32]. One layer of FRP sheet was applied to one side of each strengthened wall to quantify the shear strengthening effectiveness of an FRP sheet. The strengthening amount for

TABLE 2: Material properties of FRP and resin.

Type		W_{frp} [g/m ²]	f_t [MPa]	E [GPa]	ϵ [%]
GFPR sheet	#1	88.98	2709.01	159.47	1.69
	#2	96.45	2867.75	166.26	1.72
	#3	93.57	2838.24	169.27	1.68
Hybrid sheet	#1	139.89	2322.27	64.14	3.62
	#2	150.76	2490.39	76.24	3.27
	#3	144.35	2510.44	72.65	3.46
Resin ¹		Tensile strength (MPa)	Tensile modulus (GP)	Elongation at break [%]	Density (g/cm ³)
Epoxy		85	10.5	0.8	1.2

¹The properties are not obtained from the laboratory but are provided by the manufacturer.

TABLE 3: Material properties of URM.

Compressive strength of cement brick [MPa]	Compressive strength of mortar [MPa]	Compressive strength of prism [MPa]
#1 14.29	#1 7.54	#1 11.92
#2 15.94	#2 8.64	#2 12.77
#3 15.97	#3 9.02	#3 12.86

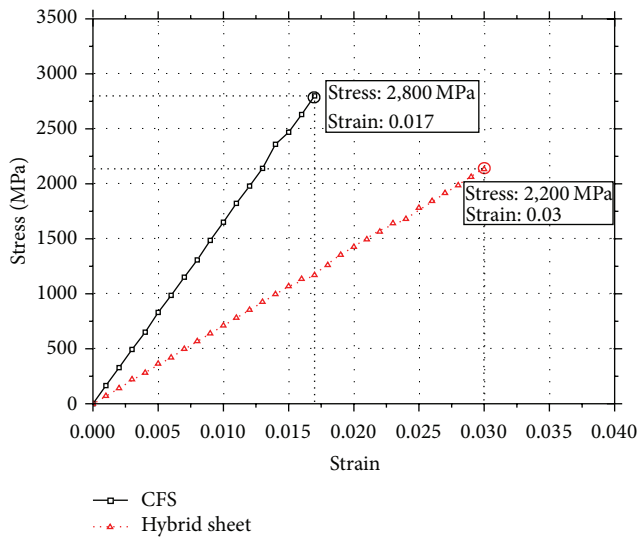


FIGURE 2: Stress-strain relationship of FRP sheet.

each strengthened specimen is listed in Table 4. The specimen dimensions and reinforcement details are illustrated in Figure 4.

3.3. Test Setup and Loading Protocol. As shown in Figure 5, the masonry wall specimens were manufactured on the precast RC base tied to the strong frame in the laboratory. A small compressive force was applied through the steel loading beam and self-weight of the masonry wall, since the masonry wall represented low-rise apartments. Lateral force was generated using a 1000 kN actuator attached to the steel loading beam on the top of the masonry wall specimen. As

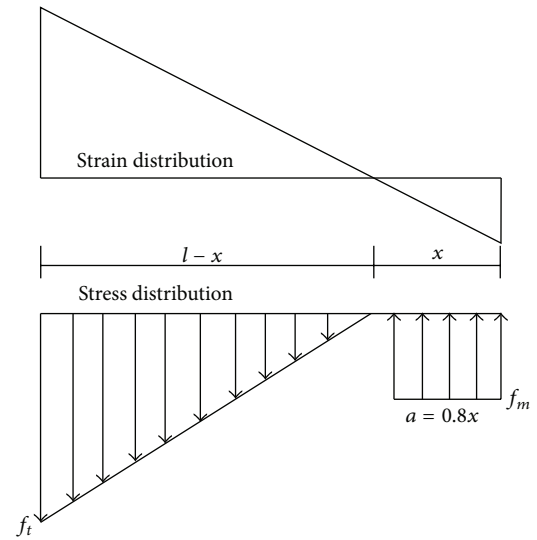


FIGURE 3: Flexural strength calculation of retrofitted specimen.

illustrated in Figure 5, the support frame was used to prevent the masonry wall from out-of-plane buckling.

The masonry wall specimens were tested using displacement control. Loading histories are depicted in Figure 6. The displacement control was based on the rotational angle of the specimens. In other words, a drift ratio of distance from the specimen bottom to the center of the actuator to lateral displacement increased from 0.1% with an increment of 0.1 (i.e., 0.1, 0.2, 0.3, 0.4, and 0.5%). Positive and negative cyclic loads were repeated three times per drift ratio.

4. Test Results

4.1. Failure Mode and Load-Displacement Relationship. Figure 7 shows crack patterns and failure modes of the tested specimens. The load-displacement relationships of the masonry wall specimens are depicted in Figure 8. The main test results are summarized in Table 5. Detailed test results of each specimen are as follows.

As a control specimen, URM-0.92 was a nonstrengthened masonry wall. After initial cracks formed, no additional load was transferred between the URM wall and base due to cracks

TABLE 4: List of specimens.

Specimen	H [mm]	L [mm]	Aspect ratio	t_{URM} [mm]	Retrofit material	t_{FRP} [mm]	FRP sheet layer	Brick element [mm]	Vertical reinforcement [mm]
URM-0.92									—
RTM-CFS-SF	2380	2400	0.92	190	CFRP	0.16	1	$190 \times 90 \times 57$	60
RTM-HBRD-SF					Hybrid	0.17	1		45

H : height of specimen, L : length of specimen, t_{URM} : URM thickness, and t_{FRP} : FRP thickness.

TABLE 5: Summary of test results.

Specimens		P_{cr} [kN]	P_y [kN]	P_{max} [kN]	δ_y [mm]	δ_{max} [mm]	δ_{failure} [mm]	θ_y [%]	θ_{max} [%]	μ	$P_{u,\text{retrofit}}/P_{\text{max,URM}}$
URM-0.92	Pos.	13	18	23	1.47	2.83	12.6	0.06	0.5	2.8	—
	Neg.	−5	−9	−12	−1.78	−9.8	−9.8	−0.08	−0.1	1.25	—
RTM-CFS-SF	Pos.	74	74	99	14.3	17.7	33.1	0.57	0.7	1.2	4.3
	Neg.	−54	−81	−108	−19	−28.1	−33	−0.94	−1.3	1.5	9
RTM-HBRD-SF	Pos.	63	104	139	17.6	32.8	43.4	0.65	1.3	1.8	6
	Neg.	−49	−90	−121	−22.6	−33.2	−43.3	−0.92	−1.4	1.5	1.2

All estimates associated with moment and shear computed based on actual material properties.

P_{cr} : initial crack load (measured), P_y : yield load by Park's method (measured), P_{max} : peak load (measured), δ_y : yield displacement (measured), δ_{max} : peak displacement (measured), δ_{failure} : failure displacement (measured), θ_y : drift corresponding to the yielding, θ_{max} : drift corresponding to the yielding, μ : ductility ($\delta_{\text{max}}/\delta_y$ = deformation capacity), and $P_{u,\text{retrofit}}/P_{\text{max,URM}}$: strength increase ratio.

in the mortar between the URM wall and base, resulting in lifting of the URM wall with an ultimate load of 23 kN at a 0.2% drift ratio. After a 0.5% drift ratio, it was observed that displacement continuously increased without load increase due to the wall rotation. Thus, it appeared that, after the ultimate load was recorded, failure occurred due to the wall lifting at a drift ratio of 0.4%.

The specimen RTM-CFS-SF, strengthened with CFRP sheet, reached an ultimate load of 99 kN at a drift ratio of +0.69%. RTM-CFS-SF showed approximately 330% larger load-carrying capacity in comparison with URM-0.92. When the strengthened specimen reached the ultimate load, rupture of FRP sheet applied between the wall and base occurred with a loud sound. This was attributed to stress concentration at the debonding area of the FRP sheet from the wall. Then, the load-carrying capacity of the strengthened specimen rapidly decreased. After wall lifting was observed, failure of the FRP sheet propagated, and ultimately RTM-CFS-SF failed due to the crushing of the brick at the bottom of the masonry wall.

The other strengthened specimen with HFRP, RTM-HBRD-SF, presented an ultimate load of 139 kN at a drift ratio of +1.31%. RTM-HBRD-SF indicated approximately 504% and 40% larger load-carrying capacity than URM-0.92 and RTM-CFS-SF, respectively. In addition, unlike RTM-CFS-SF, RTM-HBRD-SF showed continuous load resistance capability and gradual decrease of load-carrying capacity after the ultimate load was reached. Due to the mechanical properties of HFRP (low modulus of elasticity and large ultimate strain), there was no rupture of the FRP sheet between the masonry wall and base. However, due to propagation of the diagonal crack following the mortar face, RTM-HBRD-SF failed with

signs of HFRP sheet debonding from the masonry wall after a drift ratio of +1.5%.

4.2. Assessment of Deformability of FRP Sheet. To evaluate the contribution of the FRP sheet to shear strength improvement, strains were measured in the FRP sheets in the horizontal and vertical directions. Figure 9 depicts the strain distributions of the FRP sheets in the vertical direction of both strengthened specimens. Strain gages were attached on the locations of 400 and 750 mm from the wall side end and 200 mm from the connection line between the wall and base. The distance of 200 mm was chosen since the flexural crack of URM-0.92 formed at the same location. In the case of RTM-CFS-SF, it was found that a quite large stress concentration occurred at the bottom of the masonry wall at the ultimate. It seems that FRP sheets in the horizontal direction were not significantly effective in enhancing shear strength since the load-carrying capacity of RTM-CFS-SF suddenly dropped. On the contrary, strain distributions of RTM-HBRD-SF increased gradually and continuously, meaning that the FRP sheets in the horizontal direction substantially contributed to shear strength.

Figure 10 shows the strain distributions of FRP sheets in the horizontal direction of both strengthened specimens. Strain gages were attached on locations where critical cracks would most likely occur. In the case of RTM-CFS-SF, there was no additional strain increase after the ultimate. At the diagonal crack formation area, a strain of approximately 0.001 was measured. However, the strains of RTM-HBRD-SF continued to increase after the ultimate. A strain of

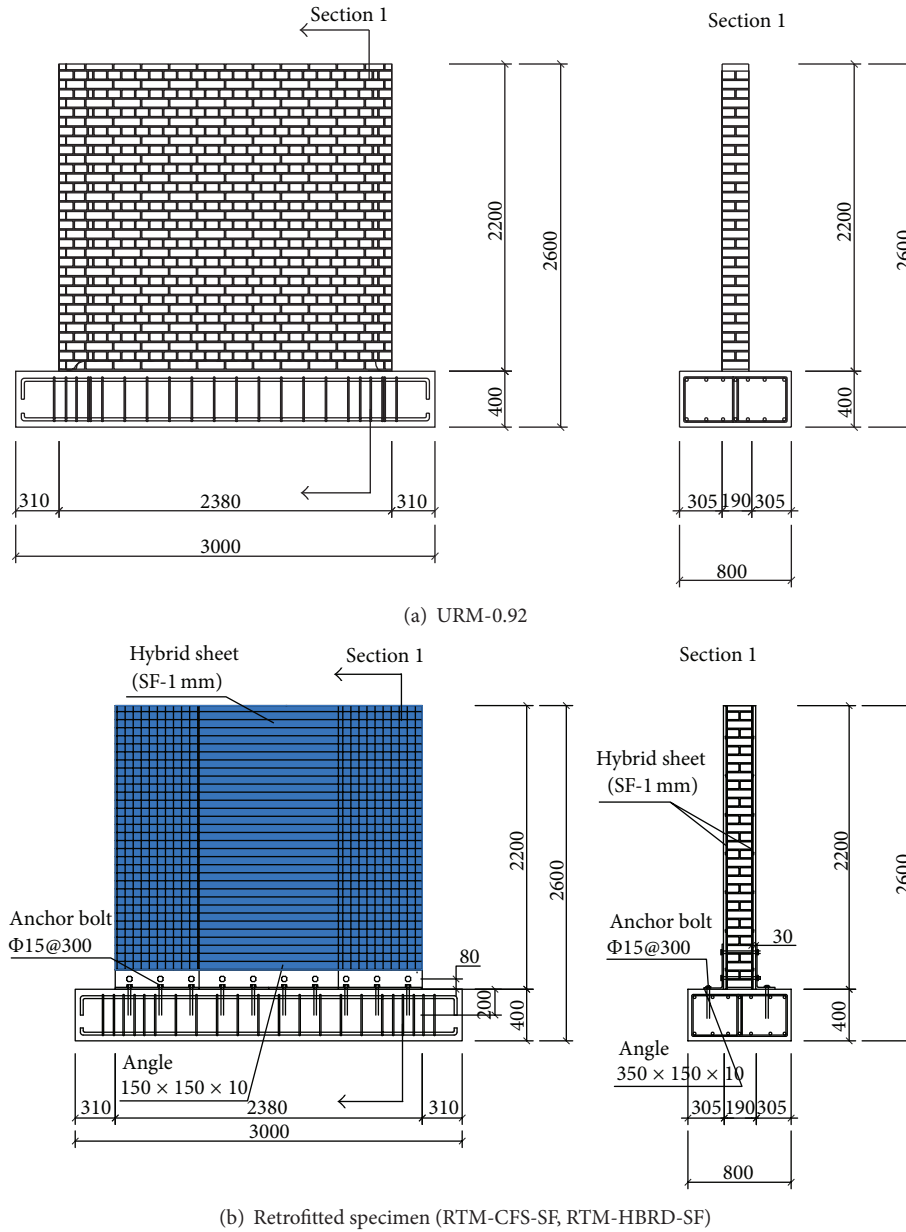


FIGURE 4: Specimen dimensions (unit: mm).

approximately 0.003 was recorded at the diagonal crack formation area.

5. Appraisal of Shear Strengthening Capability of FRP Sheet

5.1. Evaluation of Shear Resistance through Strengthening. Figure 11 shows the shear strength comparison between theoretical and experimental results for RTM-CFS-SF and RTM-HBRD-SF. The theoretical values were obtained using the shear strength model suggested by Triantafillou [29]. The estimated values present a considerably large difference from the test results (523% and 311% for RTM-CFS-SF and RTM-HBRD-SF, resp.). This was attributed to the fact that the strain

of the FRP sheet at the ultimate was fairly small in comparison with that of the shear strength model and the ultimate value.

5.2. Shear Strength Estimation through Nonlinear Regression Analysis. As stated before, the shear strength model by Triantafillou showed poor agreement with the test results. Effective strain was a critical factor of the shear strength model and obtained through nonlinear regression analysis on the basis of experimental data. In this study, a theoretical study was, therefore, conducted through nonlinear regression analysis to find a better effective strain and thus to estimate more accurate shear strength for a URM wall strengthened with FRP sheet.

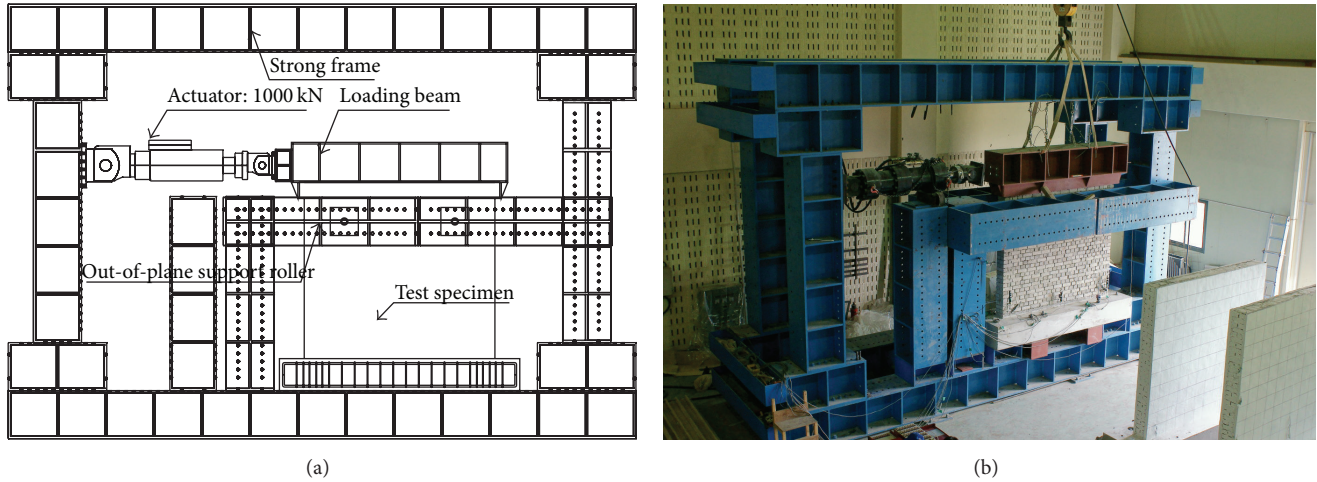


FIGURE 5: Test setup.

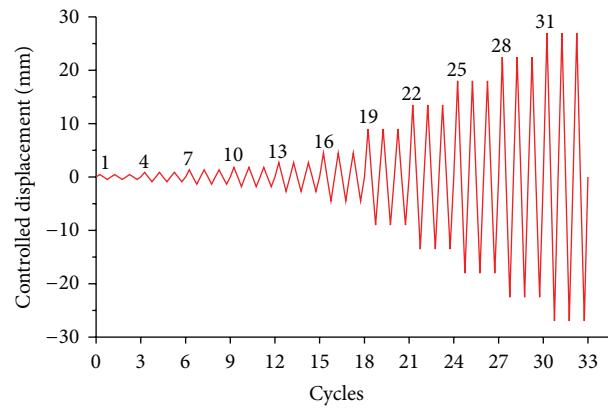


FIGURE 6: Applied displacement history.

As seen in (3) by Triantafillou [29], there are two different equations to compute effective strain. If each equation is expressed in a graphical way, parabola and straight line shapes are drawn. Then, if the parabola and strain line are connected, a new graph similar to an exponential function is created.

To consider the stress concentration phenomenon and early failure of an FRP sheet, existing experimental data were collected from studies [33–36] where strengthened specimens were similar to the specimens tested in this study. Most of the collected specimens excluding the ones by Calvi and Magenes [33] were strengthened with CFRP and indicated aspect ratios smaller than 1. The effective strain distributions versus strength ratio are depicted in Figure 12. Although the distribution curve is not the same as Triantafillou's in terms of range, its shape presents an exponential function graph as with the model by Triantafillou [29].

Therefore, an equation for URM walls strengthened with FRP composites was derived through nonlinear regression analysis using an exponential function type (5a) and is expressed in (5b). Consider

$$\varepsilon_{\text{eff}} = ae^{(-x/b)} + c, \quad (5a)$$

$$\varepsilon_{\text{eff}} = 0.11683e^{(-\rho_h E_{\text{FRP}}/0.016)} + 0.001. \quad (5b)$$

The test results were compared with the ones estimated using (5b). It was found that the proposed equation was in good agreement with the experimental data by showing a small difference less than 10%. The compared results are provided in Table 6. Relatively less accuracy for the estimation of RTM-CFS-SF was achieved compared to that of RTM-HBRD-SF. As mentioned before, this can be attributed to the fact that RTM-CFS-SF showed early failure by stress concentration of FRP sheet in the vertical direction.

6. Conclusions

In this study, the in-plane behavior of URM walls strengthened with EB FRP sheets was investigated to assess the strengthening effectiveness of FRP sheets on URM walls. Three full-scale masonry wall specimens were examined. The following conclusions can be drawn.

The FRP sheets improved the structural integrity of URM walls. Both CFRP and HFRP were effective in increasing the strength of URM walls by 4.3 and 6 times in comparison with the control specimen.

When FRP composites are used as strengthening materials, debonding and rupture of FRP composites significantly

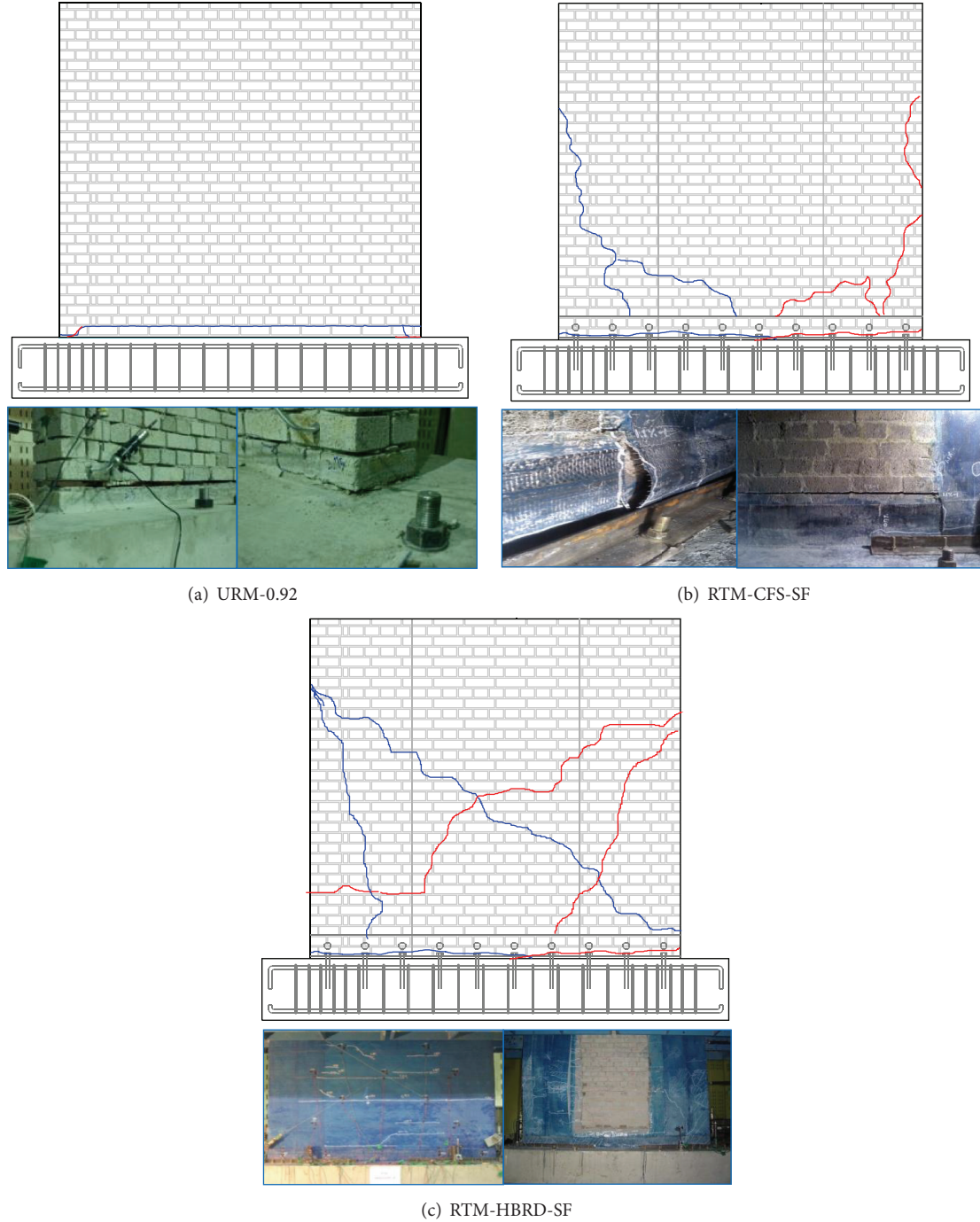


FIGURE 7: Crack pattern and failure mode.

TABLE 6: Evaluation of proposed equation.

Specimen	V_{cal}		V_{test}
	$\epsilon_{eff,estimate}$	$\epsilon_{eff,regression}$	
RTM-CFS-SF	518	80	99
RTM-HBRD-SF	308	130	139

affect the lateral resistance of specimens strengthened with FRP materials. Both phenomena occurred in RTM-CFS-SF, resulting in rapid strength decrease. On the contrary,

there was no rupture of HFRP in RTM-HBRD-SF, and thus, gradual strength degradation was obtained after the ultimate. Therefore, HFRP consisting of GFRP and AFRP appears to be superior to CFRP from the standpoint of strength and material usage.

The strength of the URM walls strengthened with FRP sheets was estimated using the shear strength model for RC beams by Triantafillou. The accuracy of the model for RC beams was significantly low for the strengthened URM walls since the measured strain of the URM walls retrofitted with

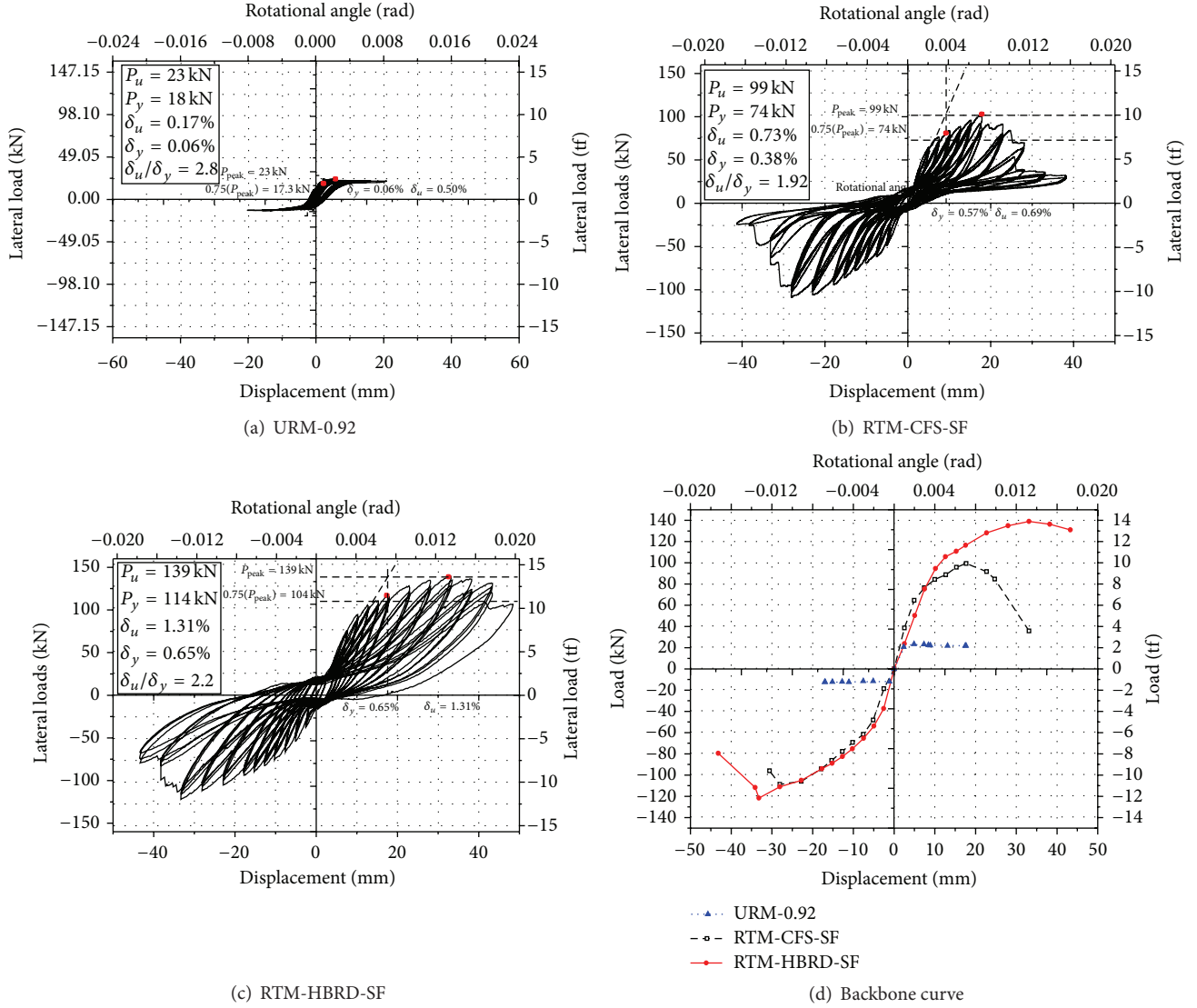


FIGURE 8: Load-displacement relationship.

FRP sheets was much smaller than that of RC beams used for the shear strength model. Therefore, effective strain is an essential variable for the design of URM walls strengthened with FRP sheet.

An equation is, herein, proposed to estimate an accurate effective strain and consequently the shear strength of URM walls retrofitted with FRP sheet. The suggested model was in good agreement with the test results by indicating a small difference less than 10%. However, it should be noted that the proposed model needs to be applied with care since the number of data used to derive the equation is insufficient.

Notations

A_{FRP} : The cross-sectional area of FRP
 A_n : The bonding area of mortar
 E_{FRP} : The elastic modulus of FRP

F_{FRP} : The effective strength of FRP material
 F_m : The strength of URM walls
 f_a : The axial compressive stress (axial compressive force/area of wall)
 f_{dt} : The diagonal tension stress
 $f_{FRP,u}$: The ultimate tensile strength of FRP sheet
 f_j : The axial force of FRP sheet
 f_m^l : The compressive strength of masonry
 h_{eff} : The wall height
 L : The wall length
 P_E : The expected axial compressive force on wall
 Q_{CE} : The shear strength of URM wall
 T_g : The glass transition temperature
 t : The wall thickness
 V_{bjs} : The shear strength in case of bed joint sliding
 V_r : The shear strength in case of bed rocking

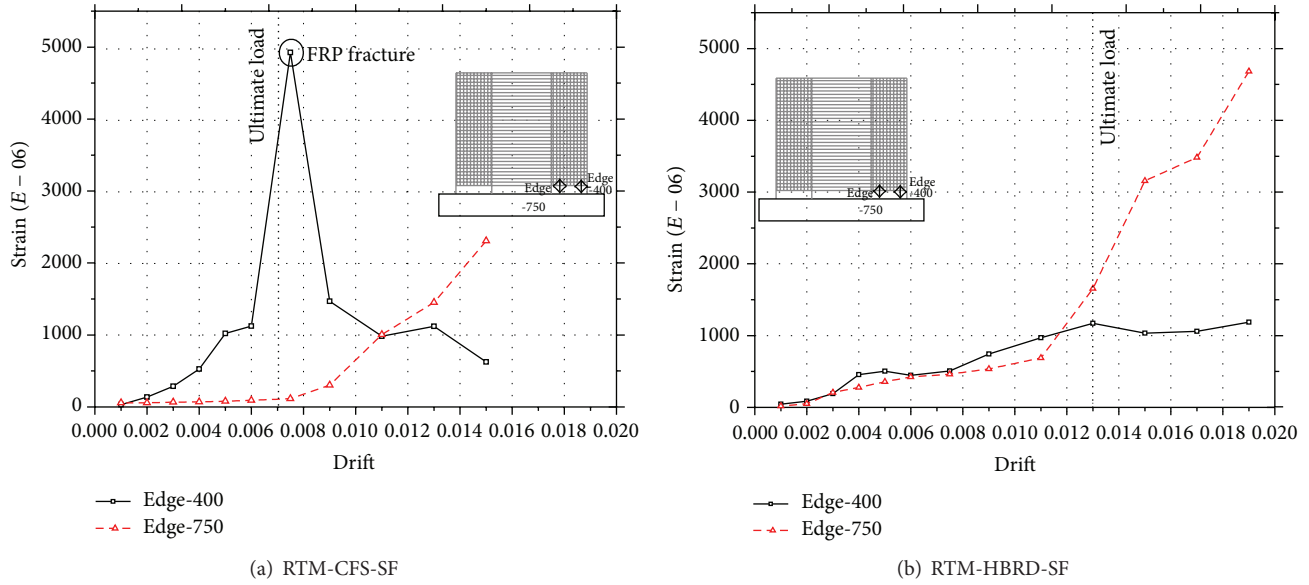


FIGURE 9: FRP sheet strain (vertical direction).

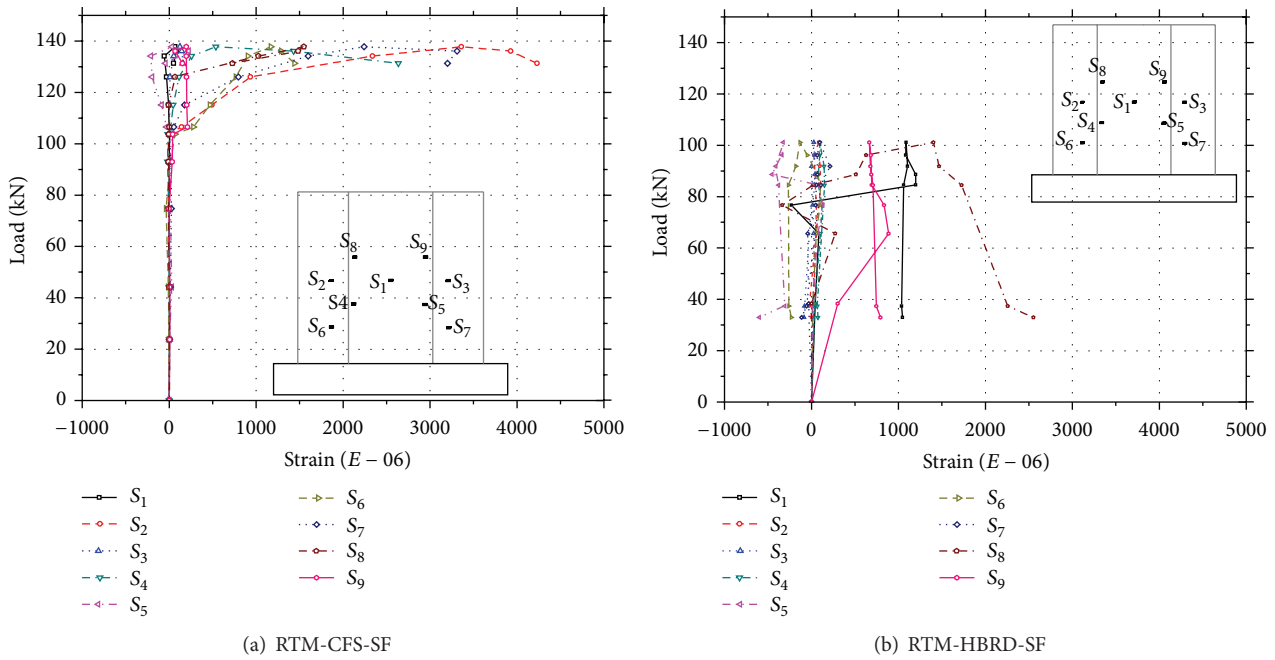


FIGURE 10: FRP sheet strain (horizontal direction).

V_{tc} : The shear strength in case of toe crushing

V_{dt} : The shear strength in case of diagonal tension

v_{me} : The shear stress in case of bed joint sliding

α : The boundary condition constant (0.5 and 1.0 for cantilever and fixed at both ends, resp.)

ε_{eff} : The effective strain of FRP

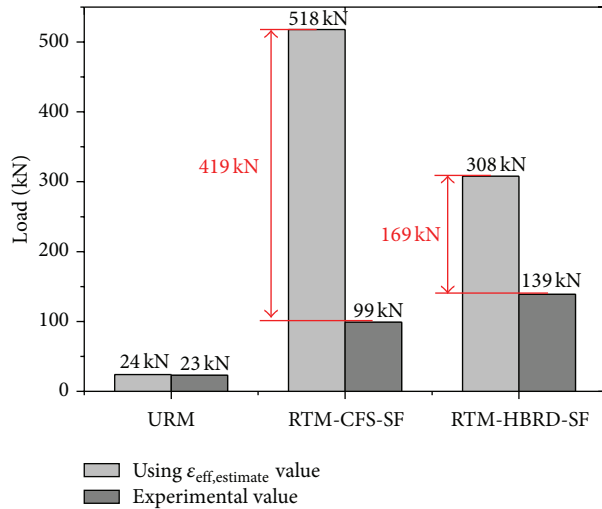
ρ_h : The strengthening ratio in horizontal direction.

Conflict of Interests

The authors declare that there is no conflict of interests regarding the publication of this paper.

Acknowledgments

This work was supported by Chungwoon University Foundation Grant 2015 and the National Research Foundation of



Specimen	$V_{cal,TR98}$ (kN)	V_{test} (kN)
RTM-CFS-SF	518	99
RTM-HBRD-SF	308	139

FIGURE 11: Evaluation of shear strength.

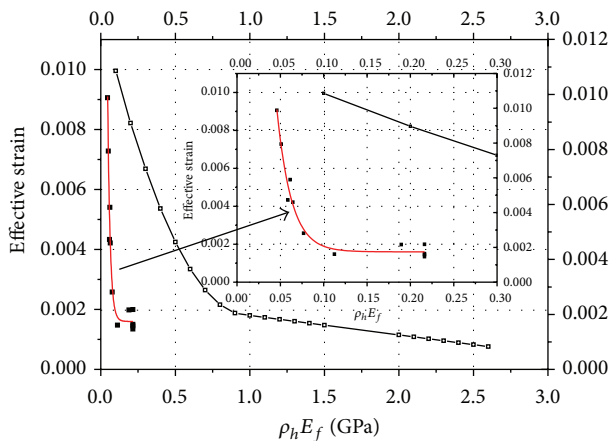


FIGURE 12: Effectiveness strain distribution according to retrofit ratio.

Korea (NRF; 2013R1A1A2010717) grant funded by the Korea government (15CTAP-C097470-01).

References

- [1] United States Geological Survey (USGS), <http://www.usgs.gov/>.
- [2] Korea Meteorological Administration (KMA), <http://www.kma.go.kr/>.
- [3] B. C. Park, J. H. Lee, H. Y. Kim, and J. S. Kim, *Study on Seismic Retrofitting Techniques for Unreinforced Masonry Buildings*, Disaster Prevention Research Department, National Disaster Management Institute (NDMI), 2009.
- [4] K. Y. Kwan, *Seismic Retrofitting Method for Unreinforced Masonry Buildings*, Earthquake and Disaster Prevention Research Institute of University of Seoul, 2000.
- [5] American Society of Civil Engineers (ASCE), "Prestandard and commentary for the seismic rehabilitation of buildings," Tech. Rep. FEMA-356, American Society of Civil Engineers (ASCE), Washington, DC, USA, 2000.
- [6] A. Çavdar, "A study on the effects of high temperature on mechanical properties of fiber reinforced cementitious composites," *Composites, Part B: Engineering*, vol. 43, no. 5, pp. 2452–2463, 2012.
- [7] A. G. Gibson, M. E. Otheguy Torres, T. N. A. Browne, S. Feih, and A. P. Mouritz, "High temperature and fire behaviour of continuous glass fibre/polypropylene laminates," *Composites Part A: Applied Science and Manufacturing*, vol. 41, no. 9, pp. 1219–1231, 2010.
- [8] S. Hinz, T. Omoori, M. Hojo, and K. Schulte, "Damage characterisation of fibre metal laminates under interlaminar shear load," *Composites Part A: Applied Science and Manufacturing*, vol. 40, no. 6–7, pp. 925–931, 2009.
- [9] W. Ningyun and J. T. Evans, "Collapse of continuous fibre composite beams at elevated temperatures," *Composites*, vol. 26, no. 1, pp. 56–61, 1995.
- [10] S. Kumahara, Y. Masuda, and Y. Tanano, "Tensile strength of continuous fiber bar under high temperature," in *Proceedings of the International Symposium on Fiber-Reinforced Plastic Reinforcement for Concrete Structures*, A. Nanni and C. W. Dolan, Eds., SP-138, pp. 731–742, American Concrete Institute, Farmington Hills, Mich, USA, 1993.
- [11] G. L. Balazs and A. Borosnyoi, "Long-term behavior of FRP," in *Proceedings of the International Workshop on Composites in Construction: A Reality*, pp. 84–91, American Society of Civil Engineers, Capri, Italy, July 2001.
- [12] J. A. M. Ferreira, J. D. M. Costa, P. N. B. Reis, and M. O. W. Richardson, "Analysis of fatigue and damage in glass-fibre-reinforced polypropylene composite materials," *Composites Science and Technology*, vol. 59, no. 10, pp. 1461–1467, 1999.
- [13] C. T. Sun and W. S. Chan, "Frequency effect on the fatigue life of a laminated composite. Composite materials: testing and design (fifth conference)," ASTM STP 674, ASTM International, West Conshohocken, Pa, USA, 1979.
- [14] W. Wu, *Thermomechanical properties of fiber reinforced plastics (FRP) bars [Ph.D. thesis]*, West Virginia University, Morgantown, WV, USA, 1990.
- [15] G. Marcari, G. Manfredi, A. Prota, and M. Pecce, "In-plane shear performance of masonry panels strengthened with FRP," *Composites Part B: Engineering*, vol. 38, no. 7–8, pp. 887–901, 2007.
- [16] H. S. Maria, P. Alcaïno, and C. Luders, "Experimental response of masonry walls externally reinforced with carbon fiber fabrics," in *Proceedings of the 8th U.S. National Conference on Earthquake Engineering*, pp. 8555–8564, San Francisco, Calif, USA, April 2006.
- [17] M. R. Valluzzi, D. Tinazzi, and C. Modena, "Shear behavior of masonry panels strengthened by FRP laminates," *Construction and Building Materials*, vol. 16, no. 7, pp. 409–416, 2002.
- [18] G. Schwegler, "Masonry construction strengthened with fiber composites in seismically endangered zones," in *Proceedings of*

- the 10th European Conference on Earthquake Engineering*, pp. 2299–2303, Rotterdam, The Netherlands, 1995.
- [19] J. Gergely and D. T. Young, “Masonry wall retrofitted with CFRP materials,” in *Proceedings of the Composites in Construction*, J. Figueiras, L. Juvandes, and R. Furia, Eds., pp. 565–569, Porto, Portugal, July 2001.
 - [20] M. A. ElGawady, P. Lestuzzi, and M. Badoux, “Shear strength of URM walls retrofitted using FRP,” *Engineering Structures*, vol. 28, no. 12, pp. 1658–1670, 2006.
 - [21] M. A. ElGawady, P. Lestuzzi, and M. Badoux, “Aseismic retrofitting of unreinforced masonry walls using FRP,” *Composites Part B: Engineering*, vol. 37, no. 2-3, pp. 148–162, 2005.
 - [22] N. Gattesco and I. Boem, “Experimental and analytical study to evaluate the effectiveness of an in-plane reinforcement for masonry walls using GFRP meshes,” *Construction and Building Materials*, vol. 88, pp. 94–104, 2015.
 - [23] M. El-Diasity, H. Okail, O. Kamal, and M. Said, “Structural performance of confined masonry walls retrofitted using ferrocement and GFRP under in-plane cyclic loading,” *Engineering Structures*, vol. 94, pp. 54–69, 2015.
 - [24] D. Zhou, Z. Lei, and J. Wang, “In-plane behavior of seismically damaged masonry walls repaired with external BFRP,” *Composite Structures*, vol. 102, pp. 9–19, 2013.
 - [25] Y. C. Choi, H. K. Choi, M. S. Lee, and C. S. Choi, “A study on retrofit method of shear wall by new openings,” *Magazine of Concrete Research*, vol. 64, no. 5, pp. 377–394, 2012.
 - [26] S. Ogiwara, N. Takeda, S. Kobayashi, and A. Kobayashi, “Effects of stacking sequence on microscopic fatigue damage development in quasi-isotropic CFRP laminates with interlaminar-toughened layers,” *Composites Science and Technology*, vol. 59, no. 9, pp. 1387–1398, 1999.
 - [27] A. Buxton and C. Baillie, “A study of the influence of the environment on the measurement of interfacial properties of carbon fibre/epoxy resin composites,” *Composites*, vol. 25, no. 7, pp. 604–608, 1994.
 - [28] M. A. ElGawady, *Seismic in-plane behavior of URM walls upgraded with composites [Ph.D. dissertation]*, École Polytechnique Fédérale de Lausanne, 2004.
 - [29] T. C. Triantafillou, “Strengthening of masonry structures using epoxy-bonded FRP laminates,” *Journal of Composites for Construction*, vol. 2, no. 2, pp. 96–104, 1998.
 - [30] AC 125, “Acceptance criteria for concrete and reinforced and unreinforced masonry strengthened using fiber-reinforced polymers (FRP), composite systems,” in *Proceedings of the International Conference of Building Officials (ICBO '01)*, Evaluation Service, Whittier, Calif, USA, 2001.
 - [31] KS F 4004, *Concrete Bricks*, Korea Standards Information Centre, Kyounggi, South Korea, 2013.
 - [32] ACI 318, “Building code requirements for reinforced concrete,” ACI 318-08, American Concrete Institute (ACI) Committee, Farmington Hills, Mich, USA, 2008.
 - [33] G. Calvi and G. Magenes, “Experimental results on unreinforced masonry shear walls damaged and repaired,” in *Proceedings of the 10th International Brick and Block Masonry Conference (IB2MaC '94)*, Calgary, Canada, July 1994.
 - [34] M. A. ElGawady, P. Lestuzzi, and M. Badoux, “A review of retrofitting of unreinforced masonry walls using composites,” in *Proceedings of the 13th IB2MC*, Paper no. 90, p. 10, Amsterdam, The Netherlands, 2004.
 - [35] H. Santa-Maria, P. Alcaino, and C. Luders, “Experimental response of masonry walls externally reinforced with carbon fiber fabrics,” in *Proceedings of the 8th U.S. National Conference on Earthquake Engineering*, San Francisco, Calif, USA, 2006.
 - [36] M. Seki, R. Vacareanu, T. Saito et al., “Cyclic shear tests on plain and FRP retrofitted masonry walls,” in *Proceedings of the 14th World Conference on Earthquake Engineering*, Beijing, China, October 2008.

Research Article

Prediction of Flexural Capacity of RC Beams Strengthened in Flexure with FRP Fabric and Cementitious Matrix

Kyusan Jung, Kinam Hong, Sanghoon Han, Jaekyu Park, and Jaehyun Kim

Department of Civil Engineering, Chungbuk National University, 1 Chungdae-ro, Seowon-gu, Cheongju, Chungbuk 362-763, Republic of Korea

Correspondence should be addressed to Kinam Hong; hong@cbnu.ac.kr

Received 1 August 2015; Revised 28 September 2015; Accepted 28 September 2015

Academic Editor: Osman Gencel

Copyright © 2015 Kyusan Jung et al. This is an open access article distributed under the Creative Commons Attribution License, which permits unrestricted use, distribution, and reproduction in any medium, provided the original work is properly cited.

This paper presents both experimental and analytical research results for predicting the flexural capacity of reinforced concrete (RC) beams strengthened in flexure with fabric reinforced cementitious matrix (FRCM). In order to assess the efficiency of the FRCM-strengthening method, six beams were strengthened in flexure with FRCM composite having different amounts and layers of FRP fabric and were tested under four-point loading. From test results, it was confirmed that the slippage between the FRP fabric and matrix occurs at a high strain level, and all of the FRCM-strengthened beams failed by the debonding of the FRCM. Additionally, a new bond strength model for FRCM considering the slippage between fabric and matrix was proposed, using a test database to predict the strengthening performance of the FRCM composite. The prediction of the proposed bond strength model agreed well with the debonding loads of the test database.

1. Introduction

Fabric reinforced cementitious matrix (FRCM) composites were developed to strengthen deteriorated reinforced concrete structures and have been employed during the last two decades [1]. Unlike externally bonded fiber reinforced polymer (FRP) systems, epoxy resin is not used for the FRCM-strengthening method. The FRP fabric used in the FRCM-strengthening method is attached by using a cementitious matrix, an inorganic material, instead of epoxy resin [2]. The use of an inorganic material can solve various problems that result from the use of epoxy resin [3]. The major problems associated with epoxy resin are its low glass transition temperature, difficulty of application at low temperatures, inability to apply to humid surfaces, and lack of vapor permeability [1]. Additionally, FRCM composite has higher fire resistance than externally bonded FRP sheets and laminates [4]. However, the mechanical properties of a cementitious matrix, such as bond strength, are generally lower than those of epoxy resin. Thus, the FRP materials in the FRCM-strengthening method are shaped like fabric or textile to improve the bond strength of the FRP reinforcement [5].

Many experimental studies have been performed to verify the efficiency of the FRCM-strengthening method. D'Ambrisi and Focacci [3] investigated the flexural performance of RC beams strengthened with FRCM composite using two different FRP net materials, carbon fiber net and polypara-phenylene benzobisoxazole (PBO) fiber net, and shapes. It was confirmed from their study that PBO-FRCM performs better than carbon-FRCM and the variation of the debonding strain with the number of layers is more gradual than that of FRP materials [3]. Additionally, they insisted that it is necessary to identify more representative material parameters which can describe the mechanical behavior of different types of matrices in relation to the adapted type of fibers [3]. Ombres [6] investigated the flexural performance of RC beams strengthened with PBO-FRCM composite and predicted their flexural behavior by using various existing bond strength models for externally bonded reinforced FRP. Based on his research results, he suggested that when debonding failures occur, the predictions of the existing bond strength model are not accurate and a more accurate and reliable debonding model for FRCM-strengthened RC beams should be developed [6]. Loreto et al. [7] evaluated the performance of RC slab strengthened with PBO-FRCM composite by

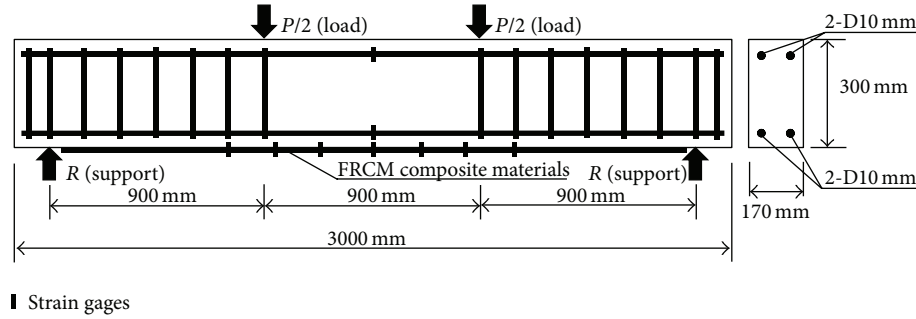


FIGURE 1: Test specimen layout.

three-point bending test and performed an analytical study to verify the level of accuracy of the ultimate capacity prediction according to the ACI 549 [8] guide, where the proposed equations are based on the conventional reinforced concrete theory. Through the results of their study, they reported that the ultimate capacity prediction according to the ACI 549 [8] guide was satisfactory because the tensile properties used in the analysis did not depend on fiber rupture but are based on the performance of the FRCM tensile coupon during the crack formation zone [7]. Babaeidarabad et al. [1] tested FRCM-strengthened beams having 1-ply and 4-ply PBO fabric and predicted the efficiency of the FRCM-strengthening method through a section analysis, following methodology in accordance with ACI 549 [8] and ACI 318 [9]. Their research results showed that the strain compatibility of a beam with 1-ply fabric was no longer satisfied, due to fabric slippage within the matrix after steel yielding. They noted that the slippage behavior can be captured in the analysis by the tensile characteristic parameters obtained from FRCM coupon testing [1].

Meanwhile, several studies to identify the bond-slip behavior between the fiber/matrix and FRCM/concrete interface have been performed by a few researchers. Ombres [4] carried out an experimental and theoretical study on the bond-slip behavior between concrete and PBO-FRCM composite and proposed a nonlinear bond-slip model for FRCM using the experimental data. However, the parameters of his model should be calibrated using more experimental data. D'Ambrisi et al. [10] experimentally and analytically evaluated the bond stress between CFRP-FRCM materials and masonry and reported that the debonding occurs at the fibers/matrix interface after a considerable fibers/matrix slip. Also, D'Ambrisi et al. [11] performed an experimental study on the bond-slip between PBO-FRCM and concrete and reported that the debonding strain in PBO fibers decreased in proportion to $1/\sqrt{n}$ with an increase in the number of layers, n .

Although some studies on the bond-slip behavior of fiber/matrix and FRCM/concrete interface have been performed, a bond strength model for FRCM has not been established yet. Moreover, the ACI 549 [8] guideline applicable for predicting the strengthening efficiency of FRCM composite also requires an additional FRCM coupon test, to define the tensile characteristic parameters of the FRCM composite. Thus, this study aimed to perform the flexural tests including

TABLE 1: Mixture properties of concrete.

W/C (%)	S/a (%)	Unit weight (kg/m^3)				
		W	C	S	G	Ad ^(a)
48.4	48.1	168	345	860	949	2.07

^(a) AE water-reducing admixture.

TABLE 2: Mechanical properties of rebar used.

Nominal diameter (mm)	Modulus of elasticity (MPa)	Yield strength (MPa)	Ultimate strength (MPa)	Elongation (%)
9.53	2.0×10^5	480	590	17.1

the number of plies and the amount of FRP fabric as test variables and to develop a bond strength model to predict the flexural behavior of FRCM-strengthened beams without an additional test.

2. Experimental Program

2.1. Test Specimens. The experimental program consisted of seven beams of 3,000 mm and a cross section of 170×300 mm. Two deformed bars were placed on the tension and compression faces, respectively. Shear reinforcements were placed in a center-to-center spacing of 150 mm to prevent shear failure in all specimens. Steel reinforcement of D10 with a nominal diameter of 9.53 mm was used for tension, compression, and shear reinforcement. The side and vertical concrete cover was kept at 30 mm for all beams. The details of the test specimens are presented in Figure 1.

2.2. Materials. Ready-mix concrete was used to fabricate the beams. The mixture properties of the concrete used are tabulated in Table 1.

Six standard concrete cylinders with dimensions of $\Phi 100 \text{ mm} \times 200 \text{ mm}$ were cast and tested according to ASTM C39/C39M [12]. The average compressive strength of the concrete obtained from the compressive tests for the cylinders was 28.0 MPa at the age of 28 days. Mechanical properties of rebar were determined by the direct tensile tests for three coupons in accordance with ASTM A370 [13] in the laboratory. Material properties of the rebar used were taken from tests and are given in Table 2.

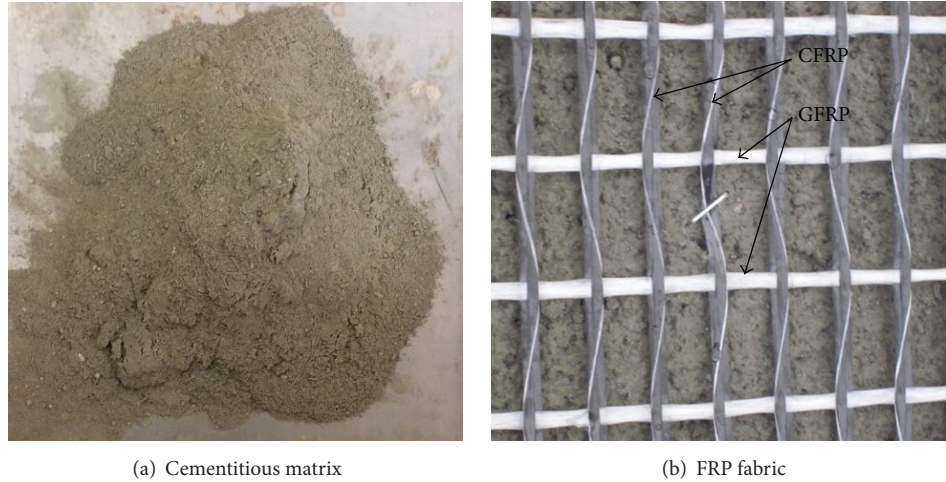


FIGURE 2: Components of FRCM composite.

TABLE 3: Mechanical properties of cementitious matrix.

	Elastic modulus (GPa)	Compression strength (MPa)
Cementitious matrix	40	45

The cementitious matrix and FRP fabric used for flexural strengthening of RC specimens are shown in Figures 2(a) and 2(b), respectively. The cementitious matrix consisted of microcement, fine aggregate, polypropylene staple fiber, and admixtures. The compressive strength of the cementitious matrix was determined from a compression test of five cubes of 50 mm size according to ASTM C109/C109M [14] and measured as 45 MPa at the age of 28 days. Table 3 presents the mechanical properties of the cementitious matrix obtained from the compression test.

As shown in Figure 2(b), the FRP fabric consisted of CFRP and GFRP strips. Black CFRP and white GFRP strips were laid in the warp direction and weft direction, respectively, at spacings of 17 mm and 33 mm. The FRP fabric was divided into Type A and Type B by the amount of CFRP fiber per strip. The cross-sectional areas of a CFRP strip for Types A and B were 1.8 and 2.7 mm², respectively. Additionally, the nominal thicknesses of FRP fabric for Types A and B were 0.0107 mm and 0.0162 mm, respectively. The mechanical properties of the FRP fabric offered by manufacturers are presented in Table 4.

2.3. Test Program. The test variables included the number of plies and the amount of FRP fabric. An unstrengthened specimen used to relatively assess the strengthening performance of FRCM was labeled as Control. Specimens strengthened with FRP fabric were labeled using a one-letter abbreviation and an Arabic number. The first letter, A or B, represents Type A or B of the FRP fabric, respectively. The following Arabic number, 1, 2, or 3, represents the application of 1-ply,

TABLE 4: Mechanical properties of FRP fabric.

Type	Nominal thickness (mm)	Elastic modulus (GPa)	Ultimate tensile strength (MPa)	Ultimate tensile strain (%)
A	0.107	240	4,300	1.75
B	0.162	240	4,300	1.75

TABLE 5: Test variables.

Group	Specimen ID	Type of FRP fabric	Number of plies
	Control	—	—
A	A1	Type A	1
	A2		2
	A3		3
B	B1	Type B	1
	B2		2
	B3		3

2-ply, or 3-ply FRP fabric on the bottom face of the specimen, respectively. Table 5 illustrates the test variables.

2.4. Strengthening Procedure. The strengthening procedure of the FRCM composite was as follows. (1) The first layer of cementitious matrix with a nominal thickness of 2 mm was applied on the bottom surface of the specimen. (2) The precut FRP fabric was laid on the cementitious matrix. (3) The second layer of cementitious matrix with a nominal thickness of 2 mm was applied on the FRP fabric. In the case of strengthening with 2-ply and 3-ply FRP fabric, the above procedure was repeated two and three times, respectively. The nominal thickness of FRCM with 1-ply FRP fabric was taken as approximately 5 mm. The bond length of FRP fabric was 2,600 mm regardless of the number of FRP fabric layers. Flexural tests were performed after 28 days of strengthening to allow the cementitious matrix to develop sufficient strength.

TABLE 6: Summary of experimental results.

Specimen ID	Ultimate load (kN)	Deflection at ultimate load (mm)	Percent increase over Control (%)	Failure mode
Control	44.5	11.0	—	Flexure
A1	58.6	18.0	131.7	Debonding
A2	62.7	15.5	141.0	Debonding
A3	83.6	22.0	187.9	Debonding
B1	65.5	22.9	147.2	Debonding
B2	73.7	15.6	165.6	Debonding
B3	97.8	21.6	219.8	Debonding



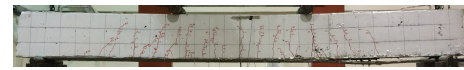
FIGURE 3: Test setup.



(a) Control



(b) A3



(c) B3

FIGURE 4: Failure modes of specimens.

2.5. Test Setup. All beams were tested using a simply supported system with a net span of 2,700 mm. The tests for all beams were performed under four-point loading, as shown in Figure 3.

Load was applied at a stroke rate of 0.4 mm/min by a hydraulic actuator with a maximum capacity of 2,000 kN. The load was measured by a load cell. The deflections were measured by Linear Variable Differential Transducers (LVDTs) at midspan. As shown in Figure 1, the strains of FRP fabric were measured by seven strain gauges attached on CFRP strip at the spacing of 200 mm. The strains in the concrete and steel rebars at the midspan of each beam were measured by strain gauges. The strain in the concrete was measured by a strain gauge placed on the top of each beam before testing. For steel rebar, strain was measured by a strain gauge mounted in each tension rebar before concrete casting. The load and strains were recorded by using a data logger. During the test, the propagation of crack and damage of FRCM composite were visually inspected and recorded on the surface of the beam.

3. Test Results and Discussion

3.1. Summary of Test Results. The test results for ultimate load, deflection, and failure mode of each specimen are presented in Table 6. The flexural strengths of beams strengthened with FRCM composite increased from 131.7% to 219.8% relative to the Control specimen. The ultimate load of the FRCM-strengthened beams increased with a higher amount of FRP

fabric, and all of them failed by the debonding of the FRCM composite.

3.2. Failure Mode. Figure 4 shows the failure modes of representative specimens in each group. The initial crack of the Control specimen occurred at the midspan under a load of 21.8 kN. New vertical cracks occurred with the increase in applied load and the initial cracks were progressed toward the compressive zone. With the increase of applied load, the vertical cracks extended about 90% of the height of the cross section. Finally, the Control specimen failed due to the yielding of tensile reinforcement followed by crushing of the concrete compressive zone (see Figure 4(a)).

In the case of specimen A3 strengthened with 3-ply FRP fabric, an initial crack occurred at the load of 25.9 kN and then the crack pattern produced by the increase of applied load was similar to that of the Control. The average spacing of vertical flexural cracks was approximately 100 mm and much closer than that of Control. The interfacial debonding of the FRCM composite started at the vertical crack under a loading point and gradually progressed toward a right support (see Figure 4(b)). However, failure began with the concrete cover ripping-off before complete debonding of the FRCM composite happened. Eventually, it failed by FRCM composite debonding followed by the crushing of the concrete compressive zone between two loading points.

The initial crack load of specimen B3 with the FRP fabric of Type B occurred at the load of 30.9 kN. Until the applied load attained approximately 95 kN, no debonding of

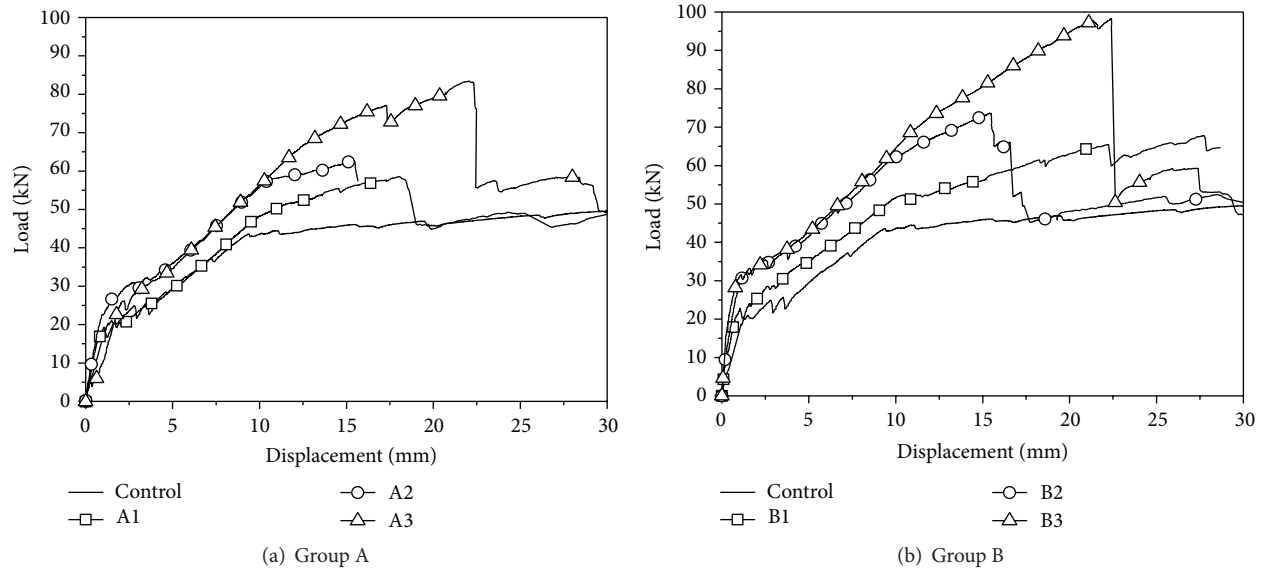


FIGURE 5: Load-displacement curves of specimens.

the FRCM composite was observed in the specimen. However, once the load reached the maximum load of 97.8 kN, the debonding of FRCM composite suddenly occurred at the right side of the specimen (see Figure 4(c)). The crack pattern of specimen B3 was similar to that of specimen A3, but the debonding process of the FRCM composite was different.

3.3. Comparison of Load-Deflection Curves. Figures 5(a) and 5(b) show the load-deflection curves of specimens in Groups A and B, respectively.

The initial flexural stiffness of specimens in Groups A and B was higher than that of the Control specimen but was not proportional to the amount of FRP fabric. This is due to the fact that the strengthening effect of an externally bonded reinforced system is exhibited after the occurrence of an initial crack. Flexural stiffness after the yielding of tensile steel represents the effect of the amount of FRP fabric, as shown in Figures 5(a) and 5(b). Additionally, the maximum load of the specimens significantly increased with a greater number of FRP fabric layers. The maximum loads of specimens A1, A2, and A3 in Group A were 58.6 kN, 62.7 kN, and 83.6 kN, respectively. The maximum loads of specimens B1, B2, and B3 were 65.5 kN, 73.7 kN, and 97.8 kN, respectively. However, the maximum loads were not proportional to the number of FRP fabric layers in both Group A and Group B. On the other hand, the strengthening performances of B1, B2, and B3 with Type B of FRP fabric were higher than those of A1, A2, and A3 with Type A, respectively. This resulted from the difference in the amount of FRP fiber. As mentioned before, the nominal thicknesses of the FRP fabric layer for Types A and B were 0.0107 mm and 0.0162 mm, respectively. Therefore, it can be concluded that Type B is more effective than Type A for the FRCM-strengthening method.

3.4. Relationship of Load-FRP Fabric Strain. Figures 6(a) and 6(b) show comparisons of load-FRP fabric strain curves measured at the midspan of specimens in Groups A and B. The load-strain curves of all specimens in Groups A and B exhibited a trend in which the tensile strain of the FRP fabric rapidly increased after the occurrence of an initial crack. In particular, the FRP fabric strain of specimen A1 increased much rapidly compared to those of other specimens. It is because the contribution of cementitious matrix to the tensile strength is transferred to FRP fabric after the formation of initial crack at midspan, so that the FRP fabric of specimen A1 with the lowest fabric amount contributes much higher tensile strength than other specimens. The strains of specimens in Groups A and B ultimately reached approximately $8,000 \mu\epsilon$ and $12,000 \mu\epsilon$, respectively. Although the maximum strains of specimens in Group B were higher than those of specimens in Group A, these were less than 70% of the strain corresponding to FRP fabric rupture, $17,500 \mu\epsilon$. Before initial crack occurrence, the relationship of load-FRCM fabric strain was linear. However, the relationship after initial crack became nonlinear, resulting from the bond-slip behavior between the FRCM fabric and cementitious matrix.

3.5. Strain Distribution at a Midspan Cross Section. Figures 7(a) and 7(b) show the strain distribution along the depth at a midspan cross section of representative specimens of Groups A and B. The strains of concrete, tensile rebar, and FRP fabric were checked at representative load stages. It can be observed from Figure 7 that the neutral axis rises and the slippage between FRP fabric and the cementitious matrix increases with the higher load. Consequently, it should be noted that the strain distribution of a section at low strain can be assumed to be linear, but it cannot be regarded as linear at

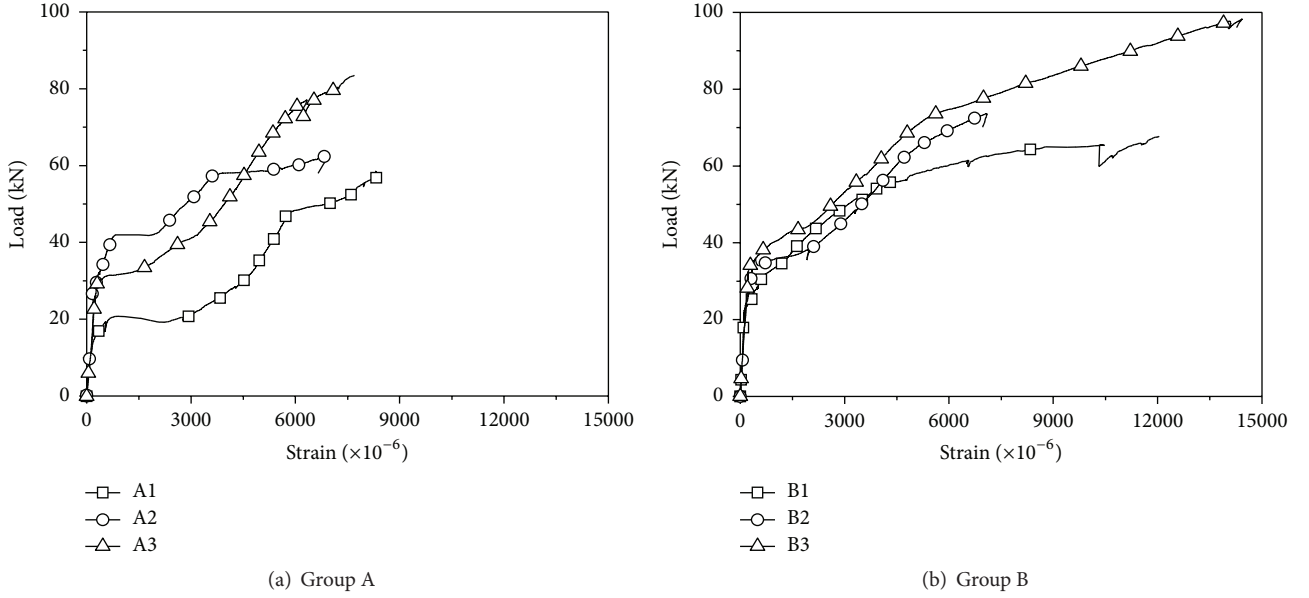


FIGURE 6: Comparisons of load-FRP fabric strain curves.

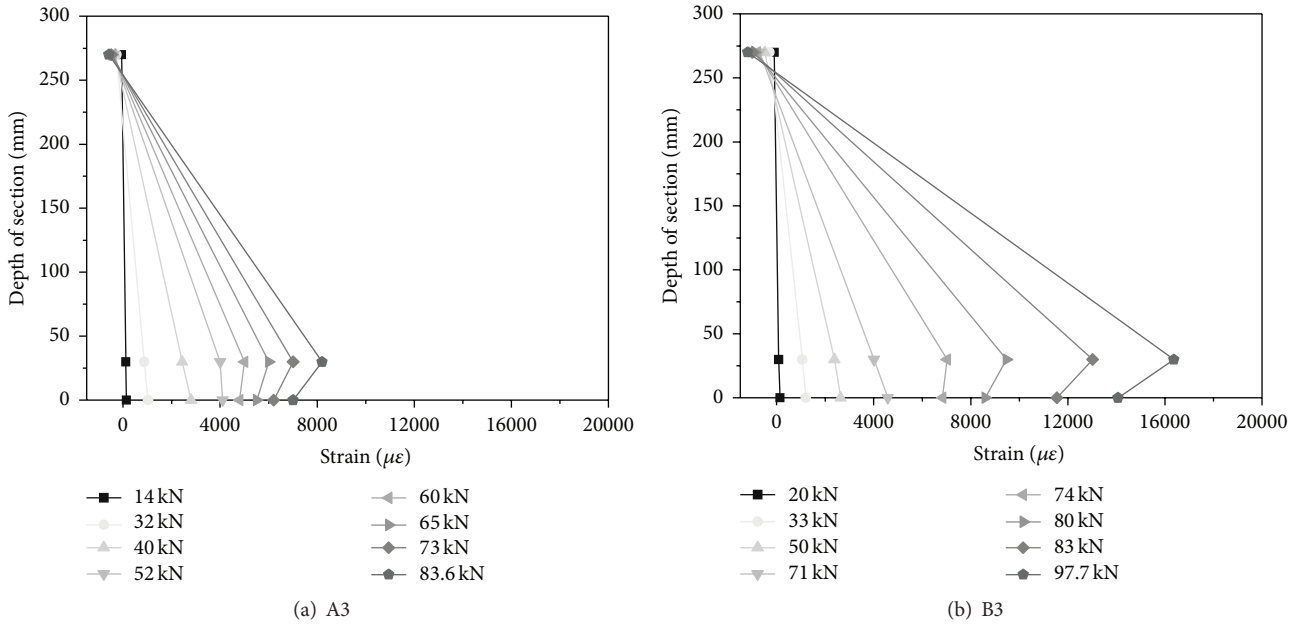


FIGURE 7: Strain distributions at a midspan section.

the high strain level, due to the slippage between FRP fabric and cementitious matrix.

4. Numerical Analysis

4.1. Proposition of Bond Strength Model. The bond strength model proposed by Teng et al. [15] has been well known as a model for externally bonded reinforcement (EBR). Although the bond-slip behavior of the FRCM composite is different from that of EBR due to the adhesive being used, it was

considered that the bond-slip concept based on fracture mechanics was similar in both cases. Therefore, a new bond strength model, which was based on the model by Teng et al. [15], was used to evaluate the effective stress of the FRCM composite in this study. Equation (1) shows the model by Teng et al. [15]:

$$\sigma_p = \alpha \beta_p \beta_L \sqrt{\frac{E_p \sqrt{f'_c}}{t_p}}, \quad (1)$$

TABLE 7: Database for RC beams strengthened with FRCM composite.

Reference	Specimen ID	b_c (mm)	d (mm)	h (mm)	A_s (mm ²)	f_y (MPa)	f'_c (MPa)	E_f (GPa)	t_1 (mm)	Number of plies
Project study	A1	170	270	300	142.6	480	28.0	240	0.107	1
	A2	170	270	300	142.6	480	28.0	240	0.107	2
	A3	170	270	300	142.6	480	28.0	240	0.107	3
	B1	170	270	300	142.6	480	28.0	240	0.162	1
	B2	170	270	300	142.6	480	28.0	240	0.162	2
	B3	170	270	300	142.6	480	28.0	240	0.162	3
Babaeidarabad et al. [1]	L.1	152	260	305	258	276	29.1	280	0.05	1
	L.4	152	260	305	258	276	29.1	280	0.05	4
	H.1	152	260	305	258	276	42.91	280	0.05	1
	H.4	152	260	305	258	276	42.91	280	0.05	4
Ombres [6]	S2.T1.P2	150	230	250	157	525.9	23.02	270	0.045	2
	S2.T1.P3	150	230	250	157	525.9	23.02	270	0.045	3
	S2.T2.P2	150	230	250	157	525.9	22.39	270	0.045	2
	S2.T2.P3	150	230	250	157	525.9	22.39	270	0.045	3
Loreto et al. [7]	L.1.X	305	129	152	213.9	414	29.1	280	0.05	1
	L.4.X	305	129	152	213.9	414	29.1	280	0.05	4
	H.1.X	305	129	152	213.9	414	42.91	280	0.05	1
	H.4.X	305	129	152	213.9	414	42.91	280	0.05	4

where

$$\beta_p = \sqrt{\frac{2 - b_p/b_c}{1 + b_p/b_c}},$$

$$\beta_L = \begin{cases} 1, & \text{if } L \geq L_e, \\ \sin \frac{\pi L}{2L_e}, & \text{if } L < L_e, \end{cases} \quad (2)$$

$$L_e = \sqrt{\frac{E_p t_p}{\sqrt{f'_c}}},$$

where b_p is the width of the bonded plate, b_c is the width of the concrete block, L is the bond length, L_e is the effective bond length, E_p is the elastic modulus of plate, t_p is the thickness of the bonded plate, f'_c is the cylinder compressive strength for concrete, and α is the reduction factor and given as 0.427 by Teng et al. [15].

In the FRCM composite, the total nominal thickness of FRP fabric t_p is defined by

$$t_p = t_1 \times n, \quad (3)$$

where t_1 is the nominal thickness of 1-ply FRP fabric and n is the number of layers.

Meanwhile, D'Ambrisi et al. [11] suggested through the experimental study for bond-slip behavior between an FRCM composite and concrete that the FRP fabric strain corresponding to its debonding $\epsilon_{f,deb}$ decreases at the rate of $1/\sqrt{n}$ with the higher amount of FRP fabric. Therefore, (3) can be modified into (4) in the bond strength model for FRCM

composite, considering the slippage between FRP fabric and matrix:

$$t_p = t_1 \times \sqrt{n}. \quad (4)$$

Finally, the bond strength model for the FRCM composite is proposed as

$$\sigma_{FRCM} = \alpha \beta_p \beta_L \sqrt{\frac{E_p \sqrt{f'_c}}{t_1 \sqrt{n}}}, \quad (5)$$

where σ_{FRCM} is the stress in the FRCM composite at debonding.

In addition, the coefficient α should be calibrated to account for the difference between FRCM and EBR. The test data of RC beams strengthened with FRCM composite were collected to calibrate the α value. Table 7 shows the collected test database for RC beams strengthened with FRCM composite. The database consists of the geometries and material properties of 18 RC beams tested under four-point or three-point loading.

For the database given in Table 7, as the strain in the FRP fabric at the critical section was not reported, the experimental value of stress in the FRP fabric at debonding, $f_{f,deb}$, was deduced from the experimental debonding moment, $M_{u,deb}$, using the conventional reinforced concrete theory. Figure 8 shows the analytical model to deduce the experimental stress in the FRP fabric at debonding from the experimental debonding moment. It illustrates the assumed basic analytical conditions of internal strain, stress, and resultant force for a FRCM-strengthened section at ultimate stage. Both strain compatibility and internal force equilibrium in the analytical model were assumed to relate the stress in the FRP fabric to the applied moment.

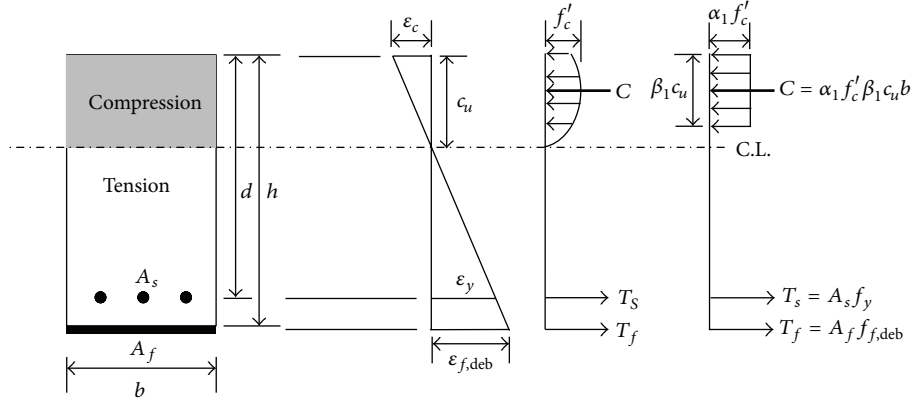


FIGURE 8: Analytical model at the ultimate stage.

In Figure 8, the experimental debonding moment, $M_{u,deb}$, is expressed according to (6a), (6b), (6c), (6d), (6e), (6f), (6g), and (6h). The tensile steel was assumed to be yielded based on the test results in the section analysis:

$$M_{u,deb} = M_s + M_f, \quad (6a)$$

where

$$M_s = A_s f_y \left(d - \frac{\beta_1 c_u}{2} \right), \quad (6b)$$

$$M_f = n A_f f_{f,deb} \left(h - \frac{\beta_1 c_u}{2} \right), \quad (6c)$$

$$\beta_1(c_u) = \frac{4\varepsilon'_c - \varepsilon_c(c_u)}{6\varepsilon'_c - 2\varepsilon_c(c_u)}, \quad (6d)$$

$$\varepsilon'_c = \frac{1.7f'_c}{E_c}, \quad (6e)$$

$$E_c = 4,700\sqrt{f'_c}, \quad (6f)$$

$$f_{f,deb} = E_f \varepsilon_{f,deb}, \quad (6g)$$

$$\varepsilon_c = \frac{c_u}{h - c_u} \varepsilon_{f,deb}, \quad (6h)$$

where M_s is the contribution of steel reinforcement to nominal flexural strength, M_f is the contribution of FRP reinforcement to nominal flexural strength, A_s is the area of steel reinforcement, M_f is the area of FRP reinforcement, d is the distance from extreme compression fiber to centroid of tension reinforcement, h is the long side cross-sectional dimension of rectangular, f_y is the yield stress of steel reinforcement, ε'_c is the compressive strain corresponding to f'_c , E_c is the modulus of elasticity of concrete, E_f is the modulus of elasticity of FRP fabric, $\varepsilon_{f,deb}$ is the strain in the FRCM composite at debonding, c_u is the neutral axis depth at the ultimate moment, β_1 is the concrete stress block factor, and ε_c is the concrete compressive strain.

The stress $f_{f,deb}$ can be expressed as (7) by using (6a)–(6c):

$$f_{f,deb} = \frac{M_{u,deb} - A_s f_y \left(d - \beta_1 c_u / 2 \right)}{n A_f \left(h - \beta_1 c_u / 2 \right)}. \quad (7)$$

Also, the stress $f_{f,deb}$ should satisfy the internal force equilibrium expressed as (8a), (8b), (8c), (8d), and (8e):

$$T_s + T_f = C, \quad (8a)$$

where

$$T_s = A_s f_y, \quad (8b)$$

$$T_f = n A_f f_{f,deb}, \quad (8c)$$

$$C = \alpha_1 f'_c \beta_1 c_u b, \quad (8d)$$

$$\alpha_1(c_u) = \frac{3\varepsilon'_c \varepsilon_c(c_u) - [\varepsilon_c(c_u)]^2}{3\beta_1(c_u) \varepsilon'^2_c}, \quad (8e)$$

where T_s is the tensile force for steel reinforcement, T_f is the tensile force for FRCM composite, C is the compressive force for concrete, and α_1 is the concrete stress block factor.

The stress $f_{f,deb}$ was computed with the trial and error method using (7) and (8a)–(8e). The value of α for each beam given in Table 7 was calculated with (9) derived from $f_{f,deb}$ and (5):

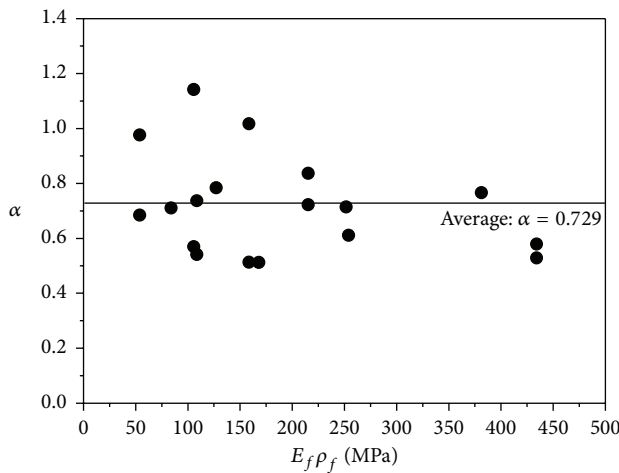
$$\alpha = \frac{f_{f,deb}}{\beta_p \beta_L \sqrt{E_p \sqrt{f'_c} / t_1 \sqrt{n}}}. \quad (9)$$

Finally, Figure 9 shows the α values calculated for test beams presented in Table 7. The average α value for total beams was taken as 0.729 from a regression analysis.

In order to verify the proposed bond strength model for FRCM, it was used to numerically predict the flexural capacity of the FRCM-strengthened RC beams. Table 8 shows the comparison between test results and analytical results. The ratio of test results to predicted values ranged from

TABLE 8: Comparisons between test results and analytical results.

Reference	Specimen ID	$P_{u.test}$ (kN)	$P_{u.analysis}$ (kN)	$P_{u.test}/P_{u.analysis}$
Project study	A1	58.58	58.57	1.00
	A2	62.70	71.26	0.88
	A3	83.60	82.25	1.02
	B1	65.52	62.70	1.05
	B2	73.68	78.14	0.94
	B3	97.76	91.46	1.07
Babaeidarabad et al. [1]	L1	67.70	62.51	1.08
	L4	99.00	90.76	1.09
	H1	63.00	64.76	0.97
	H4	96.80	96.51	1.00
Ombres [6]	S2_T1_P2	66.00	55.10	1.20
	S2_T1_P3	71.39	60.37	1.18
	S2_T2_P2	52.86	54.89	0.96
	S2_T2_P3	55.71	60.10	0.93
Loreto et al. [7]	L1_X	45.01	44.25	1.02
	L4_X	65.30	71.50	0.91
	H1_X	42.00	46.48	0.90
	H4_X	65.76	77.48	0.85
Mean				1.00
Standard deviation				0.094

FIGURE 9: Computed α values.

0.85 to 1.20. The average and standard deviation of the ratios were 1.00 and 0.094, respectively. It should be noted from comparison that the proposed bond strength model for FRCM can be used to predict the flexural capacity of the FRCM-strengthened beam because test results agree well with the predicted values.

4.2. Load-Deflection Curve. The comparisons of load-deflection curves for representative beams of Table 7 are presented in Figure 10. Theoretical curves consisted of a trilinear diagram. Thus, the corresponding load and midspan

deflection at three stages, namely, cracking, yielding, and ultimate stage, were calculated using the moment capacity and strain compatibility. The midspan deflection, Δ , of flexural beam with simple supports under three- and four-point load was calculated from the following equations, respectively:

$$\Delta_{3,p} = \frac{1}{12} \frac{ML^2}{E_c I}, \quad (10)$$

$$\Delta_{4,p} = \frac{69}{648} \frac{ML^2}{E_c I}, \quad (11)$$

where M is the applied moment, L is the beam net span, and I is the corresponding moment of inertia. The term $M/E_c I$ is the curvature of the cross section at midspan, χ , calculated from

$$\chi = \frac{\varepsilon_s}{d - c}, \quad (12)$$

where c is the corresponding neutral axis depth and ε_s is the corresponding stress of tensile rebar.

The corresponding load at ultimate stage was derived from the moment computed using the proposed bond strength model. As shown in Figure 10, the predicted load-deflection response of FRCM-strengthened beams is in satisfactory agreement with experimental results. In particular, the slope between yielding and ultimate stage, namely, the debonding in the predicted diagram, agrees with test results well. It results from the accuracy of the proposed bond strength model, predicting the FRP fabric stress at debonding.

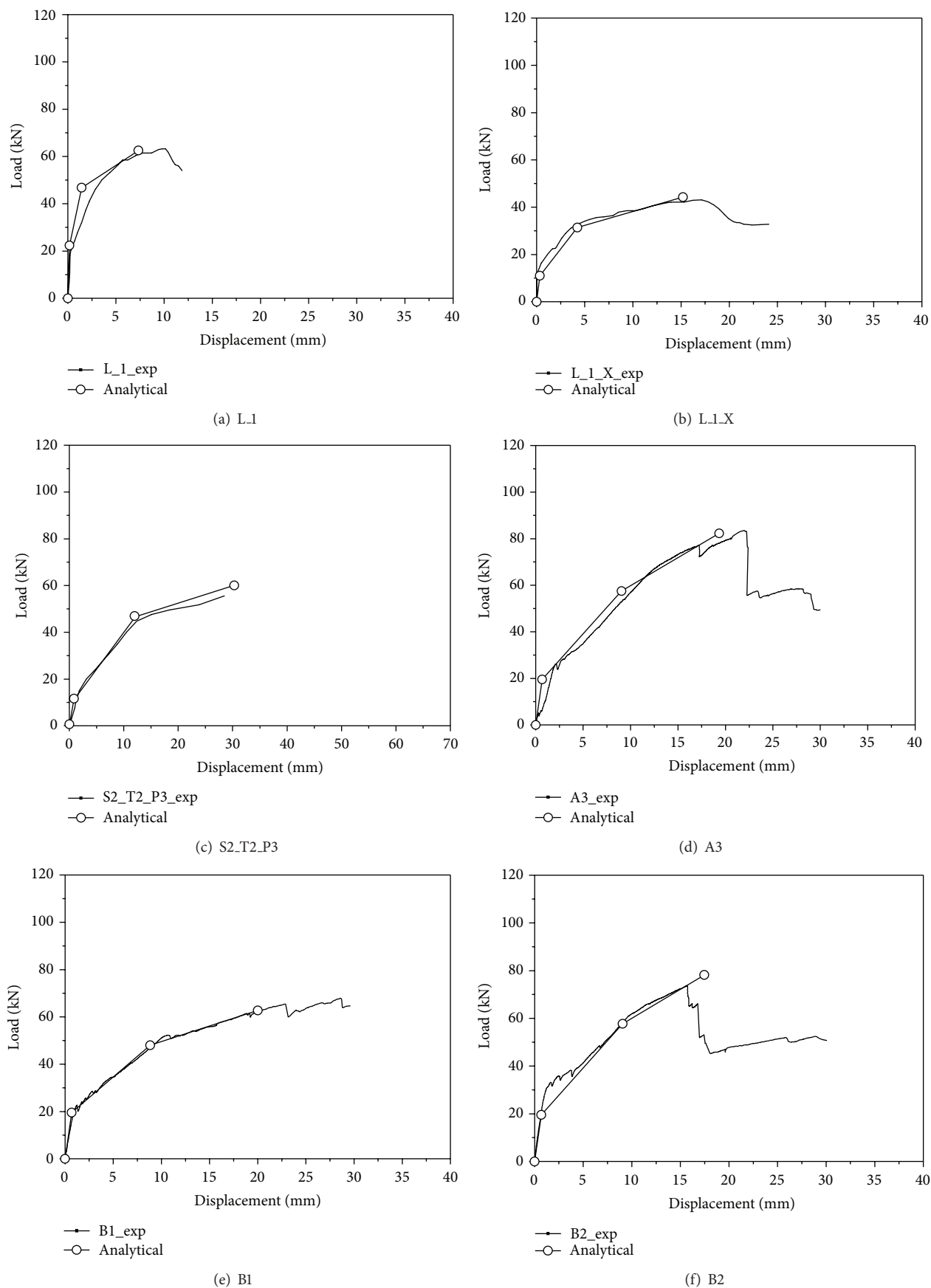


FIGURE 10: Comparisons of load-displacement curves.

5. Conclusion

The following conclusions are drawn from the results.

- (1) The flexural strengths of beams strengthened with FRCM composite ranged from 131.7% to 219.8% relative to a Control specimen, increasing with a higher amount of FRP fabric. Also, all of them failed by the debonding of the FRCM composite.
- (2) Before initial crack occurrence, the relationship of load-FRCM fabric strain was linear. However, the slippage between FRP fabric and cementitious matrix increased with the higher load after crack formation. Consequently, it should be noted that the strain distribution of a section at low strain can be assumed to be linear, but it cannot be regarded as linear at the high strain level, due to the slippage between FRP fabric and cementitious matrix.
- (3) Although the maximum strains of specimens in Group B were higher than those of specimens in Group A, these were less than 70% of the strain corresponding to FRP fabric rupture, 17,500 $\mu\epsilon$. These premature failures were due to the debonding of the FRCM composite.
- (4) A new bond strength model, which was based on the model by Teng et al. [15] and which considered the slippage between the FRP fabric and matrix, was proposed to predict the strengthening performance of the FRCM composite. The ratios of collected test results to predicted values ranged from 0.85 to 1.20. The average and standard deviation of the ratios were 1.00 and 0.094, respectively. Thus, it could be concluded that the proposed bond strength model for FRCM can be used to predict the flexural capacity of the FRCM-strengthened beam.
- (5) The predicted load-deflection response of FRCM-strengthened beams at cracking, yielding, and ultimate stage was in satisfactory agreement with experimental results, confirming the accuracy of the proposed bond strength model.

Conflict of Interests

The authors declare no conflict of interests.

Acknowledgment

This research was supported by Basic Science Research Program through the National Research Foundation of Korea (NRF) funded by the Ministry of Science, ICT & Future Planning (NRF-2013R1A1A2012521).

References

- [1] S. Babaeidarabad, G. Loreto, and A. Nanni, "Flexural strengthening of RC beams with an externally bonded fabric-reinforced cementitious matrix," *Journal of Composites for Construction*, vol. 18, no. 5, 2014.
- [2] Y. A. Al-Salloum, H. M. Elsanadedy, S. H. Alsayed, and R. A. Iqbal, "Experimental and numerical study for the shear strengthening of reinforced concrete beams using textile-reinforced mortar," *Journal of Composites for Construction*, vol. 16, no. 1, pp. 74–90, 2012.
- [3] A. D'Ambrisi and F. Focacci, "Flexural strengthening of RC beams with cement-based composites," *Journal of Composites for Construction*, vol. 15, no. 5, pp. 707–720, 2011.
- [4] L. Ombres, "Analysis of the bond between fabric reinforced cementitious mortar (FRCM) strengthening systems and concrete," *Composites Part B: Engineering*, vol. 69, pp. 418–426, 2015.
- [5] C. G. Papanicolaou, T. C. Triantafillou, M. Papathanasiou, and K. Karlos, "Textile reinforced mortar (TRM) versus FRP as strengthening material of URM walls: out-of-plane cyclic loading," *Materials and Structures*, vol. 41, no. 1, pp. 143–157, 2008.
- [6] L. Ombres, "Flexural analysis of reinforced concrete beams strengthened with a cement based high strength composite material," *Composite Structures*, vol. 94, no. 1, pp. 143–155, 2011.
- [7] G. Loreto, L. Leardini, D. Arboleda, and A. Nanni, "Performance of RC slab-type elements strengthened with fabric-reinforced cementitious-matrix composites," *Journal of Composites for Construction*, vol. 18, no. 3, 2014.
- [8] American Concrete Institute, "Design and construction guide of externally bonded FRCM system for concrete and masonry repair and strengthening," ACI 549, American Concrete Institute, Farmington Hills, Mich, USA, 2013.
- [9] American Concrete Institute (ACI), "Building code requirements for reinforced concrete," ACI 318, American Concrete Institute, Farmington Hills, Mich, USA, 2011.
- [10] A. D'Ambrisi, L. Feo, and F. Focacci, "Experimental and analytical investigation on bond between carbon-FRCM materials and masonry," *Composites Part B: Engineering*, vol. 46, pp. 15–20, 2013.
- [11] A. D'Ambrisi, L. Feo, and F. Focacci, "Experimental analysis on bond between PBO-FRCM strengthening materials and concrete," *Composites B: Engineering*, vol. 44, no. 1, pp. 524–532, 2013.
- [12] ASTM International, "Standard test method for compressive strength of cylindrical concrete specimens," ASTM C39/C39M, ASTM International, West Conshohocken, Pa, USA, 2013.
- [13] ASTM, "Standard test methods and definitions for mechanical testing of steel products," ASTM A370, ASTM International, West Conshohocken, Pa, USA, 2013.
- [14] ASTM International, "Standard test method for compressive strength of hydraulic cement mortars," ASTM C109/C109M, ASTM International, West Conshohocken, Pa, USA, 2013.
- [15] J. G. Teng, S. T. Smith, J. Yao, and J. F. Chen, "Intermediate crack-induced debonding in RC beams and slabs," *Journal of Construction and Building Materials*, vol. 17, no. 6-7, pp. 447–462, 2003.

Research Article

Waste Materials from Tetra Pak Packages as Reinforcement of Polymer Concrete

Miguel Martínez-López,¹ Gonzalo Martínez-Barrera,² Carlos Barrera-Díaz,³
Fernando Ureña-Núñez,⁴ and Witold Brostow⁵

¹Facultad de Química, Universidad Autónoma del Estado de México, Paseo Colón Esquina, Paseo Tollocan, S/N, 50120 Toluca, MEX, Mexico

²Laboratorio de Investigación y Desarrollo de Materiales Avanzados (LIDMA), Facultad de Química, Universidad Autónoma del Estado de México, km 12 de la Carretera, Toluca-Atlaconulco, 50200 San Cayetano, MEX, Mexico

³Centro Conjunto de Investigación en Química Sustentable UAEM-UNAM, Universidad Autónoma del Estado de México, Campus El Rosedal, Autopista Ixtlahuaca-Atlaconulco, km 14.5, 50200 Toluca, MEX, Mexico

⁴Instituto Nacional de Investigaciones Nucleares, Carretera México-Toluca, S/N, 52750 La Marquesa Ocoyoacac, MEX, Mexico

⁵Laboratory of Advanced Polymers & Optimized Materials (LAPOM), Department of Materials Science and Engineering and Center for Advanced Research and Technology (CART), University of North Texas, 1150 Union Circle No. 305310, Denton, TX 76203-5017, USA

Correspondence should be addressed to Gonzalo Martínez-Barrera; gonzomartinez02@yahoo.com.mx

Received 5 May 2015; Revised 5 August 2015; Accepted 28 September 2015

Academic Editor: Cornelia Vasile

Copyright © 2015 Miguel Martínez-López et al. This is an open access article distributed under the Creative Commons Attribution License, which permits unrestricted use, distribution, and reproduction in any medium, provided the original work is properly cited.

Different concentrations (from 1 to 6 wt%) and sizes (0.85, 1.40, and 2.36 mm) of waste Tetra Pak particles replaced partially silica sand in polymer concrete. As is well known, Tetra Pak packages are made up of three raw materials: cellulose (75%), low density polyethylene (20%), and aluminum (5%). The polymer concrete specimens were elaborated with unsaturated polyester resin (20%) and silica sand (80%) and irradiated by using gamma rays at 100 and 200 kGy. The obtained results have shown that compressive and flexural strength and modulus of elasticity decrease gradually, when either Tetra Pak particle concentration or particle size is increased, as regularly occurs in composite materials. Nevertheless, improvements of 14% on both compressive strength and flexural strength as well as 5% for modulus of elasticity were obtained when polymer concrete is irradiated.

1. Introduction

Cement concrete is the most widely used structural material in the world, due to its easy preparation and low cost. Some disadvantages of cement concrete are (a) pores, which can become entrance points for water, gases, water vapor, and chemical substances that might damage concrete; (b) the roughness of concrete surface that deteriorates rapidly because of its high abrasion; (c) poor resistance to aggressive substances and salty water; (d) low resistance to heat. One alternative for such problems is the incorporation of natural or synthetic polymeric materials into concrete, which have good binding with mineral aggregates of concrete.

Such kinds of materials promote the development of polymer-based materials with improved physicochemical

properties. In fact, composite materials include a matrix (continuous phase) and reinforcement (discrete phase). The material chosen as the matrix generally is less strong and rigid than the reinforcing material. In general, the reinforcement is used to increase the mechanical strength and rigidity; some reinforcements are also used to improve high temperature performance and abrasion resistance. Moreover, with synthetic polymers it is possible to produce more flexible and cheaper materials [1–4].

Among the composite materials for civil engineering applications, polymer concrete has a preferential place. This is a composite material produced from inorganic aggregates (such as sand, gravel, or fly ash) bonded together by a polymeric binder (or plastic glue), instead of water and cement binder typically used in cement concrete. Polymeric

binder can be thermoplastic or more frequently a thermosetting material. Currently polymer concrete is used for the production of industrial flooring, countertops for bathrooms and kitchens, saunas, water storage tanks, and prefabricated structures used in the field of construction. It is also used in electrical applications such as insulators for high voltage transmission, support for isolation bushings, and solid-core insulation [5–8].

Nowadays, because of the more stringent legislation regarding the environment and the market demand for environmentally-friendly products, manufacturers are concerned with developing studies aimed at reducing the environmental impact, through lowering the amount of produced residues or by treating those that are inevitably generated during production processes. High costs associated with raw material extraction, as well as the damage that extraction causes to environment, are also important reasons to motivate the use of domestic and industrial residues. Depletion of reliable, trustable raw material reserves and conservation of nonrenewable sources also contribute to reusing waste materials.

Recycling of engineering materials will contribute to the sustainability and development of industrial processes. Nowadays, metals, glass, thermal plastics, and many other engineering materials are recycled to a great extent. However, composite materials, as a special category of engineering materials, have not considerable progress in recycling, due to its heterogeneous composition [9].

In recent years, various tools and strategies have been proposed to meet environmental challenges in the building industry: (a) increasing the use of waste materials, especially those that are by-products of industrial processes; (b) using recycled materials instead of natural resources (this will make the industry more sustainable); and (c) improving durability, mechanical and other properties, by reducing the amount of materials required for replacement [10–16].

Extensive research and development activities in recycling composite materials have been conducted, and various technologies have been developed in three categories: (a) mechanical recycling, (b) thermal recycling, and (c) chemical recycling. Mechanical recycling involves shredding and grinding, followed by screening to separate the component fractions for reuse. Thermal processing uses high temperature to decompose the resin and separate the reinforcements (300–1000°C). Moreover, secondary fuel or thermal energy is produced through pyrolysis, gasification, or combustion. Finally, chemical recycling allows depolymerization or removal of the matrix and liberation of the reinforcements for further recycling by using an organic or inorganic solvent. A cleaner process based on water technology has gained more attention in the research world and shown an interesting potential [9, 17–21].

A few investigations have been carried out on the use of recycled polymeric materials in concrete, covering different objectives as (a) recycled PET of bottles for producing very good quality polymer concrete with low cost for structural applications [22, 23]; (b) waste plastic aggregates for producing lightweight concrete with low thermal conductivity and reduced values of compressive and tensile strength when

TABLE 1: Polymer concrete components.

Lot (code)	Resin (%)	Sand (%)	Waste Tetra Pak particles (%)
PC	20	80	0
PC-1	20	79	1
PC-2	20	78	2
PC-4	20	76	4
PC-6	20	74	6

the waste plastic concentration is increased [24]; (c) HDPE waste from trash bags as a potential replacement for coarse aggregate in concrete [25]; (d) ground plastic materials as substitute of fine aggregates (up to 20%) in concrete [1]. Such recycling not only helps conserve natural resources, but also helps to solve a growing waste disposal crisis [26].

A lack of information is available regarding recycling of Tetra Pak constituent materials (polyethylene, cellulose, and aluminum) and their use as replacement of aggregates in polymer concrete. Containers such as Tetra Pak packaging have short useful life, becoming a trash and a serious problem for environment. Recycling of such packaging is low, compared with its high production of 26.4 billion packages in 2012, which were produced in 36 countries.

The Tetra Pak beverage containers are made from cellulose (75%), low density polyethylene (20%), and aluminum (5%). Once the container is discarded, it can be recycled in three ways: (a) being incinerated to produce electricity, (b) being recycled for paper making, and (c) being used for production of sheets and chipboard products. Tetra Pak recycling process has many stages; first the containers are washed to remove traces of originally contained products and after the mechanical grinding process is effected. It is important to mention that cellulose located at inner layers of the container makes it difficult to remove the water absorbed during the washing process; moreover, high content of hydroxyl groups of cellulose fibers makes them susceptible to water absorption.

However, an optional recycling way for Tetra Pak packaging is its use as substitute of mineral aggregates in the elaboration of polymer concrete, improving its properties, including lower weight and density, higher mechanical strength, and toughness.

In this work the effect of waste Tetra Pak particles (from beverage packaging) on the mechanical properties of polymer concrete was studied. Such particles replaced partially siliceous sand in the polymer concrete, elaborated with polyester resin and siliceous sand. In addition, the effect of gamma radiation on the compressive and flexural strength was evaluated.

2. Experimental

2.1. Specimen Elaboration. Five different polymer concrete lots identified by different codes were prepared as seen in Table 1. For each lot six specimens were prepared. Standard prismatic molds (40 × 40 × 160 mm) were used to formulate

polymer concrete specimens according to CPT PC-2 recommendation.

In the first stage, one lot of polymer concrete specimen (control concrete) was elaborated with a commercial unsaturated preaccelerated polyester resin (orthophthalic): a viscous liquid resin with a styrene monomer concentration of 30% (Polylite 32493- 00, Reichhold, Atlacomulco, Mexico) and siliceous sand of a local company (GOSA, Tlalnepantla, Mexico). The polymer concrete specimens had a composition of 20% by mass of polyester resin and 80% by mass of siliceous sand. The sand had uniform granulometry with an average diameter of 0.25 mm (mesh 60).

The proportion of the initiator methyl ethyl ketone peroxide (MEKP) added to the polymer resin for initiating the free-radical polymerization process was 1 mL/100 g of the resin weight. After mixing for 5 minutes, the polymer concrete specimens were placed in a controlled temperature room at $30.0 \pm 3.0^\circ\text{C}$ up to 24 hours.

In the second stage, four lots of polymer concrete specimens were elaborated, but now siliceous sand was partially substituted by Tetra Pak particles (see Table 1), in different concentrations (1, 2, 4, and 6% by mass). The Tetra Pak particle sizes were bigger than those for siliceous sand, for covering a homogenous distribution of sizes: Tetra Pak particles: 0.85 mm, 1.40 mm, and 2.36 mm (mesh 20, mesh 14, and mesh 8, resp.) and siliceous sand: 0.25 mm (mesh 60).

2.2. Mechanical Tests. The mechanical tests of polymer concrete specimens were carried out in a Controls Universal testing machine, with a load cell of 30 tons. The compressive testing is at a loading rate of 1.25 mm/min, holding the charge until reaching the maximum value to assure the reliability of the test; according to the UNE 83821:1992 standard test, it is important to mention that six specimens of each lot were elaborated for compressive testing.

The flexural testing at a loading rate of 1 mm/min was according to CPTPCM-8 standard for three-point bending test. Load-displacement curves and the maximum load for the collapse bending were recorded. Each lot of the six elaborated specimens was submitted to flexural testing.

2.3. Gamma Radiation. The polymer concretes specimens were exposed to varying gamma radiation doses using ^{60}Co pencils of 5.2 years of life on average. The experiments were performed in air at room temperature; the dosages were 100 and 200 kGy at the dose rate of 3.5 kGy/h. The irradiation was provided by a Transelektro Irradiator LGI-01 manufactured by IZOTOP Institute of Isotopes Co., Ltd. (Budapest, Hungary) and located at the National Institute of Nuclear Research (ININ, Mexico).

3. Results and Discussion

3.1. Compressive Strength. Figure 1 shows compressive strength of polymer concrete containing waste Tetra Pak particles. The compressive strength of concrete without particles (control concrete) is 90 MPa. The results were analyzed in terms of two parameters: concentration and size of the waste Tetra Pak particles. With respect to waste particle

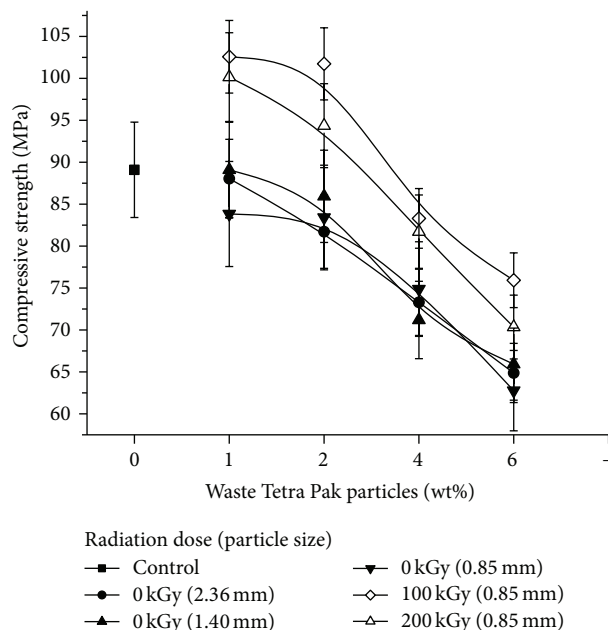


FIGURE 1: Compressive strength of polymer concrete in terms of waste particle size and irradiation dose.

concentration, increasing in the amount of added waste particles in the concrete specimens causes a gradual decrease in the compressive strength values. The lowest values were for concrete with 6% of waste particles, reducing in 28% compared with control concrete, namely, 65 MPa. Thus, waste particle concentration is a determining parameter for compressive strength of the polymer concrete. In terms of the particle size, for each particle concentration only small variations in the values were found. Thus, the particle size does not have major influence on the compressive strength.

Reduction in the compressive values can be attributed to the inefficient transfer of stresses between polymer concrete and Tetra Pak particles, which is consequence of (a) poor interaction between polymer concrete components (polyester resin and silica) and polyethylene layers of Tetra Pak containers and (b) poor adhesion between the two hydrophobic materials: polyester resin (matrix) and cellulose (from Tetra Pak containers). Despite the drying process of Tetra Pak particles prior to the preparation of concrete specimens, some moisture remained and acted as releasing agent on the waste particles-resin interface, consequently affecting the polymer concrete properties.

As was mentioned, reductions in the compressive values are attributed to the increment of particles concentration. It was corroborated with the surface morphology of the polymer concrete. Smooth and homogeneous surface on polymer concrete without Tetra Pak particles is appreciated in Figure 2(a); such surface is maintained and nonparticle agglomerations are observed when adding 2 wt% of Tetra Pak particles (Figure 2(b)). Nevertheless, for higher concentrations of particles, a rougher surface is appreciated (Figures 2(c) and 2(d)). Because there are no chemical interactions between polyester resin and waste particles, decreases of the

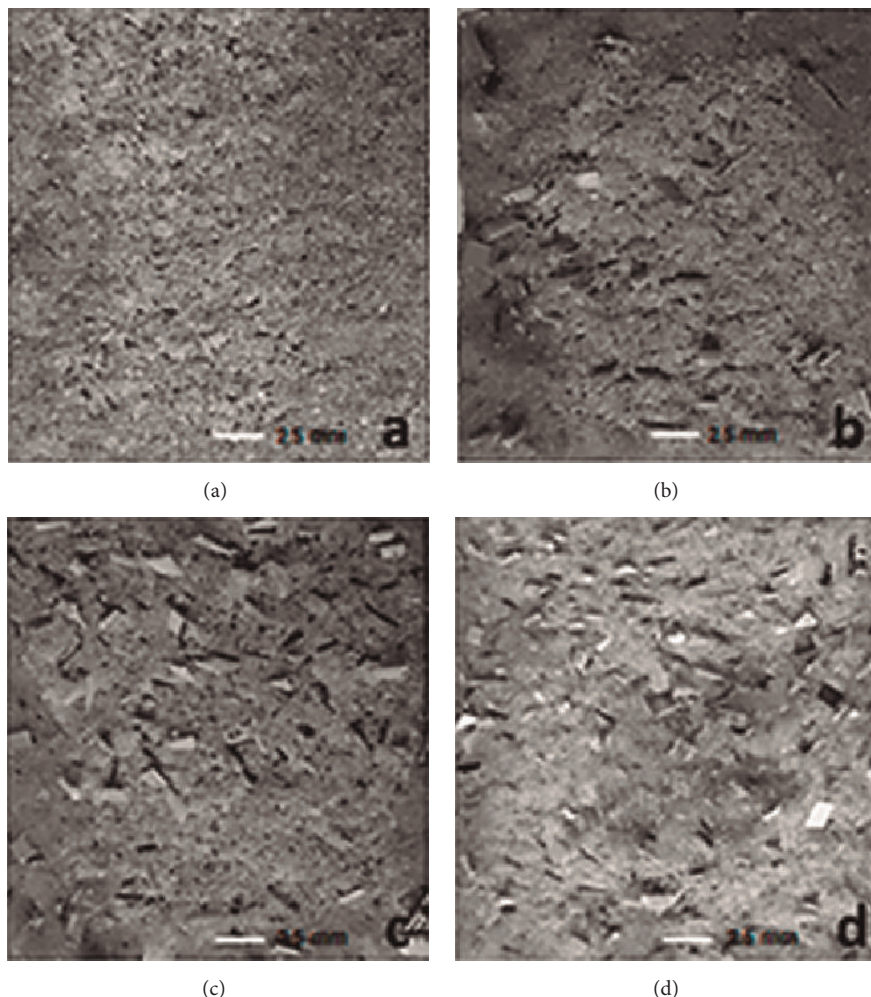


FIGURE 2: Polymer concrete (a) without Tetra Pak particles and with (b) 2 wt%, (c) 4 wt%, and (d) 6 wt%.

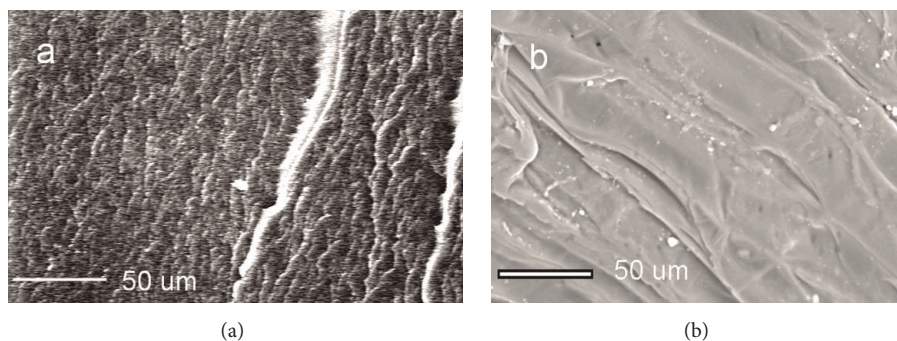


FIGURE 3: SEM images of irradiated (a) polyester resin matrix and (b) cellulose from Tetra Pak containers, at 200 kGy.

strength are consequence of the noninteractions between resin and Tetra Pak particles.

Because particle size does not have major influence on the compressive strength values, the polymer concrete with waste particle size of 0.85 mm was used to carry out the irradiation process.

In Figure 1, two different behaviors are appreciated for irradiated polymer concrete: (a) there is increment on the compressive strength for low concentrations of Tetra Pak

particles (1 and 2 wt%); such increments are 14% higher than those for simple polymer concrete, which are attributed to the gamma irradiation effects caused in polyester resin as well as in polyethylene and cellulose of the Tetra Pak particles [27–29]; (b) for higher particle concentrations (4 and 6 wt%), more interactions between the resin matrix and Tetra Pak particles are present. Nevertheless, such particles are more crystalline and generate some pores in the polymer concrete; these pores act as flaws that do not allow an

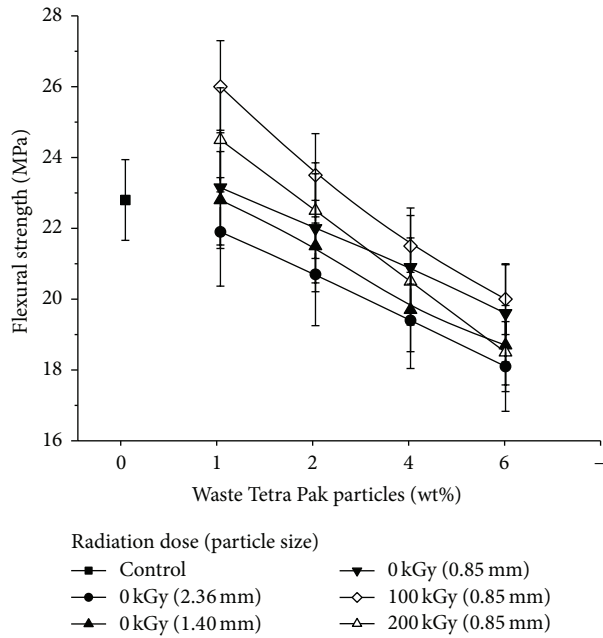


FIGURE 4: Flexural strength of polymer concrete containing waste Tetra Pak particles.

efficient transfer of charges, resulting in low compressive strength.

The increments in the compressive strength values are due to a better interfacial interaction between resin matrix and Tetra Pak particles, which happen at physical level and not through chemical bonding between them. Such assertion is based on the surface topology of the polyester resin and cellulose after irradiation. In the case of polyester resin, cross-linking of the polymeric chains produces increment on crystallinity and in consequence a rougher surface is observed (Figure 3(a)), while for cellulose of Tetra Pak more tendency toward scission of the polymer chains is detected, producing detachment of some particles (Figure 3(b)) [30].

3.2. Flexural Strength. The flexural strength values of concrete with waste Tetra Pak particles are shown in Figure 4. With respect to waste particles concentration, the flexural strength values decrease when increasing the particles concentration. The lowest value is for concrete with 6% of waste particles, which is 21% lower compared with control concrete. On the other hand, for each concentration the flexural strength values are lower when adding highest particle size, 2.36 mm. In the case of flexural strength, a moderated effect was observed with the different sizes of waste particles in the polymer concrete, in the same way as compressive strength behavior.

Gamma irradiation applied to polymer concrete improves the flexural strength values, mainly for concrete with 1% and 2% of waste particles. Such improvement is 14% higher than control concrete. For higher particle concentrations, the values decrease progressively to 12% lower than the control concrete. The diminution in the flexural values is more

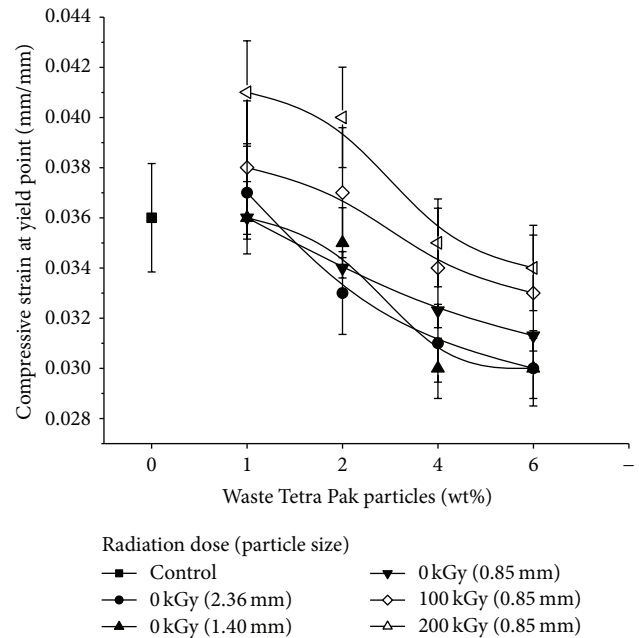


FIGURE 5: Compressive strain at yield point of concrete containing waste Tetra Pak particles.

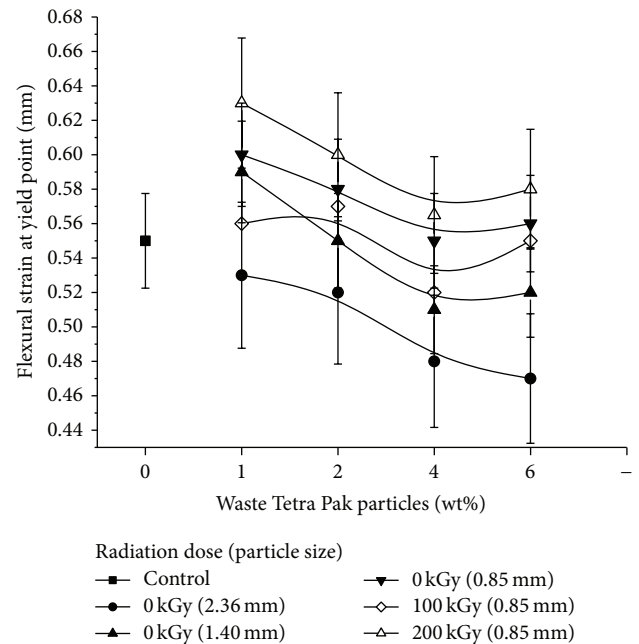


FIGURE 6: Flexural strain at yield point of concrete containing waste Tetra Pak particles.

notable when adding larger particle sizes that do not have uniform distribution in the polymer concrete, affecting the adherence with the polyester resin.

3.3. Compressive Strain at Yield Point. The compressive strains at yield point values are shown in Figure 5. In the case of control concrete, the value of 0.0036 mm/mm is lower than the standard polymer concrete reported in the literature,

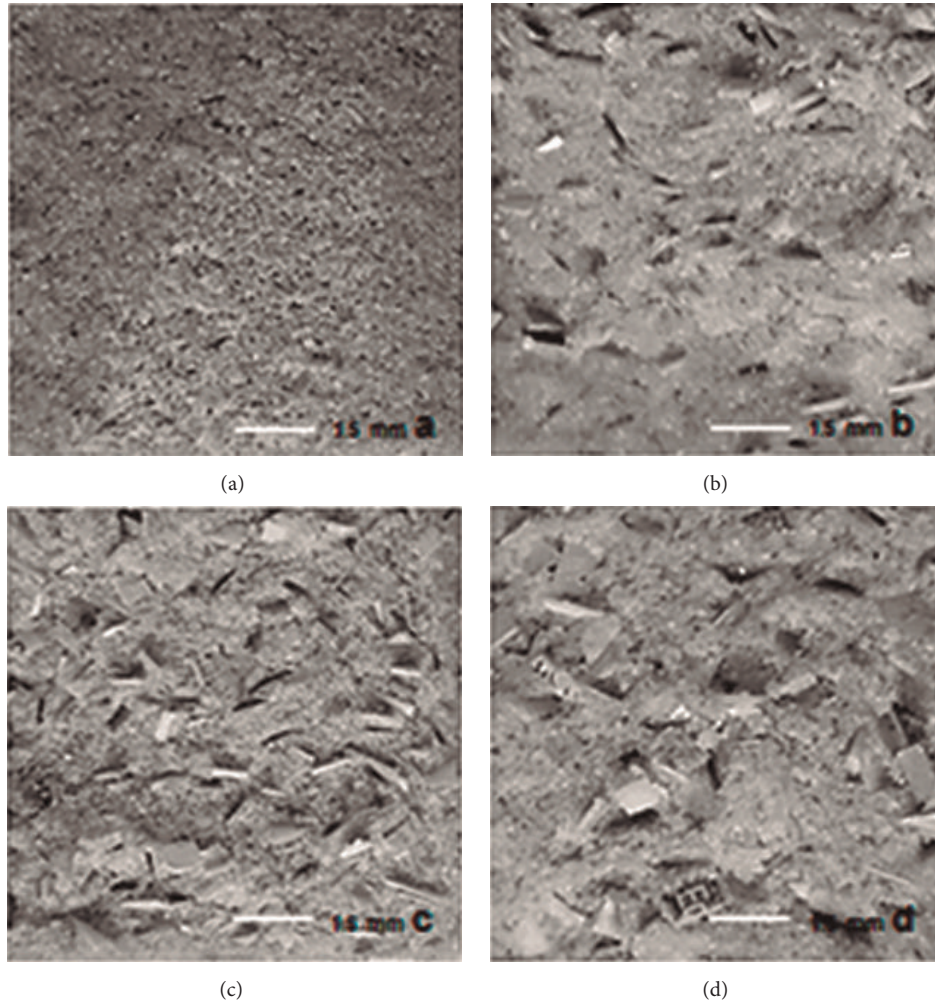


FIGURE 7: Polymer concrete without Tetra Pak particles (a) and with 1 wt% at different size; (b) 0.85 mm, (c) 1.40 mm, and (d) 2.36 mm.

namely, 0.006 mm/mm. Compressive strain values decrease progressively when adding waste particles. The lowest values are obtained for concrete with 6% of particles, which are 16% lower than control concrete. Nevertheless, a slight increment is observed for concrete with 1% of waste particles. In general, no significant variations on the values with respect to particle size were observed; thus certain strain stability was obtained.

When concrete is irradiated, a maximum improvement of 6% is obtained for concrete with 1% or 2% of particle concentrations and irradiated at higher dose (200 kGy). For concrete with higher particle concentrations a detrimental behavior of flexural strength is observed with lower values. These changes are attributed to the ionizing energy, which produces concrete with higher ductility; that is, the deformation occurs in a sustainable way before reaching the breaking point.

3.4. Flexural Strain at Yield Point. In the case of flexural strain values, significant changes were observed, as follows: with respect to particle concentrations, flexural strain value decreases when adding waste Tetra Pak particles; the highest values were obtained for 1% or 2% of particle concentrations (Figure 6). With respect to particle sizes, (a) improvements up to 8% on the values were obtained when lowest size

particles (0.85 mm) were added; thus a more ductile concrete is obtained; (b) by contrary, lowest values were obtained for concrete with large size particles (2.36 mm), being 12% lower than that for control concrete.

In the case of irradiated polymer concrete, by irradiating at 100 kGy, concrete deformation decreases up to 6%, for concrete with 6 wt% of waste particles. Nevertheless, for a dose of 200 kGy, the strain property is improved by 14%. Such improvement can be attributed to the stress transfer between polymer matrix and waste particles; it is effective for concrete with low concentrations (less than 4 wt%) of waste particles of size of 0.85 mm. As it is appreciated, a homogeneous surface for control concrete (without particles) is observed (Figure 7(a)) which presents changes when particles are added. Concrete with particles of 0.85 mm has the highest value of flexural strain values, which can be related to a greater contact area between the particles and the concrete matrix; thus the stress transfer is greater; moreover homogenous surface and good distribution of the particles are observed (Figure 7(b)), while for higher particle concentrations the values decrease and they are attributed to irregular distributions of particles (Figures 7(c) and 7(d)).

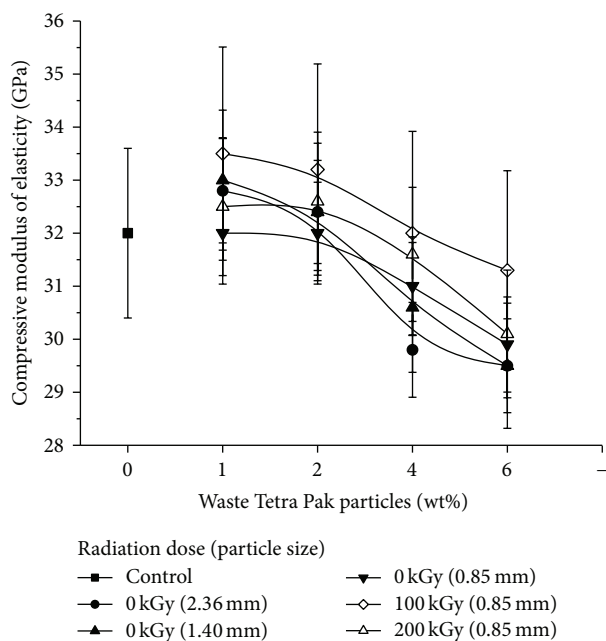


FIGURE 8: Compressive modulus of elasticity of polymer concrete at different particle concentrations.

3.5. Modulus of Elasticity. Figure 8 shows the modulus of elasticity for concrete containing waste particles. With respect to particle concentrations, a general behavior was observed: the values decrease gradually when increasing the addition of particles. Such diminution is consequence of the cellulose moisture. In fact, the water absorbed by the cellulose does not provide an efficient load transfer between polymer matrix and particles. It is important to mention that during polymer concrete elaboration temperatures over 130°C are reached by exothermic polymerization of resin; therefore the moisture in the cellulose can be evaporated and generate pores in polymeric matrix, which can modify mechanical properties of polymer concrete. The lowest value was obtained for concrete with 6% of waste particles, which means 10% lower than control concrete. With respect to particle size, slight variations in the values are observed.

Improvements of 5% are observed for irradiated concrete with 1% or 2% of waste particles; highest values were found with specimens irradiated at 100 kGy. The cross-linking effect caused by ionizing energy on the polymer matrix increases the resistance and thus Young's modulus increases [27].

4. Conclusions

In this work, the effects of the concentration and size of waste Tetra Pak particles (obtained from trash beverage bottles) on the compressive and flexural strength of polymer concrete were evaluated. The results show that the compressive and flexural strength and modulus of elasticity values decrease gradually when increasing the addition of waste particle concentration. A slight increment in the flexural strength values was observed for polymer concrete with smallest particle size. However, improvements of 14% were obtained

for compressive and flexural strength when irradiating the concrete specimens at 100 kGy. Finally the modulus elasticity was improved by 5%.

Conflict of Interests

The authors declare that none of them has a direct financial relationship with the commercial trademarks mentioned in this paper that might lead to a conflict of interests for any of the authors.

Acknowledgments

Financial support of the Autonomous University of the State of Mexico (UAEM), Toluca, by Grant UAEM 3886/2015FS is acknowledged. The authors thank National Council for Science and Technology of México (CONACYT) for the scholarship for one of the authors (Miguel Martínez-López) and Environmental Sciences Graduate Program of Universidad Autónoma del Estado de México (UAEM).

References

- [1] M. Batayneh, I. Marie, and I. Asi, "Use of selected waste materials in concrete mixes," *Waste Management*, vol. 27, no. 12, pp. 1870–1876, 2007.
- [2] M. Rahman, M. Islam, and M. Ahmed, "Recycling of waste polymeric materials as a partial replacement for aggregate in concrete," in *Proceedings of the International Conference on Chemical, Environmental and Biological Sciences (ICCEBS '12)*, pp. 99–102, Penang, Malaysia, 2012.
- [3] P. Soroushian, J. Plasencia, and S. Ravanbakhsh, "Assessment of reinforcing effects of recycled plastic and paper in concrete," *ACI Materials Journal*, vol. 100, no. 3, pp. 203–207, 2003.
- [4] R. Siddique, J. Khatib, and I. Kaur, "Use of recycled plastic in concrete: a review," *Waste Management*, vol. 28, no. 10, pp. 1835–1852, 2008.
- [5] M. C. S. Ribeiro, P. R. Nóvoa, A. J. M. Ferreira, and A. T. Marques, "Flexural performance of polyester and epoxy polymer mortars under severe thermal conditions," *Cement & Concrete Composites*, vol. 26, no. 7, pp. 803–809, 2004.
- [6] C. Vipulanandan and E. Paul, "Characterization of polyester polymer and polymer concrete," *Journal of Materials in Civil Engineering*, vol. 5, no. 1, pp. 62–82, 1993.
- [7] G. Martínez-Barrera, C. Menchaca-Campos, and F. Ureña-Núñez, "Gamma radiation as a novel technology for development of new generation concrete," in *Gamma Radiation*, F. Adrović, Ed., pp. 91–114, InTech, Rijeka, Croatia, 2012.
- [8] L. Czarnecki, "Polymer concretes," *Cement, Wapno, Beton*, no. 2, pp. 63–85, 2010.
- [9] Y. Yang, R. Boom, B. Irion, D.-J. van Heerden, P. Kuiper, and H. de Wit, "Recycling of composite materials," *Chemical Engineering and Processing: Process Intensification*, vol. 51, pp. 53–68, 2012.
- [10] K. S. Rebeiz, "Time-temperature properties of polymer concrete using recycled PET," *Cement and Concrete Composites*, vol. 17, no. 2, pp. 119–124, 1995.
- [11] K.-S. Yeon, Y.-S. Choi, and S.-H. Hyun, "Properties of recycled polymer concrete using crushed polymer concrete as an aggregate," in *Proceedings of the 2nd International Conference on*

- Sustainable Construction Materials and Technologies*, pp. 1299–1308, Ancona, Italy, June 2010.
- [12] B.-W. Jo, S.-K. Park, and C.-H. Kim, "Mechanical properties of polyester polymer concrete using recycled polyethylene terephthalate," *ACI Structural Journal*, vol. 103, no. 2, pp. 219–225, 2006.
 - [13] J. M. L. Dos Reis and M. A. G. Jurumenh, "Experimental investigation on the effects of recycled aggregate on fracture behavior of polymer concrete," *Materials Research*, vol. 14, no. 3, pp. 326–330, 2011.
 - [14] M. R. Ishak, Z. Leman, S. M. Sapuan, A. M. Edeerozey, and I. S. Othman, "Mechanical properties of kenaf bast and core fibre reinforced unsaturated polyester composites," *IOP Conference Series: Materials Science and Engineering*, vol. 11, Article ID 012006, 2010.
 - [15] M. E. Tawfik and S. B. Eskander, "Polymer concrete from marble wastes and recycled poly(ethylene terephthalate)," *Journal of Elastomers and Plastics*, vol. 38, no. 1, pp. 65–79, 2006.
 - [16] J. M. L. dos Reis, "Effect of textile waste on the mechanical properties of polymer concrete," *Materials Research*, vol. 12, no. 1, pp. 63–67, 2009.
 - [17] Y. Bai, Z. Wang, and L. Feng, "Chemical recycling of carbon fibers reinforced epoxy resin composites in oxygen in supercritical water," *Materials and Design*, vol. 31, no. 2, pp. 999–1002, 2010.
 - [18] J. M. Henshaw, "Recycling and disposal of polymer-matrix composites," in *ASM Handbook, Volume 21: Composites*, D. B. Miracle and S. L. Donaldson, Eds., pp. 1006–1012, ASM International, 2001.
 - [19] V. Goodship, *Management, Recycling and Reuse of Waste Composites*, WP, CRC Press, Cambridge, UK, 2010.
 - [20] S. Job, "Composite recycling—summary of recent research and development," Materials KTN Report, 2010.
 - [21] M. Blazsó, "Pyrolysis for recycling waste composites," in *Management Recycling and Reuse of Waste Composites*, V. Goodship, Ed., pp. 102–121, WP, CRC Press, Cambridge, UK, 2010.
 - [22] K. S. Rebeiz, S. P. Serhal, and D. W. Fowler, "Structural behavior of polymer concrete beams using recycled plastic," *Journal of Materials in Civil Engineering*, vol. 6, no. 1, pp. 150–165, 1994.
 - [23] G. Martínez-Barrera, C. Menchaca-Campos, C. E. Barrera-Díaz, and L. I. Avila-Cordoba, "Recent developments in polymer recycling," in *Gamma Rays: Technology, Applications and Health Implications*, I. Bikit, Ed., pp. 237–256, Nova Science Publishers, Hauppauge, NY, USA, 2013.
 - [24] A. A. Al-Manaseer and T. R. Dalal, "Concrete containing plastic aggregates," *Journal of Concrete International*, vol. 19, no. 8, pp. 47–52, 1997.
 - [25] A. M. Mustafa, S. Mohammad, A. R. Rafiza, and Y. Zarina, "Investigation of HDPE plastic waste aggregate on the properties of concrete," *Journal of Asian Scientific Research*, vol. 1, pp. 340–345, 2011.
 - [26] G. Martínez-Barrera and O. Gencel, "Structural modification of waste materials and its use in building materials," in *Photo Cured Materials*, A. Tiwari and A. Polykarpov, Eds., pp. 347–359, Royal Society of Chemistry, Cambridge UK, 2015.
 - [27] W. E. Loos, "Effect of gamma radiation on the toughness of wood," *Forest Products Journal*, vol. 12, no. 5, pp. 261–264, 1992.
 - [28] Shuler CE, "Gamma irradiation effects on modulus of elasticity of engelmann spruce," *Forest Products Journal*, vol. 21, no. 7, pp. 49–51, 1971.
 - [29] S. S. Cota, V. Vasconcelos, M. Senne Jr., L. L. Carvalho, D. B. Rezende, and R. F. Correa, "Changes in mechanical properties due to gamma irradiation of high-density polyethylene (HDPE)," *Brazilian Journal of Chemical Engineering*, vol. 24, no. 2, pp. 259–265, 2007.
 - [30] C. D. Nechifor, D. O. Dorohoi, and C. Ciobanu, "The influence of gamma radiations on physico-chemical properties of some polymer membranes," *Condensed Matter*, vol. 54, pp. 349–359, 2009.

Research Article

Shear Behavior of Concrete Beams Reinforced with GFRP Shear Reinforcement

Heecheul Kim, Min Sook Kim, Myung Joon Ko, and Young Hak Lee

Department of Architectural Engineering, Kyung Hee University, 1732 Deogyong-daero, Giheung-gu, Yongin-si, Gyeonggi-do 446-701, Republic of Korea

Correspondence should be addressed to Young Hak Lee; leeyh@khu.ac.kr

Received 5 August 2015; Revised 23 September 2015; Accepted 27 September 2015

Academic Editor: Gonzalo Martínez-Barrera

Copyright © 2015 Heecheul Kim et al. This is an open access article distributed under the Creative Commons Attribution License, which permits unrestricted use, distribution, and reproduction in any medium, provided the original work is properly cited.

This paper presents the shear capacities of concrete beams reinforced with glass fiber reinforced polymer (GFRP) plates as shear reinforcement. To examine the shear performance, we manufactured and tested a total of eight specimens. Test variables included the GFRP strip-width-to-spacing ratio and type of opening array. The specimen with a GFRP plate with a 3×2 opening array showed the highest shear strength. From the test results, the shear strength increased as the strip-width-to-strip-spacing ratio increased. Also, we used the experimental results to evaluate whether the shear strength equations of ACI 318-14 and ACI 440.1R can be applied to the design of GFRP shear reinforcement. In the results, the ACI 440 equation underestimated the experimental results more than that of ACI 318.

1. Introduction

Several studies have been carried out on the flexural behavior of concrete beams with fiber reinforced polymer (FRP) tensile reinforcement because FRP materials have advantages such as corrosion resistance, light weight, machinability, workability, and high strength [1–5]. Most FRP shear reinforcement for concrete members has been studied as a means of retrofitting. Hawileh et al. [6] and Al-Tamimi et al. [7] suggested techniques that involved externally bonding carbon fiber reinforced polymer (CFRP) laminates or sheets to reinforced concrete members. Hassan and Rizkalla [8] researched the bonding strength of FRP plates that were either embedded or attached to the exterior of concrete members. However, typical shear reinforcement (stirrup) for concrete members is difficult to fabricate with FRP materials because of their brittle nature and unidirectional characteristics. Therefore, FRP shear reinforcement has not yet been sufficiently investigated. The strength of the bent portion is significantly less than that of the straight part of FRP rods; hence several codes and design guidelines have specified the reduced capacity of FRP stirrups caused by bending the bars [9–12]. Recent studies investigated the shear capacities of FRP stirrups and proposed an equation of shear strength [12–15]. Kim et al. proposed

a new type of FRP shear reinforcement as a substitute for steel stirrups [16]. Plate-type FRP shear reinforcement has better constructability and easier fabrication than FRP stirrups. Also, plate shear reinforcement does not reduce the strength by concentrating stress in the bent portion. In an earlier paper, the types of FRP and shape of reinforcement did not significantly affect the shear strength.

In this paper, considering economics and ease of fabrication, we use a lattice shaped GFRP material for shear reinforcement. To evaluate the applicability of FRP plates for shear reinforcement, shear tests were conducted using concrete beams embedded with GFRP plates with openings, considering the array of the openings and the GFRP strip-width-to-spacing ratio as the main variables. We also analyzed the failure modes and strain distributions.

2. Experimental Investigation

2.1. Experimental Materials. Following ASTM C39 [17], we tested seven cylindrical specimens of 150 mm diameter and 300 mm height. The average compressive strength of the 28-day concrete was 44.6 MPa. Ten deformed steel bars with diameter of 25 mm and yield strength of 500 MPa were used

TABLE 1: Details of the experimental variations of the GFRP plate designs.

Specimen	Type	f_{fu} (MPa)	Width (w_f) (mm)	GFRP plate Thickness (t) (mm)	Center-to-center spacing of vertical strips (s) (mm)
A-1	A	480	20	4	340
A-2	A	480	30	4	340
A-3	A	480	50	4	340
A-4	A	480	70	4	340
A-5	A	480	65	4	170
A-6	A	480	70	4	110
B-3	B	480	37.5	4	230
C-3	C	480	37.5	4	230

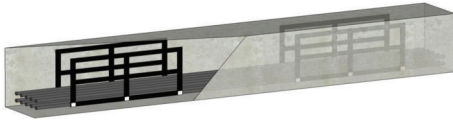


FIGURE 1: Schematic view of a concrete beam reinforced with GFRP plates.

as longitudinal reinforcement. We used GFRP plates with openings embedded in the concrete as shear reinforcement. The tensile test of the FRP was conducted based on CSA S806-02 [10]. The tensile stress was 480 MPa. Figure 1 shows a schematic view of a specimen.

2.2. Specimen Details. We considered the array of openings, GFRP strip-width-to-spacing ratio, and the amount of reinforcement as variables. The GFRP plates were manufactured in three shapes as shown in Figures 2 and 3. Each plate had the same total area ($b_f \times h_f$); the A-Type had a 2×2 opening array, B-Type a 3×2 opening array, and C-Type a 3×3 opening array. All the intersections of the horizontal (0°) and vertical (90°) components made right angles. The difference in the width of the horizontal and vertical components of each plate provided variants within each type of opening array. Details of the three plate designs and the variations within each type are given in Table 1.

We tested a total of eight concrete beams embedded with GFRP plates with openings. Figure 4 illustrates how we placed GFRP plates in the specimens depending on their shapes. The anchorage length (l_d) was 300 mm, far from the points of support. The total span (L) and clear span (l_n) were 2700 mm and 2100 mm, respectively. The thickness of the concrete cover was 40 mm, and the shear span-to-depth ratio was 2.4. All the specimens were reinforced using ten deformed steel bars with a diameter of 25 mm in two layers to ensure shear failure prior to flexural failure in the beam tests.

2.3. Test Setup. Load was applied to each specimen at a rate of 5 kN/min using a hydraulic jack with a maximum capacity of 5000 kN, as shown in Figure 5. The force generated by the hydraulic jack was transmitted to the center of a steel spreader beam installed to apply two-point loading to the beam

specimen. A load cell attached to the bottom of the jack measured the magnitude of the loading. A linear variable-differential transducer (LVDT) installed at the bottom center of the specimen measured the vertical displacement. As illustrated in Figure 5, we installed four strain gauges at the center of the horizontal and vertical components of each FRP plate. A data logger collected load, displacement, and strain data.

3. Shear Strength Equation

Figure 6 defines the width of the GFRP strip (w_f), effective depth (d), and spacing (s).

Several mechanisms contribute to the shear capacities of reinforced concrete beams, such as the concrete, shear reinforcement, mechanical aggregates interlocking, and dowel action of the tensile reinforcement. Shear reinforcement has a mechanism for resistance to shear, as shown in Figure 7. For this paper, we replaced the stirrup with a vertical strip of the FRP shear reinforcement. The function of the horizontal strip is to anchor the vertical strips. The horizontal projection of the crack is taken as d . The number of FRP vertical strips crossing the crack is d/s . Assuming that all FRP vertical strips reach their failure, the shear strength of the shear reinforcement can be obtained from

$$V_s = \frac{A_f f_{fu} d}{s}. \quad (1)$$

We assume the crack angle to be 45° when calculating the shear strength of the shear reinforcement. The tensile behavior of the FRP is characterized by a linearly elastic stress-strain relationship up to failure. Hence, shear failure is assumed to occur after fracture of the shear reinforcement.

3.1. Shear Strength Equation in ACI 318-14. As shown in (2), the shear strength equation in ACI 318-14 [15] provides the sum of the shear strength of the concrete and the shear reinforcement. The shear strength of concrete can be obtained from (3), which includes the longitudinal steel ratio (ρ_w) and shear span-to-depth ratio (a/d). Equation (4) calculates the shear strength of the shear reinforcement material based on the concept of the shear strength of a steel stirrup in ACI 318-14. Calculating the shear strength of FRP plates requires the area of the vertical components (A_f), the number of vertical

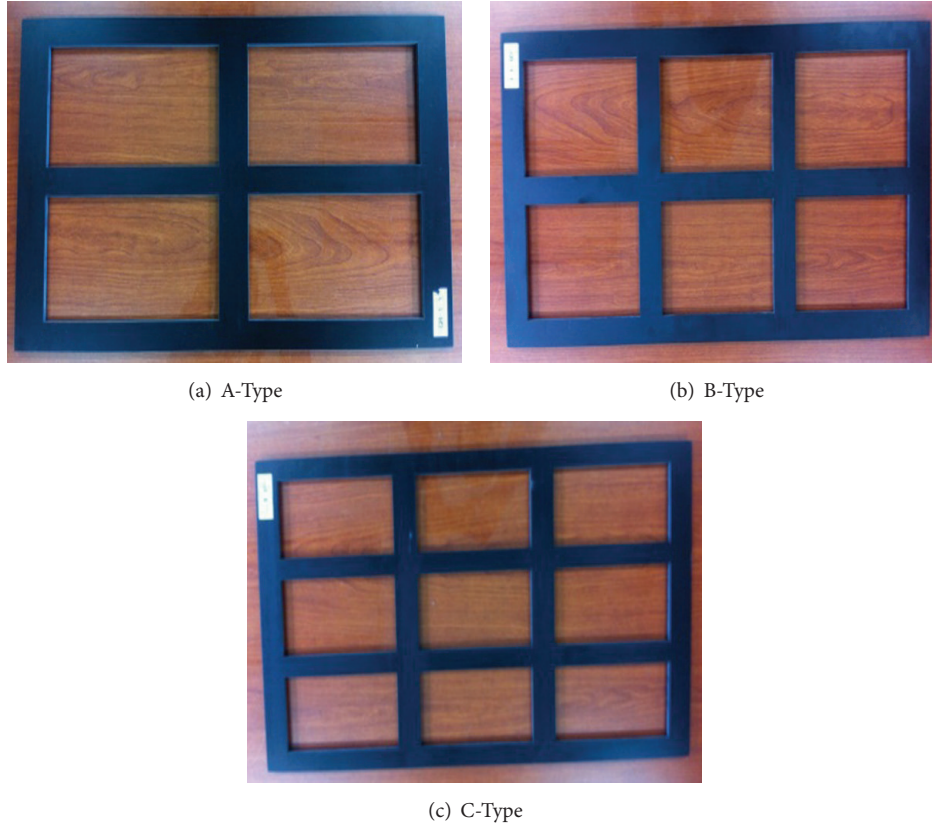


FIGURE 2: Designs of the three experimental GFRP plates.

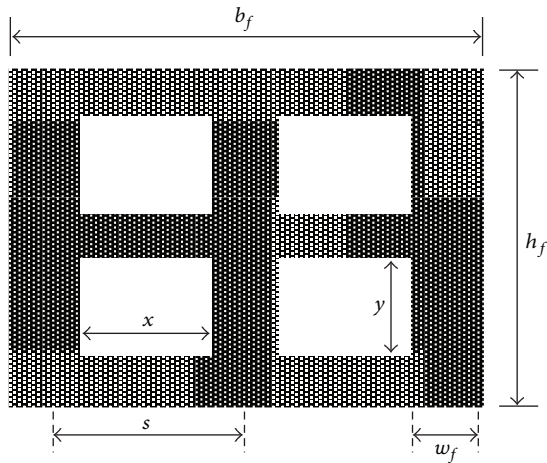


FIGURE 3: Notation of geometry for a GFRP plate.

components (n), and the tensile strength in the critical shear span, as in (4). The area of the plate (A_f) can be obtained from (5), and the number of vertical components in the critical shear span can be obtained from (6):

$$V_n = V_c + V_f, \quad (2)$$

$$V_c = \left(0.16\sqrt{f'_c} + \frac{17\rho_w d}{a} \right) b_w d, \quad (3)$$

$$V_{f,318} = nA_f f_{fu} \sin \alpha, \quad (4)$$

$$A_f = 2t_f w_f, \quad (5)$$

$$n = \frac{d}{s} (1 + \cot \alpha). \quad (6)$$

3.2. Shear Strength Equation in ACI 440.1R-06. ACI 440.1R provides a shear strength equation for concrete with FRP rebar flexural reinforcement. However, in this paper, we adopted the shear strength equation for concrete in ACI 318 because we used steel flexural reinforcement. The shear strength of the shear reinforcement can be calculated with (7). Equation (8) gives the stress level in the FRP shear reinforcement at its utmost for use in design. ACI 440.1R addresses the reduced shear strength of stirrups caused by bending the FRP bars, as shown in (9). Because our GFRP shear reinforcement is a plate type, we did not consider the bend portion. Consider

$$V_{f,440} = nA_f f_{fvd} \sin \alpha, \quad (7)$$

$$f_{fvd} = 0.004E_f \leq f_{fb}, \quad (8)$$

$$f_{fb} = \left(\frac{0.05r_b}{d} + 0.3 \right) f_{fu}. \quad (9)$$

4. Experimental Test Results

4.1. Failure Mode. As shown in Figure 8, flexural cracks occurred at the tension surface in the middle of the span, followed by the formation of inclined cracks. As the inclined

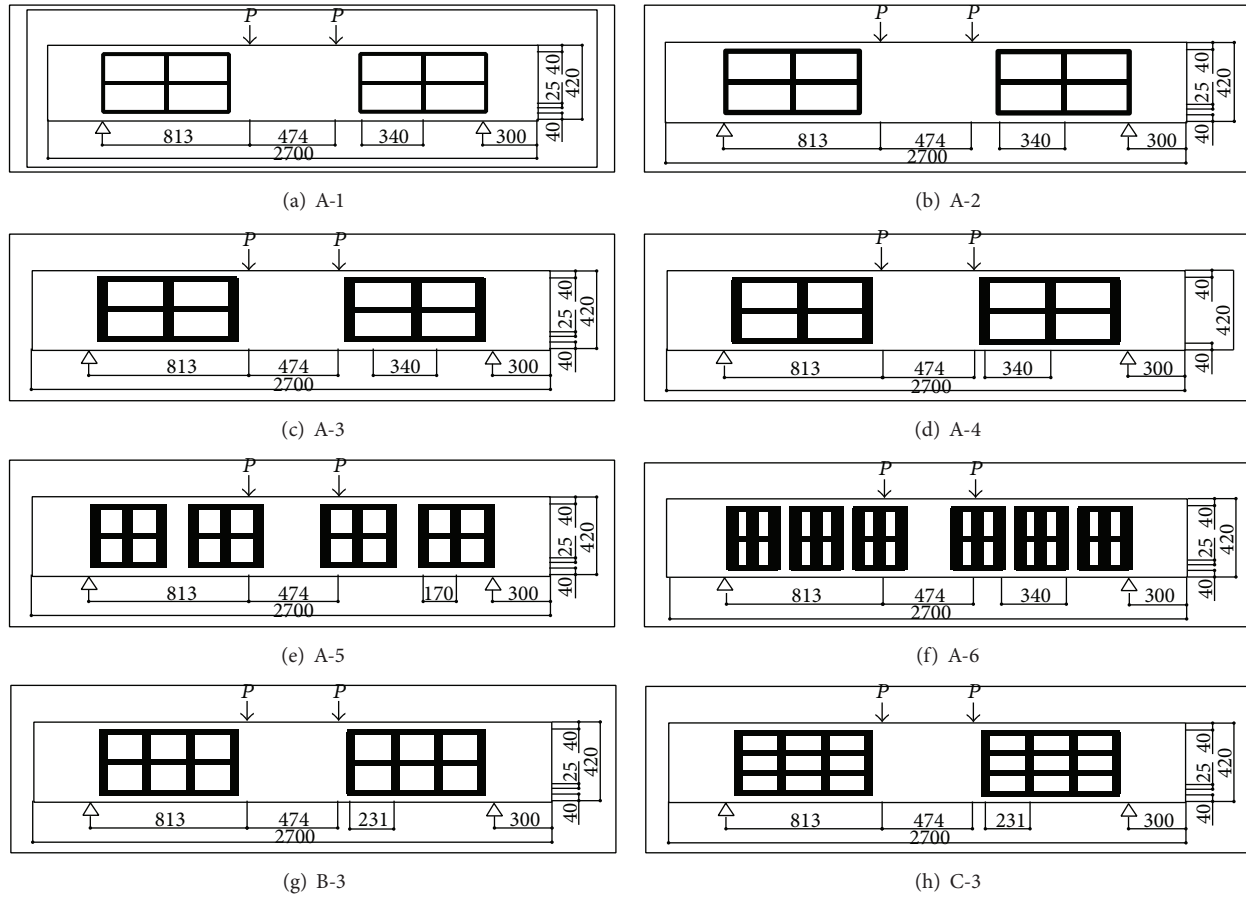


FIGURE 4: Arrangement of GFRP plates in specimens.

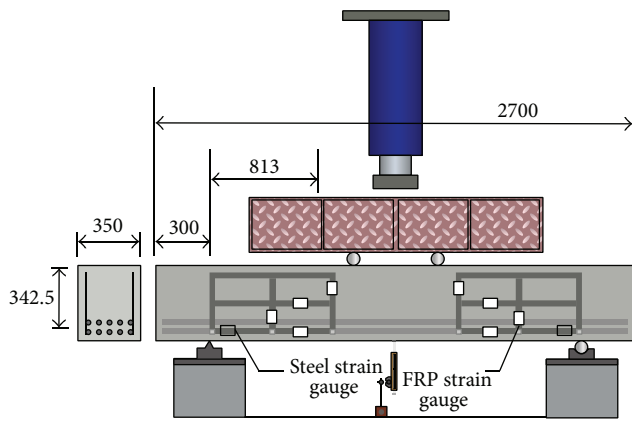
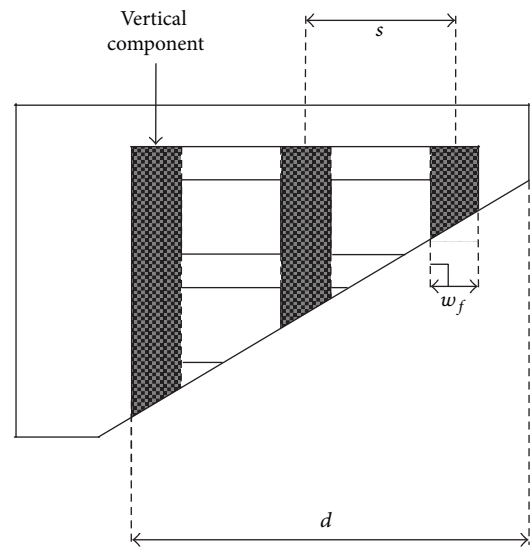


FIGURE 5: Test setup of typical specimen.

cracks propagated toward the loading point, concrete crushing occurred in the upper end region of the inclined crack at the final stage of failure. In other words, shear-compression failure (shear failure from the diagonal crack) occurred. The initial crack appeared at a load of approximately 150 kN in the middle of the beam. It appeared to be a flexural crack caused by tensile stress due to bending. At approximately 200 kN, a flexural shear crack appeared at effective depth, far from

FIGURE 6: Definitions of w_f , d , and s .

the point of support. At approximately 450 kN, the diagonal crack appeared, and then a flexural shear crack followed. The reinforcement of the GFRP plates increased resistance to the shear force as the diagonal crack occurred and elongated.

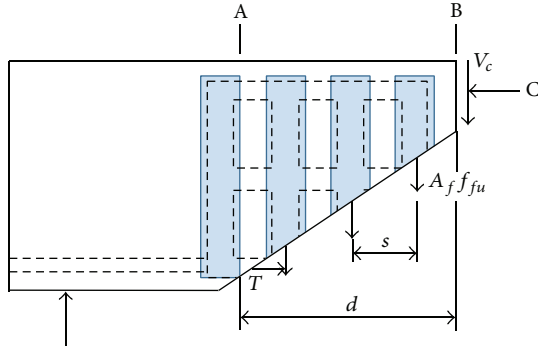
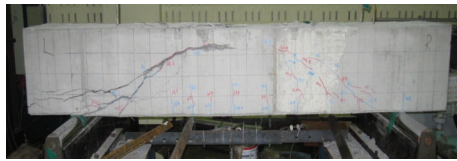


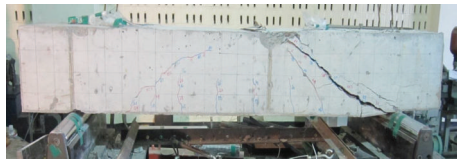
FIGURE 7: Shear resistance by FRP shear reinforcement.



(a) A-2



(b) A-3



(c) B-3



(d) C-3

FIGURE 8: Shear-compression failure in specimens.

When the GFRP plate reached the limit of its tensile strength, it fractured, and specimen failure occurred.

We observed two typical failure modes in response to the amount of reinforcement provided. First, all the specimens except A-5 and A-6 fractured, and the plates ruptured after they had demonstrated their maximum shear strength. The concrete cover of specimens A-5 and A-6, on the other hand, fractured before the plate reached its maximum shear strength. The specimens showed two different failure modes because the size of the openings in the plates and the ratio of the area of the openings varied. This result could also be caused by a lack of concrete coverage. Therefore if the opening size, ratio of the area of openings, and sufficient concrete

TABLE 2: Maximum loading and shear strength test results.

Specimen	P_{\max} (kN)	V_{\max} (kN)	Failure mode
A-1	573.20	286.60	Shear
A-2	591.73	295.87	Shear
A-3	776.83	388.42	Shear
A-4	899.76	449.88	Shear
A-5	748.74	374.37	Shear
A-6	950.27	475.14	Shear
B-3	872.64	436.32	Shear
C-3	757.93	378.97	Shear

TABLE 3: Size and opening dimensions of FRP reinforcements.

Specimen	b_f	h_f	x	y	Opening/FRP plate (%)
A-1	700	340	320	125	67.23
A-2	710	340	310	125	64.21
A-3	730	340	290	125	58.42
A-4	750	340	270	125	52.94
A-5	405	340	97.5	125	35.40
A-6	290	340	40	125	20.28
B-3	730	340	193.3	125	58.42
C-3	730	340	193.3	83	58.19

coverage conditions are met, the plate will demonstrate maximum shear strength, and the specimen will provide effective shear performance. The test results for maximum loading and maximum shear strength are summarized in Table 2.

4.2. Array of Openings and Ratio of Openings. Figure 9 shows the measurements used for each plate type and the variations of those types. The total width and height of the plates are marked as b_f and h_f , respectively; the width and height of each opening are marked as x and y , respectively. The opening size and ratio of the area of openings are listed in Table 3. *Ratio of the area of openings* is the area of all openings divided by the total area of the plate. We designed the plate to meet the following conditions: both the width (x) and depth (y) of the GFRP plate openings described in Table 3 should be at least 100 mm, and ratio of the area of openings should be higher than 50%.

In specimens A-5 and A-6, which did not meet those conditions, the concrete exhibited brittle failure before the plate reached the limit of its maximum strength. Specimen C-3, which met the ratio condition but not the size condition, showed lower maximum shear strength than Specimen B-3 did, which met both conditions. Therefore, if the opening size is larger than 100 mm and ratio of the area of openings is higher than 50%, sufficient integration between the FRP shear reinforcement and the concrete can be expected.

Figure 10 shows the load-deflection relations for three specimens (A-3, B-3, and C-3) with the same ratio of the area of openings. All three specimens exhibited the same behavior before shear failure. This test result indicates that Specimen

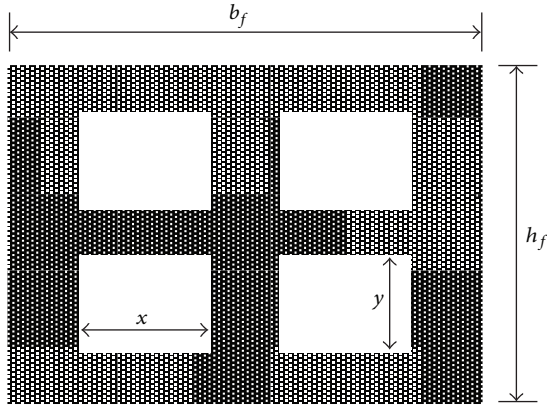


FIGURE 9: Dimensions of a GFRP plate and its openings.

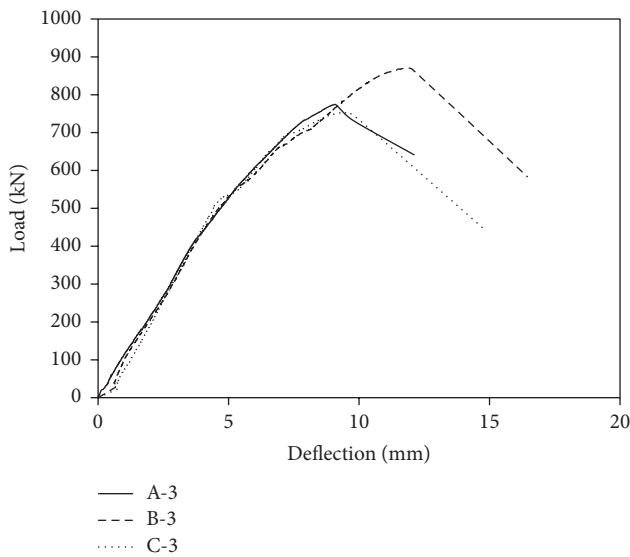


FIGURE 10: Load-deflection curves for three different arrays of openings in GFRP shear reinforcement.

B-3 had more effective integration than A-3 because of a larger bonded area between the concrete and the B-3 plate. Although C-3 had the largest bonded area among the three, its depth (y) was less than 100 mm. Specimen B-3 showed the largest shear strength. Therefore, to increase shear capacity, the bonded area between the FRP plate and the concrete should be maximized while meeting the conditions of opening size and ratio of the area of openings.

4.3. Amount of Shear Reinforcement. To examine the influence of the amount of shear reinforcement on shear strength, we designed each specimen with different amounts of reinforcement. The amount of shear reinforcement was the product of the number of vertical components in the critical shear span (n), the width of the vertical components (w_f), and the thickness of the vertical components (t_f), that is, $(n \times w_f \times t_f)$. Figure 11 shows the load-deflection relations for specimens with various shear reinforcement areas. The amount of shear reinforcement for the experimental variants

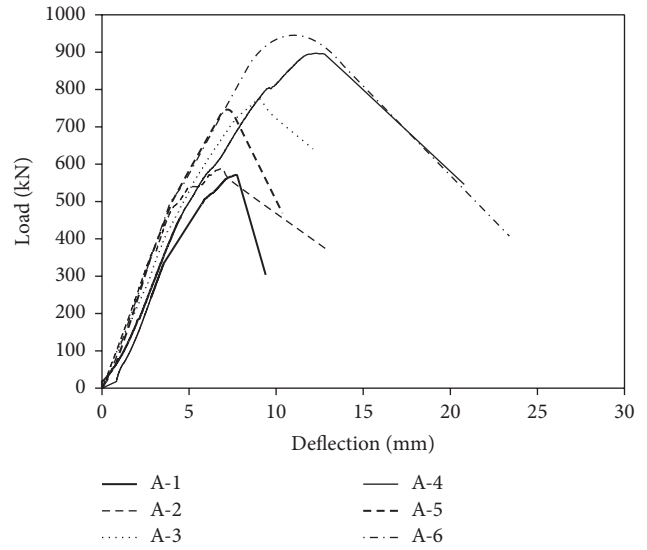
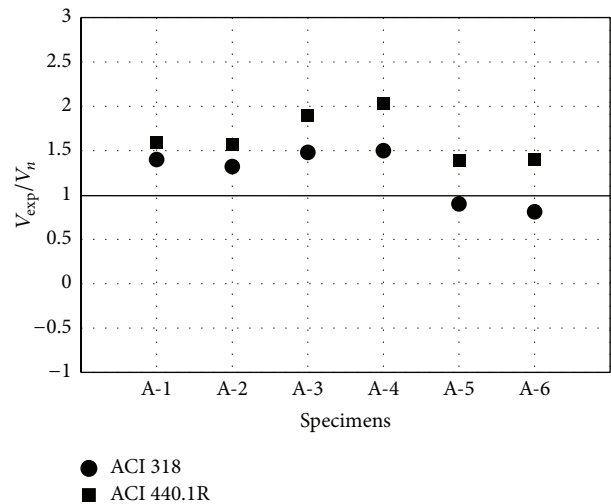


FIGURE 11: Load-deflection curves for amount of shear reinforcement.

FIGURE 12: Ratio of test results to theoretical predictions of shear strength (V_{exp}/V_n).

A-1 to A-4 was controlled by the different widths of the vertical strips; for A-5 and A-6, it was controlled by different spacing of the vertical strips. Figure 12 shows the ratio of shear strength for six specimens (A-1, A-2, A-3, A-4, A-5, and A-6) according to the amount of shear reinforcement. V_{exp} was obtained from the experiment that measured shear strength, and V_n was obtained from the equation by which shear strength was calculated.

All of the specimens, except A-5 and A-6, showed similar ratios of shear strength. In contrast, specimens A-5 and A-6 showed only 80–90% of the calculated value. Because the plate had insufficient opening size and ratio of the area of openings, brittle failure occurred in specimens A-5 and A-6 before the shear reinforcement reached the limit of its maximum strength.

TABLE 4: Experimental results and ratio of shear strength.

Specimen	V_c (kN)	$V_{f,318}$ (kN)	$V_{f,440}$ (kN)	V_{exp} (kN)	$V_{exp}/V_{n,318}$	$V_{exp}/V_{n,440}$
A-1	164.55	38.68	16.12	288.60	1.41	1.60
A-2	164.55	58.02	24.18	295.87	1.33	1.57
A-3	164.55	96.71	40.29	388.42	1.49	1.90
A-4	164.55	135.39	56.41	449.88	1.50	2.04
A-5	164.55	251.44	104.76	374.37	0.90	1.39
A-6	164.55	418.47	174.36	475.14	0.81	1.40
B-3	164.55	107.22	44.67	436.32	1.61	2.09
C-3	164.55	107.22	44.67	378.97	1.39	1.81

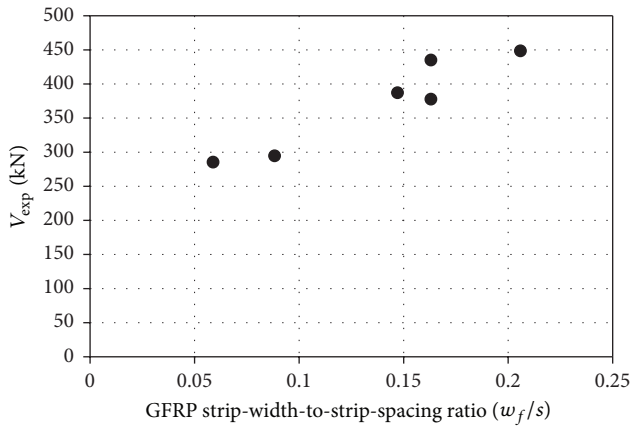


FIGURE 13: Effect of the GFRP strip-width-to-spacing ratio on shear strength.

Figure 13 shows shear strength according to the width-to-spacing ratio of the strip for all of the specimens except the two that did not meet the opening size and ratio conditions (A-5 and A-6). The results indicate that the shear strength increases as the spacing-width ratio of a strip increases. As expected, effective shear-crack control is established by providing a larger bonded area to resist shear cracks. This bonded area increases as the width-to-spacing ratio increases.

5. Comparison of Experimental Results and Shear Strength Equations

Table 4 shows the shear strength of the concrete (V_c), shear strength of the plate (V_f), and maximum shear strength (V_n), which is the sum of the shear strength of the concrete and of the plate, of the beam designed using the shear strength equations of ACI 318 and ACI 440.1R. The ratio of shear strength (V_{exp}/V_n), which compares the maximum calculated shear strength (V_n) and the experimental shear strength (V_{exp}), is also included in Table 4. The shear strength equation in ACI 318-14 calculates the shear strength of concrete as a constant. As shown in Table 4, the mean value of the shear strength ratio (V_{exp}/V_n) is 1.46 with a standard deviation of 0.10 using ACI 318, and the shear strength ratio (V_{exp}/V_n) of two values was between 1.33 and 1.61. On the other hand, ACI 440.1R gives a mean value 1.83 with a standard deviation of 0.21, with

a shear strength ratio of two values between 1.57 and 2.09. This verifies that the shear strength equation in ACI 318 can be used to predict the shear strength of concrete beams with embedded GFRP plates with openings, as long as the plate meets the minimum conditions for opening size and ratio of the area of openings. On the other hand, when using ACI 440.1R, only 40% of the design strength was applied as tensile strength; therefore, the test results were underestimated.

6. Conclusions

In this study, to analyze the shear performance of concrete beams with embedded GFRP plates with openings, we selected the array of openings, ratio of the area of openings, amounts of shear reinforcement, and GFRP strip-width-to-strip-spacing ratio as variables. We used the shear strength equations in ACI 318-14 and ACI 440.1R to compare the experimental and theoretical shear strengths. We draw the following conclusions:

- (1) The width and height of the opening should be larger than 100 mm, and the ratio of the area of openings should be greater than 50% to obtain effective shear performance.
- (2) Three different results from three different shapes of reinforcing plates show that increasing the bonded area between the GFRP plate and the concrete increases the performance of the shear reinforcement, provided the basic conditions are met.
- (3) Analysis of the GFRP strip-width-to-spacing ratio showed that as the ratio increased, the bonded area increased, which improved resistance to shear cracks.
- (4) The equations in ACI 318 and ACI 440.1R yielded generally conservative shear strength results. The ACI 318 code gives a mean value of 1.46 with a standard deviation of 0.1. The ACI 440.1R code gives a mean value of 1.83 with a standard deviation of 0.2. Therefore, the shear strength equation in ACI 318 was more applicable than that in ACI 440.1R to the GFRP plate-reinforced concrete beams.

Notations

- a/d : Shear span-to-depth ratios
 A_f : Sectional area of a vertical strip of FRP plate (mm^2)
 b_w : Web width (mm)
 d : Distance from extreme compression fiber to centroid of longitudinal tension reinforcement (mm)
 f'_c : Specified compressive strength of concrete (MPa)
 f_{fu} : Specified tensile strength of FRP plate (MPa)
 n : Number of vertical components of the FRP plate within the critical shear span
 s : Center-to-center spacing of longitudinal shear reinforcement (mm)
 t_f : Thickness of FRP plate (mm)
 V_c : Nominal shear strength provided by concrete (kN)
 V_{exp} : Shear strength provided by experiment (kN)
 V_f : Nominal shear strength provided by FRP plate (kN)

V_n : Nominal shear strength (kN)
 w_f : Width of FRP plate (mm)
 α : Angle between shear reinforcement and longitudinal axis of the member ($^\circ$)
 ρ_w : Ratio of A_s to $b_w d$.

Conflict of Interests

The authors declare that there is no conflict of interests regarding the publication of this paper.

Acknowledgment

This work was supported by a National Research Foundation of Korea (NRF) grant funded by the Korea government (MSIP) (NRF-2011-0016332).

References

- [1] C. Higgins, G. T. Williams, M. M. Mitchell, M. R. Dawson, and D. Howell, "Shear strength of reinforced concrete girders with carbon fiber-reinforced polymer: experimental results," *ACI Structural Journal*, vol. 109, no. 6, pp. 805–814, 2012.
- [2] F.-Y. Yeh and K.-C. Chang, "Size and shape effects on strength and ultimate strain in FRP confined rectangular concrete columns," *Journal of Mechanics*, vol. 28, no. 4, pp. 677–690, 2012.
- [3] A. Mofidi and O. Chaallal, "Shear strengthening of RC beams with externally bonded FRP composites: effect of strip-width-to-strip-spacing ratio," *Journal of Composites for Construction*, vol. 15, no. 5, pp. 732–742, 2011.
- [4] M. M. R. Taha, M. J. Masia, K.-K. Choi, P. L. Shrive, and N. G. Shrive, "Creep effects in plain and fiber-reinforced polymer-strengthened reinforced concrete beams," *ACI Structural Journal*, vol. 107, no. 6, pp. 627–635, 2010.
- [5] C. Mazzotti, M. Savoia, and B. Ferracuti, "An experimental study on delamination of FRP plates bonded to concrete," *Construction and Building Materials*, vol. 22, no. 7, pp. 1409–1421, 2008.
- [6] R. A. Hawileh, H. A. Rasheed, J. A. Abdalla, and A. K. Al-Tamimi, "Behavior of reinforced concrete beams strengthened with externally bonded hybrid fiber reinforced polymer systems," *Materials and Design*, vol. 53, pp. 972–982, 2014.
- [7] A. K. Al-Tamimi, R. Hawileh, J. Abdalla, and H. A. Rasheed, "Effects of ratio of CFRP plate length to shear span and end anchorage on flexural behavior of SCC RC beams," *Journal of Composites for Construction*, vol. 15, no. 6, pp. 908–919, 2011.
- [8] T. Hassan and S. Rizkalla, "Investigation of bond in concrete structures strengthened with near surface mounted carbon fiber reinforced polymer strips," *Journal of Composites for Construction*, vol. 7, no. 3, pp. 248–257, 2003.
- [9] ACI Committee 440.1R, *Guide for the Design and Construction of Concrete Reinforced with FRP Bars (ACI 440.1R-06)*, American Concrete Institute, Farmington Hills, Mich, USA, 2006.
- [10] Canadian Standard Association (CSA), *Design and Construction of Building Components with Fiber Reinforced Polymers (CSA S806-02)*, Canadian Standard Association (CSA), Mississauga, Canada, 2002.
- [11] Intelligent Sensing for Innovative Structures (ISIS), *Canada Reinforcing Concrete Structures with Fibre Reinforced Polymers (ISIS-M03-01)*, ISIS Canada Resource Centre, Winnipeg, Canada, 2001.
- [12] M. R. Ehsani, H. Saadatmanesh, and S. Tao, "Bond of hooked glass fiber reinforced plastic (GFRP) reinforcing bars to concrete," *ACI Materials Journal*, vol. 92, no. 4, pp. 391–400, 1995.
- [13] K. Ishihara, T. Obara, Y. Satao, T. Ueda, and Y. Kakuta, "Evaluation of ultimate strength of FRP rods at bent up portion," in *Proceedings of the 3rd International Symposium on Non-Metallic (FRP) Reinforcement for Concrete Structures*, pp. 27–34, Sapporo, Japan, 1997.
- [14] E. Shehata, R. Morphy, and S. Rizkalla, "Fibre reinforced polymer shear reinforcement for concrete members: behaviour and design guidelines," *Canadian Journal of Civil Engineering*, vol. 27, no. 5, pp. 859–872, 2000.
- [15] A. K. El-Sayed, E. El-Salakawy, and B. Benmokrane, "Mechanical and structural characterization of new carbon FRP stirrups for concrete members," *Journal of Composites for Construction*, vol. 11, no. 4, pp. 352–362, 2007.
- [16] D.-J. Kim, M. S. Kim, J. Choi, H. Kim, A. Scanlon, and Y. H. Lee, "Concrete beams with fiber-reinforced polymer shear reinforcement," *ACI Structural Journal*, vol. 111, no. 4, pp. 903–911, 2014.
- [17] ASTM International, "Standard test method for compressive strength of cylindrical concrete specimens," ASTM C 39, ASTM International, West Conshohocken, Pa, USA, 2001.

Research Article

Experimental Assessment on the Flexural Bonding Performance of Concrete Beam with GFRP Reinforcing Bar under Repeated Loading

Minkwan Ju¹ and Hongseob Oh²

¹Department of Civil Engineering, Kangwon National University, 1 Joongang-ro, Samcheok-si, Gangwon 245-711, Republic of Korea

²Department of Civil Engineering, Gyeongnam National University of Science and Technology, 150 Chilam-dong, Jinju, Gyeongnam 660-758, Republic of Korea

Correspondence should be addressed to Hongseob Oh; opera69@chol.com

Received 14 April 2015; Accepted 7 June 2015

Academic Editor: Joao M. L. Reis

Copyright © 2015 M. Ju and H. Oh. This is an open access article distributed under the Creative Commons Attribution License, which permits unrestricted use, distribution, and reproduction in any medium, provided the original work is properly cited.

This study intends to investigate the flexural bond performance of glass fiber-reinforced polymer (GFRP) reinforcing bar under repeated loading. The flexural bond tests reinforced with GFRP reinforcing bars were carried out according to the BS EN 12269-1 (2000) specification. The bond test consisted of three loading schemes: static, monotonic, and variable-amplitude loading to simulate ambient loading conditions. The empirical bond length based on the static test was 225 mm, whereas it was 317 mm according to ACI 440 1R-03. Each bond stress on the rib is released and bonding force is enhanced as the bond length is increased. Appropriate level of bond length may be recommended with this energy-based analysis. For the monotonic loading test, the bond strengths at pullout failure after 2,000,000 cycles were 10.4 MPa and 6.5 MPa, respectively: 63–70% of the values from the static loading test. The variable loading test indicated that the linear cumulative damage theory on GFRP bonding may not be appropriate for estimating the fatigue limit when subjected to variable-amplitude loading.

1. Introduction

Fiber-reinforced polymer (FRP) bars have been used widely in reinforced concrete structures due to their many advantages; FRP bars have superior material properties, such as a high tensile strength and corrosion resistance. From a maintenance point of view, using FRP bars inside concrete structures is clearly cost-effective with respect to life cycle costs. Although the bond performance of FRP bars is weaker than that of steel bars, FRP bars have generated interest as an advanced substitute material for reinforced concrete structures.

The bond in reinforced concrete is important in transferring stress from the reinforcing bar to the concrete. To have a composite action in reinforced concrete, perfect bond capacity is required, and conventional steel bars are usually considered to satisfy this bond performance. Unlike conventional steel reinforcing bars, however, determining the performance bond capacity of FRP reinforcing bars is

difficult. The bond between concrete and FRP reinforcing bars is complex and several factors influence the bond characteristics. According to previous research, the key factors are the concrete compressive strength, bar diameter, embedment length, geometry and surface treatment scheme of the FRP reinforcing bar, temperature changes, and environmental conditions [1].

Many experimental studies have been conducted to investigate the bond performance of FRP reinforcing bars using pullout tests [2–7]. Most of these have been monotonic and uniaxial tests based on the ASTM standard. Beam tests are believed to more realistically simulate the stress transfer of reinforced concrete subjected to flexural bending, but few studies have been reported determining the fatigue bond characteristics of FRP reinforcing bars, which is essential to understand reinforced concrete structures in a service state under repeated monotonic and amplitude loading. Investigating bond characteristics of the bond surface is important, wherein longitudinal friction of the FRP reinforcing bar is

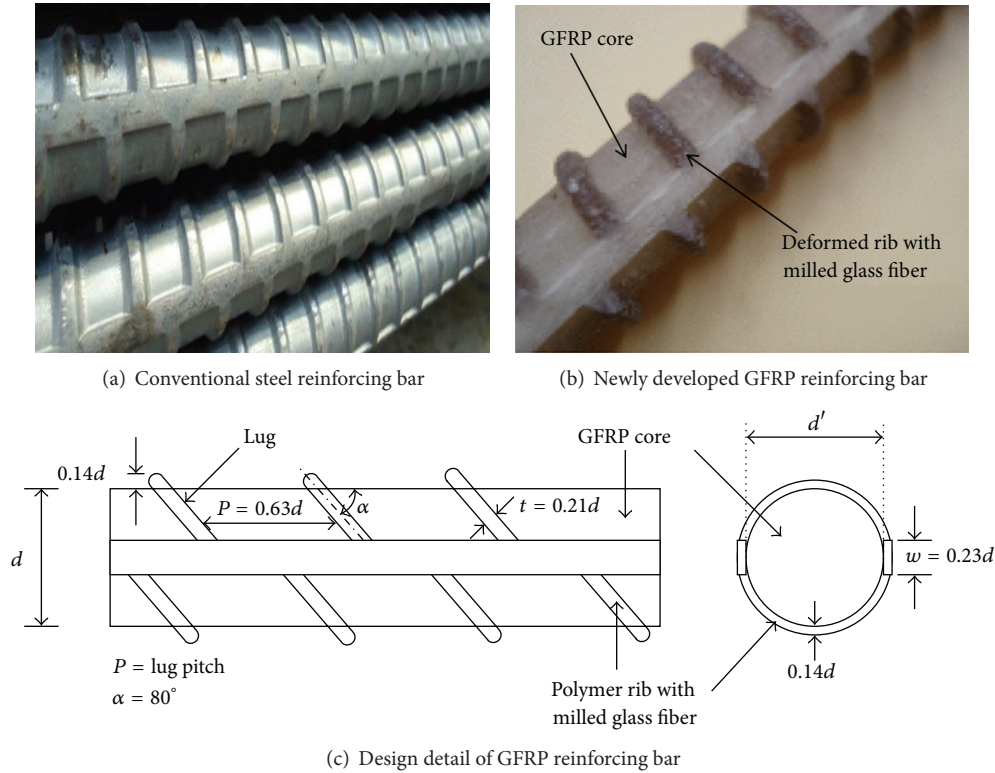


FIGURE 1: GFRP reinforcing bar used in this study.

usually concentrated when subjected to repeated external loading of the reinforced concrete beam.

This study investigated the bond performance of GFRP reinforcing bars subjected to fatigue loading. The beam tests for bonding were carried out according to the BS EN 12269-1 [8] specification. The test variables were the three types of bond length. For static and monotonic loading tests, maximum bond strength and slip were analyzed, and a reduction factor in bond strength was suggested experimentally to evaluate safety in bond design subjected to fatigue loading. For variable-amplitude loading tests, the fatigue limit was evaluated with an S-N curve based on Miner's theory, and its application to the nonlinear cumulative damage for the bonding behavior of glass fiber-reinforced polymer (GFRP) reinforcing bars subjected to variable-amplitude loading is discussed.

2. Experimental Program

2.1. Description of Properties of GFRP Reinforcing Bars, Steel Reinforcing Bars, and Concrete. The GFRP reinforcing bar, as depicted in Figure 1, used consisted of continuous longitudinal glass fibers of 67% volume fraction in a thermosetting epoxy [9]. To mold the surface pattern and to enhance the bond performance of the GFRP reinforcing bar, its external layer was manufactured by mixing milled glass fiber and epoxy at a ratio of 1:1, and it was cured for 15 min at a temperature above 160°C. To enhance bond performance, the surface pattern of the developed GFRP reinforcing bar was

treated to have ribs similar to those of a steel reinforcing bar using epoxy resin containing milled glass fiber by mechanical pressing after pultrusion of the FRP core section. The rib section was a mixture of epoxy resin and milled glass fibers. The external deformed-rib arrangement angle was set at 80°. The rib height and spacing were chosen based on a literature review to obtain optimal mechanical performance in terms of bond and tension characteristics [10]. The GFRP reinforcing bar used for the tensile area had a nominal diameter of 9.53 mm and a design tensile strength which is a guaranteed tensile strength multiplied by the environmental reduction factor in compliance with ACI 440 1R-06 of f_u (GFRP) = 616 MPa; its modulus of elasticity was 42.9 GPa [11].

2.2. Flexural Bond Strength from the Beam Test. The test method and details for evaluating the flexural bond strength of the GFRP reinforcing bar adopted the scheme of the British Standard [8]. The beam test in bonding is considered to more realistically mimic the stress conditions of the reinforced concrete (RC) structure subjected to bending. Tighiouart et al. [12] conducted beam tests in bonding according to the RILEM specification. The specimen consisted of two rectangular blocks joined at the top by a steel ball joint. The design concrete compressive strength is 27 MPa. This specimen detail may not be appropriate for fatigue but for a monotonic loading test due to the possibility of the stress concentration in the concrete at the ball joint. Thus, for the fatigue bond test in this study, the test scheme of BS EN 12269-1 [8] was adopted, whereby a concrete compressive block was used to create the stress distribution in the fatigue test.

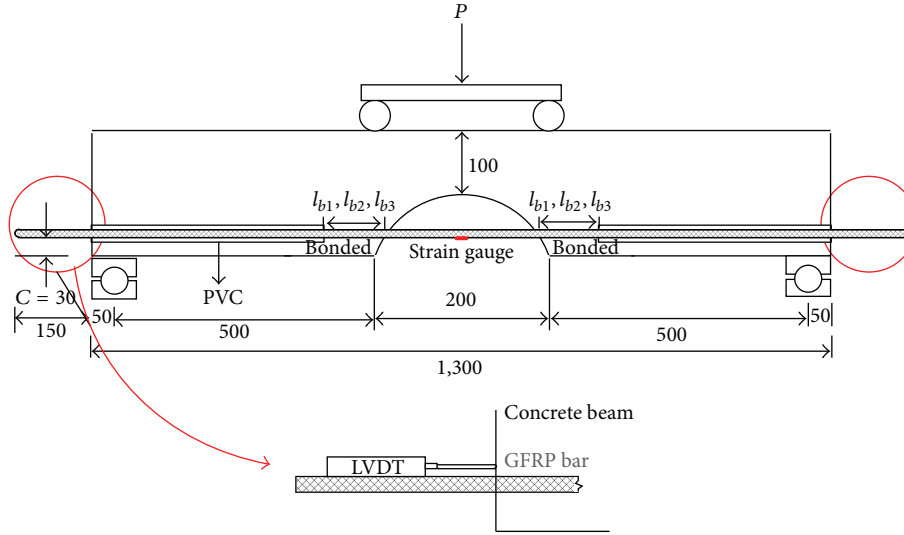


FIGURE 2: Specimen geometry of the BS beam test.

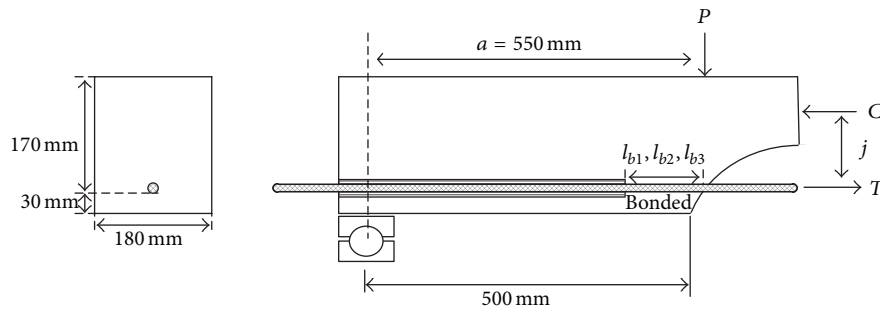


FIGURE 3: Force equilibrium of cross section at the mid-span.

The size of the test specimens was $180 \times 200 \times 1300$ mm, and the major variables according to bond length (l_b) are shown in Figure 2. The lower section of the mid-span in the beam was formed as a semicircular type to prevent stress concentration caused by flexural cracks tips. Bond lengths were set at $l_{b1} = 5d_b$ (45 mm), $l_{b2} = 10d_b$ (90 mm), and $l_{b3} = 15d_b$ (135 mm), where d_b is the diameter of the FRP reinforcing bar, for simulating pullout failure of the GFRP reinforcing bar. As shown in Figure 2, the unbounded region of the FRP reinforcing bar in the concrete beam was secured by PVC pipes that had a slightly larger inner diameter than the diameter of the GFRP reinforcing bar. The test beam was loaded using a 250 kN hydraulic actuator (MTS) and was executed with a four-point loading method. The unloaded slip was measured at both ends of the specimens (Figure 2).

Figure 3 illustrates the force equilibrium condition, and its relationship is shown in (1). Once the tensile load (T) is applied, the tensile stress (τ) at the load level is calculated by dividing by the bond surface area according to BS EN 12269-1 [8]. The optimal bond length is defined as the minimum length to transfer the ultimate load from the GFRP

reinforcing bar to the concrete through the bond surface. Consider

$$M = P \cdot a = C \cdot j = T \cdot j = E_{frp} \cdot \epsilon_{frp} \cdot j, \quad (1)$$

where T = tensile load of the GFRP reinforcing bar (kN), P = ultimate applied load (kN), ϵ_{frp} = measured strain of the steel or GFRP reinforcing bar, E_{frp} = modulus of elasticity of the steel or GFRP reinforcing bar (MPa), a = shear span (mm), and j = distance between the resulting tensile and compressive loads (mm).

As mentioned above, the fatigue loading applied maximum stress level with the ratio to the static test results as follows: 60%, 70%, 75%, 80%, 85%, and 90% of the peak load of each variable. The minimum stress level was considered to be 10% of the applied maximum load. All specimens were tested at 3 Hz, and sinusoidal loading was controlled up to fatigue failure or 2,000,000 loading cycles. Data acquisition for calculating bond stress was performed after finishing the cycle controls.

TABLE 1: Experimental bond strength and slip at peak stress.

	Measured maximum bond stress (MPa)		Slip at peak bond stress (mm)
	From force equilibrium	From reinforcing bar strain	
$5d_b$	16.34	12.63	0.193
	15.11	9.06	0.125
$10d_b$	11	7.61	0.135
	12.22	6.88	0.168
$15d_b$	9.59	5.77	0.050
	8.07	6.03	0.060

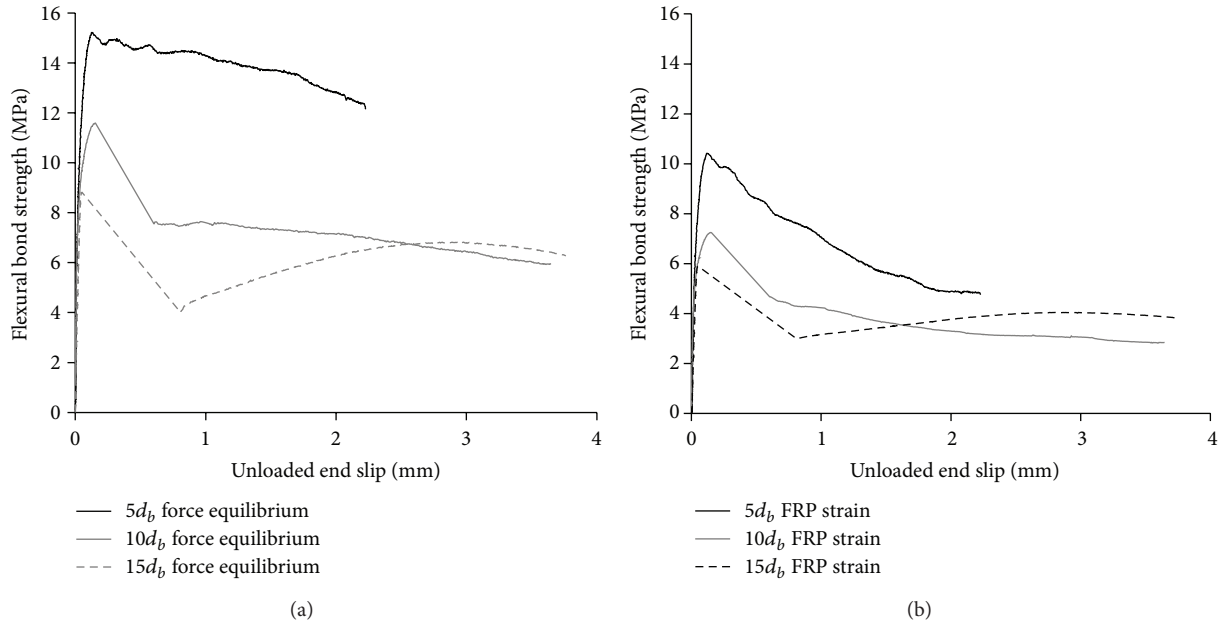


FIGURE 4: Relationship between flexural bond stress and slip under static loading conditions.

3. Test Results of the Static Loading Test

The relationship between flexural bond stress and slip from the static test, performed according to Oh et al. [11], is summarized in Figure 4 and Table 1. The bond stress of each specimen was expressed under force equilibrium conditions and reinforcing bar strain. According to the static loading test, the bond strength determined using the measured strain of the GFRP reinforcing bar was found experimentally to be lower than that using equilibrium theory. This difference might have been caused by incomplete bond stress transfer to the concrete. The reason was analyzed in terms of the bond behavior of the GFRP reinforcing bar and the change in the neutral axis of the beam section during loading.

As reported by other researchers, the bond strength calculated from force equilibrium at the beam section of the mid-span of the specimen is slightly higher than the strength calculated from FRP strain. The work energy of the pullout action of FRP reinforcing bar indicates the capacity for energy dissipation at the interface between concrete and the surface of reinforcing bar. While the bond strength decreases, according to the increase in bond length, total work energy,

defined by the area of loads and slip curves of the specimen, increases (Figure 5).

The required development length to ensure reinforcing bar strength should be calculated under force equilibrium conditions for the beam specimen and also demonstrated by the equation $l_b = d_b f_{fu} / 18.5$, as reported in ACI 440 1R-03, where l_b is the bond length, d_b is the nominal diameter of the GFRP reinforcing bar, and f_{fu} is the designed tensile strength of the GFRP reinforcing bar. The experimental length obtained from the regression data based on the test results and development length according to ACI 440 is shown in Figure 6. Both the regression curve from test results and the analytical bond length from (1) curve tended to decrease the bond strength as the bond length increased. The large discrepancy at 50 mm bond length was due to the short bond length and bond perimeter, which could be conservative as the bond length is increased further. The minimum bond length that the GFRP reinforcing bar can afford to contribute to the tensile strength of the concrete was 225 mm from the crossing point between the two curves by regression and (1). The bond length, however, was calculated as 317 mm according to ACI 440 1R-03.

TABLE 2: Stress levels in the fatigue bond test.

Specimens	Bond strength at static test (MPa)	Applied stress level (%)	Applied bond stress (MPa)	Slip at ultimate load (mm)	Number of cycles	Residual bond strength after 2 million loadings (MPa)	Failure mode
$5d_b$ (45 mm)	15.1	70	11.4	0.175	2,000,000	10.5	P*
		75	12.2	—	1,516,231	—	
		80	13.0	—	29,268	—	
		90	14.7	—	3,804	—	
$10d_b$ (90 mm)	10.2	70	7.7	0.083	2,000,000	6.4	P*
		80	8.8	—	81,063	—	
$15d_b$ (135 mm)	7.5	60	4.8	—	2,000,000	3.9	CS**
		75	6.0	—	1,981,582	—	
		80	7.2	—	193,972	—	
		85	7.7	—	114,413	—	

* Pullout failure and ** concrete splitting failure.

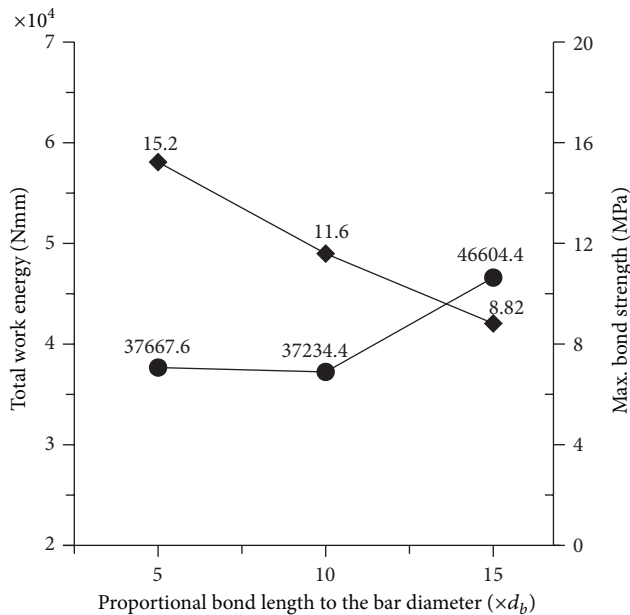


FIGURE 5: Total work energy and maximum bond strength according to the embedded bond length.

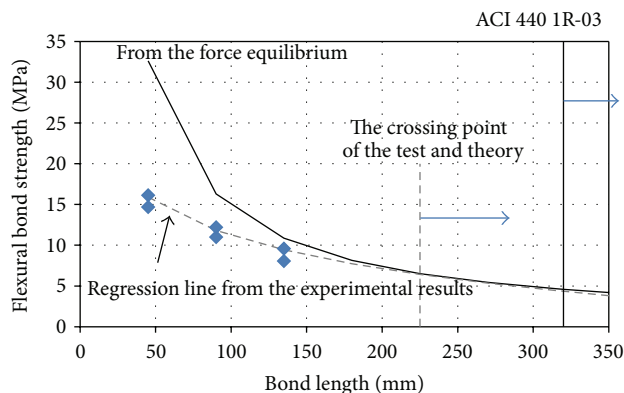


FIGURE 6: Bond strength and bond length relationship by calculation and test results.



FIGURE 7: Pullout failure.

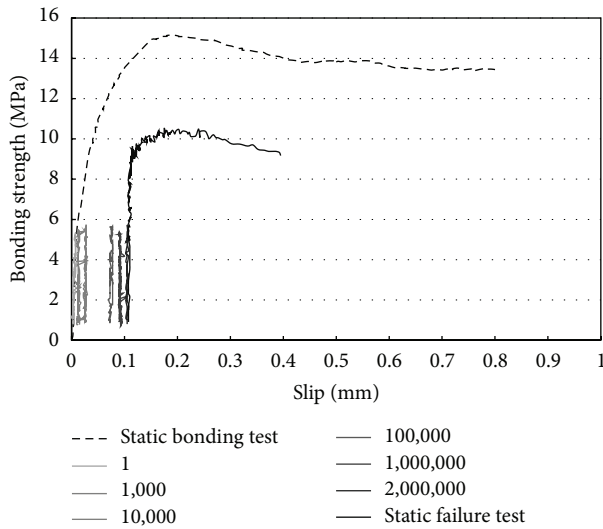
4. Test Results of the Monotonic Fatigue Loading Test

4.1. Bond Strength When Subjected to Fatigue Loading. Each specimen was tested for the designated level of stress as summarized in Table 2, and 10 specimens in total were tested. Two types of failure pattern were investigated: typical pullout failure ($5d_b$, $10d_b$) and concrete splitting failure at the end of bonded region of the reinforcing bar ($15d_b$) (Figures 7 and 8). Pullout failure occurs when the bond stress between the concrete and GFRP reinforcing bar exceeds the stress resulting from the tensile load on the bar. Concrete splitting failure must be caused by insufficient concrete strength, even though the embedded length of the reinforcing bar is sufficient to perform the composite action. As shown in Figure 6, no shear-off of the ribs on the GFRP reinforcing bar occurred with the pullout failure, indicating that the interlocking mechanism with the concrete is valid.

The bond strength was determined at the fatigue limit of 2,000,000 cycles, at which point a failure test was finally applied. The $5d_b$ and $10d_b$ specimens showed the fatigue limit at a stress level of 70%. The number of cycles increased as the development length was longer. For the pullout failure specimens of $5d_b$ and $10d_b$, the bond strengths at failure testing after 2,000,000 cycles were 10.5 MPa and 6.4 MPa,

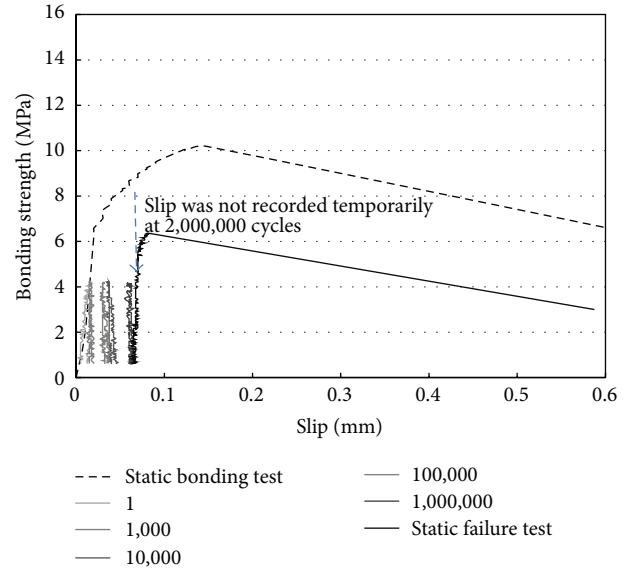


FIGURE 8: Concrete splitting failure.

FIGURE 9: Bond stress-slip relationship of the $5d_b$ specimen under 70% stress level of the ultimate strength.

respectively, which is 63–70% of those from the static bond test. This difference was caused by repeated stress on the bond surface so that fatigue stress weakened the adhesive capacity between the concrete and surface of the GFRP bar, including ribs, so that it degraded the bonding performance. For the $15d_b$ specimen, the mode of failure was concrete splitting. The bond length over $15d_b$ can be concluded to be close to having sufficient bonding performance for the GFRP reinforcing bar. This is consistent with the results of the static loading test, whereby the bond strength difference between the calculated and measured strain on the GFRP reinforcing bar and that using equilibrium theory keeps decreasing as the bond length increases.

4.2. Fatigue Bond Strength and Slip Relationship. Bond stress and slip relationships under fatigue loading are shown in Figures 9 and 10, including the results of the static bond tests. The $15d_b$ specimen was not included for slip behavior after 2,000,000 cycles due to the concrete splitting mode of failure. The slip amount at 2,000,000 cycles for the $10d_b$ specimen was not measured due to a data recording error. According to Oh et al. [11], the bond performance of the steel

FIGURE 10: Bond stress-slip relationship of the $10d_b$ specimen under 70% stress level of the ultimate strength.

reinforcing bar was better than that of the GFRP reinforcing bar, considering bars of the same diameter, due to enhanced shear action of the GFRP rib. For the fatigue test, as the number of repeated cycles increased, the residual slip amount also increased, although its scale was very small. The $10d_b$ specimen showed less than 50% slip versus the $5d_b$ specimen at the ultimate bond strength. As the bond length increased, the bond strength decreased [13, 14]. The bond strength can be defined as a mechanical performance of the rib. As the bond length is shorter, the bond strength at the rib is increased. If the bond length is longer, however, the bond strength at the rib is decreased due to the stress distribution. Consequently, the ribs with longer bond lengths can stably contribute stress transference to the concrete with much higher tensile stress of the reinforcing bar than with a short bond length.

4.3. Fatigue Limit of GFRP Reinforcing Bar Bonding. Comparing the $10d_b$ specimen with the $5d_b$ specimen at 2,000,000 cycles in Figures 8 and 9, the maximum slip of the $10d_b$ specimen was found to be less than that of the $5d_b$ specimen. This indicated that as the bond length was longer, the maximum bond strength resulted in the shorter slip. This was confirmed with experimental results of maximum slips of 0.175 mm for $5d_b$ and 0.083 mm for $10d_b$. The slip limit for longer bond length specimen of the GFRP reinforcing bar at 2,000,000 cycles can be estimated; it will diminish with a decreasing rate close to that for the $5d_b$ and $10d_b$ specimens.

For the fatigue test, the fatigue limit state can be estimated from the S-N curve based on Miner's theory, which is based mostly on linear cumulative damage concepts, as proposed by Palmgren and Miner [15]. Figure 11 shows the log-scaled S-N curve and regression analysis from the results of the fatigue tests for the $5d_b$ and $10d_b$ specimens. For S-N curve analysis, the fatigue limit of the bonding of the GFRP reinforcing bar can be investigated for pullout failure. The fatigue limit

TABLE 3: Estimation of fatigue limit stress based on a regression analysis.

Specimens	Regression formula	Fatigue limit stress at 10,000,000 cycles
$5d_b$	$-2.65 \ln(x) + 110.07$	68.0%
$10d_b$	$-3.119 \ln(x) + 115.26$	65.0%

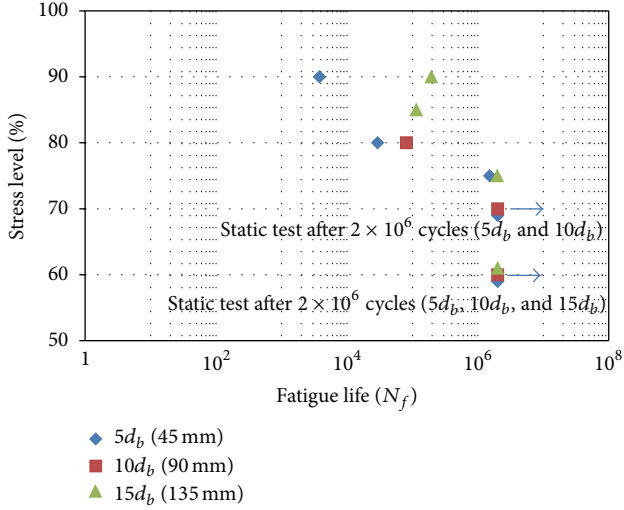


FIGURE 11: S-N relationship of the flexural bond test specimens.

state of bonding is useful in designing and analyzing flexural reinforced concrete members, especially those reinforced with GFRP reinforcing bars. Table 3 shows the estimated fatigue limit stress by regression analysis.

5. Test Results of the Variable-Amplitude Loading Test

Due to the uncertain characteristic of the bond strength of the FRP reinforcing bar, investigating only monotonic loaded fatigue test is not sufficient. Authors conducted the flexural fatigue bond test under variable-amplitude loading condition to evaluate the real bond fatigue performance. One can simulate the accelerated effect of accumulated damage on bond strength of the GFRP reinforcing bar by subjecting it to variable-fatigue loading conditions. Table 4 shows the applied load levels and cases for the variable-amplitude loading test. Each specimen was tested for the designated variable loading case, and in total six specimens were tested for $5d_b$ and $15d_b$. Loading was applied based on the designated proportion of the maximum bond strength, as in the monotonic loading test. The loading sequence, however, was set as shown in Table 4. The minimum load level was considered to be 15% of the failure number of cycles (N_f) and the variable-amplitude load was initiated at this level. Variable load cases 1 and 2 are the upward (low 75% to high 80%) and downward (high 80% to low 75%) load cases, respectively. These loading cases were performed to investigate the accumulated damage effect according to the loading sequence magnitude. Variable load

case 3 is an upward case including two steps of the minimum load level of $0.15 N_f$. The experimental results from these load cases were analyzed using the linear damage theory of fatigue.

Figure 11 shows the relationship of applied bond stress and unbounded end slip for test specimens with bond lengths of 45 mm and 135 mm. The two specimens have different performance limits, such as pullout and concrete splitting failure. For this reason, the unloaded end slips before the concrete splitting failure of the $15d_b$ specimen were compared with those of the $5d_b$ specimen. The $5d_b$ specimen showed a sudden increase in slip in the downward load case (80 to 75) as it approached failure. The $15d_b$ specimen, however, showed no such sudden increase and the slip at failure was stable at 0.2 mm. As the applied load level was increased, the $5d_b$ specimen with the shorter bond length was more sensitive to causing a larger slip. Figure 12 shows the relationship between cumulative end slip and normalized relative fatigue life (n_f/N_f).

Figure 13 illustrates the cumulative end-slip increase according to the relative fatigue life for the monotonic and the variable-amplitude loading test. The cumulative end slip under variable-amplitude loading condition, compared with that of monotonic loading condition, exhibited a sudden increase of slip at the moment of the specific fatigue life. In the case of the FRP reinforcing bar, verifying the bond characteristics based on bond length is more important than the conventional steel reinforcing bar subjected to the variable-amplitude load regarding the real loading frequency of the traffic volume. Table 5 summarizes the result of estimation of fatigue life by the Palmgren-Miner rule, which is commonly used to calculate the cumulative fatigue damage on the following equation:

$$D = \sum_{i=1}^k \frac{n_i}{N_i}, \quad (2)$$

where n_i = number of loading cycles at a given stress level sigma i , N_i = number of cycles to failure at sigma i , and D = total damage on fatigue (usually considered to be 1 at fatigue failure).

6. Results and Discussions

The bond length of the GFRP reinforcing bar in this study is “safer” than that mandated by ACI 440 1R-03, and the outer ribs can sufficiently resist the shear friction against the tensile stress of the GFRP reinforcing bar. For purposes of structural designs, the bond characteristics should also be confirmed when subjected to repeated loading conditions.

The work energy of the pullout action of FRP reinforcing bar indicates the capacity for energy dissipation at the interface between concrete and the surface of reinforcing bar. While the bond strength decreases, according to the increase in bond length, total work energy, defined by the area of loads and slip curves of the specimen, increases (Figure 5). This means that each bond stress on the rib is released and bonding force is enhanced as the bond length is increased. Appropriate level of bond length may be recommended with this energy-based analysis.

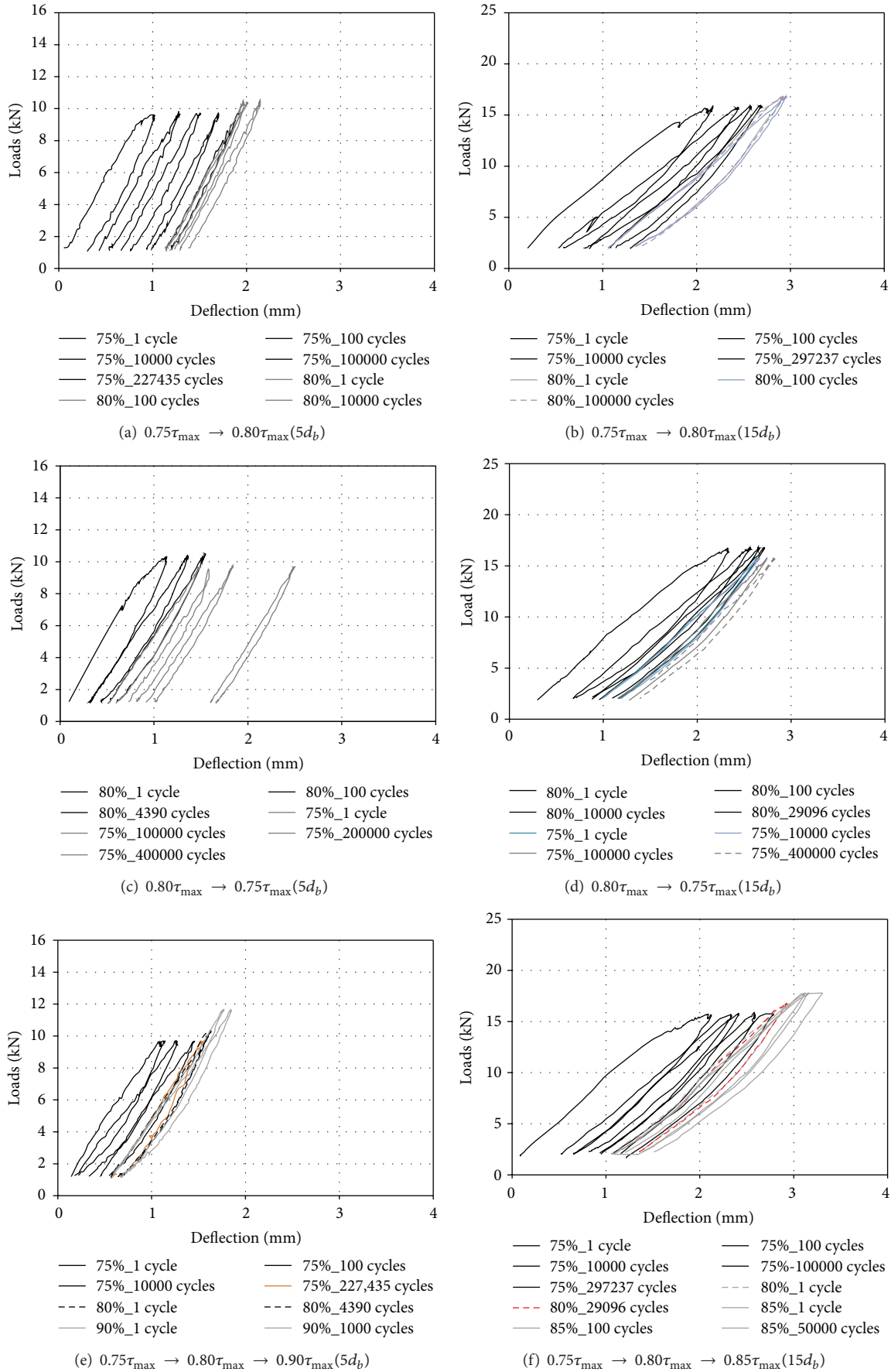


FIGURE 12: Relationship between applied loads and cumulative mid-deflection under various loading steps.

TABLE 4: Stress level of the fatigue bond test.

Load levels and cases	Applied load history	Loading sequences
Variable load case 1	$0.75\tau_{\max} (0.15N_f) \rightarrow 0.8\tau_{\max} \text{ (until failure)}$	Low \rightarrow high
Variable load case 2	$0.8\tau_{\max} (0.15N_f) \rightarrow 0.75\tau_{\max} \text{ (until failure)}$	High \rightarrow low
Variable load case 3	$0.75\tau_{\max} (0.15N_f) \rightarrow 0.8\tau_{\max} (0.15N_f) \rightarrow 0.85\tau_{\max} \text{ or } 0.85\tau_{\max} \text{ (until failure)}$	Low \rightarrow high 1 \rightarrow high 2

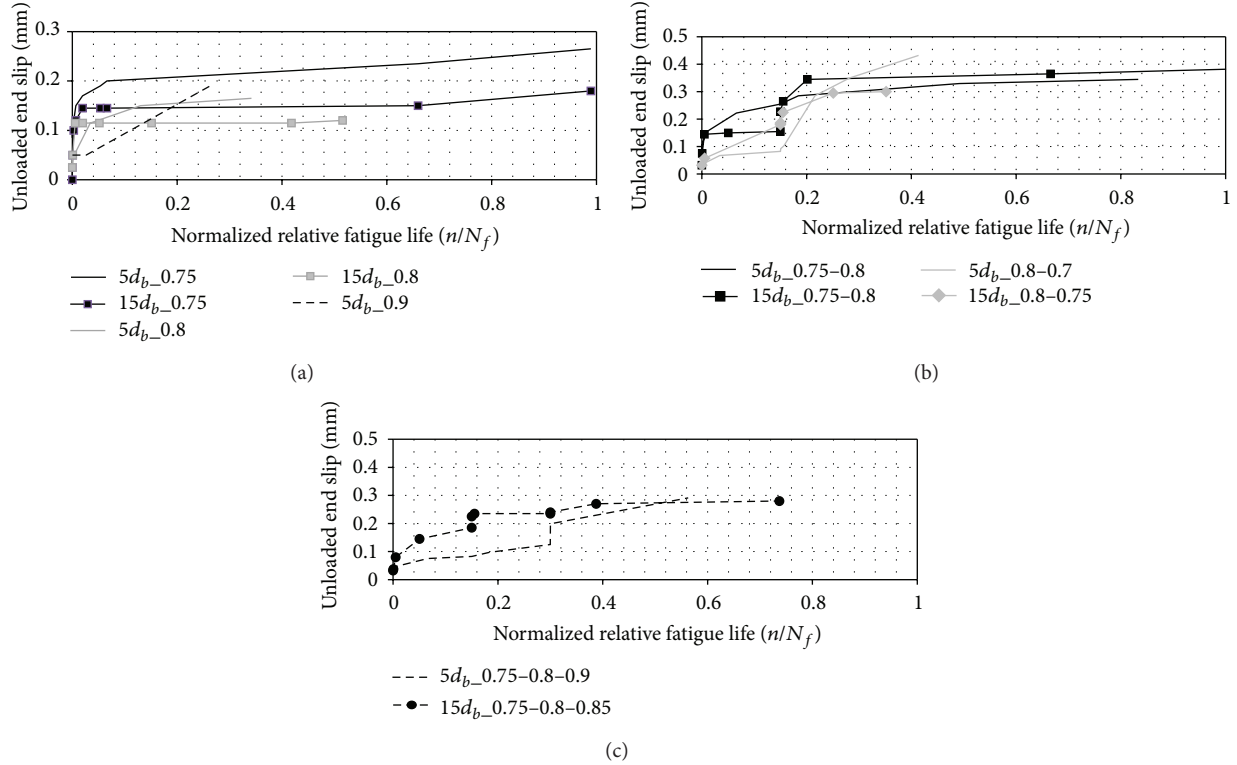


FIGURE 13: Cumulative end-slip increase according to the relative fatigue life.

TABLE 5: Linear cumulative damage of the specimens under an amplitude loading condition.

	Load case	D_1	D_2	D_3	$\sum D_i$
$5d_b$	Case 1	0.15	0.89	—	1.04
	Case 2	0.15	0.27	—	0.42
	Case 3	0.15	0.15	0.96	1.26
$15d_b$	Case 1	0.15	1.16	—	1.31
	Case 2	0.15	0.21	—	0.36
	Case 3	0.15	0.15	0.71	1.01

Compared with the static loading test, the bond strength decreased markedly for the $5d_b$ and $10d_b$ specimens, up to a maximum 63–70%, as noted above. This degraded bond strength was caused by the residual slip resulting from the repeated loading. Repeated loading of a flexural member reinforced with GFRP reinforcing bar was concluded to affect the loss of bond strength, which is a factor usually considered in the design of the bond.

At the assumed fatigue cycles of 10,000,000, the fatigue limit stresses for $5d_b$ and $10d_b$ specimens were 68.0% and

65.0%, respectively. These results showed that the GFRP reinforcing bar had sufficient bond performance in a repeated loading state, such as vehicular traffic, to be used in the design of concrete flexural members.

Initial damage was calculated by considering the applied load level of $0.15N_f$. For the total damage on fatigue, two apparent differences were detected. The low-high cases (cases 1 and 3) showed total damage over 1.0 according to test results of the fatigue failure. The high-low case (case 2), however, showed total damage still under 1.0 even though the specimen had already failed. This result indicates that the fatigue performance was more vulnerable when a high load is applied prior to a low load on the structure. The linear cumulative damage theory based on the Palmgren-Miner rule may not be appropriate for estimating the fatigue limit when subjected to variable-amplitude loading.

6.1. Reduction Factor of the Fatigue Bond Strength. From the fatigue bond test, the relationship between the reduction in bond strength and the residual slip at maximum bond strength in fatigue at 2,000,000 cycles was investigated. As the slip increased, the bond strength was found to decrease.

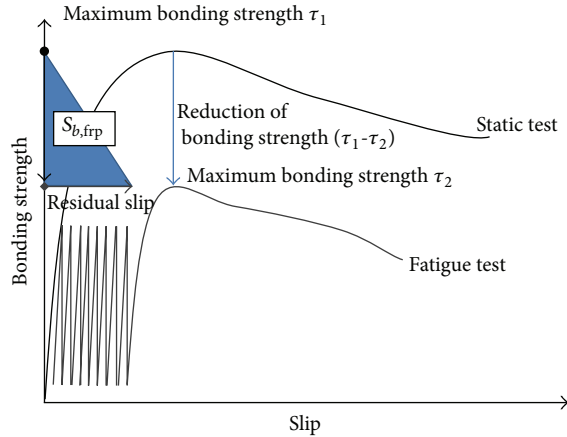


FIGURE 14: Diagram of the reduction factor of bond stiffness for an FRP reinforcing bar.

Thus, the reduction in bond strength was proportional to the amount of residual slip, which means that bond stiffness, according to repeated loading, decreases. This relationship can be redefined using an energy concept to calculate half the area of the x - y graph.

In this study, a reduction factor for bond stiffness of the FRP reinforcing bar, $S_{b,frp}$, can be defined by an energy concept using the area of the shaded section in Figure 14. The conceptual formula is as follows:

$$S_{b,frp} = \frac{1}{2} [\text{a reduction in bond strength } (\tau_1 - \tau_2) \text{ (MPa)} \times \text{the residual slip (mm)}] \quad (3)$$

$S_{b,frp}$ is suggested for evaluating the reduced capacity in bonding of an FRP reinforcing bar reinforced in a concrete flexural member when it is serviced under an ambient repeated loading state such as vehicle load. The performance standard for fatigue bonding of the FRP reinforcing bar should be used in designing the member. The reduced capacity under fatigue loading must be evaluated quantitatively because of the various types of rib shapes for the FRP reinforcing bar so that the rib shapes directly affect determining the bond capacity, especially in fatigue loading. By applying (3) to the results of the $5d_b$ and $10d_b$ specimens, $S_{b,frp}$ for the $5d_b$ and $10d_b$ specimens was found to be 0.41 and 0.16, respectively, which means that as the bond length is longer, the reduction in bond stiffness decreases. Thus, a quantitative evaluation indicated that the bond stress can be transferred to the concrete well under fatigue loading.

Using this factor for the reduced capacity of bonding of FRP reinforcing bars, one can check the reduction rate of bonding of FRP reinforcing bars under fatigue loading. For a more reliable evaluation, $S_{b,frp}$ should be formulated as a function of various experimental data so that the nonlinearity of the relationship between the reduced bond strength and the residual slip can be confirmed.

7. Conclusions

In this study, we investigated the bond performance of GFRP reinforcing bars under fatigue loading. The fatigue test was conducted until 2,000,000 cycles, and the bond strength and slip relationship were examined. The conclusions are as follows.

(1) For the static loading test, the bond length was evaluated as 225 mm, whereas it was 317 mm according to ACI 440 1R-03. The bond length of the GFRP reinforcing bar in this study well satisfied the ACI 440 1R-03 limit, and the outer ribs sufficiently resisted the shear friction against the tensile stress of the GFRP reinforcing bar. Each bond stress on the rib is released and bonding force is enhanced as the bond length is increased. Appropriate level of bond length may be recommended with this energy-based test result. For the purposes of structural design, these bond characteristics should be further confirmed when subjected to repeated loading conditions.

(2) For the pullout failure specimens, the bond strengths at failure testing after 2,000,000 cycles were 10.4 MPa and 6.5 MPa, respectively, which is 63–70% when compared with those from the static bond test. This was caused by repeated stress on the bond surface so that fatigue stress weakened the adhesive capacity between the concrete and the surface of the GFRP reinforcing bar. Thus, FRP bonding in designs should be checked with respect to the fatigue behavior of the flexural member.

(3) In this study, a reduction factor for bond stiffness for the FRP reinforcing bar, $S_{b,frp}$, was suggested experimentally. Using this factor for the reduced capacity of bonding of FRP reinforcing bars, one can quantitatively check the expected reduced bonding of the FRP reinforcing bar under fatigue. For a more reliable evaluation, $S_{b,frp}$ should be formulated as a function of various experimental data so that the nonlinearity of the relationship between the reduced bond strength and residual slip can be confirmed.

(4) For the variable loading test, the linear cumulative damage theory on GFRP bonding was found to perhaps not be appropriate to estimate the fatigue limit when subjected to variable-amplitude loading. The GFRP reinforcing bar was concluded to have sufficient bond performance in a repeated loading state, such as vehicular traffic; that is, it can be used in designing concrete flexural members. In future studies, fatigue limit estimation should be researched for bonding of GFRP reinforcing bars under ambient loading conditions.

Conflict of Interests

The authors declare that there is no conflict of interests regarding the publication of this paper.

Acknowledgments

This work was supported by research grants of Korea Institute of Marine Science & Technology Promotion (PJT200493) and Korea Institute of Energy Technology Evaluation and Planning (0000000015513).

References

- [1] E. Cosenza, G. Manfredi, and R. Realfonzo, "Behavior and modeling of bond of FRP rebars to concrete," *Journal of Composites for Construction*, vol. 1, no. 2, pp. 40–51, 1997.
- [2] E. Cosenza, G. Manfredi, and R. Realfonzo, "Development length of FRP straight rebars," *Composites, Part B: Engineering*, vol. 33, no. 7, pp. 493–504, 2002.
- [3] Z. Achillides and K. Pilakoutas, "Bond behavior of fiber reinforced polymer bars under direct pullout conditions," *Journal of Composites for Construction*, vol. 8, no. 2, pp. 173–181, 2004.
- [4] M. Baena, L. Torres, A. Turon, and C. Barris, "Experimental study of bond behaviour between concrete and FRP bars using a pull-out test," *Composites Part B: Engineering*, vol. 40, no. 8, pp. 784–797, 2009.
- [5] Z. He and G.-W. Tian, "Probabilistic evaluation of the design development length of a GFRP rod pull-out from concrete," *Journal of Engineering Structures*, vol. 33, no. 10, pp. 2943–2952, 2011.
- [6] C. G. Papakonstantinou, P. N. Balaguru, and Y. Auyeung, "Influence of FRP confinement on bond behavior of corroded steel reinforcement," *Cement and Concrete Composites*, vol. 33, no. 5, pp. 611–621, 2011.
- [7] Y. Ding, X. Ning, Y. Zhang, F. Pacheco-Torgal, and J. B. Aguiar, "Fibres for enhancing of the bond capacity between GFRP rebar and concrete," *Construction and Building Materials*, vol. 51, pp. 303–312, 2014.
- [8] British Standard, "Determination of the bond behavior between reinforcing steel and autoclaved aerated concrete by the beam test," BS EN EN 12269-1, 2000.
- [9] J. Sim, H. Oh, D. Moon, and M. Ju, "A hybrid fiber reinforced plastic rebar having a optic sensor for concrete," Patent No. 100709292, 2006 (Korean).
- [10] D. Moon, *Bond behavior of newly developed deformed GFRP bars [Ph.D. thesis]*, Hanyang University, Seoul, Republic of Korea, 2004.
- [11] H. Oh, J. Sim, T. Kang, and H. Kwon, "An experimental study on the flexural bonding characteristic of a concrete beam reinforced with a GFRP rebar," *KSCE Journal of Civil Engineering*, vol. 15, no. 7, pp. 1245–1251, 2011.
- [12] B. Tighiouart, B. Benmokrane, and D. Gao, "Investigation of bond in concrete member with fibre reinforced polymer (FRP) bars," *Construction and Building Materials*, vol. 12, no. 8, pp. 453–462, 1998.
- [13] E. Makitani, I. Irisawa, and N. Nishiura, "Investigation of bond in concrete member with fibre reinforced polymer bars," in *Proceedings of the International Symposium Fibre-Reinforced-Plastic Reinforcement for Concrete Structures*, ACI SP-138, pp. 315–331, 1993.
- [14] A. Nanni, M. M. Al-Zahrani, S. U. Al-Dulaijan, C. E. Bakis, and T. E. Boothby, "Bond of FRP reinforcement to concrete," in *Proceedings of the 2nd International RILEM Symposium (FRPRCS-2 '95)*, pp. 135–145, London, UK, 1995.
- [15] J. Schijve, *Fatigue of Structures and Materials*, Kluwer Academic Publishers, Dordrecht, The Netherlands, 2001.

Research Article

Recovery and Modification of Waste Tire Particles and Their Use as Reinforcements of Concrete

Eduardo Sadot Herrera-Sosa,¹ Gonzalo Martínez-Barrera,² Carlos Barrera-Díaz,³ Epifanio Cruz-Zaragoza,⁴ and Fernando Ureña-Núñez⁵

¹*Facultad de Química, Universidad Autónoma del Estado de México, Paseo Colón Esquina Paseo Tollocan S/N, 50180 Toluca, MEX, Mexico*

²*Laboratorio de Investigación y Desarrollo de Materiales Avanzados (LIDMA), Facultad de Química, Universidad Autónoma del Estado de México, Km 12 de la Carretera Toluca-Atlaconulco, 50200 San Cayetano, MEX, Mexico*

³*Centro Conjunto de Investigación en Química Sustentable, Universidad Autónoma del Estado de México-Universidad Nacional Autónoma de México (UAEM-UNAM), Carretera Toluca-Atlaconulco, Km 14.5, Unidad El Rosedal, 50200 Toluca, MEX, Mexico*

⁴*Unidad de Irradiación y Seguridad Radiológica, Instituto de Ciencias Nucleares, Universidad Nacional Autónoma de México, A.P. 70-543, 04510 Mexico, DF, Mexico*

⁵*Instituto Nacional de Investigaciones Nucleares, Carretera México-Toluca S/N, La Marquesa, 52750 Ocoyoacac, MEX, Mexico*

Correspondence should be addressed to Gonzalo Martínez-Barrera; gonzomartinez02@yahoo.com.mx

Received 5 May 2015; Accepted 22 June 2015

Academic Editor: Angel Concheiro

Copyright © 2015 Eduardo Sadot Herrera-Sosa et al. This is an open access article distributed under the Creative Commons Attribution License, which permits unrestricted use, distribution, and reproduction in any medium, provided the original work is properly cited.

Environmental pollution caused by solid wastes is increasing in the last decades; one of these is referred to automotive tires, which are recycled by different methods, including mechanical grinding. One of the most recurrent applications is to use recycled particles as fillers in building materials, as hydraulic concrete. Nevertheless, detrimental values on the mechanical properties are obtained when they are added. For solving these problems, in this work, a novel proposal is to modify the physicochemical properties of the waste automotive tire particles, previously obtained by grinding process, by using gamma irradiation in order to use them as reinforcements of hydraulic concrete. The results show that improvements on the mechanical properties depend of gamma irradiation as well as concentration and size of waste tire particles. Moreover, SEM images are related to mechanical properties; for instance, rough surface of the tire particles changes when applying irradiation; more smooth surfaces are created, due to the cross-linking of polymer chains. Nevertheless, for higher doses, cracks are observed which are produced by scission of the polymer chains.

1. Introduction

One of the major environmental problems around the world is the final disposal of waste of automotive tires. Nevertheless, a lack of information is concerning end-of-life of tire management issues. Innovative solutions are developed to meet the challenge of tire disposal problem. They include update of the life cycles assessments, showing the benefits of the recycling, and recovery actions. Moreover, it is necessary to have in mind how waste tires can be converted into a valuable resource [1]. Recycling of such materials has been carried out by different processes, including (a) landfilling, which diminishes in some countries due to new laws that

forbid any new landfill; (b) producing powder richer in carbon compounds by pyrolysis process, which consist in the decomposition of the organic materials by heating at 400°C in absence of oxygen; pyrolysis sometimes is not economically viable due to low quality final products; nevertheless, it is possible to obtain three different phases through all processes, (1): solid black phase composed by ZnO and ZnS; (2): gaseous phase containing aromatic compounds; and (3): liquid phase with heavy and light oils [2–4]; (c) using as fuel in cement kilns, whose cost is lower than raw tire materials, which is an example of downcycling process [4]; (d) recycling by shredding process, where waste tires particles require having certain size for specific applications, varying from 0.15 mm to

19 mm; after shredding an electromagnetic process is applied for separation of rubber particles and steel fibers, for reusing them in several applications, for making rubber products such as floor mats, carpet padding, and plastic products, and as a substitute of fine aggregate in concrete [5, 6].

Recycled waste tires have been used in the construction industry; some examples of their uses are (a) waste steel fibers from recycled tires as mechanical reinforcement of concrete, which makes possible the improvement of mechanical performances of the concrete [7–9]; (b) recovered rubber as replacement of natural aggregates (fine and coarse), in which the elasticity features were improved and a lower diminution on the compressive strength and brittleness values were found; moreover, by adding rubber particles the reduction of the water absorption was possible; thus a better protection of the steel reinforcement against corrosion is obtained, as well as reduction in the structural weight [10–15]; (c) partial replacement, either sand or cement, by crumb rubber or powder rubber in concrete. The fracture characteristics of concrete were improved when adding crumb rubber; nevertheless, flexural strength was diminished. Moreover, light increment is done when adding powder. Other study points out large reductions in the strength and tangential modulus of elasticity as well as in the brittle behavior of the concrete when adding tire chips and crumb rubber particles [16, 17]; (d) recycling tires as foundation pad for rotating machinery and as vibrations damper in the railway station or where impact resistance, energy absorption, or blast is required [18]; (e) the incorporation of crumb rubber aggregates from worn tires as lightweight aggregate in cement based materials which endows enhanced acoustic and thermal conductivity characteristics; moreover, when crumb rubber is used as insulation material allows potential savings on energy [19].

Although some advantages are obtained when adding recycled materials as rubber tire particles for improvement of the toughness of concrete, they present some disadvantages as lower values on the compressive strength, which should be attended. One alternative is the use of gamma radiation. Recent works have studied the effects of gamma radiation on compressive properties of polymer concrete; in one of them, the results show more resistance to crack propagation; moreover, compressive strain and the elasticity modulus depend on the combination of the particle sizes and the radiation dose [20].

The gamma radiation (γ) is a type of high electromagnetic energy radiation, generally produced by radioactive elements or subatomic processes such as the annihilation of a positron-electron pair. One important characteristic is its capacity to penetrate matter deeper than alpha or beta radiation. In general, the gamma rays strike and pass through the material; it depends on the photon energies, thickness, or density of the materials.

Application of gamma radiation in polymeric materials causes three different processes: cross-linking or scission of polymer chains and graft polymerization. The permanence of any of these processes depends on the nature of the radiation, the chemical structure of the polymer, and the applied dose [21]. In general, molecular weight changes are produced after

chemical reactions; content of gels with low molecular weight is obtained. After irradiating physical properties are affected.

For example, the vulcanization of chlorine butyl rubbers by using gamma radiation decreases the tensile strength and elongation at break up to 25 kGy, but after this dose stability of such properties is observed, up to 200 kGy. Moreover, thermal stability is reduced through the degradation and scission of molecular chains [22]. In another study, polydimethylsiloxane rubber foams were gamma irradiated and their mechanical properties and chemical structure were evaluated, through compression test, infrared attenuated total reflectance spectroscopy (ATR), and X-ray induced photoelectron spectroscopy (XPS). The results show a higher cross-linking of polymer chains when increasing the irradiation dose; thus foams became harder [23].

The high-energy radiation is not frequent in the preparation of composites; nevertheless it has special advantages in the control polymerization because it can be initiated uniformly within small thicknesses of material. This process, compared to thermal process or chemical attack, presents several advantages; for example, initiating radiation requires no activation energy and does not require catalysts or additives to initiate the reaction; the initiation is homogeneous throughout the system, the process can be carried out at any temperature and can be interrupted at a specific reaction time, the termination reaction is practically controlled, the polymer can be analyzed to a specific reaction step, and during temperature initialization reaction is maintained, unlike the one presented in a conventional exothermic curing without irradiation, and, above all, it is faster spending less time and money [21, 24, 25].

Some studies covered the effects of gamma radiation on composite materials, for example, on the mechanical properties and durability of cement concretes. Some applications include concrete as material for nuclear power reactors; for this purpose the specimens were submitted to dosages from 227 MGy and 470 MGy with a dose rate of 5.0 kGy/h. The results show a diminution of about 10% on the elastic and tensile properties, as well as loss of weight, caused by one or more of the following mechanisms: (a) “natural” drying (including gamma heating); (b) radiolysis-induced accelerated drying (where large gas is released); (c) radiolysis-induced carbonation; and (d) degradation of the calcium-bearing cement hydrates [26, 27].

Another study is related to cement concrete and irradiated nylon fibers; it shows higher compressive strength values, when adding nylon irradiated fibers at 50 kGy. Load transfer mechanism between the concrete and fibers under loading is seen. Moreover, a reinforced concrete is created with high elastic modulus and high deformability. Furthermore, 50 kGy seems to be the dose at which the reaction mechanism changes from cross-linking to chain scission. Ionizing energy generates more contact points on the fiber surfaces and in consequence a larger contact area between the fibers and the concrete phase [28]. Another study is devoted to polymer-ceramic composite material, as gypsum/poly(methyl acrylate) composite where the yield of polymerization increased up to 88% with increasing radiation dose and leveled off at a dose around 4 kGy [29].

TABLE 1: Components of the concrete for producing 1 m³.

Mix code	Waste tire (Vol%)	Waste tire (kg)	Portland cement (kg)	Sand (kg)	Gravel (kg)	Water (kg)
M-0	0	0	337.1	758.5	662.6	286.3
M-10-7	10	36.2	337.1	596.4	758.5	278.4
M-20-7	20	72.4	337.1	530.1	758.5	270.6
M-30-7	30	108.7	337.1	463.8	758.5	262.7
M-10-20	10	47.2	337.1	596.4	758.5	278.4
M-20-20	20	94.5	337.1	530.1	758.5	270.6
M-30-20	30	141.7	337.1	463.8	758.5	262.7

Modifications on the cement and different mineral aggregates have been done by using gamma radiation; such materials are mixing into the concrete. In other cases all concrete components are mixed and then concrete specimens are irradiated. Both kinds of concretes are evaluated by mechanical tests. The results are different, and the scanning electron microscopy has been a good tool to evaluate the contribution of each component in nonirradiated and irradiated concretes. After mechanical testing, morphological characterization on some fractured cement concrete pieces is carried out. SEM technique provides good images of distribution of dispersed phases in a matrix [30].

The effects of gamma irradiation on the compressive properties of polymer concretes show that the compressive strain and the elasticity modulus depend on the particle sizes used and the applied radiation dose; in particular, more resistance to crack propagation is obtained. Alternative studies were using recycled polymers and gamma radiation, for example, (a) polymer concrete with recycled high density polyethylene (HDPE) and tire rubber particles, irradiated from 25 to 50 kGy. The results show significant increase on the impact strength and in the elongation at break; such improvements were attributed to the good adhesion between tire rubber particles and the polymer matrix [31]; (b) polymer concrete with waste tire rubber and styrene butadiene rubber (SBR) improved its tensile strength, elongation, and heat resistance up to 75 kGy [32].

This study attempts to use gamma irradiation as modifier of the physicochemical properties of waste automotive tire particles and use them as reinforcement of cement concrete and in consequence improve their mechanical properties. This investigation promotes the use of waste materials in the construction industry, as one alternative for reducing environmental pollution.

2. Experimental

2.1. Design and Manufacture of Concrete. All mixes were elaborated with Portland cement CPC-30Rs and gravel and water (according to ASTM C 150 cement type I) [33]. The objective was to obtain a mix with 24.5 MPa in compression strength at 28 days of curing, according to ACI 211.1 standard [34]. Physical properties of the concrete components and the sieve analyses of fine and coarse aggregates are described in [35].

2.2. Mixing, Casting, and Curing Specimens. Plain concrete mixtures were prepared with dry aggregates (fine and coarse),

cement, and water. Cement was mixed with addition of 85% of water; after mixing by one minute, 15% of water was added and mixed for a total time of 5 minutes, in order to prevent fresh concrete from segregation.

Concrete with or without irradiated-tire particles was elaborated. For each concrete mixture ten specimens were casted in cylindrical molds of 150 mm diameter and 300 mm height, as well as two beams of 150 × 150 × 600 mm. After 24 hours, they were placed in a controlled temperature room at 23.0 ± 2.0°C and 95% of relative humidity. Cured process was performed in accordance with ASTM C511 standard [36].

The component concentrations of the concrete are shown in Table 1. Regarding the manufactured concrete replacing sand by waste tire particles, two different waste tire particle sizes were used (2.8 mm (mesh 7) and 0.85 mm (mesh 20)), having an approximate waste particle size ratio of 1:3. Moreover, three different concentrations of waste tire particles 10, 20, and 30% by volume were used. The mix code was labeled as Mix-Concentration-Mesh; for example, M-10-7 specimens means mix with 10% of waste tire and mesh size 7. The water/cement ratio was kept constant at 0.54.

2.3. Irradiation Procedure. Waste tire particles were irradiated at 200 and 300 kGy with a ratio of 4 kGy/h. Then, they were added to the concrete mix; finally, after mixing, the concrete was casted in molds. For irradiation process an irradiator Gamma Beam 651-PT loaded with ⁶⁰Co pencils was used; it is located at the Institute of Nuclear Sciences of the National Autonomous University of Mexico.

2.4. Mechanical Tests. Concrete specimens were tested after 28 days of curing time. Testing tolerance allowed was 28 days ±12 hours according to ASTM C/192M-00 standard [37]. Compressive strength evaluation was carried out in a universal testing machine Controls 047H4 (Milano, Italy) with capacity of 2000 kN [38]. The modulus of elasticity was determined from the slope of the stress-strain curve; while the flexural strength by using Elvec 72-4 machine with capacity of 10 kN [39]. The pulse velocity evaluation was carried out with an ultrasonic pulse velocity tester Controls 58E0048 with transmitter and receiver head (54 kHz) and pulse rate of 1/s [40].

3. Results

3.1. Unit Weight. The unit weights of concretes are shown in Figure 1. These results are discussed in terms of three

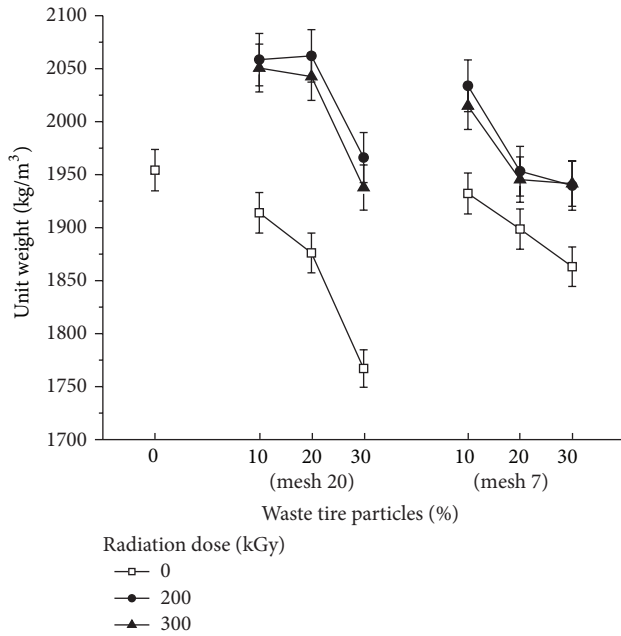


FIGURE 1: Unit weight of concrete with waste tire particles at different irradiated doses.

parameters: concentration and size of the tire particles, as well as irradiation dose. With respect to particle concentration, the unit weight diminishes progressively when it is increasing; reaching the lowest value for concrete with 30% of particles, the reduction on the values means 10% lower than those for control concrete (1954 kg/cm^3). Taking into account the particle size, lower values are observed for concrete with small size particles (0.85 mm). Moreover, all nonirradiated concretes have lower values with respect to the control concrete. Thus, a combination of small particle size and more particle concentration creates lower unit weight of concrete. In fact the values decrease because waste tire particles are porous and then air content is increased in concrete mixtures generating low unit weight. This fact is in accordance with a related research in which the air content in concrete increases when using bigger rubber particles [41].

In the case of concrete with irradiated waste tire particles, highest values are observed for 200 kGy, followed by those with irradiated particles at 300 kGy. Nevertheless, all irradiated concrete specimens show higher values than nonirradiated ones. The maximum value obtained was 5% higher than those for control concrete. It is important to mention that during mixing process with irradiated particles some small lumps were formed, different from the control concrete which showed a homogeneous surface. Then modifications on the tire particle surfaces after irradiating cause lumps when mixing to concrete and in consequence higher unit weight is seen.

3.2. Compressive Strength. Compressive strength values of concretes are shown in Figure 2. The compressive strength values vary as a function of size and concentration of waste tire particles. For concrete with nonirradiated waste tire particles, the following behaviors are observed: (a) the

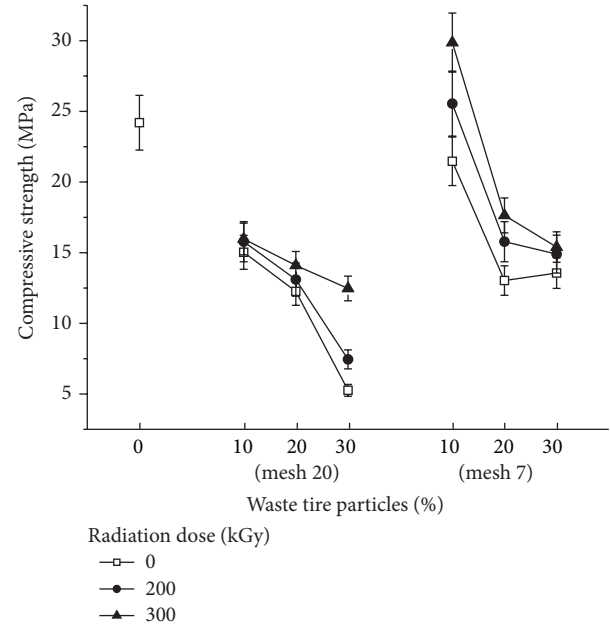


FIGURE 2: Compressive strength of concrete with waste tire particles 0.85 mm (mesh 20) and 2.8 mm (mesh 7).

values decrease progressively according to the particle concentrations increase. Moreover, all these kinds of concretes have lower values than those for control concrete, namely, 24.1 MPa; (b) with respect to the particle size, the compressive strength values are higher for concretes with particles of 2.8 mm than those with 0.85 mm. Thus, when increasing the waste particle concentration and adding large particles more air content is obtained which may cause microcracking and in consequence lower compressive values.

For concrete with irradiated waste tire particles the compressive strength values follow a similar behavior: they increase gradually according to irradiation dose increases. Due to gamma irradiation, the tire particles are progressively harder and no cracks are seen on its surfaces; such behavior generates a composite material with harder particles, which contribute to improving the resistance of the concrete. Additionally, bigger size tire particles create more mechanical resistance compared to smaller ones; such behavior is a consequence of its bigger surface area. It is important to mention that only concretes with 10% of tire particles of 2.8 mm and those irradiated at 200 or 300 kGy showed higher values than those for control concrete, up to 23% of improvement.

3.3. Splitting Tensile Strength. Splitting tensile strength values of concretes are shown in Figure 3. For concrete with nonirradiated waste tire particles, the following behaviors are observed: (a) with respect to particle concentration, the values decrease when increasing the particle concentration; when considering the particle size, higher values are found for concrete with particles of 2.8 mm. However, all values are lower than those for control concrete.

The splitting tensile strength for concrete with irradiated waste tire particles shows a peculiar behavior: at 200 kGy

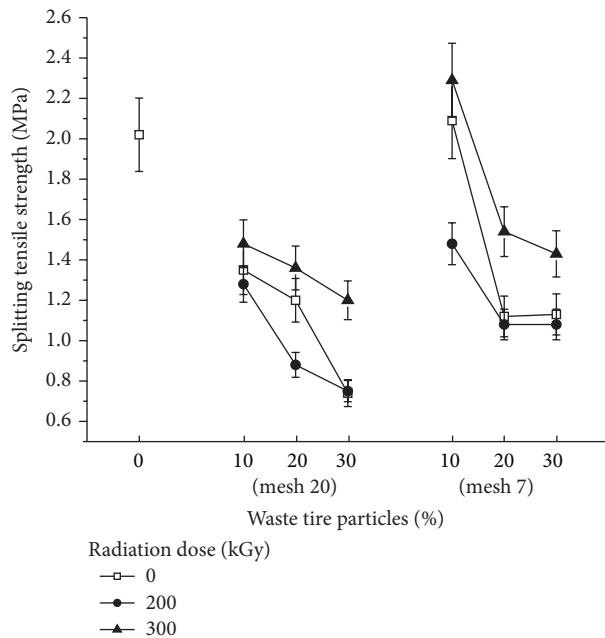


FIGURE 3: Splitting tensile strength of concrete with waste tire particles of 0.85 mm (mesh 20) and 2.8 mm (mesh 7).

the values decrease below the control concrete value; nevertheless at 300 kGy the values increase, now above the control concrete value. Such results are dependent on two parameters, the dispersion of particles into the concrete and the morphology changes on the particle surfaces. More structural damage on the particles is caused when applying higher doses. Such behavior of below-above for the values with respect to control concrete depends on the arrangement of the irradiated particles into the concrete; dose of 300 kGy allows a better arrangement and in consequence an increment of the tensile strength up to 13%. Only concretes with 10% of particles of 2.8 mm and irradiated at 300 kGy have higher values than those for control concrete.

Figure 4 shows nonirradiated and irradiated particles (at 200 kGy and 300 kGy). For nonirradiated tire particles a rough surface is observed, containing small particles of different sizes (left image); when irradiating at 200 kGy smooth surfaces are created, with some small and disperse particles. According to the literature, sometimes smooth surfaces are generated after irradiating as consequence of the cross-linking of polymer chains, while for higher dose scissions of the polymer chains are done, which is manifested by appearances of cracks on the surfaces; as it is shown in Figure 4, for 300 kGy.

3.4. Flexural Strength. The flexural strength values are shown in Figure 5. The results for concrete without irradiated particles indicate (a) progressive diminution of the values when increasing the concentration of particles; (b) variations in terms of the particle size; higher values are for concretes with particles of 2.8 mm. Inclusively, only concrete with 10% of waste particles has a higher value than those for control concrete; such improvement is of 10%.

For concrete with irradiated particles the flexural strength values are lower than those for control concrete. Conversely to compressive strength values where the values for concrete with irradiated particles are higher than those for control concrete, in the case of flexural strength, are lower. Thus a combination of particle arrangement (random distribution) and the type of mechanical test may result in higher or lower values. In the case of flexural test the induced stresses generated in the specimens are in the direction of the two load application axes. The diminution on the values is of 46% with respect to control concrete.

3.5. Modulus of Elasticity. The modulus of elasticity values is shown in Figure 6. As other mechanical features discussed in previous sections, the modulus of elasticity values follows similar behaviors: (a) the values decrease when increasing the concentration of particles; (b) the values are higher for concrete with particles of 2.8 mm. Nevertheless, the values are lower with respect to control concrete. This is due to the fact that the concrete without tire particles is more rigid and does not allow large deformations; nevertheless when adding particles the slope of its stress-strain curve in the elastic deformation region is changing; thus elastic modulus is lower; a stiffer material will have a higher elastic modulus.

For concrete with irradiated particles, modulus of elasticity values has different behaviors: (a) when adding irradiated particles of 0.85 mm, the values increase according to increasing the irradiation dose; (b) when adding large irradiated particles (2.8 mm), the values for concrete with irradiated particles at 200 kGy are lower with respect to control concrete values but higher for those that are using irradiated particles at 300 kGy. Such behaviors can be related to the morphological changes of the irradiated particles as well as their distribution into the concrete. The irradiated particles contribute to incrementing the deformations into the concrete and to diminution of crack formation which results in lower modulus of elasticity. Despite this, improvement of 20% is obtained for concrete with 10% of irradiated particles with respect to those for control concrete.

3.6. Pulse Velocity. In Figure 7 the ultrasonic pulse velocities applied to concrete are shown. Results show similar behavior to compressive strength values; as for concrete with nonirradiated particles the values decrease when increasing the concentration of waste tire particles, and they are bigger when using larger particles of 2.8 mm. Nevertheless, the highest value corresponds to control concrete.

In the case of concrete with irradiated waste particles, a similar behavior is observed: the values diminish when increasing the irradiation dose. Detrimental values are 56% lower with respect to control concrete value. Moreover, the morphological changes on the particles and the increment of their hardness after irradiating contribute to nonpropagation of sound waves.

4. Conclusions

The results show that gamma irradiation as well as concentration and size of waste tire particles are adequate tools

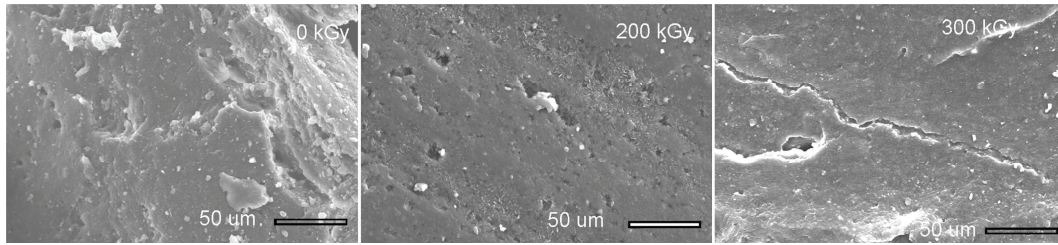


FIGURE 4: SEM image of waste tire particles at different irradiation dose.

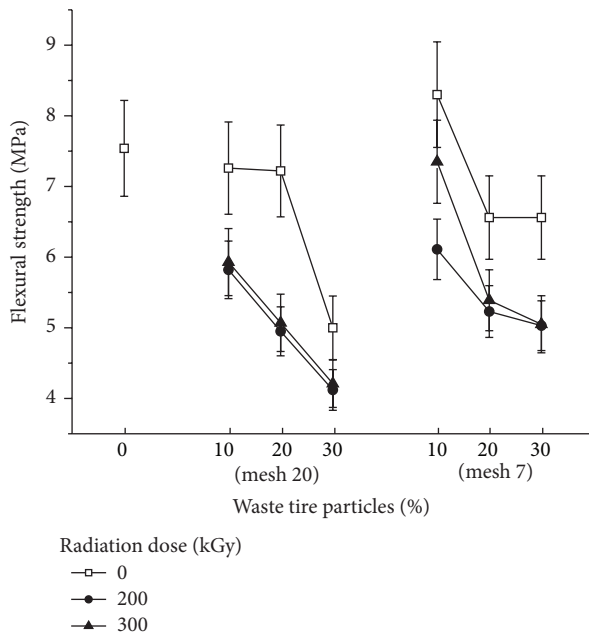


FIGURE 5: Flexural strength of concrete with waste tire particles of 0.85 mm and 2.8 mm.

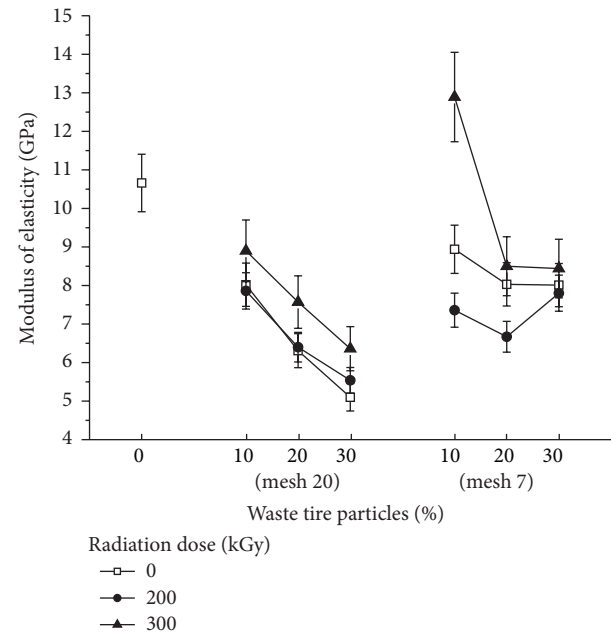


FIGURE 6: Modulus of elasticity of concrete with waste tire particles of 0.85 mm and 2.8 mm.

for improvement of the mechanical properties of cement concrete. It can be seen that concrete with concentrations no greater than 10% of particles of 2.8 mm and irradiated at 300 kGy show the highest values compared to those for the control concrete for compressive strength, tensile strength, and elastic modulus. Different behaviors were observed in terms of the particle sizes and the irradiation doses. In general terms, higher values are obtained with addition of large particles and high irradiation dose. The gamma irradiation generates more homogeneous and smooth surfaces as well as some cracks on the tire particles. Smooth surfaces are related to a hard particle, and the cracks to a better bond between cement matrix and the tire particles; both characteristics can prevent earliest cracks and in consequence soon failures. The morphological characteristics along with the geometrical arrangement of the tire particles into the concrete allow improvements on the mechanical properties.

Conflict of Interests

The authors do not have a direct financial relation or conflict of interests with the commercial identities mentioned in this

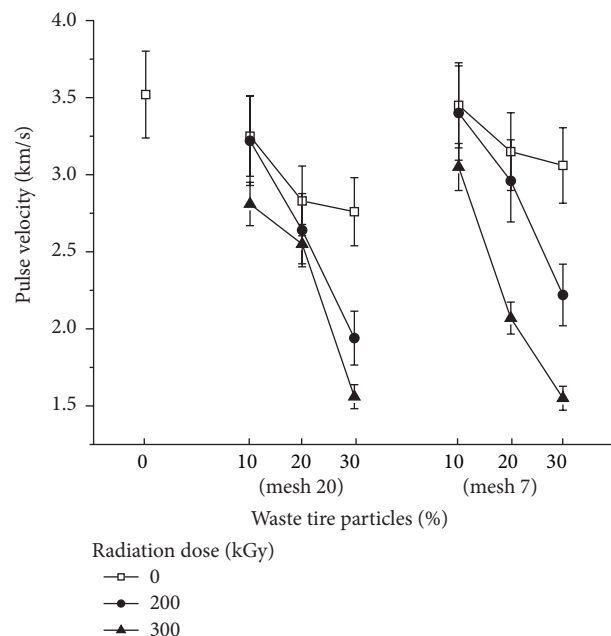


FIGURE 7: Pulse velocity of concrete with waste tire particles of 0.85 mm and 2.8 mm.

paper, and the commercial trademarks, such as Controls and Elvec, only were reported to guarantee the reproducibility, in the same conditions, of the different tests.

Acknowledgments

Thanks are due to the National Council for Science and Technology of México (CONACYT), for both the scholarship support of one of the authors (Eduardo Sadot Herrera-Sosa) and the achievement of this research and to the Environmental Sciences Graduate Program of the Universidad Autónoma del Estado de México (UAEM).

References

- [1] Á. Uruburu, E. Ponce-Cueto, J. R. Cobo-Benita, and J. Ordieres-Meré, "The new challenges of end-of-life tyres management systems: a Spanish case study," *Waste Management*, vol. 33, no. 3, pp. 679–688, 2013.
- [2] R. Siddique and T. R. Naik, "Properties of concrete containing scrap-tire rubber—an overview," *Waste Management*, vol. 24, no. 6, pp. 563–569, 2004.
- [3] J. Karger-Kocsis, "Editorial corner—a personal view: waste tyre rubber—what to do next?" *Express Polymer Letters*, vol. 7, no. 5, article 406, 2013.
- [4] R. Mis-Fernandez, J. A. Azamar-Barrios, and C. R. Rios-Soberanis, "Characterization of the powder obtained from wasted tires reduced by pyrolysis and thermal shock process," *Journal of Applied Research and Technology*, vol. 6, no. 2, pp. 95–105, 2008.
- [5] Ch.-T. Chiu, "Use of ground tire rubber in asphalt pavements: field trial and evaluation in Taiwan," *Resources, Conservation and Recycling*, vol. 52, no. 3, pp. 522–532, 2008.
- [6] K. Neocleous, H. Tlemat, and K. Pilakoutas, "Design issues for concrete reinforced with steel fibers, including fibers recovered from used tires," *Journal of Materials in Civil Engineering*, vol. 18, no. 5, pp. 677–685, 2006.
- [7] M. A. Aiello, F. Leuzzi, G. Centonze, and A. Maffezzoli, "Use of steel fibres recovered from waste tyres as reinforcement in concrete: pull-out behaviour, compressive and flexural strength," *Waste Management*, vol. 29, no. 6, pp. 1960–1970, 2009.
- [8] H. Tlemat, K. Pilakoutas, and K. Neocleous, "Demonstrating steel fibres from waste tyres as reinforcement in concrete: material characterisation," in *Proceedings of the 1st International Conference on Innovative Materials and Technologies for Construction and Restoration*, Liguori, Ed., vol. 1, pp. 172–185, Varenna, Italy, June 2004.
- [9] K. Neocleous, K. Pilakoutas, and P. Waldron, "From used tyres to concrete fibre reinforcement," in *Proceedings of the 2nd FIB Congress*, Naples, Italy, June 2006.
- [10] I. B. Topçu, "The properties of rubberized concretes," *Cement and Concrete Research*, vol. 25, no. 2, pp. 304–310, 1995.
- [11] I. B. Topçu and N. Avcular, "Collision behaviours of rubberized concrete," *Cement and Concrete Research*, vol. 27, no. 12, pp. 1893–1898, 1997.
- [12] B. S. Mohammed, K. M. Anwar Hossain, J. T. Eng Swee, G. Wong, and M. Abdullahi, "Properties of crumb rubber hollow concrete block," *Journal of Cleaner Production*, vol. 23, no. 1, pp. 57–67, 2012.
- [13] F. Pelisser, N. Zavarise, T. A. Longo, and A. M. Bernardin, "Concrete made with recycled tire rubber: effect of alkaline activation and silica fume addition," *Journal of Cleaner Production*, vol. 19, no. 6–7, pp. 757–763, 2011.
- [14] M. Bravo and J. de Brito, "Concrete made with used tyre aggregate: durability-related performance," *Journal of Cleaner Production*, vol. 25, pp. 42–50, 2012.
- [15] A. Benazzouk, O. Douzane, T. Langlet, K. Mezreb, J. M. Roucoult, and M. Quéneudec, "Physico-mechanical properties and water absorption of cement composite containing shredded rubber wastes," *Cement and Concrete Composites*, vol. 29, no. 10, pp. 732–740, 2007.
- [16] M. M. Al-Tayeb, B. H. Abu Bakar, H. M. Akil, and H. Ismail, "Effect of partial replacements of sand and cement by waste rubber on the fracture characteristics of concrete," *Polymer—Plastics Technology and Engineering*, vol. 51, no. 6, pp. 583–589, 2012.
- [17] A. R. Khaloo, M. Dehestani, and P. Rahmatabadi, "Mechanical properties of concrete containing a high volume of tire-rubber particles," *Waste Management*, vol. 28, no. 12, pp. 2472–2482, 2008.
- [18] N. I. Fattuhi and L. A. Clark, "Cement-based materials containing shredded scrap truck tyre rubber," *Construction and Building Materials*, vol. 10, no. 4, pp. 229–236, 1996.
- [19] J. N. Eiras, F. Segovia, M. V. Borrachero, J. Monzó, M. Bonilla, and J. Payá, "Physical and mechanical properties of foamed Portland cement composite containing crumb rubber from worn tires," *Materials & Design*, vol. 59, pp. 550–557, 2014.
- [20] G. Martínez-Barrera and O. Gencel, "Structural modification of waste materials and its use in building materials," in *Photo Cured Materials*, A. Tiwari and A. Polykarpov, Eds., pp. 347–359, Royal Society of Chemistry, Cambridge, UK, 2015.
- [21] E. Cruz-Zaragoza and G. Martínez-Barrera, "Ionizing radiation effects on the matter and its applications in research and industry," in *Gamma Radiation Effects on Polymeric Materials and Its Applications*, C. Barrera-Díaz and G. Martínez-Barrera, Eds., pp. 1–14, Research Signpost, Kerala, India, 2009.
- [22] S. R. Scagliusi, E. L. C. Cardoso, and A. B. Lugao, "Effect of gamma radiation on chlorobutyl rubber vulcanized by three different crosslinking systems," *Radiation Physics and Chemistry*, vol. 81, no. 9, pp. 1370–1373, 2012.
- [23] H. L. Sui, X. Y. Liu, F. C. Zhong, X. Y. Li, L. Wang, and X. Ju, "Gamma radiation effects on polydimethylsiloxane rubber foams under different radiation conditions," *Nuclear Instruments and Methods in Physics Research, Section B: Beam Interactions with Materials and Atoms*, vol. 307, pp. 570–574, 2013.
- [24] R. L. Clough, "High-energy radiation and polymers: a review of commercial processes and emerging applications," *Nuclear Instruments and Methods in Physics Research Section B: Beam Interactions with Materials and Atoms*, vol. 185, no. 1–4, pp. 8–33, 2001.
- [25] M. Barbuta and M. Hrja, "Properties of fiber reinforced polymer concrete," *Buletinul Institutului Politehnic din Iași*, vol. 43, pp. 13–22, 2008.
- [26] Y. Le Pape, K. G. Field, and I. Remec, "Radiation effects in concrete for nuclear power plants. Part II. Perspective from micromechanical modeling," *Nuclear Engineering and Design*, vol. 282, pp. 144–157, 2015.
- [27] B. Kelly, J. Brocklehurst, D. Mottershead, and S. McNearney, "The effects of reactor radiation on concrete," in *Proceedings of the 2nd Information Meeting on Pre Stress Concrete and Reactor Pressure Vessels and their Thermal Isolation*, pp. 237–265, Brussels, Belgium, 1969.

- [28] C. Menchaca-Campos, C. E. Barrera-Díaz, G. Martínez-Barrera, and O. Gencel, "Influence of irradiated polymeric fibers on the mechanical properties of concretes: analysis by microscopy," in *Current Microscopy Contributions to Advances in Science and Technology*, A. Méndez-Vilas, Ed., pp. 1123–1129, Formatex Research Center, Badajoz, Spain, 2012.
- [29] M. H. P. Gazineu, V. A. dos Santos, C. A. Hazin, W. E. de Vasconcelos, and C. C. Dantas, "Production of polymer-plaster composite by gamma irradiation," *Progress in Nuclear Energy*, vol. 53, no. 8, pp. 1140–1144, 2011.
- [30] L. I. Avila-Córdoba, G. Martínez-Barrera, F. Ureña-Nuñez, and C. E. Barrera-Díaz, "Electron microscopy for the evaluation of concrete surfaces modified by gamma radiation," in *Current Microscopy Contributions to Advances in Science and Technology*, A. Méndez-Vilas, Ed., pp. 1115–1122, Formatex Research Center, Badajoz, Spain, 2012.
- [31] R. Sonnier, E. Leroy, L. Clerc, A. Bergeret, and J. M. Lopez-Cuesta, "Compatibilisation of polyethylene/ground tyre rubber blends by γ irradiation," *Polymer Degradation and Stability*, vol. 91, no. 10, pp. 2375–2379, 2006.
- [32] T. Yasin, S. Khan, M. Shafiq, and R. Gill, "Radiation crosslinking of styrene-butadiene rubber containing waste tire rubber and polyfunctional monomers," *Radiation Physics and Chemistry*, vol. 106, pp. 343–347, 2015.
- [33] American Society for Testing Materials (ASTM), "Standard specification for Portland cement," ASTM C 150-07, 2007.
- [34] American Concrete Institute, "Standard practice for selecting proportions for normal, heavyweight, and mass concrete," ACI 211.1-91, 2002.
- [35] E. S. Herrera-Sosa, G. Martínez-Barrera, C. Barrera-Díaz, and E. Cruz-Zaragoza, "Waste tire particles and gamma radiation as modifiers of the mechanical properties of concrete," *Advances in Materials Science and Engineering*, vol. 2014, Article ID 327856, 7 pages, 2014.
- [36] American Society for Testing Materials (ASTM), "Standard specification for mixing rooms, moist cabinets, moist rooms, and water storage tanks used in the testing of hydraulic cements and concretes," ASTM C 511-09, American Society for Testing Materials (ASTM), Philadelphia, Pa, USA, 2009.
- [37] American Society for Testing Materials (ASTM), *Standard Practice for Making and Curing Concrete Test Specimens in the Laboratory*, ASTM C 192/C 192M-00, American Society for Testing Materials (ASTM), West Conshohocken, Pa, USA, 2000.
- [38] American Society for Testing Materials (ASTM), *Standard Test Method for Compressive Strength of Cylindrical Concrete Specimens*, ASTM C 39/C 39M-01, American Society for Testing Materials (ASTM), West Conshohocken, Pa, USA, 2001.
- [39] American Society for Testing Materials (ASTM), "Standard test method for flexural strength of concrete (using simple beam with third point loading)," ASTM C 78-00, American Society for Testing Materials (ASTM), Philadelphia, Pa, USA, 2000.
- [40] American Society for Testing Materials (ASTM), *Standard Test Method for Pulse Velocity Through Concrete*, ASTM C 597-09, American Society for Testing Materials (ASTM), West Conshohocken, Pa, USA, 2009.
- [41] G. Skripkiunas, A. Grinys, and M. Dauksys, "Using tires rubber waste for modification of concrete properties," in *Sustainable Construction Materials and Technologies*, Y.-M. Chun, P. Claisse, T. R. Naik, and E. Ganjian, Eds., pp. 85–90, Taylor & Francis Group, London, UK, 2007.

Research Article

An Experimental Investigation on the Failure Behavior of a Notched Concrete Beam Strengthened with Carbon Fiber-Reinforced Polymer

Xia Huang,¹ Jian Wang,¹ Feng Zhang,¹ Song-shan Niu,² and Jun Ding¹

¹College of Mechanical Engineering, Chongqing University of Technology, Chongqing 400054, China

²China Merchants Chongqing Communications Technology Research & Design Institute Co. Ltd., Chongqing 400067, China

Correspondence should be addressed to Jun Ding; dingjunawen@126.com

Received 11 June 2015; Revised 21 August 2015; Accepted 24 August 2015

Academic Editor: Osman Gencel

Copyright © 2015 Xia Huang et al. This is an open access article distributed under the Creative Commons Attribution License, which permits unrestricted use, distribution, and reproduction in any medium, provided the original work is properly cited.

This paper presents an experiment investigation on the failure behavior of a notched concrete beam reinforced with CFRP, by exploring the influences of the length, thickness, and CFRP bonding methods on the ultimate bearing capacity and failure mode. The interfacial shear stress has first been analytically derived and parametric analyses are then made to predict the failure mode. The experiment observation finds that failure mode significantly depends on CFRP length. The brittle fracture occurs only for nonstrengthened beams; the shear failure I mode mainly occurs when CFRP laminate is 100 mm long; the shear failure II mode mainly occurs when CFRP laminate is 200 mm long; and the delamination failure mode mainly occurs when CFRP laminate is 350 mm long. Meanwhile, the thickness and the bonding methods of CFRP also influence the final failure modes in terms of CFRP length. The measurement on ultimate load shows that an increase in the length of CFRP up to 200 mm significantly improves the bearing capacity of the reinforced beam. A comparison between a theoretical analysis and the experimental observation shows a good agreement in terms of failure modes indicating the accuracy and the validity of the experiment.

1. Introduction

The rapid development of the economy of the world has resulted in an unprecedented development of the urban infrastructure construction. Along with this growth is the rapid expansion of e-commerce and logistics, which in turn possess considerable challenges to the existing highway and bridge infrastructures. Highways and bridges are subjected to increasing levels of cyclic loading and overloading. Furthermore, these concrete structures often suffer from pavement cracks, fractures, and other similar damage, to aggravate the already aging structures. Yet, some of these structures have adequate bearing capacities and must therefore be repaired and reinforced instead of being rebuilt to maintain the requirements for safety, serviceability, and durability [1, 2].

In the field of structural engineering, the common methods for repairing and reinforcing damaged structures mainly include section enlargement, steel-encasing, prestressed reinforcement, sticking steel plate, and glass fiber-reinforced plastic strengthening. However, these methods have a number of

technical defects and are sometimes associated with poor corrosion resistance. With the advancement in materials science and technology, carbon fiber-reinforced polymer (CFRP) is increasingly being used to reinforce and repair concrete structures due to its high tensile strength, high stiffness, good fatigue resistance, and corrosion resistance. In addition, they do not add to the self-weight of the structure being reinforced or cause chain reinforcement reaction among other structures in the architecture [3–6]. Thus, CFRP has broad application prospects for the retrofitting and strengthening of reinforced concrete (RC) beams and steel beams, both of them similar in flexural behavior.

A review of previous studies shows that fiber-reinforced polymers, including CFRP, GFRP, and other ordinary FRPs (they are similar in essence other than their constituent materials), have been effectively used for strengthening the flexural and shear resistance of the reinforced concrete beams and steel beams. Edberg et al. [7] reported an experimental investigation in which five different configurations of CFRP

and GFRP were used to attach them on the tensile side of small-scale RC beams. Mazzotti et al. [8] presented an experiment study on FRP-concrete delamination, in which specimens with varying bonded lengths and plate widths were tested. The results showed an increase in the maximum shear stress with decreasing plate width; however, no significant effect of plate width was observed on fracture energy and delamination. Nakaba et al. [9] studied the mechanical behavior of the adhesive layer between a CFRP layer and concrete. They conducted a single-sided shear failure test on CFRP to clarify the relationship between the shear stress of the bond layer and the slip of the CFRP. The stiffness of CFRP laminate was found to influence the bonding force and the stress distribution on the bonding interface. Malek et al. [10] studied the basic mechanisms of concrete beams reinforced with fiber-reinforced plates (FRPs). They proposed a model for predicting the shear and normal stresses between a fiber composite plate and the undersurface of a concrete beam and obtained the analytical solution for the shear and normal stresses near the end of the fiber plate. Saadatmanesh and Ehsani [11] studied glass fiber plate-reinforced (GFRP) concrete beams to investigate the responses of different cross sections of a concrete beam under four-point bending load. The results showed that GFRP can significantly increase the bending strength of a cross section of a concrete beam under tension and that even a low reinforcement ratio produces a strong reinforcement effect. Meanwhile, GFRP-strengthened concrete beams may result in reduced plasticity of the beam structures. Saadatmanesh and Mohammad [12] also studied the influence on the reinforcement effect of the bonded area, the stiffness and the strength of GFRPs, the compressive strength of concrete, and the reinforcement ratio. The conclusion was consistent with that of [11]. While an increased compressive strength of concrete had no obvious effect on the bending strength of the unreinforced beams, an increase in concrete compressive strength significantly increased the bending strength of the reinforced beams. Sierra-Ruiz et al. [13] studied the shear stress distribution between concrete beams and CFRPs under three conditions, namely, pure shear, pure tension, and pure bending, and analyzed several important factors that affect the shear stress distribution under the three conditions. They also determined that the maximum shear stress is directly related to the tensile strength of a fiber composite plate.

Some studies have focused on the prediction and identification of CFRP failure modes. Buyukozturk et al. [14] mentioned that use of FRP to strengthen and repair structural members has become a mainstream application on structural engineering even though it had not been emerged for a long time. A particular emphasis was made on the fact that the debonding failure could significantly decrease the effectiveness of the repair application which deserves a concentration of research efforts. Colombi [15] studied the delamination failure of steel beams reinforced with FRP. A simplified fracture mechanics-based approach was illustrated for the edge delamination, thus, contributing to establish a fracture mechanics-based failure criterion for the delamination failure. Benachour et al. [16] derived a closed-form rigorous solution based on linear elasticity for the interfacial stress in a

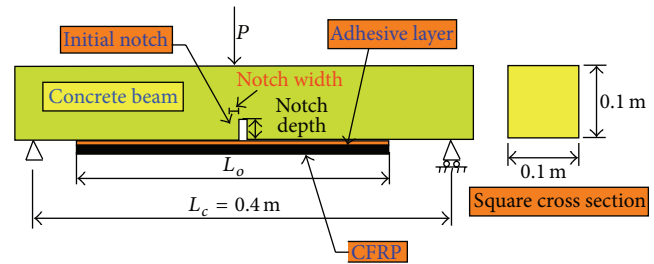


FIGURE 1: The geometrical configuration for the reinforced concrete beam.

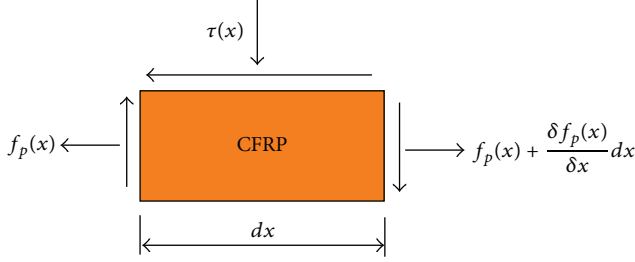
simply supported beam reinforced with CFRP and subjected to a uniformly distributed load, single point load, and two symmetric point loads. The results showed that a high concentration of both shear and normal stresses occurred at the ends of the CFRP layer, thus, causing a premature failure mode at the locations.

The present work is aimed at understanding the effect of CFRP bonded to the concrete beam on the strength enhancement and the failure modes of the beam. The concrete beam is embedded with an initial notch at the central part of the beam so as to simulate the damage, defect, or crack in beam structures in need of repairing. This paper investigates the influences of the length and thickness of CFRP laminates and the methods of bonding CFRP on the ultimate load capacity and the final failure modes of the reinforced beam structure. Based on the experimental results, a parametric study is performed to derive an equation for the interfacial shear stress. Finally, a calculation is made to determine an optimal reinforcement ratio that can provide a reference for improving the reinforcement technology and maximizing the potential of CFRP-strengthening method.

2. Theoretical Analysis

2.1. Geometrical Configuration of the Notched Concrete Beam.

A concrete beam containing an initial notch of rectangular shape is considered to represent the engineering structures that are in need of repairing. Figure 1 shows the geometric configuration of the notched concrete beam as a simplification of a three-point bending beam model [3–5, 8–11]. The reinforced structure consists of three layers: (a) the plain concrete beam of square cross section with an initial notch at the middle of the beam (marked as light green color in Figure 1), (b) a CFRP sheet (marked as black color), and (c) a very thin layer of adhesive located at the interface between concrete beam and CFRP (marked as orange color). Given that the plain concrete beam is much thicker than the CFRP sheet and the adhesive layer (epoxy resin), the following assumptions are made: (1) The deformation of the concrete beam and that of the carbon fiber plate comply with the assumption for the plane cross section; thus, the strains of the concrete beam are linearly distributed along the height of the reinforced beam. However, since the CFRP thickness is very small, the variation in the strain along the thickness direction can be ignored, and the strain in the thickness direction of the CFRP

FIGURE 2: The force equilibrium of CFRP of dx .

layer is constant. (2) The principles of small deformation theory and the basic theory of solid mechanics are applicable. (3) No sliding occurs at the interface between CFRP and the concrete beam (perfect bond condition). (4) Both concrete and CFRP are considered as linear elastic materials.

2.2. Derivation for the Shear Stress. The shear stress at the interface between CFRP and adhesive layer has been considered as the key factor that affects the final failure mode of the reinforced concrete structures [3–5, 10–13]. Consequently, it is necessary to obtain an analytical solution to the interfacial shear stress at the end of the CFRP plate. We consider the force equilibrium of an infinitesimal CFRP with a length of dx (Figure 2) according to its equilibrium in the horizontal direction.

The following equation can be obtained:

$$df_p(x)t_p - \tau(x)dx = 0, \quad (1)$$

where $f_p(x)$ is the tensile stress acting on the CFRP, t_p is the thickness of the CFRP, and $\tau(x)$ is the shear stress at the interface between the CFRP and the adhesive layer.

Thus, the expression for shear stress $\tau(x)$ can be obtained:

$$\tau(x) = \frac{df_p(x)}{dx}t_p. \quad (2)$$

In addition,

$$\tau(x) = G_a\gamma_a \quad (3)$$

$$\gamma_a = \frac{du}{dy} + \frac{dv}{dx}. \quad (4)$$

By combining (2), (3), and (4), the following equation can be obtained:

$$\frac{df_p(x)}{dx} = \frac{G_a}{t_p} \left(\frac{du}{dy} + \frac{dv}{dx} \right), \quad (5)$$

where u and v represent the horizontal and vertical displacements of the adhesive layer, respectively, and G_a is the shear modulus of the adhesive.

By differentiating both ends of (5), the following are obtained:

$$\frac{d^2f_p(x)}{dx^2} = \frac{G_a}{t_p} \left(\frac{d^2u}{dx dy} + \frac{d^2v}{dx^2} \right). \quad (6)$$

According to the principles of solid mechanics, the following equation can be obtained for concrete:

$$\frac{1}{\rho} = \frac{M}{E_c I_c} = \frac{d^2v}{dx^2}, \quad (7)$$

where ρ is the curvature radius of the reinforced concrete beam after deformation, E_c is its elastic modulus, I_c is the inertia moment of the cross section of the concrete beam, and M is the bending moment of the concrete beam. $d^2u/dx dy$ can be expressed as follows:

$$\frac{d^2u}{dx dy} = \frac{1}{t_a} (\varepsilon_p - \varepsilon_c), \quad (8)$$

where t_a is the thickness of the adhesive and ε_p and ε_c are the strains of the CFRP and the concrete beam, respectively.

By substituting (7) and (8) into (6), the following are obtained:

$$\frac{d^2f_p(x)}{dx^2} = \frac{G_a}{t_p} \left(\frac{\varepsilon_p}{t_a} - \frac{\varepsilon_c}{t_a} + \frac{M}{E_c I_c} \right). \quad (9)$$

Equation (7) indicates that $M/E_c I_c$ is equivalent to the inverse of the curvature radius of the concrete beam after deformation. Given that concrete is usually considered as a brittle material, the concrete beam is assumed to have a large curvature radius during deformation. Thus, $M/E_c I_c$ is very small, and its influence on the result can be ignored. $M/E_c I_c$ can then be omitted to obtain the following:

$$\frac{d^2f_p(x)}{dx^2} = \frac{G_a}{t_p} (\varepsilon_p - \varepsilon_c). \quad (10)$$

According to the constitutive relation of the CFRP and the concrete beam, both $\varepsilon_p = f_p(x)/E_p$ and $\varepsilon_c = f_c(x)/E_c$ are valid. By substituting them into the equation and by organizing this equation, the following can be obtained:

$$\frac{d^2f_p(x)}{dx^2} - \frac{G_a}{t_a t_p} \frac{f_p(x)}{E_p} + \frac{G_a}{t_a t_p} \frac{f_c(x)}{E_c} = 0. \quad (11)$$

According to the theory of beam, tensile stress at any point in the beam can be expressed as follows:

$$f_c(x, \bar{y}) = \frac{M_c(x) \cdot \bar{y}}{I_c}, \quad (12)$$

where \bar{y} is the vertical distance of the point on the beam from the neutral plane.

Given the assumptions made in Section 2.1, the influence of the CFRP on the position of the neutral plane of the concrete beam can be ignored. Thus, the distance of the bottom

surface contacting the glue line from the neutral plane is as follows:

$$\bar{y} = \frac{t_c}{2}, \quad (13)$$

where t_c is the height of the concrete beam.

The following is the bending moment of the concrete beam:

$$M_c(x) = \begin{cases} \frac{p}{2}(x + L_0) & \left(0 \leq x < \frac{L_p}{2}\right) \\ \frac{p}{2}(L_c - x - L_0) & \left(\frac{L_p}{2} \leq x \leq L_p\right), \end{cases} \quad (14)$$

where L_c is the span of the three-point bending concrete beam, L_p is the length of the CFRP bonded at the bottom of the concrete beam, the origin of the coordinate in the X direction is the starting point of the CFRP, P is the external load, and L_0 is the distance from the support of the concrete beam to the starting point of the CFRP.

The expression of the tensile stress at the bottom surface of the concrete beam can be obtained by substituting (13) to (12):

$$L_0 = \frac{(L_c - L_p)}{2}. \quad (15)$$

The normal stress at the bottom of the concrete beam can be obtained by substituting (13) and (14) into (12):

$$f_c(x) = \begin{cases} \frac{Pt_c}{4I_c}(x + L_0) & \left(0 \leq x < \frac{L_p}{2}\right) \\ \frac{Pt_c}{4I_c}(L_c - x - L_0) & \left(\frac{L_p}{2} \leq x \leq L_p\right). \end{cases} \quad (16)$$

The control equation of the tensile stress distribution $f_p(x)$ in the CFRP can be obtained by substituting (16) to (11):

$$\begin{aligned} \frac{d^2 f_p(x)}{dx^2} - \frac{G_a}{t_a t_p} \cdot \frac{f_p(x)}{E_p} + \frac{G_a}{t_a t_p} \cdot \frac{Pt_c(x + L_0)}{4I_c E_c} &= 0 \\ \left(0 \leq x < \frac{L_p}{2}\right) \\ \frac{d^2 f_p(x)}{dx^2} - \frac{G_a}{t_a t_p} \cdot \frac{f_p(x)}{E_p} + \frac{G_a}{t_a t_p} \cdot \frac{Pt_c(L_c - x - L_0)}{4I_c E_c} &= 0 \\ \left(\frac{L_p}{2} \leq x < L_p\right). \end{aligned} \quad (17)$$

After solving the differential equation, the expression of $f_p(x)$ can be obtained:

$$f_p(x) = \begin{cases} C_1 e^{-\sqrt{G_a/E_p t_a t_p} x} + C_2 e^{\sqrt{G_a/E_p t_a t_p} x} + \frac{E_p t_c P x}{4E_c I_c} + \frac{E_p t_c P L_0}{4E_c I_c} & \left(0 \leq x < \frac{L_p}{2}\right) \\ C_3 e^{-\sqrt{G_a/E_p t_a t_p} x} + C_4 e^{\sqrt{G_a/E_p t_a t_p} x} - \frac{E_p t_c P x}{4E_c I_c} + \frac{E_p t_c P (L_c - L_0)}{4E_c I_c} & \left(\frac{L_p}{2} \leq x < L_p\right). \end{cases} \quad (18)$$

The expression of the shear stress can be obtained by differentiating the equation and substituting it into (2):

$$\tau(x) = \begin{cases} -C_1 \sqrt{\frac{G_a t_p}{E_p t_a}} e^{-\sqrt{G_a/E_p t_a t_p} x} + C_2 \sqrt{\frac{G_a t_p}{E_p t_a}} e^{\sqrt{G_a/E_p t_a t_p} x} + \frac{E_p t_c t_p P}{4E_c I_c} & \left(0 \leq x < \frac{L_p}{2}\right) \\ -C_3 \sqrt{\frac{G_a t_p}{E_p t_a}} e^{-\sqrt{G_a/E_p t_a t_p} x} + C_4 \sqrt{\frac{G_a t_p}{E_p t_a}} e^{\sqrt{G_a/E_p t_a t_p} x} - \frac{E_p t_c t_p P}{4E_c I_c} & \left(\frac{L_p}{2} \leq x < L_p\right). \end{cases} \quad (19)$$

The integration constants C_1 , C_2 , C_3 , and C_4 in the preceding equation can be determined according to the following boundary conditions:

$$\begin{aligned} 0 \leq x < \frac{L_p}{2}, \\ f_p(0) &= 0, \\ \tau\left(\frac{L_p}{2}\right) &= 0, \end{aligned}$$

$$\frac{L_p}{2} \leq x < L_p,$$

$$f_p(L_p) = 0,$$

$$\tau\left(\frac{L_p}{2}\right) = 0.$$

(20)

The following two equations can be obtained by substituting the boundary conditions into (18) and (19):

$$C_1 + C_2 + \frac{E_p t_c P L_0}{4E_c I_c} = 0, \quad (21)$$

$$-C_1 \sqrt{\frac{G_a t_p}{E_p t_a}} e^{-\sqrt{G_a/E_p t_a t_p} \cdot L_p/2} + C_2 \sqrt{\frac{G_a t_p}{E_p t_a}} e^{\sqrt{G_a/E_p t_a t_p} \cdot L_p/2} + \frac{E_p t_c t_p P}{4E_c I_c} = 0,$$

$$C_3 e^{-\sqrt{G_a/E_p t_a t_p} \cdot L_p} + C_4 e^{\sqrt{G_a/E_p t_a t_p} \cdot L_p} - \frac{E_p t_c P L_p}{4E_c I_c} + \frac{E_p t_c P (L_c - L_0)}{4E_c I_c} = 0, \quad (22)$$

$$-C_3 \sqrt{\frac{G_a t_p}{E_p t_a}} e^{-\sqrt{G_a/E_p t_a t_p} \cdot L_p/2} + C_4 \sqrt{\frac{G_a t_p}{E_p t_a}} e^{\sqrt{G_a/E_p t_a t_p} \cdot L_p/2} - \frac{E_p t_c t_p P}{4E_c I_c} = 0.$$

Supposing $A = G_a/E_p t_a t_p$ and $B = E_p t_c/4E_c I_c$, the above boundary conditions can be simplified as the following:

$$C_1 + C_2 + BPL_0 = 0,$$

$$-C_1 \sqrt{A} e^{-\sqrt{A} \cdot L_p/2} + C_2 \sqrt{A} e^{\sqrt{A} \cdot L_p/2} + BP = 0,$$

$$C_3 e^{-\sqrt{A} \cdot L_p} + C_4 e^{\sqrt{A} \cdot L_p} - BPL_p + BP(L_c - L_0) = 0,$$

$$-C_3 \sqrt{A} e^{-\sqrt{A} \cdot L_p/2} + C_4 \sqrt{A} e^{\sqrt{A} \cdot L_p/2} - BP = 0. \quad (23)$$

Then, the values for the integration constants C_1, C_2, C_3 , and C_4 can be solved, respectively:

$$C_1 = \frac{e^{L_p \sqrt{A}/2} - L_0 \sqrt{A} e^{L_p \sqrt{A}}}{\sqrt{A} (1 + e^{L_p \sqrt{A}})} BP;$$

$$C_2 = -\frac{e^{L_p \sqrt{A}/2} + L_0 \sqrt{A}}{\sqrt{A} (1 + e^{L_p \sqrt{A}})} BP, \quad (24)$$

$$C_3 = -\frac{e^{L_p \sqrt{A}} (e^{L_p \sqrt{A}/2} - \sqrt{A} (L_c - L_0 - L_p))}{\sqrt{A} (1 + e^{L_p \sqrt{A}})} BP;$$

$$C_4 = -\frac{e^{-L_p \sqrt{A}} - \sqrt{A} e^{-L_p \sqrt{A}/2} (L_c - L_0 - L_p)}{\sqrt{A} (e^{-L_p \sqrt{A}/2} + e^{L_p \sqrt{A}/2})} BP.$$

Combining (24) and (19), the shear stress at the interface between the CFRP and the adhesive layer $\tau(x)$ can be expressed as the following:

$$\tau(x) = \begin{cases} -t_p BP \left(\frac{e^{L_p \sqrt{A}/2} - L_0 \sqrt{A} e^{L_p \sqrt{A}}}{(1 + e^{L_p \sqrt{A}})} e^{-\sqrt{A}x} + \frac{e^{L_p \sqrt{A}/2} + L_0 \sqrt{A}}{(1 + e^{L_p \sqrt{A}})} e^{\sqrt{A}x} + 1 \right) & \left(0 \leq x < \frac{L_p}{2} \right) \\ t_p BP \frac{e^{L_p \sqrt{A}} (e^{L_p \sqrt{A}/2} - (L_c - L_0 - L_p) \sqrt{A})}{(1 + e^{L_p \sqrt{A}})} e^{-\sqrt{A}x} + t_p BP \left(\frac{e^{L_p \sqrt{A}} - \sqrt{A} e^{-L_p \sqrt{A}/2} (L_c - L_0 - L_p)}{(e^{-L_p \sqrt{A}/2} + e^{L_p \sqrt{A}/2})} e^{\sqrt{A}x} - 1 \right) & \left(\frac{L_p}{2} \leq x < L_p \right). \end{cases} \quad (25)$$

2.3. Parametric Analysis. In this section, based on (25), selected parameters that affect shear stress as CFRP length and CFRP thickness are parametrically analyzed to provide a reference for the subsequent experiment design. Given the geometrical symmetry of the reinforced concrete beam, only one half of the structure is adopted for analysis. The mechanical model is illustrated in Figure 1.

2.3.1. Effect of the Length of CFRP Layer on Shear Stress. The values for material properties and geometrical dimension are shown Table 1. The same values are applicable for the experimental study to be discussed below. Considering the CFRP length of 0.1 m, 0.2 m, and 0.35 m, the shear stress distribution corresponding to the three different lengths of CFRP length was obtained from a calculation and is shown

in Figure 3. For the different lengths of CFRP, the shear stress at the interface between the CFRP and the concrete beam was uniform except for the first 0.02 m length from the starting point. This result shows that an increase in CFRP length results in an obvious improvement in the stress concentration. It also indicates that the failure mode of the reinforced beam bonded with a longer CFRP layer is more likely to follow the shear failure mode than would a beam bonded with a shorter CFRP layer. The subsequent experimental observation supports the prediction, as will be shown in Section 3.

2.3.2. Effect of the Thickness of CFRP Layer on the Interfacial Shear Stress. Analogous to the previous section, for the CFRP thicknesses of 1 mm (single layer of CFRP) and 2 mm

TABLE 1: Material properties for CFRP and concrete material and dimensions for the specimen.

The category	Material property	Values
Typical material properties for CFRP, concrete, and adhesive layer	Elastic modulus for CFRP	150 GPa
	Elastic modulus for concrete	32.89 GPa
	Shear modulus for the adhesive	4.3 GPa
Geometrical dimension for the concrete specimen	The height of concrete beam	0.1 m
	The thickness for the adhesive	0.0005 m
	The thickness for the bonded CFRP	0.001 m
	The moment of inertial for concrete beam	$8.33e - 6 \text{ m}^4$

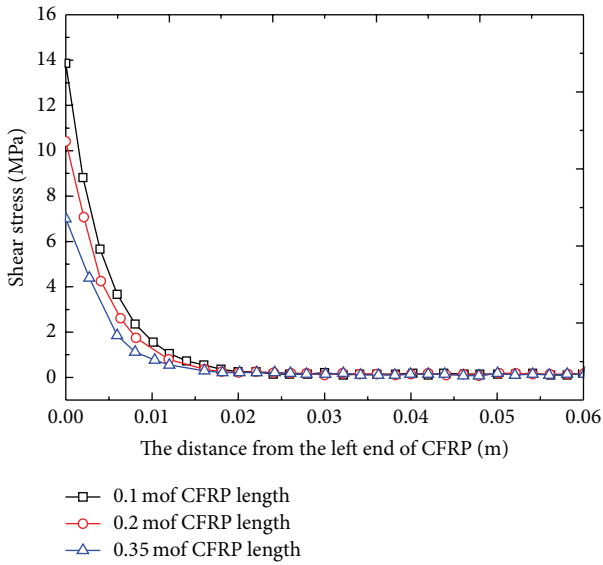


FIGURE 3: The plot of shear stress for various CFRP lengths against the distance from the left CFRP end.

(double layers of CFRP), the corresponding parameters were calculated based on the material properties as shown in Table 1. The thicknesses of 1 mm and 2 mm were chosen to study the influence of CFRP thickness on the mode of failure of the CFRP-strengthened beam. The shear stress distribution for the two thicknesses was obtained as shown in Figure 4. It shows that as the CFRP thickness increases, the shear stress decreases, and the stress concentration at the end of the CFRP layer becomes less obvious. Alternatively, it indicates that, with a reduction in the CFRP thickness, the shear stress concentration at the end of the CFRP layer becomes more significant, thus, increasing the possibility of shear failure mode for a thinner layer of CFRP than for a thicker layer.

2.4. Determination for the Ultimate Load

2.4.1. The Fracture Criterion. In this study, the ultimate load is defined as the magnitude of load at which the initial

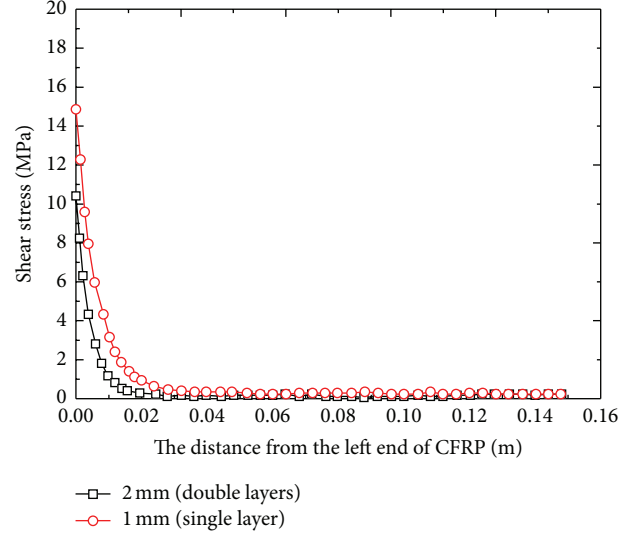


FIGURE 4: The plot of shear stress for various CFRP thicknesses against the distance from CFRP end.

crack (notch) located at the middle of the beam starts to propagate. There are commonly three fracture criteria in linear elastic fracture mechanics as K (stress intensity factor), J integral, and strain energy release rate (SERR), which are used to determine whether and when crack propagates [17]. The criteria for both K and SERR are for linearly elastic materials, while J integral criterion is for plastic materials. As illustrated in Figure 1, since the initial notch is predefined at the middle of the beam, the failure mode for the geometrical configuration of the concrete beam is responsible for the opening mode (mode I) of failure. In addition, the concrete behaves in brittle manner and is considered as an elastic material [1, 8, 10, 18]. Consequently, K criterion is chosen as the fracture criterion to define the ultimate load, as shown in

$$K_I \geq K_{IC}. \quad (26)$$

Equation (26) states that the crack will grow when the stress intensity factor of the given concrete beam structure K_I is greater than or equal to the critical value K_{IC} . The quantity K_{IC} is the critical stress intensity factor which is considered to be a material property independent of the applied load and the geometric configuration of the beam.

2.4.2. The Calculation for Stress Intensity Factor. For the three-point bending concrete beam, the expression calculating the value for K_I follows (27), wherein P is the load applied at the mid-span of the concrete beam, S is the span distance between two supports of the concrete beam, t is the thickness of the concrete beam, a is the notch depth (also crack depth, shown in Figure 1), and the expression for $F(\alpha)$ can follow (28), as follows:

$$K_I = \frac{3SP}{2tW^2} \sqrt{\pi a} F(\alpha), \quad (27)$$

$$F(\alpha) = \frac{1.99 - \alpha(1 - \alpha)(2.15 - 3.93\alpha + 2.7\alpha^2)}{\sqrt{\pi}(1 + 2\alpha)(1 - \alpha)^{3/2}}, \quad (28)$$

$$\text{where } \alpha = \frac{a}{w}.$$

TABLE 2: The specific proportion for component material.

Material	Cement	Coarse aggregate	Fine aggregate	Water	Concrete admixture	Fly-ash
Weight per concrete cubic meter (kg)	300	615	1210	185	6.60	95
Mass ratio	1.000	2.050	4.033	0.617	0.022	0.317

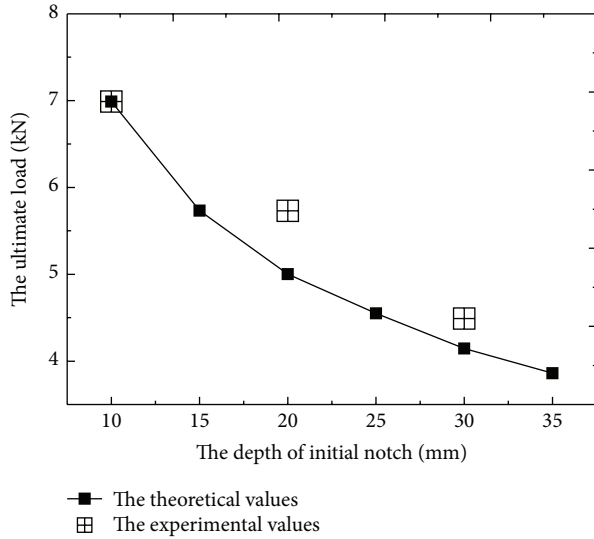


FIGURE 5: The comparison of the ultimate load between theoretical calculation and experimental measurement.

2.4.3. Verification for the Ultimate Load. In order to assure the accuracy in the calculation of the ultimate load for the concrete beam, the ultimate loads corresponding to different depths of the initial notch were compared between a theoretical calculation and the experimental measurement. The critical stress intensity factor in the present work was taken as $K_{IC} = 0.62 \text{ MPa}\cdot\text{m}^{1/2}$ [19]. Substituting the geometric dimensions and the lengths of initial notch in (27), the ultimate load capacities were calculated and are shown as the cross air dots in Figure 5 for 10 mm, 20 mm, and 30 mm, respectively. Additionally, the solid dots represent the values for the ultimate load capacities from the theoretical derivation. It can be seen that they are in good agreement with each other, especially for the case of 10 mm, which indicates the accuracy of the experiment.

3. Experiment Procedures

3.1. Materials Preparation. Concrete was used for the fabrication of the concrete specimens, with the specific composition for each constituent material as summarized in Table 2. The strength class for cement was 42.5R, which belonged to an ordinary Portland cement and was manufactured by Chongqing Tenhui-Diwei Limited Corporation, China. The mud contents for the fine and coarse aggregates were less than 3.0% and less than 5.0%, respectively. A pumping admixture, manufactured by Chongqing Chuanqing Chemical Plant, was used in the concrete mix design to make a concrete block

TABLE 3: The ultimate strength variation with curing days.

Curing days	Compressive strength (MPa)
3	23.4
7	29.9
28	41.4

with a higher compressive strength and to achieve a better pumping performance for concrete. A slump test was firstly performed on the fresh concrete mixed according to the mix proportion shown in Table 2 to investigate the workability of the concrete, thus, ensuring a successful casting of the concrete beams.

CFRP is normally manufactured in the shape of a plate, which is mainly attached to the surface of a flexural member in structures to resist the tension along the fiber direction. CFRP used in this study was produced by Taiwan Zhongyi Company. The tensile strength and the ductility for CFRP were 4640 MPa and 1.7%, respectively. The elastic modulus for CFRP along the longitudinal direction was 165 GPa and Poisson's ratio was 0.25.

The bonding performance of a structural adhesive plays a significant role in the overall mechanical behavior of a CFRP-strengthened concrete beam. It acts as a medium to solidify carbon fibers into a bundle as the shape of a sheet, to transfer shear stress from the interface, and to resist the tension from the notched concrete beam. The structural adhesives used in the experiment were of three types as the surface repair adhesive (type: YZJ-CZ), assembly glue (type: YZJ-CD), and impregnating adhesive (type: YZJ-CQ). All the adhesive products used in this study were produced by Wuhan-Yangtze-River Limited Company (Table 3).

3.2. Manufacturing of the Concrete Specimen

3.2.1. Fabrication of the Notched Concrete Specimen. The initial notch was fabricated during manufacturing the concrete beam specimens. The notches were located at the middle part of the concrete beams as shown in Figure 1. According to the literature [20], they were cut at the middle span of the concrete beams with a steel saw after hardening of concrete. The notches in the different specimens had various widths due to errors during the cutting process. Thus, when all of the initial notches in concrete specimens were processed completely, they were uniformly extended to rectangular ones measuring 3 mm in width. According to the recommendation of Japanese Society of Civil Engineering, the dimensions of the concrete samples were $0.1 \text{ m} \times 0.1 \text{ m} \times 0.4 \text{ m}$ (refer to Figure 1). To eliminate the randomness of the concrete material, each group of test specimens contained three

replicates of concrete beams assigned as numbers 1, 2, and 3, respectively. Each concrete beam was subjected to a load test. The production process for each beam can be summarized as follows: (1) casting concrete into a mold; (2) vibrating it for 30 seconds, leveling and finishing the upper surface, and maintaining it in the mold for one day; (3) demolding and cutting notches on the concrete beams; and (4) maintaining it at a room temperature of $20 \pm 3^\circ\text{C}$ for 28 days.

3.2.2. Procedures for Bonding the CFRP Layer on the Concrete Beam. The procedure for bonding CFRP at the bottom of a concrete beam plays an important role in reinforcing structures since the reinforcement efficiency of the CFRP on the concrete beam, whose middle section is embedded with an initial notch, is governed mainly by the adhesive layer that transmits shear stress load from the concrete material to CFRP, thus preventing further crack development. To obtain a better bonding performance, the following procedures were adopted: (1) polishing the surface of the concrete beams with an abrasive cloth, cleaning the debris in the notches, and washing the samples with acetone solvent to remove oil stains; (2) gluing the surface repair adhesive on the surface of the concrete samples with flaws to level them; (3) brushing the resulting surface of concrete after solidification of the surface repair adhesive; (4) brushing the impregnating adhesive on the two surfaces of the CFRP that had been cut, sticking this adhesive on the surface of the concrete, and scraping the bubbles and unnecessary impregnating adhesive with a scraping tool; (5) repeating steps (3) and (4) to bond the second layer of the CFRP on the beams with two layers of CFRP; and (6) repeating steps (3) and (4) to bond the U-shaped caps on some of the beam specimens.

3.3. Experiment Design. In the experiment, the factors affecting the mechanisms of CFRP-reinforced concrete beams were investigated in terms of failure behavior (ultimate load and final failure mode) of the reinforced structures subjected to three-point bending load. In the experiment, the plain concrete beam with an initial notch was used to be reinforced by CFRP. No steel reinforcement was used in any beams. A number of notches with different depths were first prepared on the tensile surface of the concrete beam before reinforcement. Then, CFRPs of different lengths were bonded to the tensile surface comprising an initial notch. The experimental design can be grouped into four cases as case 1: to determine the effect of the CFRP length on the failure modes and on the ultimate load capacity when the initial crack is identical; case 2: to determine the effect of the notch depth on the failure modes and on the ultimate load capacity when the length of CFRP remains constant; case 3: to determine the effect of CFRP thickness on the failure modes and on the ultimate load capacity; and case 4: to determine the effect of bonding methods such as U-shaped caps wrapped at the plate end on the failure modes and the ultimate load capacity. Table 4 lists the details of the test specimens in the experiment. In total, 54 concrete specimens were tested in the experiment and were observed for the ultimate load and the final failure behavior.

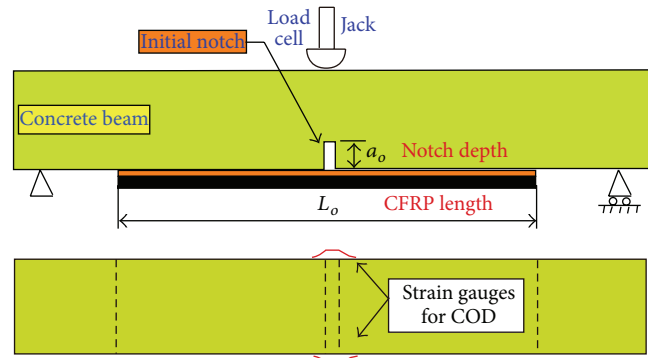


FIGURE 6: The sketch for test setup.

3.4. Test Setup. As a continuation to our previous research [21], the purpose in the present experimental work was to qualitatively investigate the failure behaviors of CFRP-strengthened concrete beams and to quantitatively analyze how the length of CFRP, the thickness of CFRP, and the methods of bonding affect the ultimate load capacity and the final failure mode of the CFRP-strengthened concrete beams. Meanwhile, although the crack opening displacement (COD) for the initial notch was not adopted in the present analysis, to assure the integrity of experiment, COD was also measured for the test specimens. A detailed discussion on COD can be found in [21]. As illustrated in Figure 6, the middle section of the concrete beam was subjected to a jack pressure and the load was applied at the mid-length of the concrete beam. The reaction was provided by the two roller supports near the two ends of each specimen. The values for the ultimate load for the CFRP-reinforced concrete beam were logged at an instrument. Two strain gauges were attached close to the root of the initial notch on both sides of the specimen for measuring the average COD for the notch under the applied loading.

4. Results and Discussions

4.1. Failure Modes. Figure 7 shows four different failure modes of the CFRP-strengthened concrete beams as observed in the experiment. The four failure modes from Figures 7(a)–7(d) are termed as brittle fracture, shear failure I, shear failure II, and delamination failure, respectively. As shown in Figure 7, the brittle fracture mode refers only to the case of an unreinforced concrete beam. The fracture was caused by the propagation of the main crack located at the middle of the concrete due to the tensile stress concentration at the tip of the initial notch and to the subsequent extension of the crack as the applied load increased. From the experimental observation, the fracture surface for the brittle failure was uneven that resembled a skew path of crack propagation.

Figure 7(b) shows one of the shear failure modes observed in the experiment, which is defined as shear failure I mode in this paper. The letter “I” just signifies one kind of failure mode in order to distinguish it from the second shear failure mode (II) in the experiment, which is dramatically different from the modes I, II, and III in the classical fracture mechanics. The crack development process

TABLE 4: The details for the tested concrete specimens.

Objective	Type	No.*	Description	CFRP length (mm)	Notch depth (mm)
The effect of CFRP length	Group I	10-000	Without CFRP	0	10
		10-100	Single-layer CFRP	100	
		10-200	Single-layer CFRP	200	
		10-350	Single-layer CFRP	350	
	Group II	20-000	Without CFRP	0	20
		20-100	Single-layer CFRP	100	
		20-200	Single-layer CFRP	200	
		20-350	Single-layer CFRP	350	
	Group III	30-000	Without CFRP	0	30
		30-100	Single-layer CFRP	100	
		30-200	Single-layer CFRP	200	
		30-350	Single-layer CFRP	350	
The effect of notch depth	(Group IV)	10-000	Without CFRP	0	10
		20-200	Single-layer CFRP	200	20
		30-200	Single-layer CFRP		30
The effect of CFRP thickness and bonding method	Group V	20-000	Without CFRP	0	20
		20-100	Single-layer CFRP	100	
		20-100s	Two-layer CFRP		
		20-100b	Single-layer CFRP and using U-shaped cap		
	Group VI	20-000	Without CFRP	0	20
		20-200	Single-layer CFRP	200	
		20-200s	Two-layer CFRP		
		20-200b	Single-layer CFRP and using U-shaped cap		
	Group VII	20-000	Without CFRP	0	20
		20-350	Single-layer CFRP	350	
		20-350s	Two-layer CFRP		
		20-350b	Single-layer CFRP and using U-shaped cap		

* Explanation for No. A-B (the 3rd column): A is for the length of the initial notch, B for the bonded CFRP length, s for two layers of CFRP, and b for U-shaped cap used for one single layer of CFRP.

for shear failure I mode is depicted in Figure 8. For the concrete beams reinforced with CFRP, a number of minor cracks were generated because of the stress concentration at the tip of the initial notch (Figure 8(a)) at the beginning of the applied load. During the loading process, minor cracks continued to develop, with some of them coalescing to form macrocracks (Figure 8(b)). As the load P increased, the CFRP bonded at the tensile surface of the concrete beam started to prevent the macrocracks from propagating. This prevention, consequently, reduced the stress concentration at the tip of the initial notch. However, the shear stress at the interface between the concrete beam and the CFRP increased successively because of the continuous increase in the load on the concrete beam (Figure 8(c)). Furthermore, smeared cracks were generated on the interface between concrete and CFRP. These cracks were formed at a 45-degree angle along

the horizontal axis of the beam. The macrocracks (smeared cracks) developed rapidly towards the direction of the 45-degree angle until the beam was fractured (Figure 8(d)). Note that the smeared cracks did not intersect the main crack but maintained a certain distance with them (Figure 8(d)). The resulting crack surface was more even than for the brittle failure mode.

Figure 7(c) shows the other shear failure mode in the experiment, termed as mode II. Figure 9 shows a schematic of the gradual development for the shear failure II. The initiation of cracks for this failure mode was similar to that for shear failure I mode (Figures 9(a) and 9(b)). However, when the shear cracks developed at a 45-degree angle to the direction of the horizontal axis of the beam, CFRP peeled off slightly at a small length. This is attributed to (a) the relatively shorter length of CFRP layer for the specimens with

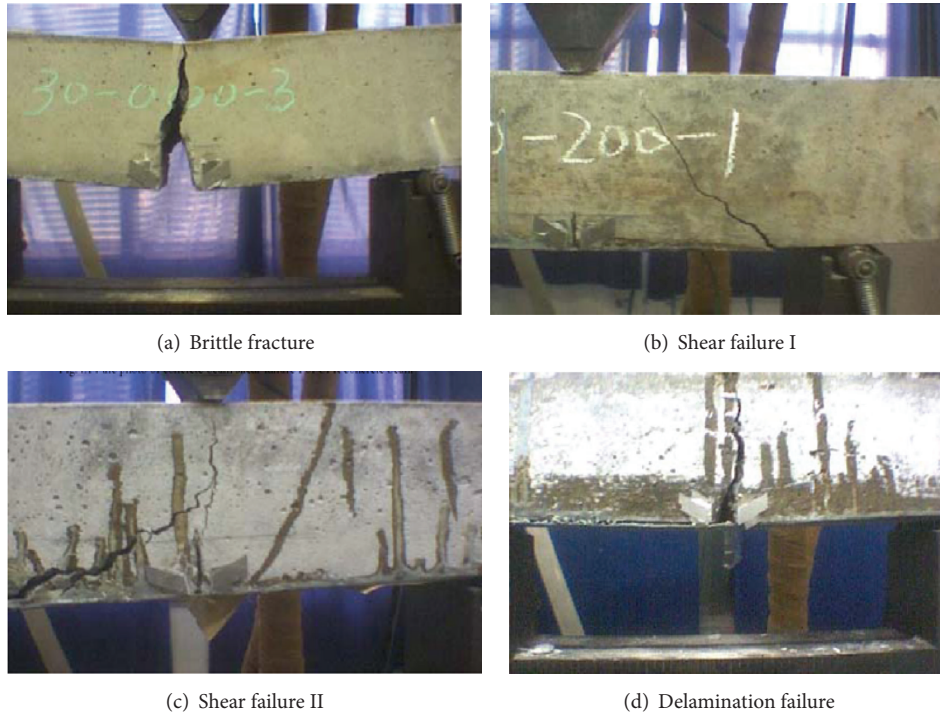


FIGURE 7: Final failure modes observed in experiment: (a) brittle fracture; (b) shear failure I; (c) shear failure mode II; (d) delamination failure.

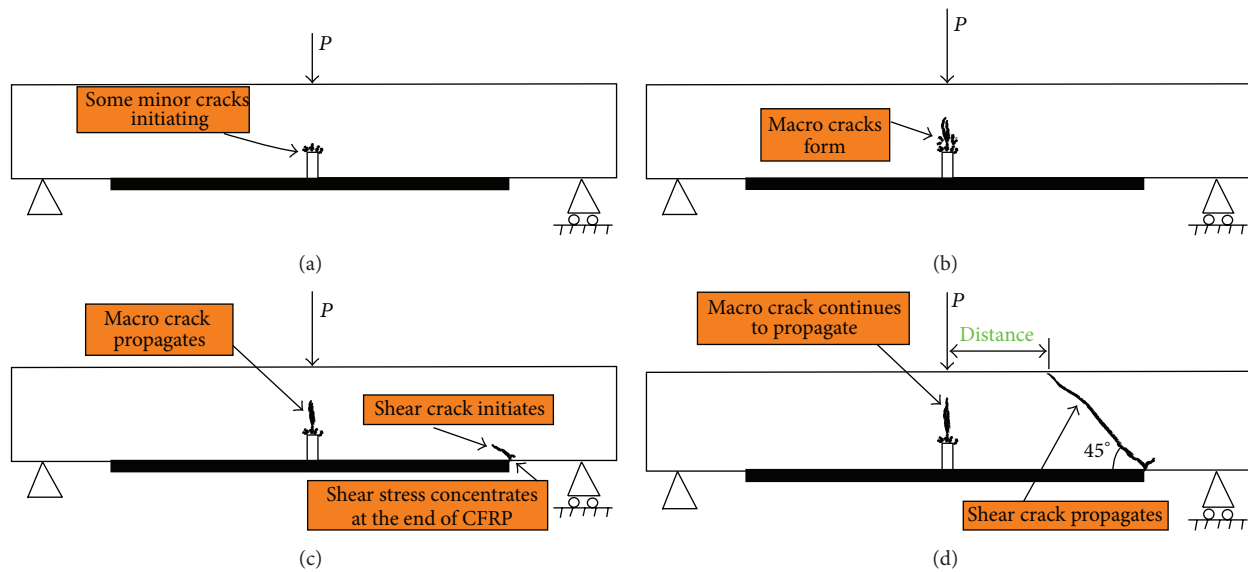


FIGURE 8: The sketch for the development of shear failure I mode.

this mode of failure and (b) the failure of the adhesive at the CFRP end (Figure 9(c)). At the same time, one smeared crack occurred at this site. Given that the newly created shear cracks were close to the mid-span of the concrete beam, they easily approached the initial main crack located at the mid-span of the concrete beam, which resulted in a relatively large macrocrack that penetrated the concrete portion of the reinforced beam (Figure 9(d)). Given that both the bending

moment and the tensile stress of the cross section of the crack were the largest, the macrocracks penetrated by the shear cracks and the initial main cracks propagated along the axis of the beam instead of along the path of the 45-degree angle. This phenomenon led to the failure of the reinforced beam. It should be noted that the essential difference between the shear I and II modes is the approaching of the two cracks for the shear II mode but not for the shear I mode. The possible

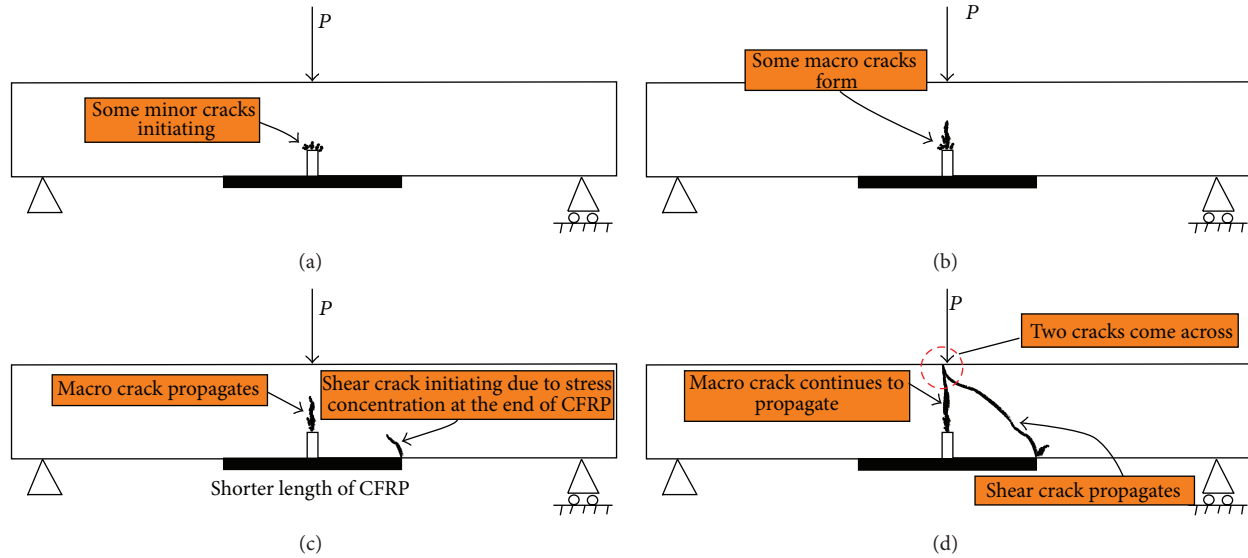


FIGURE 9: The sketch for the development of shear failure II mode.

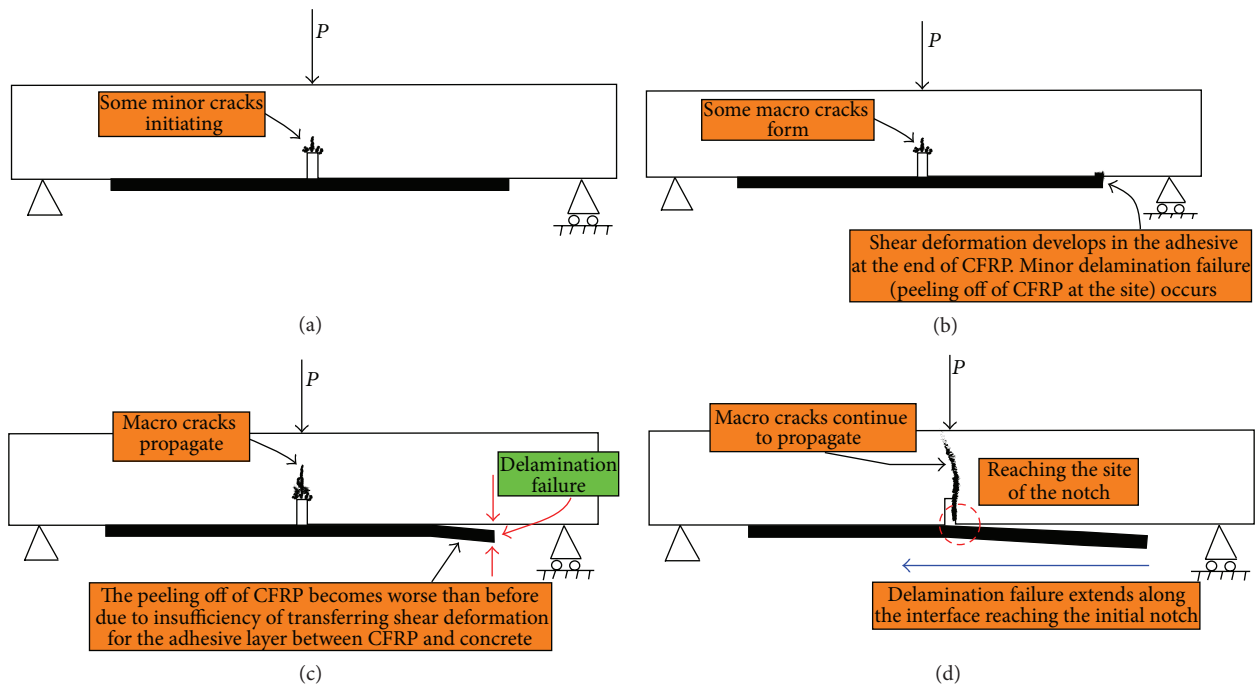


FIGURE 10: The sketch for the development of delamination failure mode.

reason for this could be the length of the CFRP layer bonded at the bottom of concrete beam. A shorter layer led to a larger stress concentration at CFRP end and created one smeared crack closer to the main crack unlike in the case of a longer CFRP layer.

Figure 7(d) shows the delamination failure mode. From the experimental observation, the delamination failure mode occurred for the case of the longest CFRP layer (350 mm) in this experiment. The reason for such failure mode could be explained as follows and can also be illustrated in Figure 10.

When the beam was loaded, the main crack located at the mid-span was extended because of the stress concentration at the tip (Figure 10(a)). Since the length of the bonded CFRP was significantly greater than in the other cases, it helped to relieve the shear stress concentration at CFRP end, thus causing relatively fewer shear cracks developed at the end (Figure 10(b)). However, as the load increased, propagation of the main crack was prevented because of the tensile stress developed in the CFRP layer. Incremental load was transferred to CFRP because of its high modulus. Meanwhile,

TABLE 5: The statistics of failure modes for the tested specimens.

The failure mode	Statistics for the corresponding specimens
Brittle fracture	Totally 9 specimens, all for concrete beams without CFRP reinforcement
Shear failure I	Totally 12 specimens: 3 for 10-100, 2 for 20-100, 3 for 30-100, 2 for 20-100b, and 2 for 30-350 specimens
Shear failure II	Totally 14 specimens: 1 for 20-100, 3 for 10-200, 3 for 20-200, 3 for 30-200, 2 for 20-100s, 1 for 20-200s, and 1 for 20-200b specimens
Delamination failure	Totally 19 specimens: 3 for 10-350, 3 for 20-350, 1 for 30-350, 1 for 20-100s, 2 for 20-200s, 3 for 20-350s, 1 for 20-100b, 2 for 20-200b, and 3 for 20-350b specimens

Note. The description for failure modes can refer to the subsequent section, and the details for the specimen can refer to Table 4.

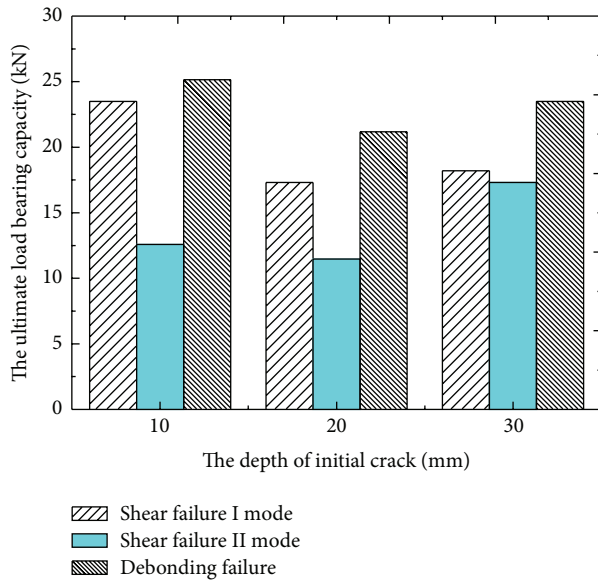


FIGURE 11: The column representation for the ultimate load for reinforced concrete beam versus the depth of initial notch under various failure modes.

the adhesive layer between the concrete beam and the CFRP layer had to sustain more shear stress and also had to transfer a part of the incremental load by undergoing shear deformation. When the shear deformation exceeded the shear deformation capacity, the CFRP slid along the interface between the CFRP and the concrete beam. The main crack at the mid-span continued to propagate rapidly until the CFRP started to peel off the adjacent concrete material from the beam. The peeling off of CFRP at the end grew to ultimately cause the delamination failure (Figure 10(c)). Once delamination failure was initiated, which could significantly decrease the capability of concrete beam resisting the deformation, the phenomenon of peeling off of CFRP rapidly deteriorated until it reached the location of the initial notch (Figure 10(d)). It is worth mentioning that the delamination observed in the experiment (Figure 7(d)) differed slightly from the schematic shown in Figure 10(d) since the length of CFRP in Figure 7(d) happened to fall at the two supports of the beam. Nevertheless, a closer observation can find the similarity in essence between them.

Table 5 summarizes the final failure modes for the 54 test specimens in the experiment, and Figure 11 shows the

variation in ultimate load capacity for the specimens with the initial depth of notch for different failure modes, shear failure I mode, shear failure II mode, and delamination failure, respectively. The presented statistics shows that nine specimens demonstrated the brittle fracture mode. They are the concrete beams not reinforced with CFRP. Twelve specimens demonstrated the shear failure I mode, 14 specimens demonstrated the shear failure II mode, and 19 specimens demonstrated the delamination failure. The specimens that exhibited the delamination failure comprised the largest group, accounting for 35% of the total. It also shows that, for concrete beams reinforced with CFRP, except for those beams with double layers of CFRP, 13 specimens failed in the delamination failure mode, but 26 specimens failed in the shear failure mode. These results strongly support the previous theoretical analysis, as discussed in Section 2.3.1. It can be explained as follows.

From (25), increasing CFRP length can significantly improve the shear stress $\tau(x)$, as seen in Figure 3. The shear stress at the end of CFRP was increased from 7 MPa to 14 MPa when the length of the CFRP layer increased from 0.1 m to 0.35 m resulting in a much larger concentration of the shear stress at the end of CFRP. Equation (25) also indicates that the shear stress increases linearly with the applied load. Consequently, as the applied load increased at the mid-span of the beam, the shear stress concentration at the CFRP end further deteriorated. The concrete material at the end of the CFRP layer was subjected to significantly greater shear stress than at other locations till it exceeded the shear strength of concrete. As a result, the shear failure mode occurred for the beams with longer CFRP layer.

Table 5 also shows that the thinner the CFRP layer is, the more likely the failure is of the beam in the shear failure mode. In total, 3 out of 49 specimens reinforced with double layers of CFRP failed in the shear failure mode. This experimental observation supported the theoretical prediction as discussed in Section 2.3.2. The expression for the shear stress at the end of the CFRP layer (see (25)) explicitly includes a term, t_p , which stands for the thickness of CFRP. Figure 4 graphically illustrates the variation of shear stress at the CFRP end with an increase in the thickness of CFRP. The shear stress was increased from 10 MPa to 15 MPa when CFRP thickness decreased from 2 mm to 1 mm. The thinner CFRP led to an increased concentration of the shear stress at the end of the CFRP layer. As the thickness of the CFRP layer increased, the shear stress was largely reduced, which was possibly caused

TABLE 6: The ultimate load for concrete beams.

Number of specimen	Ultimate load (N)	Number of specimen	Ultimate load (N)	Number of specimen	Ultimate load (N)	Average load (N)
10-000-1	6700	10-000-2	6850	10-000-3	7250	6933.3
10-100-1	12064	10-100-2	13085	10-100-3	12574	12574.3
10-200-1	21636	10-200-2	25400	10-200-3	23034	23356.7
10-350-1	27179	10-350-1	20983	10-350-3	26966	25042.7
20-000-1	5527	20-000-2	6725	20-000-3	5005	5752.3
20-100-1	12002	20-100-2	10975	20-100-3	12090	11689
20-200-1	20021	20-200-2	21020	20-200-3	16787	19276
20-350-1	21280	20-350-2	20674	20-350-3	21376	21110
20-100s-1	12632	20-100s-2	11465	20-100s-3	13935	12677.3
20-200s-1	20574	20-200s-2	16679	20-200s-3	20473	19242
20-350s-1	21285	20-350s-2	27275	20-350s-3	21365	23308.3
20-100b-1	10517	20-100b-2	11120	20-100b-3	11789	11142
20-200b-1	26059	20-200b-2	23680	20-200b-3	18530	22756.3
20-350b-1	20169	20-350b-2	25114	20-350b-3	23996	23093
30-000-1	4714	30-000-2	4564	30-000-3	4425	4567.7
30-100-1	10696	30-100-2	10382	30-100-3	10064	10380.7
30-200-1	18051	30-200-2	18492	30-200-3	17875	18139.3
30-350-1	31214	30-350-2	24210	30-350-3	23496	26306.7

by the shift of shear stress from the CFRP closet concrete side to the outer bottom of CFRP along the thickness direction of CFRP.

In regard to the shear failure modes I and II, the theoretical expression presented in this paper does not have the capability to predict the direction of crack propagation once it extends. This is one of the motivations in this paper to discuss the failure mechanism in the viewpoint of theory. However, as seen from the experimental observation, the shear cracks generated in the beams with the relatively shorter length of CFRP more easily penetrated the main crack located at the mid-span of the beam when compared to the shear cracks generated in the same beam types but with longer CFRP layers. This condition results in shear failure mode II. Figure 11 shows the relationship between the failure modes of the beams and their ultimate load capacities. For the same depth of the initial crack, the ultimate load capacity of the specimens in the delamination failure mode was the largest, followed by those in the shear failure I mode and subsequently the shear failure II mode. Delamination failure corresponded to the largest ultimate load capacity because of the least shear stress concentration. Given that the shear cracks run through the initial cracks after development, shear failure II has corresponded to the least ultimate load capacity.

4.2. Effect of the Length of CFRP and the Depth of Notch on the Ultimate Load Capacity of the Reinforced Beams. Table 6 lists the ultimate load capacities for the concrete beams in the experiment. The first, third, and fifth columns in Table 6 represent the three replicates of a particular type of concrete beam in the experiment; that is, “10-000” corresponds to three beams, marked as 10-000-1, 10-000-2, and 10-000-3,

respectively. The last column is for the average value for the three concrete beams. Comparing with the theoretical derivation discussed in Section 2.4, the method for calculating the ultimate load for the concrete beam showed a good agreement with the experimental measurement (Figure 5). However, for the reinforced concrete beams, a detailed analysis requires a combination with finite element method [21–23]. Equations ((26)–(28)) aim especially for the case in which the stress intensity factor can be explicitly calculated. However, for the concrete beams reinforced with CFRP, (26)–(28) are not in relation with the length and the thickness of the CFRP layer. In combination with the previous works [21–23], (26)–(28) can work very well in calculating the ultimate load capacity for any CFRP-reinforced concrete beams.

Figure 12 shows the effects of the length of CFRP and the initial notch depth on the ultimate load capacity of the CFRP-reinforced beams. Figure 12(a) presents the values of the ultimate bearing capacity of the unreinforced concrete beam. The experimental results showed that a longer initial notch corresponds to a smaller ultimate load capacity of the concrete beam. As the notch depth increased, the fracture toughness of the crack approached the critical value of the concrete beam, and hence the bearing capacity was decreased. Figure 12(a) shows that when the depth of the initial notch increased to 30 mm, the ultimate load capacity of the concrete beam decreased from 7.25 kN to 4.564 kN, which represents a decrease by 37%.

However, with an increase in the length of the CFRP layer, the ultimate bearing capacity of the CFRP-reinforced beam was increased (Figures 12(b), 12(c), and 12(d)). The greatest ultimate load capacity of the CFRP-reinforced beam was seven times greater than that of the otherwise identical

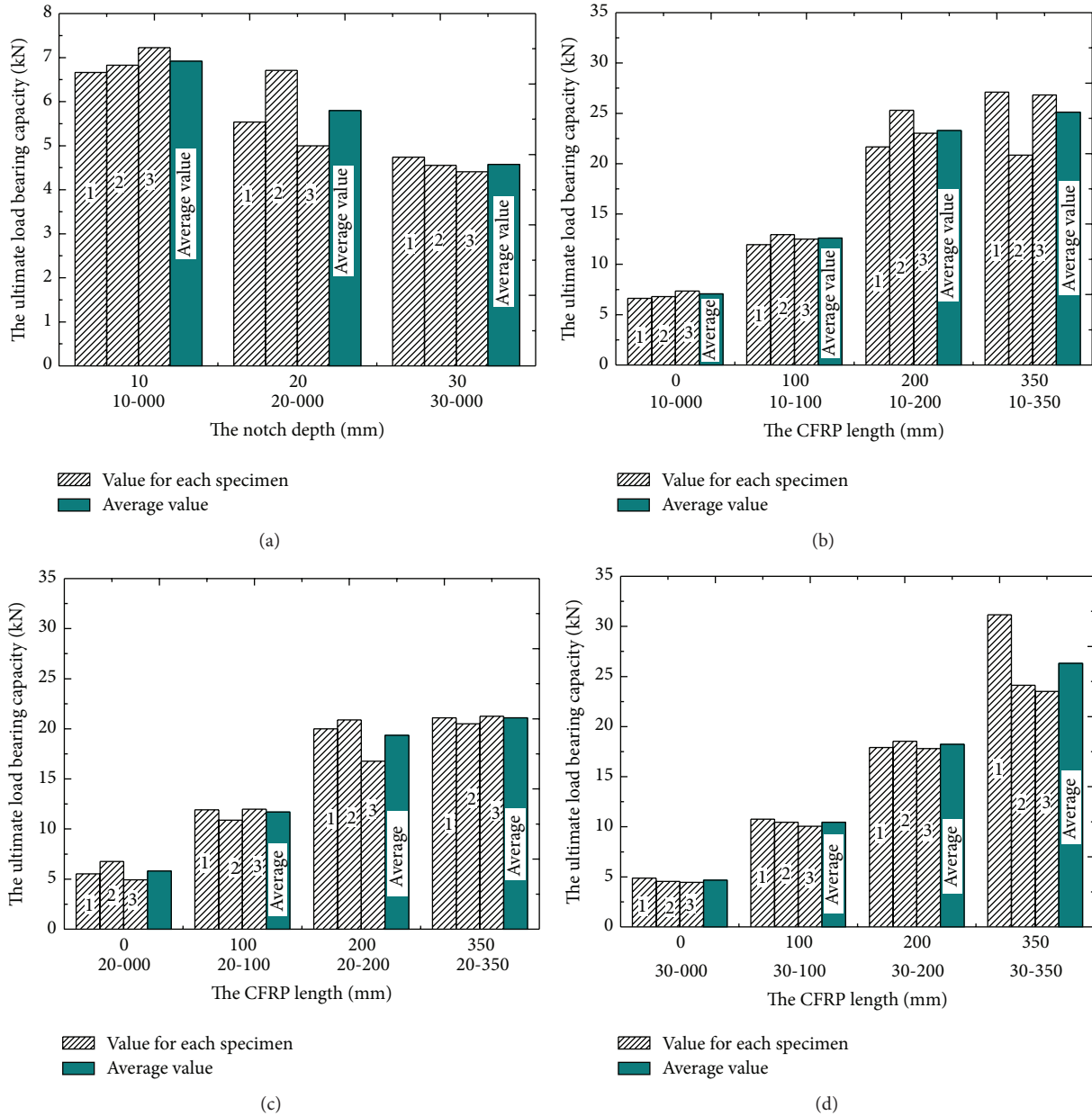


FIGURE 12: (a) The effects of initial notch depth on the ultimate bearing capacity of concrete beam without CFRP strengthened; (b) the effect of CFRP length on the ultimate load bearing capacity of reinforced concrete beam for the notch depth of 10 mm; (c) the effect of CFRP length on the ultimate load bearing capacity of reinforced concrete beam for the notch depth of 20 mm; (d) the effect of CFRP length on the ultimate load bearing capacity of reinforced concrete beam for the notch depth of 30 mm.

unreinforced beam (as shown in Figure 12(d)). However, the bearing capacity of the reinforced beam did not increase linearly with an increase in the length of the CFRP layer. The experiment results indicated that the bearing capacities of the reinforced beam did not increase further when the length of the CFRP layer was increased in excess of 200 mm. This observation reveals the maximum reinforcement effect of the CFRP-reinforced concrete beam structure.

However, the effectiveness of the additional length of the CFRP layer was seen to increase with an increase in the initial notch depth. Figure 12(d) shows that the bearing

capacity of the beam when the carbon fiber plate was 350 mm long increased more significantly than that when the carbon fiber plate is 200 mm long. This finding indicates that when the depth of the initial crack is small, its influence on the bearing capacity of the reinforced beam is not obvious. When CFRP length increases, its influence becomes obvious. An increase in the depth of the initial notch reduced the overall stiffness of the concrete beam. However, the bonded CFRP not only compensated for the structural flaw of the cracks but also increased the stiffness of the structure. When CFRP layer was longer, its role in reinforcement became significant.

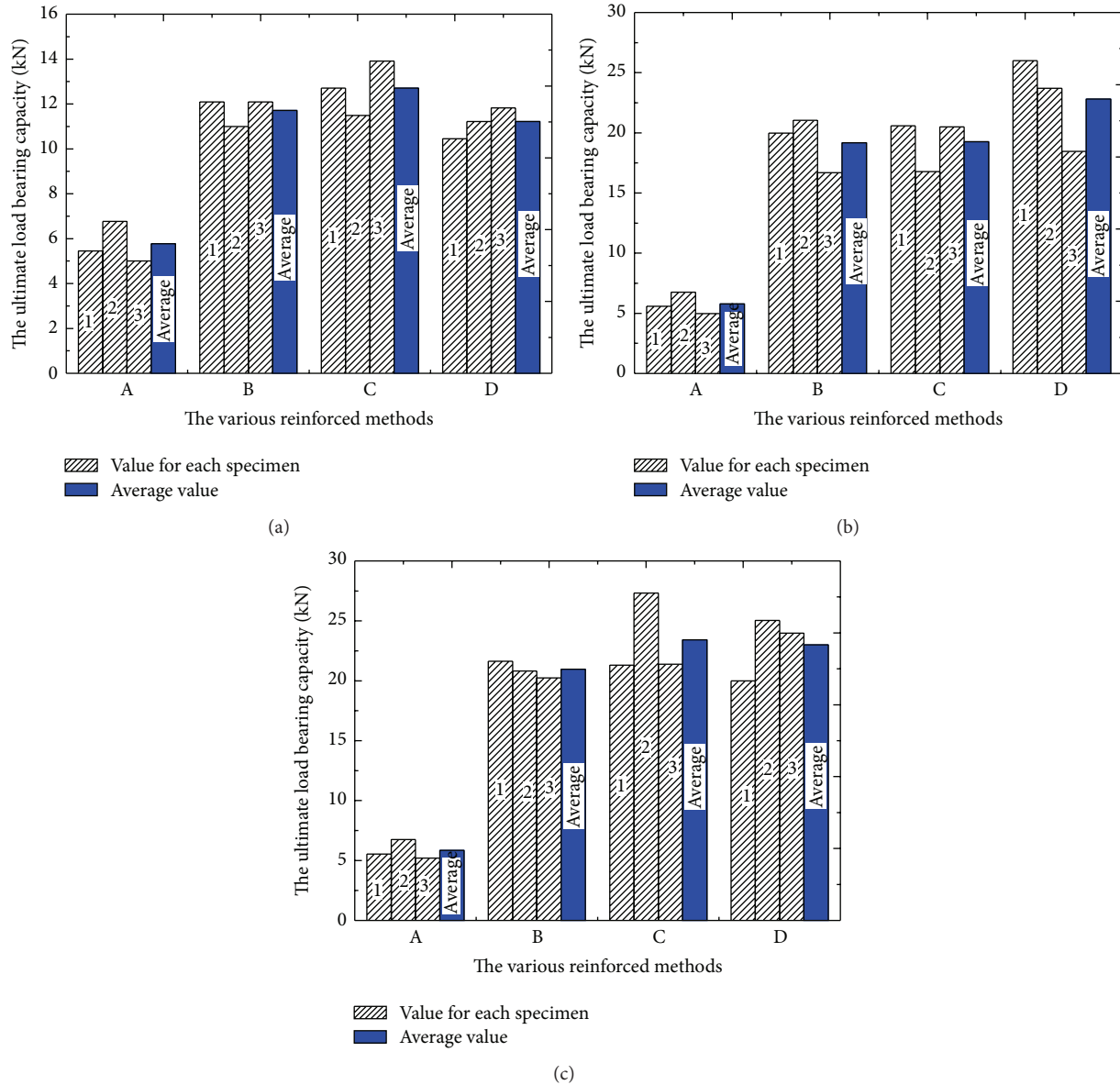


FIGURE 13: The plot of the ultimate bearing load of beams against various reinforcement methods for different CFRP length but with the same notch depth of 20 mm. (a) CFRP length of 100 mm, (b) CFRP length of 200 mm, and (c) CFRP length of 350 mm. A for without reinforcement, B for single-layer CFRP reinforcement, C for two-layer CFRP reinforcement, and D for single-layer CFRP reinforcement using U-shaped caps at the plate ends.

The shear stress at the end of the carbon fiber plate reduced significantly with an increase in the length of the CFRP layer. The increased length relieved the stress concentration at the end, reduced the failure potential of the reinforced structure at the end, and increased the bearing capacity of the structure.

4.3. Effect of Reinforcement Methods on the Ultimate Bearing Capacity of the Reinforced Beams. In this section, various reinforcement methods, including no CFRP reinforcement, single-layer CFRP reinforcement, two-layer CFRP reinforcement, and single-layer CFRP reinforcement using U-shaped caps at the plate ends, are discussed to investigate the effects of CFRP thickness and various bond methods on the ultimate

bearing load of reinforced concrete beams. Even though the theoretical derivation in this paper does not consider different types of reinforcement methods, they are discussed in the viewpoint of the experimental findings in order to elucidate the role of various reinforcement methods on the CFRP-strengthening of concrete beams. A further research is expected to focus on the derivation of an analytical expression for the effect of various reinforced methods.

Figure 13 shows the influence of CFRP lengths of 100, 200, and 350 mm and various reinforcement methods on the ultimate bearing capacity of the concrete beam for a notch depth of 20 mm. When the CFRP layer was relatively short, such as 100 and 200 mm long, its thickness had insignificant

influence on the ultimate bearing capacity of the reinforced structure. When the CFRP was 350 mm long, the ultimate bearing capacity of the reinforced structure bonded with two CFRP layers increased by 12% when compared with that of the reinforced structure bonded with one CFRP layer. The influence of wrapping the CFRP ends with the U-shaped caps also showed a similar trend. When the length of the CFRP was 100 mm, the bearing capacity of the structure with the ends wrapped with U-shaped CFRP caps was considerably low. However, when the CFRP length increased to 200 mm, the reinforcement effect of the CFRP-reinforced concrete beam was the most. With regard to the failure modes for the CFRP-strengthened concrete beams, as shown in Table 6, there were six test specimens with the U-shaped caps wrapped at the end of the CFRP layer. Out of the six, three followed the delamination failure mode, one followed the shear failure I mode, and two followed the shear failure II mode. Among the nine test specimens that used double layers of CFRP in the experiment, three specimens followed the shear failure II mode and six specimens followed the delamination failure mode. The possible reason for that is the usage of the U-shaped cap wrappings at the CFRP end fastened the CFRP on the bottom of the concrete beam much strongly compared to that in the cases with no cap wrapping. Even though the applied load increased sharply, CFRP could resist tension and shear deformation at the U-shaped cap. However, the interface between the CFRP and the concrete could not sustain the shear deformation and consequently led to the delamination failure. Nevertheless, with an increase in the thickness of CFRP, CFRP at the bottom of the concrete beam could withstand larger tensile stress at the end of the CFRP layer than a thinner CFRP layer would do, thus, relieving the tensile stress concentration at the end of the CFRP layer. However, as the load increased, the shear stress that transferred from the concrete beam to the interface also increased; the thicker interface enhanced its toughness, which results in an ease of peeling off of concrete from the concrete beam at the interface.

5. Conclusions

An experimental investigation was performed in this study on the failure mechanisms of concrete beams strengthened with a CFRP layer. The following conclusions were drawn:

- (1) An analytical expression for the shear stress at the interface between concrete and CFRP was derived. The shear stress was found to be the key factor affecting the failure mode of the reinforced concrete beams. A parametric analysis for the effects of the length and the thickness of the CFRP layer was made for predicating the failure mode. Theoretical methods for calculating the ultimate load capacity of CFRP-strengthened beams were also presented.
- (2) Four failure modes were observed in the experiment, namely, brittle fracture mode, shear failure I mode, shear failure II mode, and delamination failure mode. The failure mechanism for concrete beam without CFRP showed the brittle fracture mode; the concrete beam strengthened with shorter CFRP layer

(100 mm) showed the shear failure I mode; the concrete beam with long CFRP layer (200 mm) showed the shear failure II; and the beams with the longest CFRP layer (350 mm) showed the delamination failure mode.

- (3) The length of the CFRP layer affected the ultimate load capacity of the CFRP-strengthened concrete beams. When CFRP length was 100 mm long, the ultimate load capacity is increased by 1.81~2.27 times compared to that of the nonreinforced concrete beams. It can even be increased by 3.35~3.97 and 3.61~5.76 times compared to that of nonreinforcement beams when the length of the CFRP layer was 200 mm and 350 mm, respectively.
- (4) When the CFRP layer was relatively short, its thickness had insignificant influence on the ultimate bearing capacity of the reinforced beam. However, when the CFRP length was 350 mm, the ultimate bearing capacity of the concrete beam bonded with two CFRP layers increased by 12% compared to that of the beam bonded with one CFRP layer. The influence of the wrapping of the CFRP ends with the U-shaped caps on the ultimate bearing capacity of the structure also showed similar trend. When the length of the CFRP layer was 100 mm, the bearing capacity of the structure with the ends wrapped with the U-shaped CFRP caps was considerably low. However, when the CFRP length increased to 200 mm, the reinforcement effect of the concrete beam with the U-shape caps was the largest.
- (5) Comparison between a theoretical analysis and the experimental observation showed a good agreement for the effect of the length and the thickness of the CFRP layer, as well as the ultimate load capacity for the CFRP-reinforced concrete beams. However, the effect of various reinforced methods on strengthening could not be explained by the theoretical derivation. A further research will focus on this topic.

Conflict of Interests

The authors declare no conflict of interests.

Authors' Contribution

Xia Huang is responsible for performing the theoretical derivation and has contributed to the writing of all the sections within paper. Jian Wang is working on experimental measurement and Feng Zhang has been in charge of data processing. Song-shan Niu is responsible for planning for experiment. Jun Ding is responsible for the whole research project.

Acknowledgments

This work is financially supported by the Natural Science Foundation of China (11302272), by the Natural Science Foundation of China (11272368), and by the 2013 Program

for Innovation Team Building at Institutions of Higher Education in Chongqing (KJTD201319).

References

- [1] T. Zhao, *The New Technology for Retrofitting Concrete Structures with CFRP*, Tianjing University Press, Tianjing, China, 1st edition, 2001.
- [2] Y. Meng and B. Lu, *The Reinforcement and Rehabilitation for the Bridge*, Chongqing University Press, Chongqing, China, 1st edition, 2005.
- [3] J. Michels, R. Christen, and D. Waldmann, "Experimental and numerical investigation on postcracking behavior of steel fiber reinforced concrete," *Engineering Fracture Mechanics*, vol. 98, no. 1, pp. 326–349, 2013.
- [4] H. C. Biscaia, C. Chastre, and M. A. G. Silva, "Nonlinear numerical analysis of the debonding failure process of FRP-to-concrete interfaces," *Composites Part B: Engineering*, vol. 50, pp. 210–223, 2013.
- [5] M. C. Sundarraja and S. Rajamohan, "Strengthening of RC beams in shear using GFRP inclined strips-an experimental study," *Construction and Building Materials*, vol. 23, no. 2, pp. 856–864, 2009.
- [6] A. K. M. A. Islam, "Effective methods of using CFRP bars in shear strengthening of concrete girders," *Engineering Structures*, vol. 31, no. 3, pp. 709–714, 2009.
- [7] W. Edberg, D. Mertz, and J. Gillespie Jr., "Rehabilitation of steel beams using composites materials," in *Proceedings of the ASCE 4th Material Engineering Conference*, pp. 502–508, Washington, DC, USA, 1996.
- [8] C. Mazzotti, M. Savoia, and B. Ferracuti, "An experimental study on delamination of FRP plates bonded to concrete," *Construction and Building Materials*, vol. 22, no. 7, pp. 1409–1421, 2008.
- [9] K. Nakaba, T. Kanakubo, T. Furuta, and H. Yoshizawa, "Bond behavior between fiber-reinforced polymer laminates and concrete," *ACI Structural Journal*, vol. 98, no. 3, pp. 359–367, 2001.
- [10] A. M. Malek, H. Saadatmanesh, and M. R. Ehsani, "Prediction of failure load of R/C beams strengthened with FRP plate due to stress concentration at the plate end," *ACI Structural Journal*, vol. 95, no. 2, pp. 142–152, 1998.
- [11] H. Saadatmanesh and M. R. Ehsani, "RC beams strengthened with GFRP plates. Part I: experimental study," *Journal of Structural Engineering*, vol. 117, no. 11, pp. 3417–3433, 1991.
- [12] H. Saadatmanesh and R. E. Mohammad, "RC beams strengthened with GFRP plates. Part II: analysis and parametric study," *Journal of Structural Engineering*, vol. 117, no. 11, pp. 3434–3455, 1991.
- [13] V. Sierra-Ruiz, J.-F. Destrebecq, and M. Grédiac, "The transfer length in concrete structures repaired with composite materials: a survey of some analytical models and simplified approaches," *Composite Structures*, vol. 55, no. 4, pp. 445–454, 2002.
- [14] O. Buyukozturk, O. Gunes, and E. Karaca, "Progress on understanding debonding problems in reinforced concrete and steel members strengthened using FRP composites," *Construction and Building Materials*, vol. 18, no. 1, pp. 9–19, 2004.
- [15] P. Colombi, "Reinforcement delamination of metallic beams strengthened by FRP strips: fracture mechanics based approach," *Engineering Fracture Mechanics*, vol. 73, no. 14, pp. 1980–1995, 2006.
- [16] A. Benachour, S. Benyoucef, A. Tounsi, and E. A. A. Bedia, "Interfacial stress analysis of steel beams reinforced with bonded prestressed FRP plate," *Engineering Structures*, vol. 30, no. 11, pp. 3305–3315, 2008.
- [17] T. L. Anderson, *Fracture Mechanics: Fundamentals and Applications*, CRC Press, Boca Raton, Fla, USA, 3rd edition, 2005.
- [18] P. Y. Huang, Q. Q. Wang, L. F. Luo, and G. S. Zhang, "The experimental study on failure load for the reinforced concrete beams with FRP," *Guangdong Highway Communications*, vol. 66, pp. 254–257, 2001.
- [19] Chinese Aeronautical Establishment, *The Handbook for Stress Intensity Factors*, Beijing Science Press, Beijing, China, 1981.
- [20] S. S. Niu, *The experimental study on concrete beams strengthened with CFRP [M.S. thesis]*, Chongqing University, Chongqing, China, 2002.
- [21] J. Ding, F. Wang, X. Huang, and S. Chen, "The effect of CFRP length on the failure mode of strengthened concrete beams," *Polymers*, vol. 6, no. 6, pp. 1705–1726, 2014.
- [22] J. Ding, *Crack failure study of CFRP reinforced concrete beams [M.S. thesis]*, Chongqing University, Chongqing, China, 2004.
- [23] J. Ding, X. Huang, G. Zhu, S. Chen, and G. Wang, "Mechanical performance evaluation of concrete beams strengthened with carbon fiber materials," *Advances in Materials Science and Engineering*, vol. 2013, Article ID 572151, 9 pages, 2013.

Research Article

Behavior of Full-Scale Porous GFRP Barrier under Blast Loads

D. Asprone,¹ A. Prota,¹ G. Manfredi,¹ and A. Nanni^{1,2}

¹Department of Structures for Engineering and Architecture, University of Naples "Federico II", 80125 Naples, Italy

²Department of Civil, Architectural and Environmental Engineering, University of Miami, Coral Gables, FL 33124, USA

Correspondence should be addressed to D. Asprone; d.asprone@unina.it

Received 13 May 2015; Accepted 11 August 2015

Academic Editor: Osman Gencel

Copyright © 2015 D. Asprone et al. This is an open access article distributed under the Creative Commons Attribution License, which permits unrestricted use, distribution, and reproduction in any medium, provided the original work is properly cited.

This research paper is part of the SAS (Security of Airport Structures) Project funded by the European Programme for Critical Infrastructure Protection, whose objective was to develop and deploy a fiber reinforced polymer (FRP) fencing system intended to protect airport infrastructures against terrorist acts. In the paper, the efficacy of the proposed glass FRP discontinuous (porous) barrier under blast loads is presented by showing the results of the blast test campaign conducted on full-size specimens with a focus on the reduction of the blast shock wave induced by the barrier. A simplified model predicting the reduction of the shock wave beyond the barrier is proposed and validated via the experimental data obtained in the project.

1. Introduction

Recent terrorist acts have contributed to change of the design approach to critical infrastructures; in fact, malicious disruptions, blasts, or impacts have unfortunately become part of the possible load scenarios that could act on constructed facilities during their life span. Consequently, specific protection interventions are introduced to minimize disruptive effects, guarantee the safety of the occupants of a facility, and, to the extent possible, maintain the functionality of a facility. Hence, highly dynamic loading conditions represent nowadays a fundamental challenge in structural engineering as critical buildings and infrastructures need to resist extreme loads events that can occur during their lifetime as a result of natural and man-made hazards (e.g., explosions, collisions, and severe earthquakes). As a corollary, there is a growing interest in the scientific and practicing communities to design and/or assess protection systems to reduce the vulnerability of critical infrastructures (e.g., shelters and barriers). With this objective, a research program named Security of Airport Structures (SAS) was undertaken and completed by a consortium of European entities led by the research center AMRA (<http://www.amracenter.com/>), in order to (a) design and validate a protection barrier intended to deter malicious actions against critical airport infrastructures carried out by

ecoterrorists and (b) mitigate the effects of blast events on protected targets.

A porous glass fiber reinforced polymer (GFRP) barrier was designed and its components were subjected to mechanical tests. The material of choice for this barrier system became GFRP and not steel or steel reinforced concrete, as widely used in practical engineering because of the necessity of maintaining radiotransparency without interference with airport radio communications. To assess this property radiotransparency tests of the barrier were also conducted in anechoic chamber [1]. Furthermore, a blast test campaign was performed on full assemblies in order to validate the capability of the system in withstanding blast loads and protecting a target placed beyond it by reducing the effects of the incident blast shock wave.

Mitigation techniques used for other extreme events such as earthquakes could be adopted to resist blast loads [2], and fiber reinforced polymer (FRP) composites comprise a promising strengthening solution in the form of an externally bonded system [3]. Conversely, using FRP for the construction of barriers or similar security has not yet been explored [4] even though glass FRP (GFRP) porous barriers have been identified as a possible measure to prevent malicious disruptions, provide a standoff distance in case of blast actions, and reduce the consequences of an impact.

According to the end-user requirements, the main objective of the research project was to develop and deploy a structural fencing system able to protect VHF omnidirectional range (VOR) stations against malicious actions consisting of intrusion and/or blast loads of relatively small explosive charges placed in the vicinity or in contact with the barrier. A critical feature of any protective barrier for this type of facility is radiotransparency, which is necessary to avoid any disturbance to radio communications of specific frequencies. Hence, to achieve such goals, a discontinuous (porous) barrier composed by GFRP and precast concrete elements reinforced with GFRP bars was designed to take advantage of electromagnetic and mechanical properties of composites. The proposed barrier provides protection through two contributions. First, its geometrical and mechanical characteristics ensure protection against intrusions and blast loads. Second, its shape provides an attenuation of the blast shock wave, adding some level of additional protection for facilities located beyond it. The end-user specified the design charge for the blast action equal to 5 kg of commercial explosive, intended to represent the possible disruptive action of an ecoterrorist attacking radio communication infrastructures. Given the amount of explosive as a fixed parameter, in addition to contact charge configuration employed in third test, the first two tests investigated two different standoff distance configurations aiming at reproducing the cases of prevented direct access to the barrier.

The objective of this paper is to describe some results of the blast test campaign conducted on full-size specimens of the proposed barrier and to discuss their effectiveness in mitigating blast shock waves. A simplified model is also proposed to predict the reduction of the peak pressure due to the porous barrier; an example of the computational procedure is described in Appendix. Numerical tests, using the applied elements method, were also conducted, providing further details about the structural behavior of the barrier, and are presented in [5]. These analyses were used to validate the forces acting on the barrier and the structural response of the pipes.

2. Materials and Methods

2.1. Geometry and Mechanical Properties of the Barrier. The barrier is composed of vertical GFRP pipe elements secured in a precast reinforced concrete pedestal base. Each individual pipe is not connected to the adjacent ones to avoid the domino effect in case of failure. Each pipe has an external diameter of 85 mm and a wall thickness of 5.5 mm. Pipes are spaced 75 mm on centers. The GFRP pipe wall is a typical pultruded product with an internal core reinforced with unidirectional E-glass fibers (to provide strength and stiffness in the longitudinal direction) and two external layers reinforced with a mat of E-glass chopped fibers (to facilitate manufacturing and allow for a resin rich surface). Both core fibers and mats are impregnated with a polyester resin.

The concrete base and the GFRP pipes are 0.5 m and 2.5 m high, respectively. The barrier is represented in Figure 1. The concrete base is made of interconnected precast segments



FIGURE 1: Prototype of the barrier.

(dry joint, male-female connection to provide shear inter-lock) having a thickness of 150 mm. Each segment has an inverted T cross section, whose web and flange are 0.3 m and 0.7 m wide, respectively. The overall height and flange thickness are equal to 0.5 m and 0.2 m, respectively.

One pipe is installed in each precast concrete segment in a 0.3 m deep, 100 mm diameter hole centered on the web of the precast element. The interspace between pipe and concrete is filled with a no-shrink cementitious mortar. Two additional holes for tie anchors are present in the flanges of each segment. Two GFRP bars can be inserted through these holes and secured with cementitious mortar to create a deep foundation system. The diameter and depth of these GFRP tie bars have to be determined based on ground characteristics.

The GFRP's mechanical behavior was investigated for a quality control process and to collect data that will be used in performance modeling (together with high strain-rate properties) not discussed herein. To this aim, coupon tests were conducted on flat GFRP specimens taken from the pipe to evaluate their direct tension properties [5]. Two typologies of specimens were tested:

- (i) Integral one, composed of the internal core and the external layers.
- (ii) Peeled one, composed only of the internal core (after machining the surface layers).

All the specimens exhibited a linear behavior up to failure. Table 1 shows the results derived from such tests.

Four-point bending tests were also performed on five pipe specimens to investigate their flexural behavior. This type of test is complementary to the tensile test on coupons in terms of quality control. The data were processed to obtain moment-curvature relationships, and those slopes indicate the flexural stiffness of the tested pipes. An average value for the flexural stiffness of 41.2 kNm^2 was obtained. A global Young's modulus was obtained that combines both tensile and compression contributions. To separate them and determine

TABLE 1: Summary of the results of tensile failure tests on GFRP specimens.

	Failure stress [†] [MPa]	Experimental ultimate strain [†]	Chord modulus of elasticity ^{†,‡} [GPa]	Theoretical ultimate strain [*]
Integral specimens (5 samples)	648.3 (11.5%)	0.0150 (4.8%)	44.1 (3.5%)	0.0147
Peeled specimens (6 samples)	736.5 (6.4%)	0.0153 (2.5%)	51.3 (2.1%)	0.0143

[†] Terms in parentheses represent the coefficient of variation.

[‡] According to [5], chord modulus is evaluated as the ratio of stress increment over strain increment, corresponding to the strain interval from 0.001 to 0.003.

^{*} Evaluated as the ratio of the failure stress over the chord modulus of elasticity.

the compression Young's modulus, the following equation was used:

$$(EI)_{\text{exp}} = E_{\text{tens}} I_{\text{tens}} + E_{\text{comp}} I_{\text{comp}} \quad (1)$$

in which $(EI)_{\text{exp}}$ is the experimental flexural stiffness, E_{tens} is tensile Young's modulus obtained from the tensile tests performed on the integral specimens, equal to 44.1 GPa, I_{tens} and I_{comp} represent the moment of inertia of the tensile and compression zone, respectively, related to neutral axis, and E_{comp} is the compression Young's modulus to be evaluated.

The results reveal average global tension and compression Young's moduli of 38.4 and 32.7 GPa, respectively, in good agreement with values commonly exhibited by GFRP [6]. These results are used, as clarified in next session, to assess the stress level of the GFRP during the blast tests.

To complete the mechanical characterization, a dynamic tensile characterization campaign was performed, where high strain-rate values of interest ranged from 1 s^{-1} to 700 s^{-1} . The tests were conducted on the internal core of the composite elements, composed of unidirectional fiber reinforced polymer. The performed tests revealed an increase in tensile strength, which reached 88% in case of the highest strain-rate. The Young modulus presented an even higher enhancement, increasing up to 178%, in case of the highest strain-rate. A detailed discussion of these characteristics is reported in [7]. The results of the dynamic tensile characterization campaign will be used to construct complete constitutive laws and to validate the dynamic behavior of the barrier system via sophisticated numerical models.

2.2. Blast Tests. Three blast tests were performed on distinct barrier specimens to validate the system's capability to withstand blast-induced loads and reduce the shock wave propagating beyond the barrier. In these tests, a TNT charge was detonated at a specified distance from a specimen composed of 13 pipes, installed as described previously, to form a 2 m long barrier. Figure 1 shows a specimen before the test. The charge was placed at 1.5 m from the ground to avoid energy dissipation in the formation of the crater and consequent lack of accuracy in evaluating the quantity of energy propagating in air. In each test, 5 kg of commercial grade quarry explosive, corresponding to 4 kg of equivalent TNT explosive was used, and the distances between the charge and the barrier were set at 5 m, 3 m, and 0.5 m, respectively. The tests were filmed with high-speed cameras and specimens were instrumented with accelerometers, contact pressure gauges, and strain gauges, located on the central pipe, as depicted in Figure 2, reporting strain gauges labels. Free air pressure gauges were

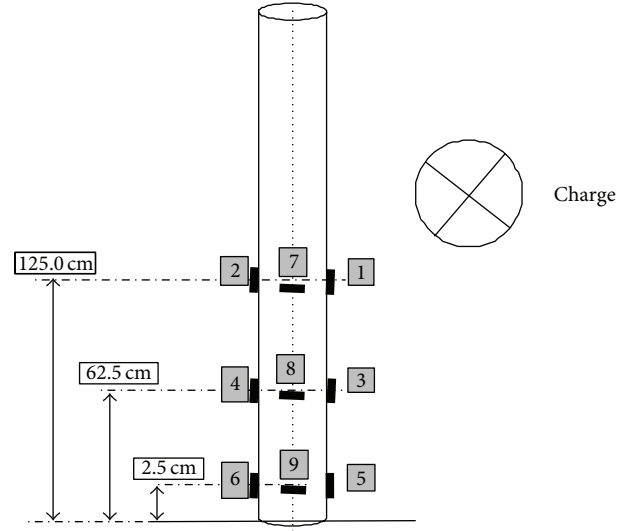


FIGURE 2: Strain gauges setup.

distributed around the barrier to measure the evolution of the pressure field induced by the explosion. The most of the acquired data was only used to validate the blast tests and to assure that results are consistent. However, hereafter only the experimental data useful for the scope of the work are presented.

3. Results and Discussion

3.1. Results of the Blast Tests. Strain gauge records allow evaluating the structural response of the central pipe under blast action; such data are available for the first and second blast tests, since damage occurred on the strain gauges during the third test. A preliminary elaboration of strain data is presented, aiming at (a) evaluating the stress levels occurring on instrumented pipes during blast excitation and (b) performing a comparison with levels reached during mechanical static tests.

Maximum absolute strains recorded by strain gauges 1–6 during the first and the second test are reported in Table 2. The largest values were recorded at sensors 5 and 6, placed close to the base of the pipe; in particular, both sensors recorded the same maximum values of 0.0007 and 0.0019, during the first and the second test, respectively. These values are much lower than the failure strain obtained in the laboratory for quasi-static tensile tests (0.0150) (Table 1), quasi-static four-point bending tests (0.0064), and high strain-rate

TABLE 2: Maximum absolute GFRP pipe strains during blast tests.

Strain gauge	First shot [m/m]	Second shot [m/m]
1	0.0003	0.0014
2	0.0003	0.0013
3	0.0005	0.0012
4	0.0004	0.0013
5	0.0007	0.0019
6	0.0007	0.0019

tensile tests (0.0124). Furthermore, the pipes were carefully inspected and no local damage was visually observed. This allows affirming that no structural damage occurred in the GFRP during the first and the second test.

Furthermore, strain data were employed to derive the internal bending moment acting on the instrumented pipe during blast excitation. Onto this end, strain gauges pairs 1-2, 3-4, and 5-6 (Figure 2) were used. Each of these pairs was placed at a different level and diametrically opposite sides of the pipe element (specifically 125.0, 62.5, and 2.5 cm from the concrete base, resp.), identifying a cross section. For each pair, the curvature χ was derived as shown below, assuming that a plane section remains plane under loading:

$$\chi = \frac{\varepsilon_1 + \varepsilon_2}{h}. \quad (2)$$

Then, the bending moment history was determined at each instrumented cross section as

$$M = \chi (EI)_{\text{exp}}, \quad (3)$$

where the average flexural stiffness $(EI)_{\text{exp}}$ obtained from four-point bending tests was used. To conduct such calculation, the quasi-static Young modulus was used, since it was verified, from recorded strain data, that a strain-rate of about 1 s^{-1} was induced; at this strain-rate value it was verified that the material does not exhibit a significant increase in Young modulus value [8]. Furthermore, the transverse strain gauges measurements (strain gauges 7, 8, and 9 in Figure 2) allowed concluding that ovalization of the cross section could be neglected with respect to its influence on variations of the inertia modulus.

Figures 3 and 4 report bending moment histories at instrumented cross sections for the first and the second test, respectively. In both cases, bending moment histories exhibited sinusoidal trends, clearly induced by oscillating displacements. Maximum values are equal to 0.65 kNm and 1.81 kNm in the first and the second blast, respectively, occurring, in both cases, at the base of the pipe, as it could be expected by a cantilever beam behavior. As further proof of the absence of damage, computed moment values are below 7 kNm, representing failure bending moment experienced during four-point bending tests. In both the first and the second blast tests, oscillation started about 330 ms after explosion time. Considering that the blast pressure reduced to zero not more than 40 ms after explosion time, as recorded from contact pressure sensors, pipe displacements can be considered as elastic free vibrations, induced by an initial impulsive action.

Figure 5 provides a schematic plan view of the test setup showing the location of the two air pressure gauges S1 and S6, placed at opposite sides with respect to the charge. Gauge S1 measures the free air pressure at a given distance while gauge S6 measures the free air pressure at the same distance from the charge, but behind the barrier. Hence, by comparing the pressure history acquired by these sensors, the interference of the barrier on the shock wave can be directly evaluated. With reference to Figure 5, the distance between gauge S6 and the center of the barrier ($D_T - D_B$) was kept constant at 4 m for all tests. For this reason, D_T was set equal to 9 m, 7 m, and 4.5 m for the first, second, and third blasts, respectively, with D_B equal to 5 m, 3 m, and 0.5 m. The length of the barrier test article was chosen recognizing that the blast wave beyond the barrier, recorded by rear sensors, is surely affected by diffractions occurring around the barrier. This effect is governed by the height of the barrier, a constant value in this program; hence, specimen width was selected so that the barrier boundaries, both horizontal and vertical, are at the same approximate distance from the charge.

After the first and second tests, the barrier was carefully inspected and no damage was observed, even in the concrete composite interface; the third blast determined the failure of five of the central pipe elements as depicted in Figure 6. Figures 7 to 9 show the pressure-time curves obtained from gauges S1 and S6 in each test (data from gauge S1 in the second test are not available). All diagrams also show the peak pressure estimated according to numerical formulations of Henrych [9] based on the amount of equivalent TNT and the distance of the sensor. These numerical formulations are currently used in the scientific community for free air explosions and are considered reliable. The acquisition of the pressure histories was triggered by the explosion. Therefore, the first portion of the acquired signals reporting zero values represents the delay time as the shock waves traveled to the sensors. As shown in the figures, such time decreases from the first to the third test, as the distance between the explosive and the sensor D_T decreases. While the arrival time of the shock wave decreases as the distance D_T decreases, the three diagrams show that acquired pressure values increase as distance D_T decreases.

Focusing on the barrier's effect in the attenuation of the blast wave's peak pressure, a percentage reduction factor η_{exp} , representing the mitigation effect, can be derived from Figures 7 to 9. η_{exp} was evaluated using

$$\eta_{\text{exp}} = \frac{p_{\text{NB,exp}} - p_{\text{B,exp}}}{p_{\text{NB,exp}}} 100 \quad (4)$$

with $p_{\text{NB,exp}}$ being the peak pressure recorded by gauge S1 (or derived with the numerical model) and $p_{\text{B,exp}}$ being the peak pressure evaluated and recorded by gauge S6. As a general observation, the maximum reduction factor η_{exp} was obtained for the second test, with a distance between the charge and the barrier of 3 m. This result likely occurs because, in the first test ($D_B = 5 \text{ m}$), the blast wave had more space to grow and surmount the barrier without losing much energy. On the contrary, in the third test ($D_B = 0.5 \text{ m}$), the porosity of the barrier permits the blast wave to pass through

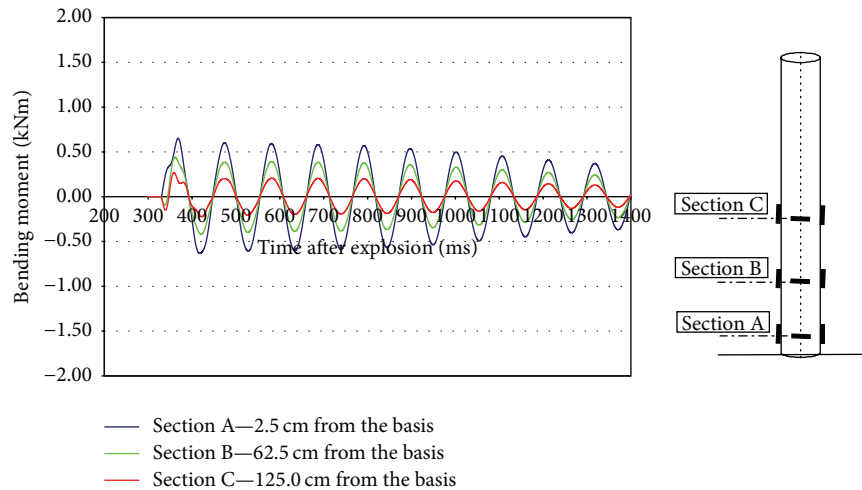


FIGURE 3: Bending histories at instrumented cross sections, first test.

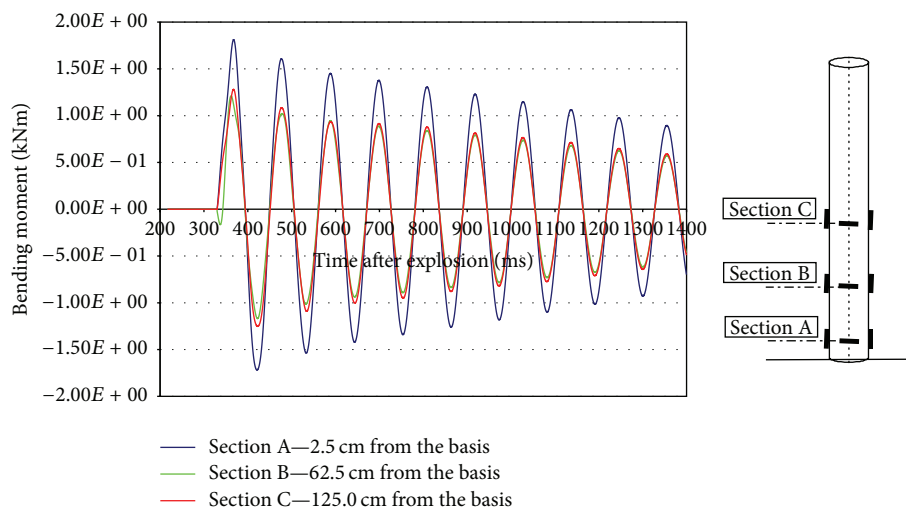


FIGURE 4: Bending histories at instrumented cross sections, second test.

the pipes more easily than in the previous tests. Additionally, in the third test, even if the barrier was seriously damaged, a reduction of the peak pressure was experienced; however it could be argued that the damage to the pipes in the third test could have limited the barrier mitigation effect on the blast wave; unfortunately, no strain gauge data are available for this test to provide an experimental confirmation of this explanation. During each blast test, no crater formation occurred, as desired for the reasons stated above.

3.2. Experimental-Theoretical Comparisons. The availability of these experimental data provides an opportunity to validate a simplified numerical procedure to predict the mitigation effects of a porous barrier. In cases of other potential targets requiring specific protection measures, such procedures could facilitate designing the optimum geometrical configuration of a porous barrier to limit the blast wave to an acceptable value.

Available literature addresses the interaction of shock waves with porous barriers, with many papers focusing on grid configuration [10–13] and stressing the importance of porosity in the fluid-dynamic interaction with shock waves. Other studies investigate the attenuation of different blast waves' impact on a porous barrier [14–16]. Different geometrical configurations of the porous surface were also analyzed, and the interaction with a target placed beyond the barrier was discussed [17–20]. However, differently from continuous barriers, no simple numerical model is available to predict the attenuation of a blast-induced shock wave due to a porous barrier. To this effect, Chapman et al. [21] conducted a blast test campaign, investigating the protection offered by a continuous rigid barrier against a blast-induced shock wave and proposed a simple formulation providing the peak pressure reduction factor. A similar study was conducted by Zhou and Hao [22], who, after an experimental campaign, proposed another numerical formulation.

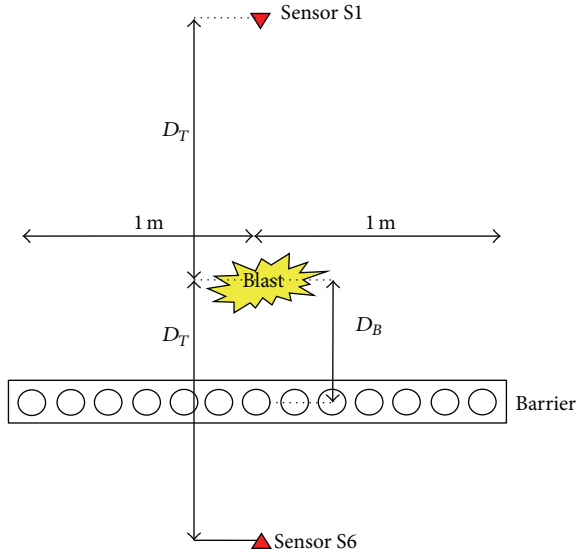


FIGURE 5: Pressure gauges setup.



FIGURE 6: Barrier specimen after the third test.

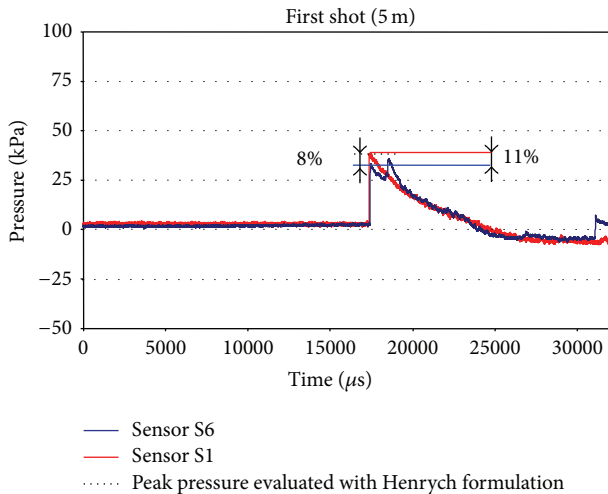


FIGURE 7: Acquired pressure histories: first blast.

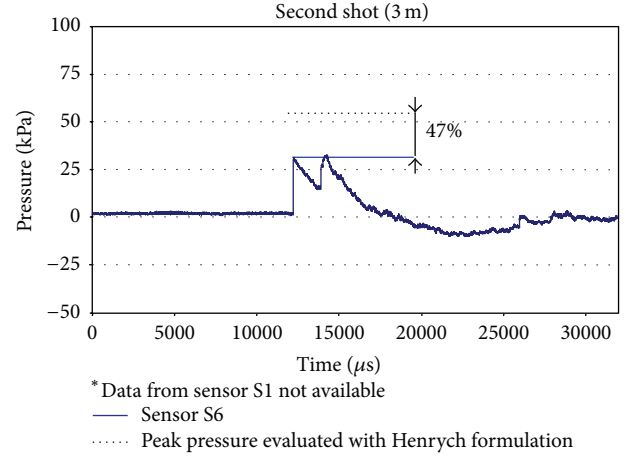


FIGURE 8: Acquired pressure histories: second blast.

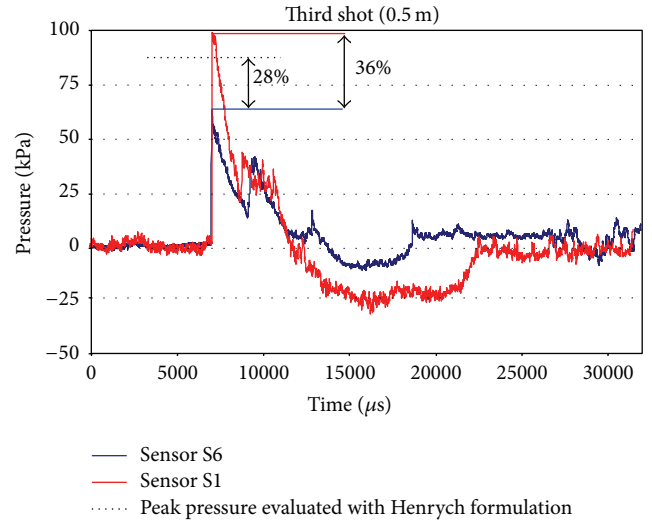


FIGURE 9: Acquired pressure histories: third blast.

Based on available literature, the main parameters governing the wave abatement phenomenon can be identified as follows:

- (i) Equivalent TNT charge weight W .
- (ii) Height of the charge H_C from the ground.
- (iii) Height of the barrier H_B .
- (iv) Height of the target H_T .
- (v) Distance between the charge and the barrier D_B .
- (vi) Distance between the charge and the target D_T .
- (vii) Porosity of the barrier r computed as the ratio of the voids area over the total frontal area of the barrier.

The proposed procedure does not take into account the material properties of the barrier. This assumption is consistent with the hypothesis used in the analysis of continuous barriers [20, 21]; that is, the barrier is rigid during the first part of the shock wave when the peak pressure is moving

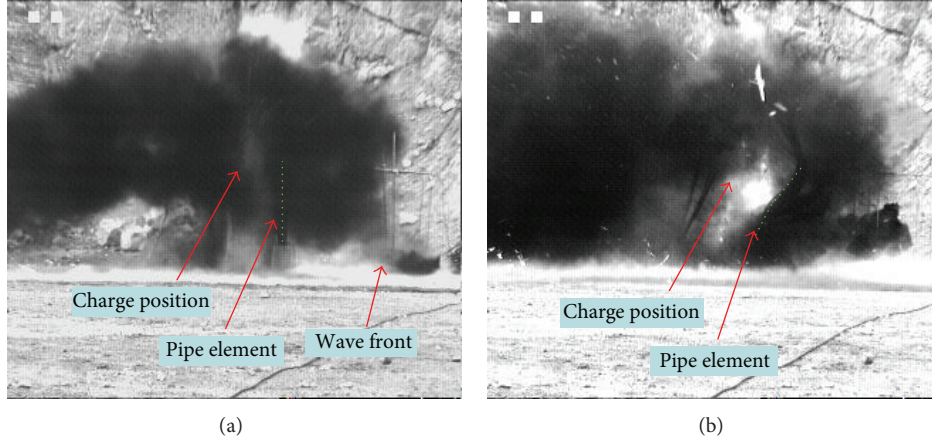


FIGURE 10: Acquired frames 2 ms (a) and 20 ms (b) after the explosion in the third shot.

throughout it. Since the barrier response is much slower than the shock wave time, as mentioned above, the barrier can be assumed to behave as a rigid body, even though significant damage could occur later, as happened in the third test. Recorded high-speed video confirmed that barrier failure and disaggregation started when the wave front had already overcome the barrier. Indeed, in Figure 10(a), representing the frame acquired 2 ms after the shot, it can be caught as a glimpse of the barrier, still in its undeformed position, whereas the blast wave front is already beyond the barrier, as it can be guessed looking at the raised dust on the ground. On the contrary, in Figure 10(b), representing the frame acquired 20 ms after the shot, the barrier in its deformed configuration can be clearly seen. However, this assumption may not be valid in the case of very weak barriers, not capable of withstanding the first part of the shock wave. For these cases, more sophisticated numerical models should be used. The procedure does not account for blast wavelength, but, for the case at hand, this is not detrimental since the ratio blast wavelength-to-barrier porosity is very large and a small change in this ratio would not affect the procedure effectiveness. In particular, the blast wavelength at the barrier was nearly equal to 2 m in each of the conducted tests. For this reason, the proposed procedure remains valid for blast scenarios in which the ratio blast wavelength-to-barrier porosity is similar to that occurring in the investigated cases. Moreover, the procedure does not account for boundary effects, occurring at the lateral sides of the barrier; actually lateral boundaries should not provide significant effects, since, in the test setup, the top boundary is as far as lateral boundaries from the detonation point and should provide similar interactions with blast waves. More sophisticated models could be developed to account for this effect and remain valid in a wider set of cases.

The proposed simplified procedure allows for evaluating the reduction factor of the peak pressure at a given distance from the charge, because of the interposition of a porous barrier. This procedure, summarized through the steps listed below, is presented in Appendix using the data from the first blast test.

Step 1. The peak pressure p_1 , corresponding to the barrier (Figure 11) at the distance D_B , due to the detonation of W is evaluated according to the numerical formula [9], since it is a typical free air phenomenon.

Step 2. The blast pressure p_1 is divided into two components, depending on the porosity of the barrier:

$$\begin{aligned} p_{1V} &= p_1 \cdot \rho, \\ p_{1S} &= p_1 \cdot (1 - \rho). \end{aligned} \quad (5)$$

The pressures p_{1V} and p_{1S} represent the impacting actions on the voids and the solid parts, respectively.

It is underlined that the porosity of the barrier is not affected by its width, since the barrier is assumed to work in an indefinite configuration, as the case when the target to be protected is fenced by a closed barrier.

Step 3. Working backwards with procedures from the numerical formula [9], two fictitious TNT charges are determined to be W_1 and W_2 , as the amounts able to generate the peak pressure values p_{NB1} and p_{NB2} at the distance D_B . The sum of the fictitious charges does not correspond to W , since pressure does not decrease according to a linear law.

Step 4. The peak pressure $p_{B,num}$ on the target is then evaluated as the sum of two contributions p_{B1} and p_{B2} :

$$p_{B,num} = p_{BV} + p_{BS}, \quad (6)$$

where p_{BV} is the peak pressure generated by the detonation of the fictitious charge W_1 in free air at the distance D_T evaluated according to the numerical model [9] and p_{BS} is the peak pressure generated by the detonation of the fictitious charge W_2 at the distance D_T behind a continuous barrier with the height of the porous barrier evaluated according to procedures found in the literature [20] or [21]. The peak pressure p_{BV} is evaluated accounting for eventual ground reflection, since the numerical model [9] does consider potential interaction with reflected Mach wave, generated below the triple point [4, 9].

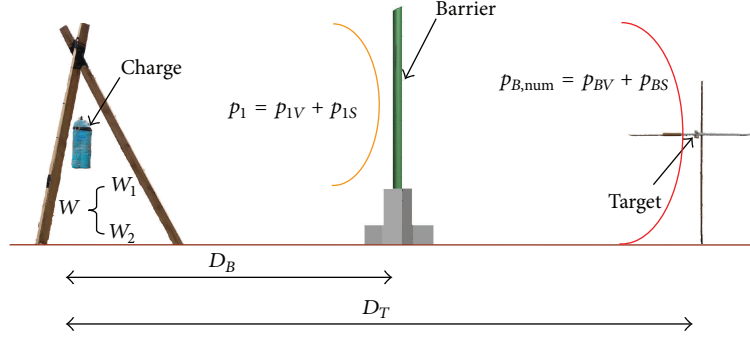


FIGURE 11: Geometrical representation of the proposed model.

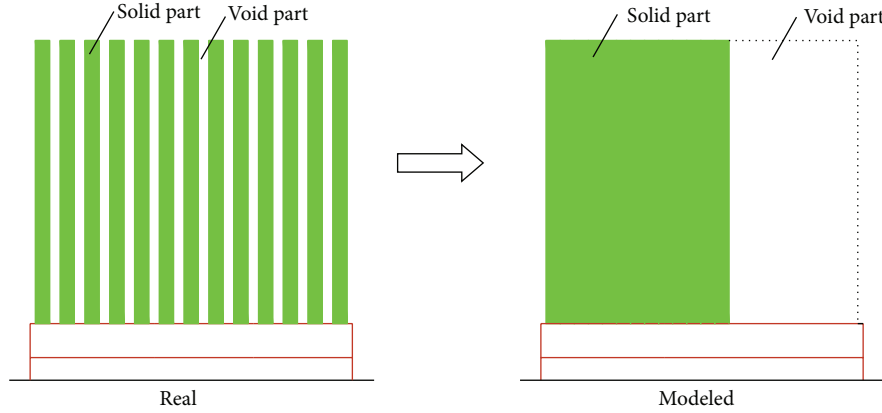


FIGURE 12: Modeling of the barrier.

Step 5. The reduction factor h_{num} is finally evaluated as

$$\eta_{\text{num}} = \frac{p_{\text{NB,num}} - p_{\text{B,num}}}{p_{\text{NB,num}}} \cdot 100, \quad (7)$$

where $p_{\text{NB,num}}$ is the pressure generated by the charge W in free air at the distance D_T evaluated according to the numerical model [9].

The proposed simplified model neglects the fluid-dynamic turbulence close to the pipes, assuming that the barrier could be equivalently reduced into a void and a solid part, as shown in Figure 12. It is underlined that this does not mean that the porous barrier is equivalent to smaller solid one; in fact the peak pressure reduction is mainly due to the diffraction of the shock wave passing through the pores. Hence, the scheme in Figure 12 is only used in the simplified numerical procedure. The described procedure was applied to the configuration used in the blast tests; in this case, the porosity ρ of the barrier, evaluated as the ratio of the voids over the spacing of the pipe elements, equals 0.43. In Step 4, the Zhou and Hao model [22] was used. Table 3 summarizes both experimental and numerical results in terms of free air peak pressure and behind the barrier. For the numerical peak pressure in free air, both Henrych formulations [9], $p_{\text{NB,exp}}$, and UFC (Unified Facilities Criteria) formulations [4], $p_{\text{NB,exp,UFC}}$, were used, revealing being in good agreement. Table 4 reports the reduction factors evaluated using

both experimental and numerical results. In particular, h_{exp} and h_{num} values are reported. A hybrid reduction factor h_{hyb} , evaluated using $p_{\text{B,num}}$ against $p_{\text{NB,exp}}$ values, is also presented, and its expression is as follows:

$$\eta_{\text{hyb}} = \frac{p_{\text{NB,exp}} - p_{\text{B,num}}}{p_{\text{NB,exp}}} \cdot 100. \quad (8)$$

It can be observed that free air peak pressure for the second test is not available. However, the numerical reduction factor was also derived, given the reliability of the free air numerical formulations used [9]. When experimental and analytical results are compared, good agreement is observed. In order to quantify completely the blast action, the total impulse (i.e., area below the pressure curve) was also considered. Values recorded during the tests are presented in Table 5. The total impulse reduction factors of 6% and 25% were experienced in first and third experiments, respectively, whereas, in second test unavailability of data from sensor S1 does not allow performing such comparison. As depicted in Figures 7–9, pressure histories are characterized by a non-monotonic decreasing trend, presenting more peak values, which increase total impulse; this can be attributed to both multiple ground reflections and wave diffractions occurring at the boundaries. It is underlined that the procedure applies to the first peak, which can be attributed to the direct blast wave. Nevertheless, the barrier provides a reduction of total impulse, which, as for peak pressures, is larger in the third

TABLE 3: Experimental and theoretical peak pressure.

	Pressure without the barrier			Pressure behind the barrier		
	Experimental	Theoretical	Theoretical	Experimental	Theoretical $p_{B,num}$ [kPa]	
	$p_{NB,exp}$ [kPa]	$p_{NB,num,UFC}$ [kPa]	$p_{NB,num}$ [kPa]	$p_{B,exp}$ [kPa]	Zhou and Hao model [22]	Chapman model [21]
1° shot (5 m)	37	39	36	33	33	24
2° shot (3 m)	Not available	61	58	31	31	28
3° shot (0.5 m)	98	94	88	63	57	64

TABLE 4: Experimental and theoretical peak pressure reduction factors.

	Experimental $h_{exp}(p_{B,exp} \text{ to } p_{NB,exp})$	Theoretical $h_{num}(p_{B,num} \text{ to } p_{NB,num})$	Hybrid $h_{hyb}(p_{B,num} \text{ to } p_{NB,exp})$
1° shot (5 m)	11%	8%	11%
2° shot (3 m)	Not available	47%	Not available
3° shot (0.5 m)	36%	35%	42%

TABLE 5: Experimental total impulse and relative reduction factors.

	Total impulse without the barrier [kPa.ms]	Total impulse behind the barrier [kPa.ms]	Reduction factor
1° shot (5 m)	99.9	93.9	6%
2° shot (3 m)	Not available	85.2	Not available
3° shot (0.5 m)	167.4	133.9	25%

test than in the first one. A theoretical evaluation of impulse at sensor S1 in the second test is not performed here since such evaluation would be quite uncertain due to the difficulty of predicting such spurious contributions. It is underlined that the numerical procedure used to predict the reduction factor does not depend on width of the barrier, which actually does not affect the reduction factor, whereas the height is accounted in the Zhou and Hao method [22] used in the procedure.

4. Conclusions

Results of a blast test campaign conducted on a blast protection porous barrier composed of GFRP pipe elements mounted on a precast, GFRP-reinforced concrete foundation were presented. The results show the capability of the barrier in disrupting the shock wave generated by an explosion and consequently reducing the induced loads on a target placed beyond the barrier.

As the distance between a detonating charge and the barrier decreased from the first to the third blast, the effectiveness in attenuating the blast wave, evaluated through the reduction factor h_{exp} , increased from the first to the second test and then decreased in the third test. This result probably occurs because of the two opposite mechanisms related to such distances. In general, as the charge gets closer

to the barrier, a smaller blast sphere impacts the barrier as less space is available for it to develop; consequently, the blast wave cannot surmount the barrier and dissipates a greater portion of its energy to pass beyond it. On the contrary, for small distances, the barrier porosity effect probably becomes more significant, and the blast wave transits more easily through the voids. In order to enrich the experimental research, additional test configurations will be numerically investigated. In fact, future work will include the development of a numerical model of the test, in order to conduct simplified fluid-dynamic analyses. The objective is to validate the proposed procedure for the evaluation of the blast wave reduction, focusing attention on the following issues:

- (i) Understanding the actual phenomenon evolution, discerning between the boundary effects, and the actual wave diffraction due to the porous barrier.
- (ii) Simulating additional test configurations with different charge weights and locations.

A simplified model predicting the reduction effect of the porous barrier on the peak pressure is proposed following the protocol used for a continuous barrier. The proposed model was validated using the experimental data obtained in the experimental campaign and showed good predictions. The model cannot capture complicated fluid-dynamic phenomena occurring close to the barrier; however, the discrepancies between numerical and experimental results appear to be below the uncertainty related to the evaluation of a blast-induced pressure.

Appendix

The proposed simplified model is here applied to the first test configuration. In such case, the input parameters assume the following values:

- (i) Equivalent TNT charge weight $W = 4$ kg.
- (ii) Height of the charge from the ground $H_C = 1.5$ m.
- (iii) Height of the barrier $H_B = 3.0$ m.
- (iv) Height of the target $H_T = 1.5$ m.
- (v) Distance between the charge and the barrier $D_B = 5.0$ m.
- (vi) Distance between the charge and the target $D_T = 9.0$ m.
- (vii) Porosity of the barrier $\rho = 0.43$.

Step 1. According to the numerical model [9], the free air pressure at the distance D_B can be evaluated as follows:

$$p_1 = \left(\frac{0.662}{\bar{R}} + \frac{4.05}{\bar{R}^2} + \frac{3.288}{\bar{R}^3} \right) k_R = 1.15 \text{ Kg/cm}^2 \quad (\text{A.1})$$

$$= 115 \text{ KPa}$$

having obtained the scaled distance \bar{R} as

$$\bar{R} = \frac{D_B}{W^{1/3}} = \frac{5.0}{\sqrt[3]{4}} = 3.14 \text{ m/Kg}^{1/3}, \quad (\text{A.2})$$

where k_R accounts for the ground reflected pressure and depends on the geometry and the intensity of the blast. It is set equal to 1.6, as suggested in the numerical model [9].

Step 2. Based on the porosity of the barrier,

$$p_{1V} = p_1 \cdot \rho = 115 \cdot 0.43 = 50 \text{ KPa}, \quad (\text{A.3})$$

$$p_{1S} = p_1 \cdot (1 - \rho) = 115 \cdot (1 - 0.43) = 65 \text{ KPa}.$$

Step 3. Working backwards from the procedure for free air pressure calculation, with few iterations, the fictitious TNT amounts W_1 and W_2 are obtained:

$$W_1 = 0.93 \text{ Kg}, \quad (\text{A.4})$$

$$W_2 = 1.47 \text{ Kg}.$$

Step 4. Amount W_1 is used to evaluate the free air pressure p_{BV} at the distance D_T :

$$\bar{R} = \frac{D}{W^{1/3}} = \frac{9}{\sqrt[3]{0.93}} = 9.22 \text{ m/Kg}^{1/3},$$

$$k_R = 1.6, \quad (\text{A.5})$$

$$p_{BV} = \left(\frac{0.662}{\bar{R}} + \frac{4.05}{\bar{R}^2} + \frac{3.288}{\bar{R}^3} \right) k_R = 0.19$$

$$= 19 \text{ KPa}.$$

The Zhou and Hao model [22] is used to evaluate the pressure p_{BS} generated by the charge W_2 at the distance D_T , behind a rigid continuous barrier. Consider

$$p_{BS} = p_{BSF} * A_p, \quad (\text{A.6})$$

where p_{BSF} represents the pressure generated by the same charge at the same distance without the barrier, here evaluated using the model from [9], and A_p is given as follows:

$$A_p = -0.1359 + \left(0.3272 + 0.1995 \lg \left(\frac{H_B}{D_T} \right) \right) \lg \bar{R} \quad (\text{A.7})$$

$$- 0.5626 \lg \left(\frac{H_B}{D_T} \right) + 0.4666 \left(\frac{D_B}{D_T} \right)$$

and therefore

$$p_{BSF} = 24 \text{ kPa},$$

$$A_p = 0.60, \quad (\text{A.8})$$

$$p_{BS} = p_{BSF} * A_p = 24 * 0.60 = 14 \text{ kPa}.$$

The reduced pressure is evaluated as shown below and is equal to 33 KPa:

$$p_{B,num} = p_{BV} + p_{BS}. \quad (\text{A.9})$$

Step 5. According to the numerical model [9], the free air pressure generated by W at the distance D_T without the barrier can be evaluated as

$$p_{NB,num} = \left(\frac{0.662}{\bar{R}} + \frac{4.05}{\bar{R}^2} + \frac{3.288}{\bar{R}^3} \right) k_R \quad (\text{A.10})$$

$$= 0.36 \text{ Kg/cm}^2 = 36 \text{ KPa}$$

since

$$\bar{R} = \frac{D_T}{W^{1/3}} = \frac{9}{\sqrt[3]{4}} = 5.67 \text{ m/Kg}^{1/3} \quad (\text{A.11})$$

and, in this case,

$$k_R = 1.4 \quad (\text{A.12})$$

and then the numerical reduction factor h_{num} can be evaluated as given below and is equal to 8 percent:

$$\eta_{num} = \frac{p_{NB,num} - p_{B,num}}{p_{NB,num}} \cdot 100. \quad (\text{A.13})$$

Conflict of Interests

The authors declare that there is no conflict of interests regarding the publication of this paper.

Acknowledgment

The authors gratefully thank European Commission Directorate General Justice, Freedom and Security for the financial support through EPCIP 2006.

References

- [1] D. Asprone, D. Assante, A. Chiariello et al., "Case study: assessment of the electromagnetic disturbance of a glass fiber reinforced composite fencing structure," *ASCE Journal of Composites For Construction*, vol. 14, pp. 629–635, 2010.
- [2] W. G. Corley, M. A. Sozen, C. H. Thornton, and P. F. Mlakar, "The Oklahoma City bombing: improving building performance through multi-hazard mitigation," Tech. Rep. FEMA-277, Mitigation Directorate, U.S. Government Printing Office, Washington, DC, USA, 1996.
- [3] L. J. Malvar, J. E. Crawford, and K. B. Morrill, "Use of composites to resist blast," *Journal of Composites for Construction*, vol. 11, no. 6, pp. 601–610, 2007.
- [4] US Departments of the Army-the Navy and the Air Force, *UFC 3-340-02 Structures to Resist the Effects of Accidental Explosions*, US Departments of the Army, the Navy and the Air Force, 2008.
- [5] D. Asprone, A. Nanni, H. Salem, and H. Tagel-Din, "Applied element method analysis of porous GFRP barrier subjected to blast," *Advances in Structural Engineering*, vol. 13, no. 1, pp. 153–169, 2010.

- [6] J. G. Teng, J. F. Chen, S. T. Smith, and L. Lam, *FRP: Strengthened RC Structures*, John Wiley & Sons, 2002.
- [7] D. Asprone, E. Cadoni, A. Prota, and G. Manfredi, "Strain-rate sensitivity of a pultruded E-glass/polyester composite," *Journal of Composites for Construction*, vol. 13, no. 6, pp. 558–564, 2009.
- [8] ASTM, "Standard test method for tensile properties of polymer matrix composite materials," ASTM D 3039/D 3039M, 2003.
- [9] J. Henrych, *The Dynamics of Explosion and Its Use*, Elsevier, 1979.
- [10] A. Britan, O. Igra, G. Ben-Dor, and H. Shapiro, "Shock wave attenuation by grids and orifice plates," *Shock Waves*, vol. 16, no. 1, pp. 1–15, 2006.
- [11] D. S. Dosanjh, "Interaction of grids with traveling shock waves," NACA TN 3680, 1956.
- [12] W. J. Franks, "Interaction of a shock wave with a wire screen," UTIA TN 13, 1957.
- [13] B. E. Gelfand, S. P. Medvedev, A. N. Polenov, and S. M. Frolov, "Interaction of non-stationary pressure waves with perforated partitions," *Archivum Combustionis*, vol. 7, pp. 215–222, 1987.
- [14] O. Igra, X. Wu, J. Falcovitz, T. Meguro, K. Takayama, and W. Heilig, "Experimental and theoretical study of shock wave propagation through double-bend ducts," *Journal of Fluid Mechanics*, vol. 437, pp. 255–282, 2001.
- [15] O. Igra, X. Wu, G. Q. Hu, and J. Falcovitz, "Shock wave propagation into a dust-gas suspension inside a double-bend conduit," *Journal of Fluids Engineering*, vol. 124, no. 2, pp. 483–491, 2002.
- [16] A. Sasoh, K. Matsuoka, K. Nakashio et al., "Attenuation of weak shock waves along pseudo-perforated walls," *Shock Waves*, vol. 8, no. 3, pp. 149–159, 1998.
- [17] B. W. Skews and K. Takayama, "Flow through a perforated surface due to shock-wave impact," *Journal of Fluid Mechanics*, vol. 314, pp. 27–52, 1996.
- [18] G. J. Ball and R. A. East, "Shock and blast attenuation by aqueous foam barriers: influences of barrier geometry," *Shock Waves*, vol. 9, no. 1, pp. 37–47, 1999.
- [19] B. W. Skews, M. D. Atkins, and M. W. Seitz, "The impact of a shock wave on porous compressible foams," *Journal of Fluid Mechanics*, vol. 253, no. 1, pp. 245–265, 1993.
- [20] H. Naiman and D. D. Knight, "The effect of porosity on shock interaction with a rigid, porous barrier," *Shock Waves*, vol. 16, no. 4-5, pp. 321–337, 2007.
- [21] T. C. Chapman, T. A. Rose, and P. D. Smith, "Reflected blast wave resultants behind cantilever walls: a new prediction technique," *International Journal of Impact Engineering*, vol. 16, no. 3, pp. 397–403, 1995.
- [22] X. Q. Zhou and H. Hao, "Prediction of airblast loads on structures behind a protective barrier," *International Journal of Impact Engineering*, vol. 35, no. 5, pp. 363–375, 2008.

Research Article

Bond Characteristics of Macro Polypropylene Fiber in Cementitious Composites Containing Nanosilica and Styrene Butadiene Latex Polymer

Jae-Woong Han,¹ Ji-Hong Jeon,² and Chan-Gi Park³

¹Department of Bio-Industry Mechanical Engineering, Kongju National University, Yesan 70-340, Republic of Korea

²Department of Environmental Engineering, Andong National University, Andong 74-760, Republic of Korea

³Department of Rural Construction Engineering, Kongju National University, Yesan 70-340, Republic of Korea

Correspondence should be addressed to Chan-Gi Park; cgpark@kongju.ac.kr

Received 16 April 2015; Revised 27 July 2015; Accepted 4 August 2015

Academic Editor: Osman Gencel

Copyright © 2015 Jae-Woong Han et al. This is an open access article distributed under the Creative Commons Attribution License, which permits unrestricted use, distribution, and reproduction in any medium, provided the original work is properly cited.

This study evaluated the bond properties of polypropylene (PP) fiber in plain cementitious composites (PCCs) and styrene butadiene latex polymer cementitious composites (LCCs) at different nanosilica contents. The bond tests were evaluated according to JCI SF-8, in which the contents of nanosilica in the cement were 0, 2, 4, 6, 8, and 10 wt%, based on cement weight. The addition of nanosilica significantly affected the bond properties between macro PP fiber and cementitious composites. For PCCs, the addition of 0–2 wt% nanosilica enhanced bond strength and interface toughness, whereas the addition of 4 wt% or more reduced bond strength and interface toughness. The bond strength and interfacial toughness of LCCs also increased with the addition of up to 6% nanosilica. The analysis of the relative bond strength showed that the addition of nanosilica affects the bond properties of both PCC and LCC. This result was confirmed via microstructural analysis of the macro PP fiber surface after the bond tests, which revealed an increase in scratches due to frictional forces and fiber tearing.

1. Introduction

Recently, a wide variety of high-performance and high-durability cementitious composites have been developed by improving structural functionality through the use of admixture materials such as nanomaterials [1–4]. Nanomaterials are currently attracting intense attention for their broad applicability to cementitious composites. Nanomaterials can produce tougher interfaces between aggregates and cement particles [5–8]. Such properties are advantageous for improving mechanical properties and long-term durability in cementitious composites [1–8]. Despite these advantages, introducing nanomaterials may increase the brittleness of composites; improved strength can lead to more cracking, especially if the particle size of the admixture is much smaller than that of the cement [1–4]. To resolve this problem, reinforcing fibers can be added [2, 9–15].

The ductile fracture of reinforcing fibers results from controlling the generation and growth of cracks in cementitious composites [9, 10, 12–15]. The degree of increase in

energy-absorbing capacity attributable to fiber reinforcement of cementitious composites is determined by the bonding mechanism between the fibers and the cementitious composites, including fiber bridging, fiber debonding, fiber pullout, and fiber fracture when cracks occur [9, 12–15]. Bond characteristics are influenced by a variety of factors, such as the morphological shape and length of the reinforcing fiber, the surface properties, the interface between the cement composite and the reinforcing fiber, and the strength of the cement composite [9, 10, 12–15].

Nanomaterials consist of very small particles. As the material fineness increases, the increase in surface area leads to an increase in moisture absorption, which decreases the workability of the material [1–4]. More water can be added to ensure sufficient workability, but adding water also increases the risk of crack formation during drying. Mechanical properties, such as strength and long-term durability, may also be negatively affected by the addition of water. Therefore, in general, it is important to increase the workability without increasing the unit water content. Latex polymer is

TABLE 1: Properties of latex polymer.

Solids content (%)	Styrene content (%)	Butadiene content (%)	pH	Density (g/mm ³)	Surface tension (dyne/cm)	Particle size (Å)	Viscosity (cps)
49	34 ± 1.5	66 ± 1.5	11.0	1.02	30.57	1700	42

TABLE 2: Physical properties of cement.

Surface area (cm ² /g)	Density (g/mm ³)	Stability (%)	Setting time		Compressive strength (MPa)		
			Initial (min)	Final (min)	3 days	7 days	28 days
3,200	3.15	0.02	220	400	20	30	38

a semitransparent, milky liquid containing organic polymer colloidal microparticles (0.5–5.0 μm diameter) [16–19]. The particles, coated by surfactant, are dispersed in the solute, and the surfactant enables the formation of single-polymer cells via chain polymerization of the monomers. The surfactant delays solidification, stabilizes the particles, and increases the workability at a low water/cement ratio, while the latex polymer particles form a film during hydration [16–24]. Therefore, latex polymer may be used to resolve the problem of decreased workability of nanocementitious composites. The decrease in the amount of water used to secure the workability of nanocementitious composites can improve their mechanical properties and durability. In particular, in fiber-reinforced cementitious composites, the bonding performance of the reinforcing fibers can be improved by strengthening the interface between the fibers and cementitious composite.

This study evaluated the bond properties of macro polypropylene (macro PP) fibers in plain cementitious composites (PCCs) and styrene butadiene latex polymer cementitious composites (LCCs) containing varying amounts of nanosilica. Styrene butadiene latex polymer (latex polymer) replaced some (15 wt%) of the binder, and 0–10 wt% of the binder was replaced with nanosilica.

2. Experimental Procedure

2.1. Materials. Latex polymer was obtained from Jungang Polytech, Korea. Table 1 lists its properties. Tables 2 and 3 list the properties of ASTM Type 1 cement and nanosilica, respectively. Macro PP fiber is a hydrophobic material widely used for cementitious composites. The fibers used in this study were straight, smooth monofilaments made of noncorrosive PP. Table 4 lists their properties.

2.2. Mix Proportions and Mixing Procedure. Table 5 lists the mix proportions of nanosilica used in this study to evaluate the bond properties between LCCs and macro PP fibers. The nanosilica contents ranged from 0 to 10% of the binder weight; latex polymer was used at 15% of the binder weight, and the water-to-binder ratio was 0.47. The latex polymer used in this study was dispersion of 49 wt% solid polymer particles with the balance as water and surfactants. The “total latex polymer addition” noted in Table 5 refers to the amount of latex polymer used, that is, the combined solid and liquid contents. Latex polymer solid polymer particles were added at

TABLE 3: Properties of nanosilica.

Mean diameter (nm)	Surface area (cm ² /g)	SiO ₂ (%)
10	5,000,000	>99.8

TABLE 4: Properties of macro polypropylene fiber.

Property	Polypropylene fiber
Elastic modulus (GPa)	4.7
Density (g/mm ³)	0.91
Fiber length (mm)	30
Fiber diameter (mm)	1
Tensile strength (MPa)	470
Surface	Hydrophobic

a weight ratio of latex polymer to binder of 15% (i.e., 90.9 kg = 606 kg \times 15/100 (%)). The amount of water contained was 94.61 kg/m³, and the added mixing water was 190.39 kg/m³. However, the total amount of water was maintained at a constant level of 285 kg/m³, and the water/binder ratio for the entire mixing process was maintained at a constant level of 0.47. For the process of material mixing, cement, nanomaterials, and fine aggregates were added and dry-blended with a mixer for 30 minutes. Generally, mixing water was added over a period of 2 minutes and 30 seconds. Since the decrease of fluidity caused by the addition of nanomaterials makes thorough mixing difficult, an extra 5-minute blending time was used after adding all of the materials, to ensure sufficient blending of the mixture.

2.3. Slump Test. The slump test was carried out according to the ASTM C 143 standard to investigate how the added nanosilica affected the workability of the composite. Typically, when coarse aggregates are not used, the standard test method for flow of hydraulic cement mortar, ASTM C 143, is applied to measure composite workability. However, because latex polymer was used in this study, ASTM C 1437 could not be applied; the flowability was too high if nanosilica was not used. Therefore, the slump test was conducted according to ASTM C 143 instead.

2.4. Flexural Test. Flexural tests were conducted in accordance with the KS L ISO 679 standard [25]. Test mortar prism specimens measuring 40 \times 40 \times 160 mm were cured in water

TABLE 5: Mix proportions.

Number of mix	W/B* (%)	Cement	Water		Unit weight (kg/m ³)		Latex polymer		
			Total water**	Water	Fine aggregate	Nanosilica	Total	Solid	Water
Number 1	47	606.00				0.00			
Number 2		593.88				12.12			
Number 3		581.76	285	285		24.24	0.00	0.00	0.00
Number 4		569.64				36.36			
Number 5		557.52				48.48			
Number 6		545.40			1363	60.60			
Number 7		606.00				0.00			
Number 8		593.88				12.12			
Number 9		581.76	285	188.59		24.24	185.51	90.90	94.61
Number 10		569.64				36.36			
Number 11		557.52				48.48			
Number 12		545.40				60.60			

*Total water/(binder = cement + nanosilica).

**Water + water from the latex polymer.

at $23 \pm 2^\circ \text{C}$. Each test was performed on six specimens that had been cured for 28 days. However, when nanosilica was added, it became difficult to cast and compact the test specimens due to increased viscosity and reduced workability. Thus, the mixing time was increased to 5 minutes after all materials were added, and compaction was carried out using vibrating table and rods. Each test was performed on six specimens that had been cured for 28 days.

2.5. Bond Test. Bond tests were conducted in accordance with the Japan Concrete Institute (JCI) SF-8 standard for fiber-reinforced concrete [26]. Bond tests were performed using a 50 kN universal testing machine at a displacement rate of 0.5 mm/min in the displacement-controlled mode. Figure 1 presents a schematic diagram of the preparation of specimens.

Tests were based on the assumption that the bond strength was distributed equally over the embedded length of the macroscale synthetic fiber. Therefore, (1) is not representative of the local bond stresses that occur over differing bond lengths. The pullout strength of the macroscale synthetic fiber was calculated according to [9, 20–22]

$$\tau_{\max} = \frac{P_{\max}}{\pi DL}, \quad (1)$$

where τ_{\max} is the maximum pullout strength, P_{\max} is the maximum pullout load, D is the fiber diameter, and L is the embedded fiber length.

Interface toughness is critical for enhancing the ductility of reinforcing fibers in cementitious composites. This property is usually defined as the mechanical energy consumed during fiber pullout and can be determined by integrating the area under the pullout curve. The displacement required to measure the interface toughness in the JCI SF 8 standard is 2.5 mm. The results of the pullout performance tests are presented as the mean values for six specimens.

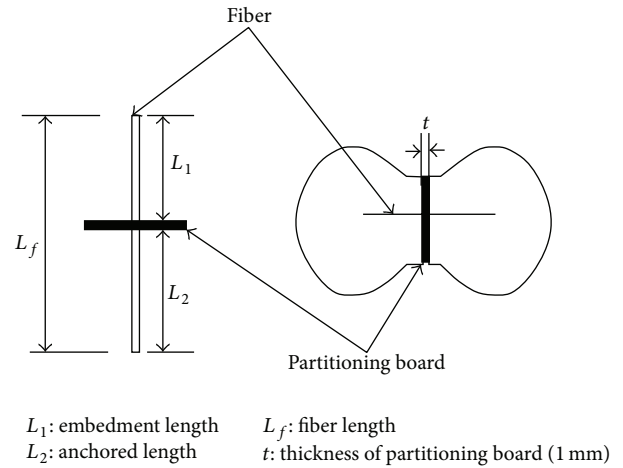


FIGURE 1: Arrangement of the partitioning board and fiber and setting in the mold.

2.6. Microstructure Analysis. To evaluate how the addition of nanosilica and latex polymer affected the behavior of the adhesion interface between the macro PP fiber and the cement matrix, the pullout resistance mechanism was analyzed using scanning electron microscopy (SEM) analyses of the macro PP fiber surface after the pullout test. After completing the pullout test, SEM images (100x magnification) of the fiber pulled out of the cement matrix were obtained, and the influence of the added nanosilica and latex polymer on the friction resistance during the fiber pullout was analyzed based on the scratches observed on the fiber surface.

3. Results and Discussion

3.1. Slump. Figure 2 presents the results of slump testing of PCCs and LCCs as a function of added nanosilica. The slump value for PCCs decreased below 50 mm when more than 2 wt% of nanosilica was added, and was 0 mm when 4 wt%

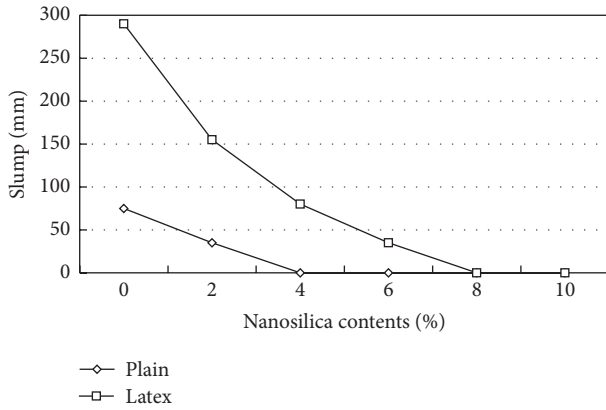


FIGURE 2: Slump value of PCC and LCC with nanosilica contents.

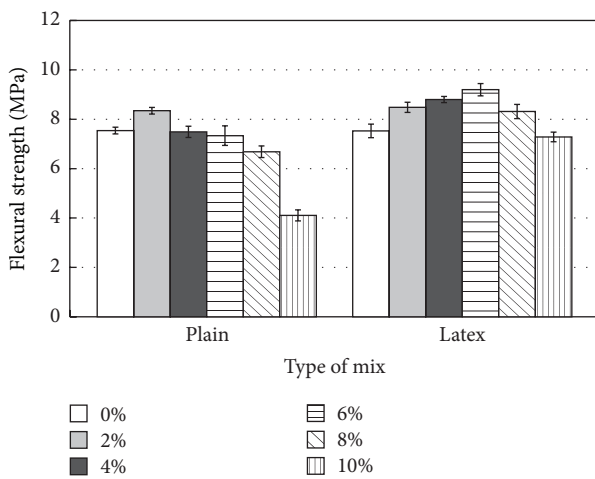
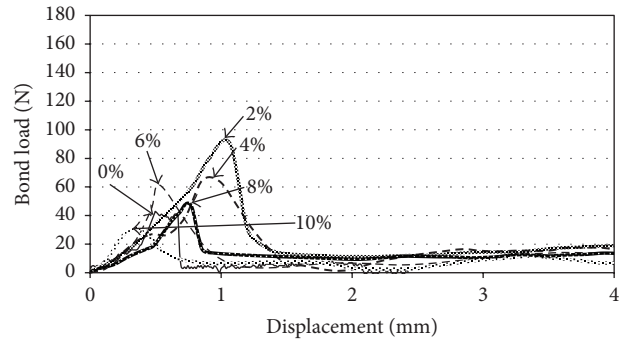


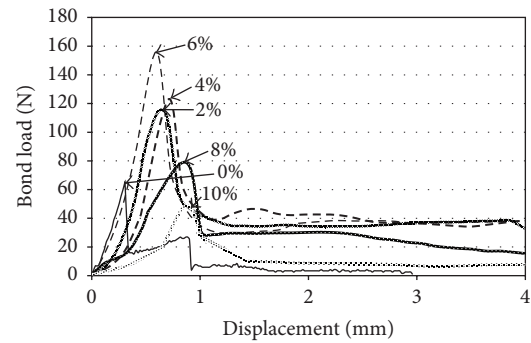
FIGURE 3: Flexural strength of PCC and LCC with nanosilica contents.

was used. The slump value for LCCs decreased strongly with increasing nanosilica content and was 0 mm at weightings of 8 wt% or more. Therefore, latex polymer is effective at increasing the workability of cementitious composites [16–24]. The latex polymer particles, coated with surfactant, are dispersed in the solute, and the surfactant enables the formation of single-polymer cells via chain polymerization of the monomers. The surfactant delays solidification, stabilizes the particles, and increases the workability at a low water/cement ratio [16–24].

3.2. Flexural Strength. Figure 3 presents the results for flexural strength testing of PCCs and LCCs containing various nanosilica contents. The flexural strength of LCCs increased in the presence of nanosilica at contents up to 6 wt% and decreased at contents of 8 wt% or more. However, in the case of PCCs, flexural strength increased at contents up to 2 wt% of nanosilica but decreased at levels greater than 4 wt%. Initially, the nanosilica particles filled the voids in the cementitious composites [5–8], thereby increasing the flexural strength. However, as the addition rate increased, so did the specific surface area and absorption of water [1–4]. This increase in water absorption deteriorated the workability and hindered



(a) PCC



(b) LCC

FIGURE 4: Pullout behavior of macro PP fiber in PCC and LCC with nanosilica contents.

material mixing, casting, and compacting of test specimens. Air voids formed in the test specimens and decreased the flexural strength. Latex polymer was effective at improving the workability of cementitious composites [16–24], so LCCs exhibited better workability at the same addition rate of nanosilica compared to PCCs. Additionally, latex polymer formed a film around the aggregate and improved flexural strength [18, 19, 23].

3.3. Bond Behavior. Figure 4 presents the bond load versus displacement curves of the macro PP fiber at different nanosilica contents. The bonding behavior of the reinforcing fibers in LCCs and PCCs can be classified into precracked zones and debonded zones [9, 10, 13–15, 27]: the former exhibits linear elastic behavior, while the latter displays different behaviors depending on the frictional forces and the rate of crack growth at the interface between the reinforcing fibers and the cementitious composites [9, 10, 13–15]. In this study, linear elastic behavior was observed in the precracked zone, and pullout behavior was observed in the debonded zone after cracks occurred and the bond load was reduced. In the case of LCCs, the peak bond load in the precracked zone increased up to 6 wt% of nanosilica but decreased at levels greater than 8 wt%. The behavior in the debonded zone exhibited a similar pattern: up to 6 wt% of nanosilica, the displacement at the same bond load increased, and the bond load at the same displacement increased. However, at nanosilica contents of 8 wt% or more, the displacement at the same bond load decreased, and the bond load at the same displacement decreased. For PCCs, the peak bond load in

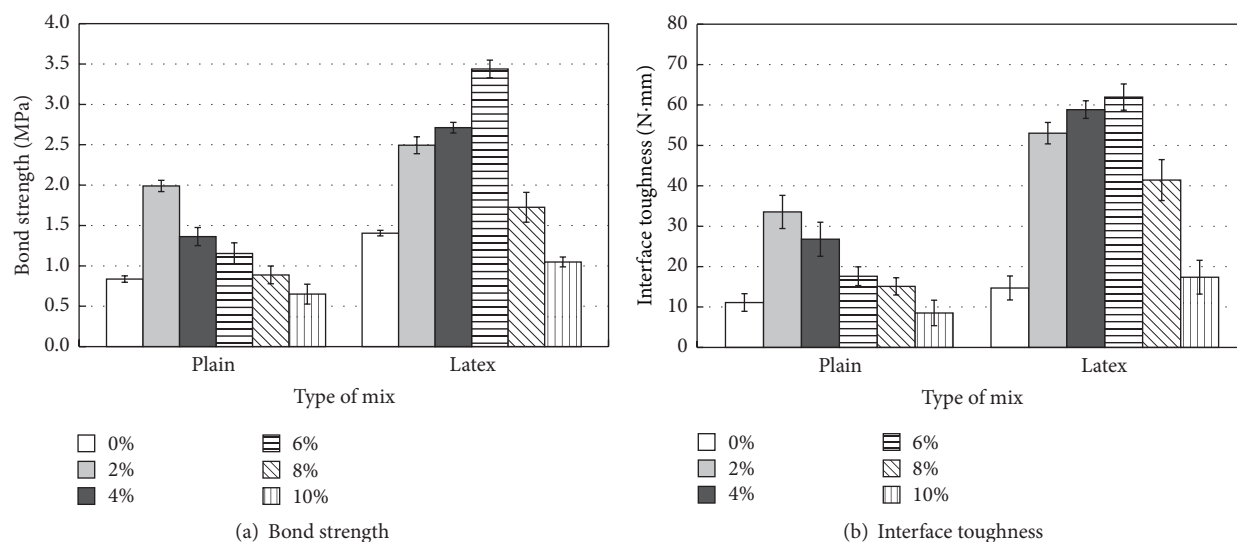


FIGURE 5: Bond strength and interface toughness of macro PP fiber in PCC and LCC with nanosilica contents.

the precracked zone increased up to 2 wt% of nanosilica but decreased at levels greater than 4 wt%. The behavior in the debonded zone showed a similar tendency. This result can be attributed to two factors. First, given the much smaller particle size of the nanosilica compared to that of the cement, the nanosilica particles filled the voids at the interface of the macro PP fiber and the cementitious composites, thereby strengthening the interface so that the peak bond load increased. Second, increased frictional forces at the interface after the occurrence of cracks suppressed pullout of the macro PP fibers. However, the more nanosilica was added, the more mixing water was absorbed because of the increased specific surface area, which resulted in higher cement viscosity and decreased workability [1–4]. The higher viscosity hindered casting and compacting of the cementitious composites and tended to weaken the bonding between the cementitious composites and macro PP fibers. By contrast, the superior workability of LCCs enabled easier casting and compacting of test specimens and improved bonding in LCCs compared to PCCs.

3.4. Bond Strength and Interface Toughness. Figure 5 shows the bond strengths and interface toughness values for different nanosilica contents. For LCCs, the bond strengths in the composites at nanosilica contents from 0 to 10 wt%, in 2 wt% increments, were 1.41, 2.49, 2.71, 3.43, 1.72, and 1.04 MPa, respectively. The bond strength increased with nanosilica contents up to 6 wt% and then decreased for contents greater than 8 wt%. In the case of PCCs, at the same nanosilica contents in 2 wt% increments from 0 to 10 wt%, the values were 0.84, 1.99, 1.36, 1.15, 0.88, and 0.65 MPa, respectively. In this case, the bond strength increased for nanosilica contents of up to 2 wt% and then decreased for contents greater than 4 wt%. For LCCs, the interface toughness values for nanosilica contents from 0 to 10 wt%, in 2 wt% increments, were 14.72, 53.03, 58.56, 61.96, 41.42, and 17.38 N-mm, respectively. As with bond behavior and bond strength, the interface toughness of the LCCs increased

for nanosilica contents of up to 6 wt% and then decreased when the content was 8 wt% or greater. For PCCs, the corresponding interface toughness values were 11.12, 33.53, 26.27, 17.63, 15.11, and 8.54 N-mm for nanosilica contents in 2 wt% increments from 0 to 10 wt%, respectively. Thus, interface toughness in PCCs increased when the nanosilica content increased from 0 to 2 wt% and then decreased when the content was 4 wt% or more. These trends can be attributed to decreasing cement workability caused by greater absorption of mixing water with increasing nanosilica contents. This decreased workability hindered compaction of test specimens and introduced voids at the bond interface between the macro PP fiber and the cementitious composites, thereby resulting in decreased bond strength and interface toughness. However, the addition of latex polymer increased the workability of cementitious composites and facilitated compaction of test specimens [16–24]. The latex polymer also formed a film that improved adhesion between materials and improved the bond strength and toughness at the same nanosilica content compared with PCCs.

3.5. Relationship between Flexural Strength and Bond Performance. Figure 6 presents the correlation between flexural strength and bond performance at different nanosilica contents. The flexural strength, bond strength, and interface toughness behaviors at different nanosilica contents were quite similar. For LCCs, the flexural strength, bond strength, and interface toughness increased with increasing nanosilica content up to 6 wt% and then decreased at contents of 8 wt% or more. For PCCs, the flexural strength, bond strength, and interface toughness increased with increasing nanosilica content up to 2 wt% but decreased at nanosilica contents of 4 wt% or more. These results indicate that strength and bond characteristics are closely related.

3.6. Relative Bond Strength. The relative bond properties were analyzed to evaluate the effects of nanosilica on bond

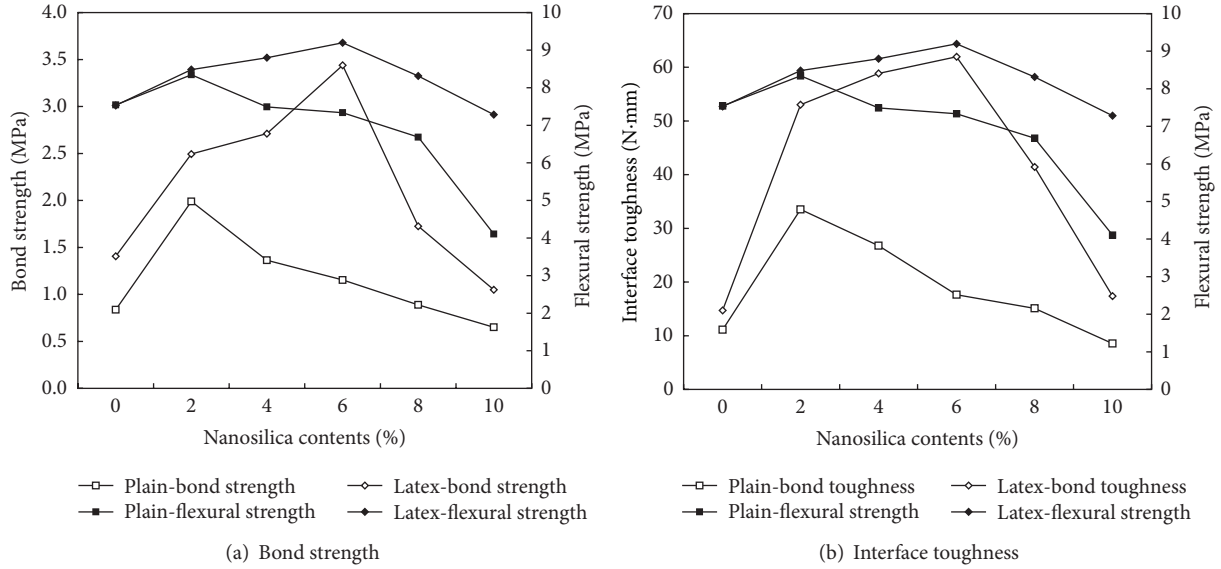


FIGURE 6: Relationship between flexural strength and bond performance.

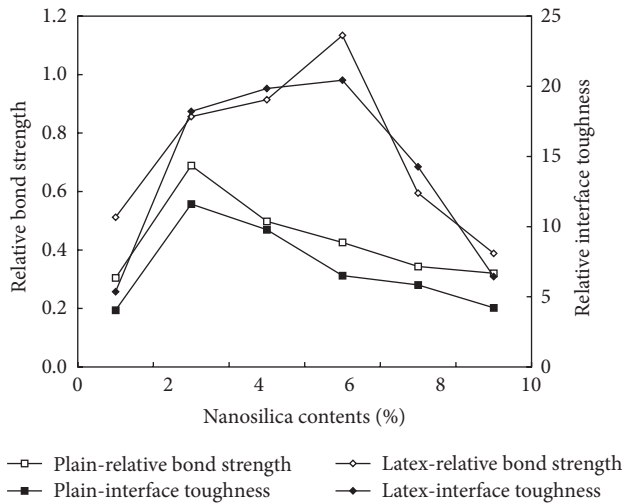


FIGURE 7: Relative bond strength of macro PP fiber in PCC and LCC with nanosilica contents.

properties. The relative bond properties were determined using [27]

$$R_b = \frac{\tau_{\max}}{\sqrt[2]{f_T}}, \quad (2)$$

where R_b is the relative bond strength, τ_{\max} is the maximum bond strength, and f_T is the flexural strength.

Figure 7 presents the results for relative bond strength and relative interface toughness. Both bond strength and interface toughness in the composites were influenced by the nanosilica content, regardless of flexural strength. In the case of PCCs, the relative bond strengths were 0.30, 0.69, 0.49, 0.42, 0.34, and 0.32 for nanosilica contents of 0, 2, 4, 6, 8, and 10 wt%, respectively. In the case of LCCs, the relative bond strengths were 0.51, 0.85, 0.91, 1.13, 0.59,

and 0.39, respectively, for the same nanosilica contents. For LCCs, the relative interface toughness values were 5.37, 18.21, 19.84, 20.43, 14.27, and 6.44 for nanosilica contents of 0, 2, 4, 6, 8, and 10 wt%, respectively. For PCCs, the interface toughness values at the same nanosilica contents were 4.05, 11.61, 9.78, 6.51, 5.84, and 4.21, respectively. The relative bond strength and interface toughness exhibited the same tendency as bond strength with increasing nanosilica content. Thus, the nanosilica content significantly influenced the bond strength and interface toughness of macro PP fiber in PCCs and LCCs.

3.7. Microstructural Analysis. After the bond tests, the surface morphology of the macro PP fiber was studied using SEM. Figure 8 shows images of the fiber surface after the bond tests for PCCs to which nanosilica was added. Figures 8(a)–8(f) correspond to fibers after bond tests at nanosilica contents of 0, 2, 4, 6, 8, and 10 wt%, respectively. Figure 8(a) shows the scratching and tearing of fibers on the surface at both ends of the fibers. In Figure 8(b), the scratching and tearing increased, and the tearing extended to the central part of the fibers; a considerable amount of nanosilica powder is seen on the surface. Figure 8(c) shows that the surface of the fiber caved in as a result of the tearing, due to the friction force on the fibers. In Figure 8(d), nanosilica powder is seen on the surface along with tearing of the fiber. In Figure 8(e), there is less tearing of the surface and some nanosilica powder. In Figure 8(f), slight tearing of the surface and only a small amount of nanosilica powder on the surface were evident.

Figure 9 presents SEM images of the fiber surface after bond tests of LCCs to which nanosilica was added. Figure 9(a) shows evidence of scratching on the surface. Figure 9(b) shows the remaining nanosilica powder and tearing of the surface. Figure 9(c) shows tearing of the fibers, although the tearing appeared to be partial. Figure 9(d) shows tearing of the fiber and surface scratching over a significant portion of the fiber surface. Figure 9(e) shows that although

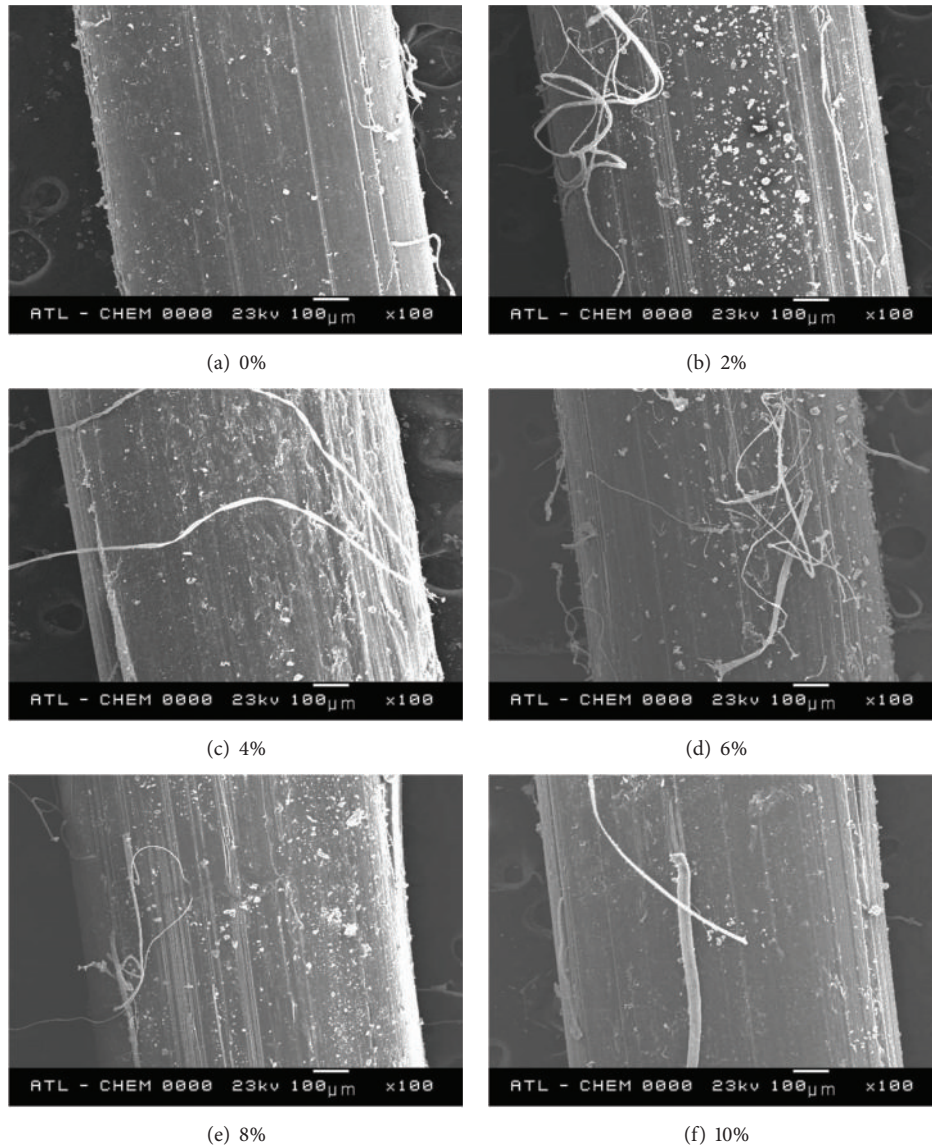


FIGURE 8: SEM investigation of macro PP fiber surface in PCC with nanosilica contents.

tearing and scratching appeared over the entire fiber surface, this phenomenon tended to decrease after 6% nanosilica addition. Figure 9(f) shows the tearing and scratching of the fiber over a portion of the fiber surface.

Scratching of the fiber surface and tearing of the fiber occurred for PCCs and LCCs during pullout of macro PP fibers. Pullout resistance of the fibers improved as frictional forces increased, and greater pullout resistance improved interface toughness. Scratches generated by frictional forces at the fiber surface caused fiber tearing and exhibited a trend similar to that observed for interface toughness.

4. Conclusions

This study evaluated the bond behavior of macro PP fiber in PCCs and LCCs at different nanosilica contents. Dog-bone specimens were used for the bond tests according to the JCI

SF-8 standard. The microstructures of the fiber surfaces after the bond tests were studied to investigate the bonding mechanisms between the fibers and the cementitious composites containing nanosilica. The results are summarized as follows:

- (i) Slump tests indicated that, for both PCCs and LCCs, at higher nanosilica contents, the viscosity increased and the slump value decreased. However, at the same nanosilica content, the slump value of LCCs was greater than that of PCCs, because latex polymer increased the workability of cementitious composites.
- (ii) Bond strength and interface toughness tests revealed that both properties increased for nanosilica contents of up to 2 wt% but then decreased at contents greater than 4 wt%. Bond strength and interface toughness of macro PP fiber and LCCs increased at nanosilica contents up to 6 wt%. However, the bond strength and interface toughness decreased for contents of

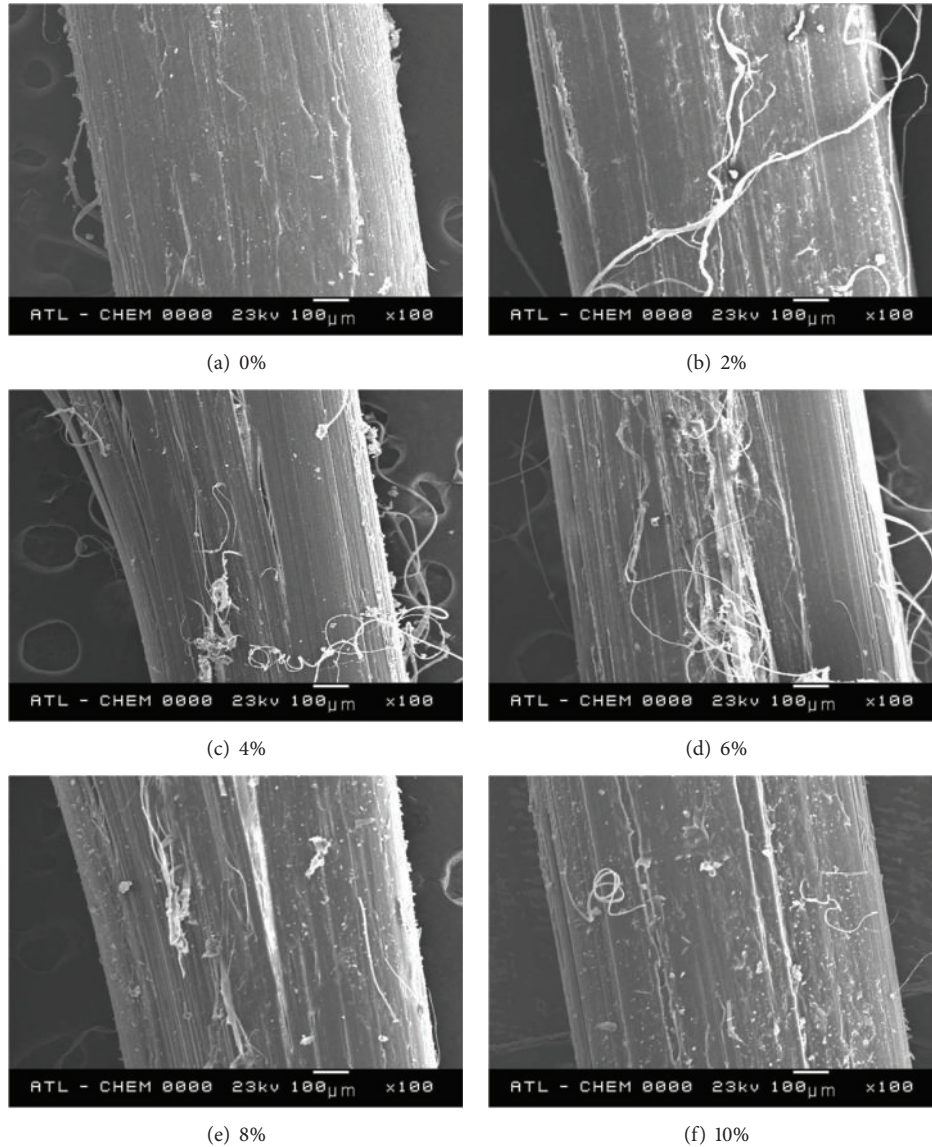


FIGURE 9: SEM investigation of macro PP fiber surface in LCC with nanosilica contents.

8 wt% and greater. Latex polymer also increased the adhesion between materials, so the bond strength and interface toughness were relatively better in LCCs than in PCCs.

- (iii) Relative bond performance was also analyzed to evaluate how the addition of nanosilica to the composites influenced the bond performance between macro PP fiber and cementitious composites. Nanosilica significantly affected the bond performance between the macro PP fiber and the cementitious composites. The addition of latex polymer increased the relative bond strength between the cementitious composites and the macro PP fiber at a given nanosilica content.
- (iv) Post-bond-test microstructural analyses of the fiber surfaces confirmed the results of the bond performance tests. The severity of scratching and fiber

tearing of the macro PP fiber surface due to frictional forces followed the same trend as that observed for bond strength and interface toughness. Nanosilica particles filled the interface voids between the macro PP fiber and the cementitious composites and affected the bonding mechanism.

Conflict of Interests

The authors declare that there is no conflict of interests regarding the publication of this paper.

Acknowledgment

This work was supported by the research grant of the Kongju National University in 2014.

References

- [1] L. Senff, J. A. Labrincha, V. M. Ferreira, D. Hotza, and W. L. Repette, "Effect of nano-silica on rheology and fresh properties of cement pastes and mortars," *Construction and Building Materials*, vol. 23, no. 7, pp. 2487–2491, 2009.
- [2] M. Ali, X. Li, and N. Chouw, "Experimental investigations on bond strength between coconut fibre and concrete," *Materials and Design*, vol. 44, pp. 596–605, 2013.
- [3] M.-H. Zhang and H. Li, "Pore structure and chloride permeability of concrete containing nano-particles for pavement," *Construction and Building Materials*, vol. 25, no. 2, pp. 608–616, 2011.
- [4] M.-H. Zhang, J. Islam, and S. Peethamparan, "Use of nano-silica to increase early strength and reduce setting time of concretes with high volumes of slag," *Cement and Concrete Composites*, vol. 34, no. 5, pp. 650–662, 2012.
- [5] T. Ji, "Preliminary study on the water permeability and microstructure of concrete incorporating nano-SiO₂," *Cement and Concrete Research*, vol. 35, no. 10, pp. 1943–1947, 2005.
- [6] M. Amin and K. Abu El-Hassan, "Effect of using different types of nano materials on mechanical properties of high strength concrete," *Construction and Building Materials*, vol. 80, pp. 116–124, 2015.
- [7] J. Nirmala and G. Dhanalakshmi, "Influence of nano materials in the distressed retaining structure for crack filling," *Construction and Building Materials*, vol. 88, pp. 225–231, 2015.
- [8] H. Li, H.-G. Xiao, J. Yuan, and J. Ou, "Microstructure of cement mortar with nano-particles," *Composites Part B: Engineering*, vol. 35, no. 2, pp. 185–189, 2004.
- [9] A. Bentur and S. Mindess, *Fibre Reinforced Cementitious Composites*, Elsevier Applied Science, London, UK, 1997.
- [10] Y.-W. Chan and S.-H. Chu, "Effect of silica fume on steel fiber bond characteristics in reactive powder concrete," *Cement and Concrete Research*, vol. 34, no. 7, pp. 1167–1172, 2004.
- [11] F. D. A. Silva, B. Mobasher, C. Soranakom, and R. D. T. Filho, "Effect of fiber shape and morphology on interfacial bond and cracking behaviors of sisal fiber cement based composites," *Cement and Concrete Composites*, vol. 33, no. 8, pp. 814–823, 2011.
- [12] B. Mobasher and C. Y. Li, "Effect of interfacial properties on the crack propagation in cementitious composites," *Advanced Cement Based Materials*, vol. 4, no. 3-4, pp. 93–105, 1996.
- [13] A. E. Naaman and H. Najm, "Bond-slip mechanisms of steel fibers in concrete," *ACI Materials Journal*, vol. 88, no. 2, pp. 135–145, 1991.
- [14] M. J. Shannag, R. Brincker, and W. Hansen, "Pullout behavior of steel fibers from cement-based composites," *Cement and Concrete Research*, vol. 27, no. 6, pp. 925–936, 1997.
- [15] S. Singh, A. Shukla, and R. Brown, "Pullout behavior of polypropylene fibers from cementitious matrix," *Cement and Concrete Research*, vol. 34, no. 10, pp. 1919–1925, 2004.
- [16] B. Muhammad, M. Ismail, M. A. R. Bhutta, and Z. Abdul-Majid, "Influence of non-hydrocarbon substances on the compressive strength of natural rubber latex-modified concrete," *Construction and Building Materials*, vol. 27, no. 1, pp. 241–246, 2012.
- [17] C. T. Sumathy, M. Dharakumar, M. Saroja Devi, and S. Saccubai, "Modification of cement mortars by polymer latex," *Journal of Applied Polymer Science*, vol. 63, no. 10, pp. 1251–1257, 1997.
- [18] M. Sprinkel, "Very-early-strength latex-modified concrete over-lays," Tech. Rep. TAT99-TAR3, Virginia Transportation Research Council, Charlottesville, Va, USA, 1998.
- [19] D.-H. Kim and C.-G. Park, "Strength, permeability, and durability of hybrid fiber-reinforced concrete containing styrene butadiene latex," *Journal of Applied Polymer Science*, vol. 129, no. 3, pp. 1499–1505, 2013.
- [20] J.-Y. Jung, C.-G. Park, and J.-S. Park, "Bond properties of structural polypropylene fiber in hybrid nonstructural polypropylene and structural polypropylene fiber-reinforced latex-modified cement-based composites," *Journal of Applied Polymer Science*, vol. 127, no. 2, pp. 1221–1227, 2013.
- [21] J.-Y. Jung, J.-H. Lee, and C.-G. Park, "Effect of styrene-butadiene latex on the bond performance of macro synthetic fiber in micro jute/macro synthetic hybrid fiber-reinforced latex-modified cement-based composites," *Journal of Applied Polymer Science*, vol. 127, no. 5, pp. 3522–3529, 2013.
- [22] C.-G. Park and J.-H. Lee, "Effect of styrene butadiene latex polymer contents on the bond properties of macro polypropylene fiber in polymer-modified cement-based composites," *Journal of Applied Polymer Science*, vol. 126, no. 2, pp. E330–E337, 2012.
- [23] J.-P. Won, J.-H. Kim, S.-W. Lee, and C.-G. Park, "Durability of low-heat, ultra rapid-hardening, latex-modified polymer concrete," *Progress in Rubber, Plastics and Recycling Technology*, vol. 25, no. 2, pp. 91–102, 2009.
- [24] C. T. Sumathy, M. Dharakumar, M. Saroja Devi, and S. Saccubai, "Modification of cement mortars by polymer latex," *Journal of Applied Polymer Science*, vol. 63, no. 10, pp. 1251–1257, 1997.
- [25] Korea Standard Association, *Korea Standard Testing Method L ISO 679, Testing Method for Strength of Hydraulic Cement Mortar*, Korea Standard Association, Seoul, Republic of Korea, 2002.
- [26] Committee on Fiber Reinforced Concrete JCI-SF8, *Method of Testing for Bonds of Fibers*, Japan Concrete Institute, Tokyo, Japan, 1984.
- [27] J. Xiao and H. Falkner, "Bond behaviour between recycled aggregate concrete and steel rebars," *Construction and Building Materials*, vol. 21, no. 2, pp. 395–401, 2007.

Research Article

Inverse Emulsion Polymerization for the Synthesis of High Molecular Weight Polyacrylamide and Its Application as Sand Stabilizer

Mahmoud A. Mohsin¹ and Nuha F. Attia²

¹Department of Chemistry, University of Sharjah, P.O. Box 27272, Sharjah, UAE

²Abu Dhabi Polytechnic, P.O. Box 111499, Abu Dhabi, UAE

Correspondence should be addressed to Mahmoud A. Mohsin; mmohsin@sharjah.ac.ae

Received 13 April 2015; Revised 11 June 2015; Accepted 14 June 2015

Academic Editor: Gonzalo Martínez-Barrera

Copyright © 2015 M. A. Mohsin and N. F. Attia. This is an open access article distributed under the Creative Commons Attribution License, which permits unrestricted use, distribution, and reproduction in any medium, provided the original work is properly cited.

Polyacrylamides constitute a class of polymers that can entirely dissolve or swell in water to form a solution or hydrogel, respectively. Free radical polymerization of acrylamide monomer, using both solution and inverse emulsion polymerization, was applied to produce polyacrylamide with various molecular weights. This investigation was focused on the production of polymers with varying molecular weight, depending on monomer to initiator ratio. Experimental conditions were designed to produce high molecular weight polymers that can be used in stabilization of sand dunes in the arid regions. Synthesized polyacrylamide samples were characterized using Gel Permeation Chromatography and solution viscosity in order to determine the molecular weights and molecular weights distribution. The rheological behavior was also investigated in different polymer concentrations and at various temperatures using Brookfield Rheometer. Lab-scale wind tunnel was used to determine the stability of the sand before and after treatment with the polymer. Compressive stress-strain test was also used to establish the mechanical behavior of the polymer-sand composite under controlled compressive load up to failure. The results showed that the use of high molecular weight polymer gave excellent mechanical and thermal stability.

1. Introduction

Arid Climate. The United Arab Emirates (UAE) climate is described as subtropical, warm, and arid. Air temperatures range from 35°C to 50°C around midday between May and October and from 20°C to 35°C during winter months. Deeper in the desert, the temperature on the ground during summer months can reach 70°C and can fall down to freezing in winter in some areas of the UAE. The average rainfall over the Emirates is less than 100 mm per annum. Moisture also condenses in the form of fog and dew especially on coastal belts. Strong winds and sand storms are of common occurrence throughout the Emirates and are frequent and severe especially during the summer. Sand dunes are a dominant landscape feature in the UAE.

Soils are generally coarse, sandy, and undeveloped. Most of the country is extremely arid, and sustained agriculture is not possible without artificial irrigation. For a successful

agriculture, some protection against high velocity winds and moving sand is required. Sand dunes cover the area of north, west, and southwest of Al-Ain city in the eastern province of Abu Dhabi, UAE. These dunes vary from small crescent-shaped to giant star and range in height from 10 m to 70 m above the ground level [1, 2]. The accumulated sand after a storm has to be physically removed by using heavy earth-moving machinery in particular along the highway systems, townships, and plantation farms. To minimize sand invasion, barriers such as cement asbestos sheets, galvanized iron sheets, or date-palm fronts are erected across the prevailing wind direction to restrain further sand invasion and piles against these barriers are periodically removed [3]. Sand invasion and wind erosion reduce soil productivity causing loss of plant nutrients, degradation of soil structure, loss of storage capacity for water for plants, and a reduction in soil uniformity. Dust arises after a sand storm abrades and buries plants and blocks sunlight. In addition, clog streams and

drainage channels damage water distribution systems and pollute drinking water with agricultural chemicals.

The inception of research of using chemicals as sand stabilizers dates back to the mid-1930s. More than half a century of research and practice has shown that chemical stabilizers are particularly suitable for the control of shifting sand and significantly help in reducing damage to vegetation and highway systems in deserts and arid zones, which are characterized by mobile or moving sand [4, 5]. Chemical stabilization of sand forms a binding surface crust that conserves soil water beneath the crust that prevents or impedes wind erosion and stabilizes the sand. Depending on their chemical properties, sand stabilizers can form three types of binding crust: (i) a rigid crust, (ii) a flexible crust, or (iii) an elastic crust. All these crusts have smooth surfaces that protect the sand surface from direct erosion by strong winds [5, 6]. Ideal chemical sand stabilizers should offer good adhesion and rapid infiltration of the sand when a liquid stabilizer is sprayed onto the sand surface.

As early as 1934, scientists started to study the stabilization of shifting sands using asphalt emulsions. In 1959, scientists conducted dune stabilization experiments using synthesized polymer solution to replace the asphalt. Following this, in 1964, scientists performed a series of dune stabilization experiments in the laboratory as well as in the field. They obtained a large amount of data on their infiltration rates and depths. Between 1969 and 1972, researchers conducted shifting-sand stabilization experiments using a chemical called Nerosine, and in recent years, they have tested butadiene-styrene latex [4]. Other scientists have developed sand stabilizers such as urea-formaldehyde, urea-dicyandiamide, and polyacrylamide [7]. Researchers have also tested more than 30 kinds of organic and inorganic materials to control wind erosion. Other countries, including Germany, Iran, Libya, Algeria, Saudi Arabia, China, Egypt, United Arab Emirates, and Iraq, have also conducted dune stabilization experiments using oil products. These systems were used to stabilize sandy areas disturbed by wind erosion or construction activities, to protect roads, buildings, and valued farmed areas from encroachment by blowing sand [8–12]. In areas that are subject to strong winds, chemical stabilizers keep soil and sand from blowing off the ground and potentially being deposited in nearby wetlands, watercourses, roads, and sewers. Chemicals, which are used as sand stabilizers, including both organic and inorganic substances, must be nontoxic, nonpolluting, adaptable to the climatic and environmental conditions in the area being treated, highly effective, and long lasting. In the UAE, a number of field trials have been carried out in order to combat encroachment and to halt sand dune movements. Various methods were used, such as the erection of fences and barriers, protective forestation, and leveling followed by covering and spraying with crude oil or other oil stabilizers.

Petroleum mulch was also used for dune stabilization, and it seemed to have given better results; however, the area sprayed produced dirty appearance and possibly polluted the local environment. It would be worthwhile to try other sand stabilizers, which do not produce the bad effects of petroleum mulch. Another method, which can be regarded as more

environmentally friendly, was planting the arid zone with species such as *Acacia* and *Calligonum*, but this proved to be very expensive to maintain over a long period of time. In this work, a high molecular weight sand stabilizer based on polyacrylamide was synthesized by both solution and inverse emulsion processes to produce polymers in powder and emulsion forms, respectively, for easy application. These materials were applied for wind erosion control and sand dune stabilization in Al-Ain town of the UAE.

Inverse Emulsion Polymerization. Acrylamide based polymers or copolymers of high molecular weight can be obtained by solution polymerization in aqueous media. However, solution polymerization is limited to relatively low monomer concentrations because of the high viscosity of the final polymer or copolymer solution. These difficulties are overcome by using heterophase water-in-oil (inverse emulsion) polymerizations. This process involves the dispersion of an aqueous monomer(s) solution in an aliphatic continuous oil phase. The polymerization takes place in a batch reactor under inert atmosphere using free radical initiator. Temperatures ranging between 25 and 55°C are employed with continuous vigorous agitation. There has been a considerable progress in the field of inverse emulsion polymerization since the pioneering work of Vanderhoff [13].

This study focuses on the examination of the molecular weight distribution of a water-soluble polyacrylamide, which was polymerized in solution and in inverse emulsion (water in oil) polymerization. The shape of this distribution as a function of the amount of chain transfer agent (Sodium formate) and of initiator was examined to obtain information on the mechanisms involving free radical polymerization.

In a water-in-oil polymerization, a hydrophilic monomer (usually in aqueous solution) was dispersed in a continuous organic phase using a water-in-oil emulsifier. The free radical polymerization was carried out to yield inverse latex, that is, a colloidal dispersion of water swollen polymer particles in oil. Such a process is well suited to the preparation of high molar mass polymers at rapid reaction rates [14, 15]. It should be mentioned at this stage that the economic advantages of using the synthesized polyacrylamide in this work compared to the commercial ones are perhaps not that significant. However, it could be very much economical if a commercial plant would be built locally to produce such polymer on a large scale. The important issue is that the commercial polymers, when applied in the UAE, will degrade the polymer significantly due to the extreme weather conditions. Full degradation study of the synthesized polymer will be explored in future research.

2. Experimental

2.1. Materials. Acrylamide (AM) monomer was recrystallized twice from chloroform. The purity of transfer agent (sodium formate) (A) was measured and an aqueous solution (5 wt%) of transfer agent was added to the reaction solution for selected experiment. Deionized water was used in all experiments. Potassium persulfate (KPS) was used as the initiator (I), purified by recrystallization with methanol, dried

in a vacuum, and stored at 5°C in a freezer. For inverse emulsion polymerization, the oil was a narrow cut isoparaffinic mixture and was used as supplied. The emulsifier was a polymeric surfactant, which also contained some sorbitan monooleate. Sodium ethylene diamine tetraacetic acid was used as a chelating agent, to eliminate catalysis of persulfate decomposition by traces of transition metal ions. All chemicals were purchased from Sigma-Aldrich Chemicals Company.

2.2. Polymer Synthesis. Solution polymerizations were carried out in a 5 L jacketed glass reactor fitted with a mechanical stirrer, thermocouple, and a condenser. The reactor temperature was controlled by using a circulating water bath. The reactor was also connected to a Nitrogen gas inlet. The starting recipe (without the KPS solution) was first purged with purified Nitrogen to remove most residual Oxygen. The reaction temperature was maintained between 50°C and 60°C. The initiator solution was then injected after thermal equilibrium.

Emulsion polymerizations were performed using the same reactor settings. The aqueous phase and oil phase were prepared separately. The aqueous phase was then poured into the reactor, which contained the oil phase, under vigorous stirring. The emulsion was formed and continuously purged with purified Nitrogen gas. The agitation rate was fixed first at 200–350 rpm and then increased to 3000 rpm when all the ingredients were added and the reaction temperature achieved the desired setting of 50°C. Initiator solution with a specific concentration was then injected into the reactor. For each procedure (solution and emulsion polymerization), three experiments were carried out as follows: (a) reference experiment, (b) where the concentration of initiator was doubled (“2I”), and (c) where the concentration of the transfer agent was divided by three (“A/3”).

Solution polymerizations were stopped after 20 minutes, and the polymer was analyzed. However, the emulsion polymerization reactions were kept continuously going, and two aliquots were withdrawn at 20-minute intervals for analysis. Following this, the reaction was then terminated.

2.3. Polymer Characterization. Polymer characterization was conducted simultaneously in order to achieve a polymer with high molecular weight. Characterization techniques including NMR and FTIR were used for routine analysis. Gel Permeation Chromatography (GPC) and solution viscosity were also used continuously for the determination of molecular weight and molecular weight distribution. For both, solution and emulsion polymerizations, polyacrylamide was recovered from the reaction medium by precipitation in excess methanol containing a small amount of hydroquinone, followed by several washings and drying overnight in an oven at 45°C. GPC analysis was carried out with an Agilent HPLC/GPC (1100 Series) with ultraviolet (UV) and Refractive Index (RI) detectors. The mobile phase consisted as a solution containing sodium nitrate (0.25 M) and sodium hydrogen phosphate (0.01 M). Two mix bed Agilent hydrogel columns were used. Calibration was carried out with narrow molecular weight distribution water-soluble polyethylene

oxide (PEO) standards (twelve standards covering a wide range of molecular weights). Solution viscosity measurements for the determination of viscosity molecular weight M_v were also used to verify the molecular weight values.

2.4. Polymer Rheology. The application of polyacrylamide as a sand dune stabilizer ultimately depends on the way in which it is sprayed on the field or on the sand dune. Rheological properties and how the polymer solution behaves at various concentrations and temperatures were examined. Factors affecting these properties were also determined. The Brookfield Viscometer model LVDV- II+ was used to determine the shear viscosity of the polymer sample. This instrument applies *Hooke's law* which states that the force (F) required to extend or compress a spring by some distance (x) is directly proportional to that distance. That is, $F = Kx$, where K is a constant factor characteristic of the spring and its stiffness. This equation was used to calculate the torque produced between the liquid in the concentric cylinder. The measurement of viscosity and the behavior of the viscous flow at different concentrations and temperatures were examined. The Brookfield Viscometer model LVDV- II+ with small sample adapter has a cylindrical spindle, which rotates in the fluid to measure the torque needed to overcome the viscous resistance to the induced movement. The spindle is inserted in the test material until the fluid level reaches the immersion mark on the spindle's shaft at a constant temperature. The motor speed was turned on, and the readings of viscosity in centipoise (cP) and shear stress versus different shear rates were taken. To start the experimental part, the viscometer was calibrated and the viscosity was measured for a series of prepared polymers with different concentrations for all polymers which had been prepared by both emulsion and solution polymerization. At a constant temperature, the polymer solution was poured into the viscometer cell to determine the values of the shear stress, the shear rate, and the viscosity. A series of graphs were obtained for varying concentrations of different polymers at a constant temperature.

2.5. Wind Tunnel Experiment. Laboratory scale wind tunnel (Armfield Technical Education Company Limited, Ringwood, Hampshire, England) was used to simulate the wind pattern for the wind erosion experiment. The wind speed was calibrated and monitored by a manometer.

For laboratory experiments, rectangular shape plastic trays with fixed dimension (length 12 cm × width 4 cm × height 2 cm) were filled with known weight of local sand and were placed on the tunnel floor upwind. The effect of flow interference from the surrounding trays was ignored. Sand erosion tests were conducted under three different wind speed levels (4, 5, and 10 m·s⁻¹) measured by a nanometer on the side of the tunnel. During the test, three trays containing sand, which has been treated with the sand stabilizer, were placed next to each other. The fourth tray was placed 10 cm away from the side of the other three. This tray was filled with a known weight of the same sand but without any stabilizer treatment. This will be used as a control sample for comparison. All four trays were placed at the flat surface of the wind tunnel and facing the upwind direction.

TABLE 1: Recipes of solution (S) and emulsion (E) polymerization experiment of acrylamide at 50°C. All quantities are given in grams. The weight average molecular weight M_w was calculated from the GPC and the viscosity average molecular weight M_v was calculated from viscosity measurement and given in $\text{g}\cdot\text{mol}^{-1}$.

Sample number	Sample code	Polymer	Monomer Am	Water	Initiator	Surfactant	Oil	Transfer agent A	Mol. wt. M_w	Mol. wt. M_v
1	S	PAM-Sa	52.4	3000	0.1	0	0	53.7	5.0×10^5	4.1×10^5
2	S:2I	PAM-Sb	52.4	3000	0.2	0	0	53.7	2.4×10^5	1.9×10^5
3	S:A/3	PAM-Sc	52.4	3000	0.1	0	0	17.9	7.5×10^5	6.6×10^5
4	E	PAM-Ea	52.4	900	0.1	212	2100	53.7	1.4×10^6	7.0×10^5
5	E:2I	PAM-Eb	52.4	900	0.2	212	2100	53.7	8.3×10^5	5.1×10^5
6	E:A/3	PAM-Ec	52.4	900	0.1	212	2100	17.9	2.2×10^6	1.8×10^5

2.6. Mechanical Properties. Compression test was used to determine the mechanical behavior of the polymer-sand composite under escalating compressive load until failure is reached. Compressive stress and strain were calculated and plotted as stress-strain diagram was used to measure the load bearing capacity in compression and the stiffness (modulus of elasticity) for the polymer composites. Other parameters such as the peak load, peak stress, and elongation at peak were also determined. Composite specimens were prepared by mixing various weight percentages of the highest molecular weight polymer ($2.2 \times 10^6 \text{ g/mol}$) obtained from the inverse emulsion process with 300 g of sand and compressed in a cylindrical mold. The mold was then placed in an oven held at 50°C for 48 hours to completely evaporate the excess water which was used to dissolve the polymer. The detailed sample compositions and mixing components are given in Table 1. At least four samples for each composition were made for the compressive test. Compressive strength for all six fully dried composite samples with varying weight percentage of the polymer was determined using 100 KN, MTS universal testing machine under displacement controlled conditions.

The tests were conducted at ambient temperature and under a constant cross head speed (CS) of 0.05 cm/min until the test sample fractured. At least three valid results for each sample have been completed in order to calculate the mechanical properties. The average value of the results obtained from three valid samples was calculated and presented herein. Cylindrical shaped test composite (diameter of 50 mm and thickness of 50 mm) was loaded across its diameter and subjected to static compression test with escalating compressive load until sample failure occurred. Such loading generates a tensile stress at the center of the cylinder in a direction perpendicular to the direction of applied load. Tensile strengths for each specimen (σ) were calculated using the following equation:

$$\sigma = \frac{2P}{\pi t D}, \quad (1)$$

where P = maximum applied compressive load recorded during the test (Newton), D = diameter of the test specimen (mm), and t = thickness of the test specimen (mm).

3. Results and Discussions

As for the synthesis and characterization of all polymers that were prepared using both solution (S) and emulsion (E)

polymerization methods, three polymers were synthesized in each method and were characterized by NMR and FTIR. All polymers showed typical bands associated with stretching and bending of various groups and in particular the carbonyl and the amine groups. Details of characterization were presented elsewhere [16, 17]. Table 2 shows the specific experimental conditions for each batch of polymerization in solution and emulsion method. Those synthesized polymers by solution polymerization were given codes: PAM-Sa, PAM-Sb, and PAM-Sc, referring to the method of synthesis and condition (PAM is referring to polyacrylamide); the capital letter S refers to solution polymerization and the letter (a) is for the reference or standard experiment; (b) is for doubling the initiator concentration (2I), while the letter (c) is for the reduced concentration of the transfer agent by one-third (A/3). Polymer obtained using emulsion polymerization followed the same coding with the letter E to refer to emulsion method.

Molecular weight measurements were obtained from two different techniques, namely, Gel Permeation Chromatography (GPC) and dilute solution viscosity. Synthesized polymers were characterized by their intrinsic viscosity. The viscosity average molecular weight of the polymers was estimated from the intrinsic viscosity data at an appropriate temperature (30°C) in a specific solvent (distilled water). All viscosity measurements were performed using an Ubbelohde type viscometer immersed water bath held at 30°C.

The data was calculated and listed in Table 1. A reasonable agreement was observed between the two molecular weight values obtained from the two different techniques. This could primarily be due to the use of ethylene oxide standard for the calibration of the GPC system. The value of molecular weight obtained using emulsion polymerization was much higher than those obtained using solution polymerization. It is possible to increase the molecular weight of the polymer to even a higher extent if the viscosity of the reaction solution is reduced and the monomer/initiator ratio is increased. Emulsion polymerization has some advantages over the solution method in which the resulting polymer can readily be used as sand stabilized after making the required concentration. In addition, the control of the reaction exotherm is much easier, and the solution viscosity can be managed better to ensure the maximum mixing of reacting materials.

Figure 1 shows the molecular weight distribution obtained from the GPC system for the three polymer samples, which

TABLE 2: Composition of six polymer-sand composite samples with different weight % of the polymer.

Sample number	1	2	3	4	5	6
Solid PAM g	0.33	0.66	0.99	1.33	1.66	1.99
Mix of PAM solution with 300 g of sand	13 mL	26 mL	39 mL	52 mL	65 mL	78 mL
Constant H ₂ O %	2.5	2.5	2.5	2.5	2.5	2.5
Weight % of PAM in 300 g of sand	0.11	0.22	0.33	0.44	0.55	0.66

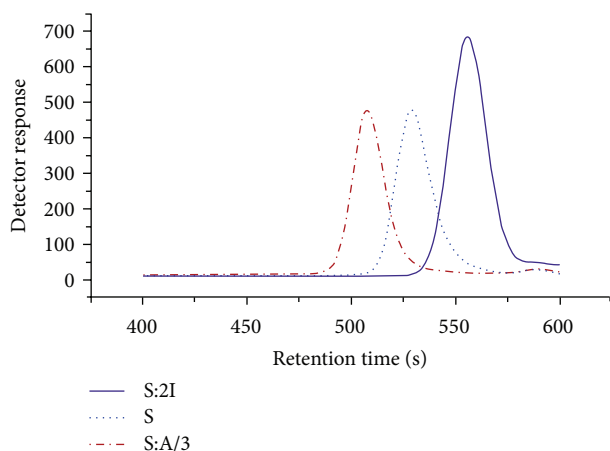


FIGURE 1: Molecular weight distribution curves for three polymers obtained in solution polymerization.

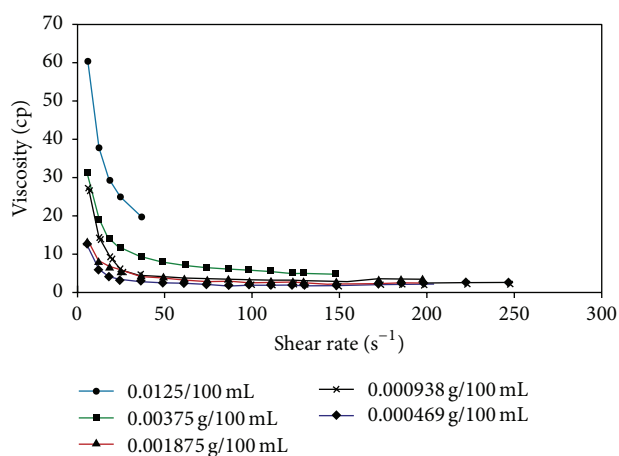


FIGURE 2: Shear rate versus viscosity for PAM-Sa at 20°C at different concentrations.

were polymerized in solution method. The polydispersity indexes for these polymers were excellent as they were between 1.05 and 1.10, which is not usually achieved in a free radical polymerization.

Figure 2 shows the shear rate versus solution's viscosity at 20°C for different polymer concentrations. As one can see from the graph, the concentration of the polymer solution contributed to the increase in viscosity. In addition, the increase of molecular weight increased the viscosity of the polymer at constant concentration and temperature. As the shear rate increased, the viscosity decreased because it

breaks down the polymer chains resulting in a less viscous solution. The viscosity can be said to be non-Newtonian and shear thinning for high concentrations, while at low concentrations the viscosity behavior is almost the same with a Newtonian behavior. Lower viscosity is desirable in the current application in which the polymer solution has to be spread over the sand dune in order to form a thin film to stabilize the sand.

Before conducting tests on the sand, 0.1% polymer stock solutions (based on total solids) were prepared. In this study, deionized water produced by a Millipore laboratory water purification system was used. The polymer was dissolved in warm water (25°C to 35°C); then stirred for 30 minutes to form 0.1% aqueous solutions. This concentration was adopted for all experiments in order to control the solution viscosity by keeping it to a minimum, allowing the spraying process to be easy and uniform. Two types of sand structures and formations were constructed outside the laboratory using locally available sand. One of the structures was a flat surface and the other was a dune or hill profile. Both formations were sprayed with the polymer solution prepared earlier and left to the effect of local wind and temperatures. These structures were visually inspected over a period of time. Photographs of the sand dune patterns were taken at regular intervals to study the effects of wind on these formations. Figure 3 shows the dune pattern over the entire period after the application of the sand stabilizer. Figure 3(a) was taken during the first week of application; Figure 3(b) was taken after three weeks; and Figure 3(c) was taken after nine weeks of exposure to local weather.

The dune was divided into two halves using a marking tape; the left hand side of the dune was treated with the polymer solution and the other half was used as a control. It was clear from Figures 3(a), 3(b), and 3(c) that the prepared polymer worked reasonably well in holding the sand from drifting under the effects of the local wind. It should be noted that the yearly average wind speed in Al-Ain city is 5 meters per second or just above 18.5 kilometer per hour [1]. This is considered to be light to moderate all year around. Such wind force is capable of moving and depositing large volumes of sand on local highways, vegetation farms, and residential areas. Application of sand stabilizers could potentially solve these problems by preventing accumulation of sand in these crucial areas.

On the flat surface, the polymer's performance was as good as on the dune pattern. Two wooden trays of equal dimensions were filled with local sand. As in the previous experiment, the right hand tray, this time, was treated with the polymer solution, and the left hand side was left without

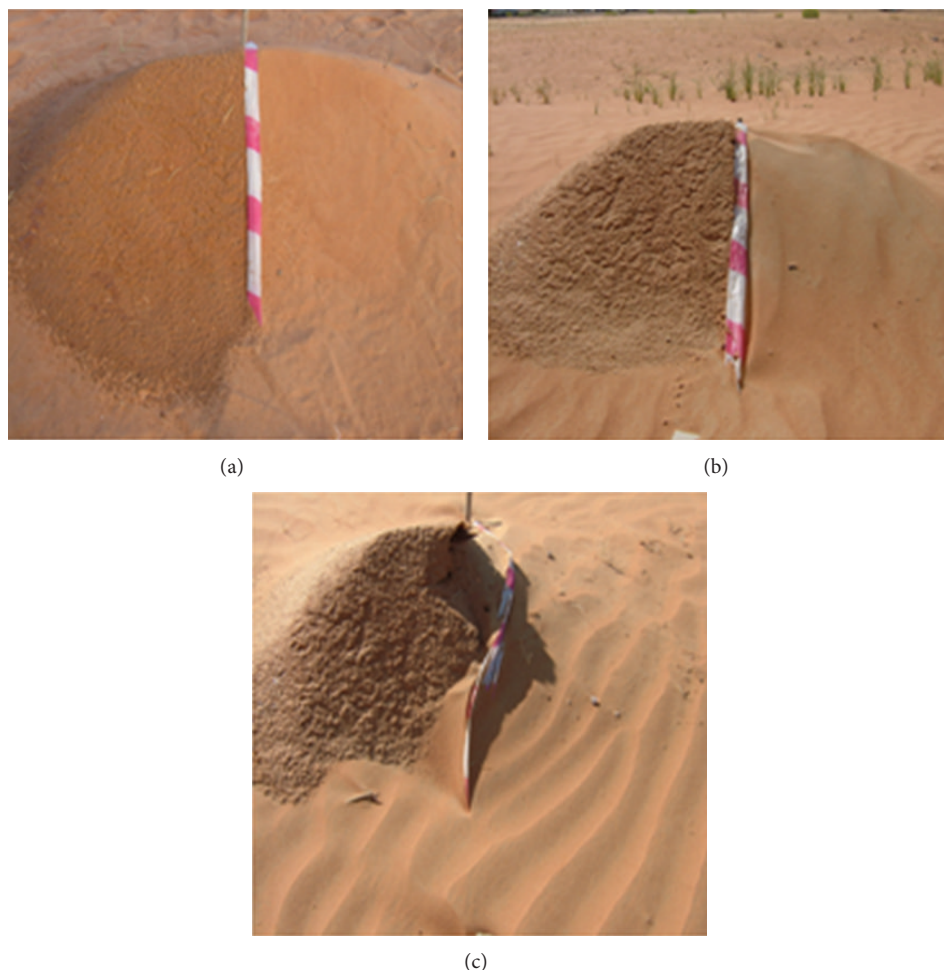


FIGURE 3: Shows sand erosion in a dune formation over 9-week exposure to weathering condition in Al-Ain in which the treated half is completely preserved. (a) After one week, (b) after three weeks, and (c) after nine weeks.

treatment. These trays were placed on a flat surface in an open air and fixed to the ground. Figure 4 shows the sand erosion over a period of nine weeks. After nine weeks of exposure to the local weather and wind, the sand in the left hand tray had completely been dispersed and was removed out of the tray by the effect of wind. On the other hand, the sand, which had been treated with the prepared sand stabilizer, remained unchanged over the same period of time. This effect can be shown in Figures 4(a), 4(b), and 4(c).

For more accurate assessment of the durability of the sand stabilizer and its stabilizing strength over the sand, a laboratory-scale wind tunnel was used to carry out a number of experiments at different wind speeds, namely 4, 5, and $10 \text{ m}\cdot\text{s}^{-1}$, bearing in mind that the annual average wind velocity in Al-Ain city is $5 \text{ m}\cdot\text{s}^{-1}$. In this test, the sand was collected from nearby dune sites and used for the evaluation. The sand was used to fill four identical rectangular trays. Three of these trays were sprayed with the polymer solution and left over night at room temperature to dry. Only one tray was left without the polymer and was used as a control. Those four trays were placed inside the wind tunnel and the wind

speed was selected. To determine the correct weight loss, the trays containing the sand sample were weighed before and after the test using an electronic balance with an accuracy of 0.1 g. The weight loss at the end of the test corresponded to the sand blowing off at particular wind speeds. The weight loss was monitored with time and recorded every 5 minutes. Figure 5 shows the sand weight loss versus the time at $5 \text{ m}\cdot\text{s}^{-1}$ wind speed. The weight loss for the three trays filled with sand, which were sprayed with the polymer, was found to be zero as the final weight remained the same as the original weight. This is clear evidence that the polymer stabilizer has held the sand grains together and prevented them from blowing off with the wind. On the other hand, the weight loss from the control sample exhibits a gradual weight loss with time. In fact, after 30 minutes of exposure, the tray has lost almost 50% of its original weight. At this stage, the wind direction was changed by 180° ; and a further weight loss of 25% has occurred. Finally, only less than 25% of the original sand weight was left in the tray after 45 minutes of inside exposure to the wind tunnel. The latter happened as the sand has accumulated and sheltered around the edges of the tray.

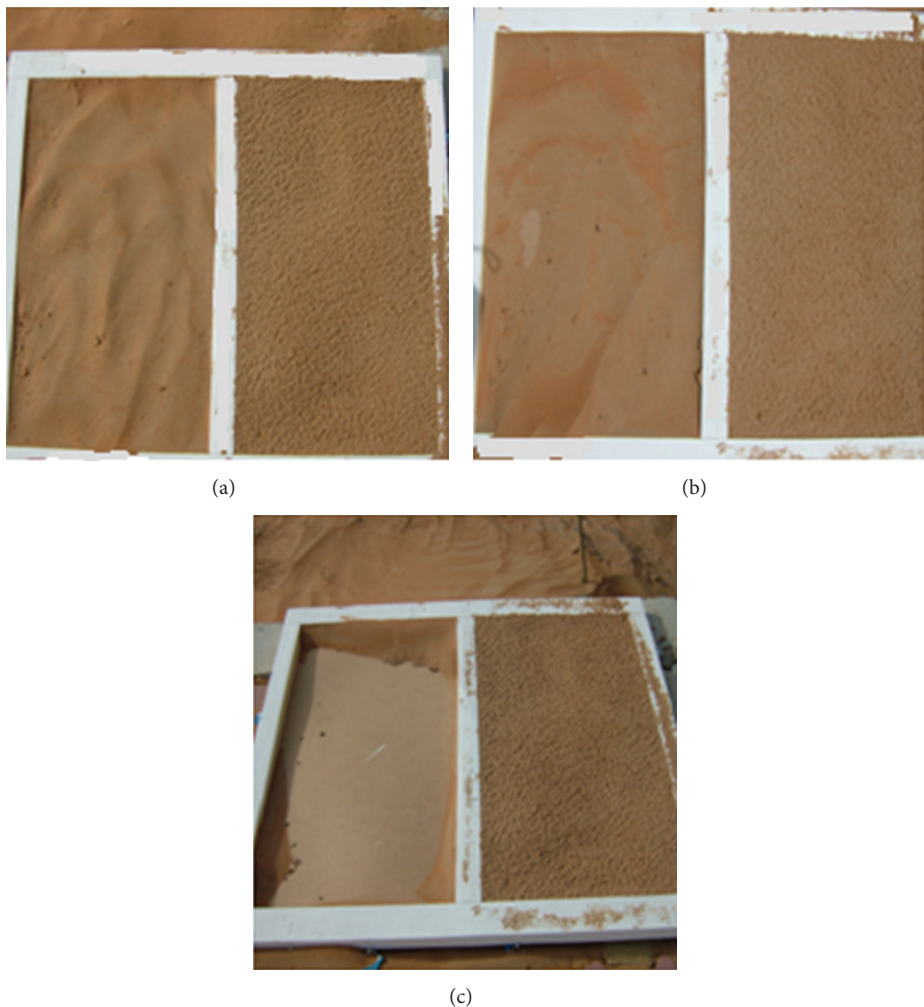


FIGURE 4: Shows sand erosion in a flatbed formation over 9-week exposure to weathering condition in Al-Ain in which the treated half is completely preserved. (a) After one week, (b) after three weeks, and (c) after nine weeks.

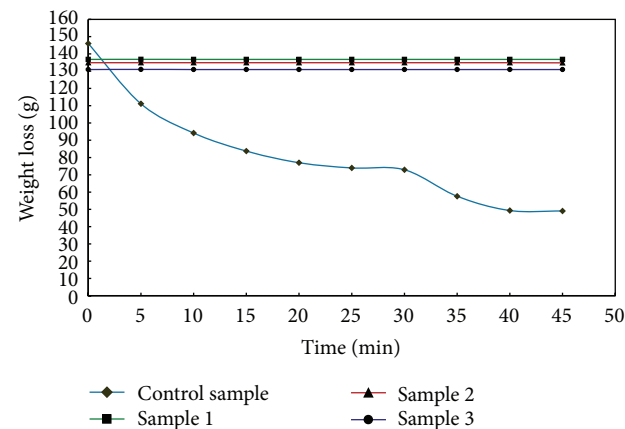


FIGURE 5: Weight loss versus time at 5 m/s wind speed.

When the wind speed was lowered to $4 \text{ m}\cdot\text{s}^{-1}$, a similar trend was observed, but with a reduced weight loss from the control tray. Only 11% of the total sand weight was lost as depicted in Figure 6.

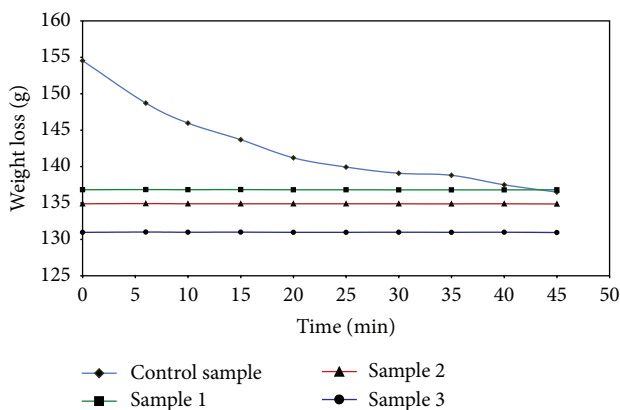


FIGURE 6: Weight loss versus time at 4 m/s wind speed.

Once again, the treated trays remained unaffected by the reduced wind speed. Figure 7 illustrates the sand weight loss versus time at $10 \text{ m}\cdot\text{s}^{-1}$ wind speed. Only 4 minutes were required to reduce the sand weight by almost 75%. The wind

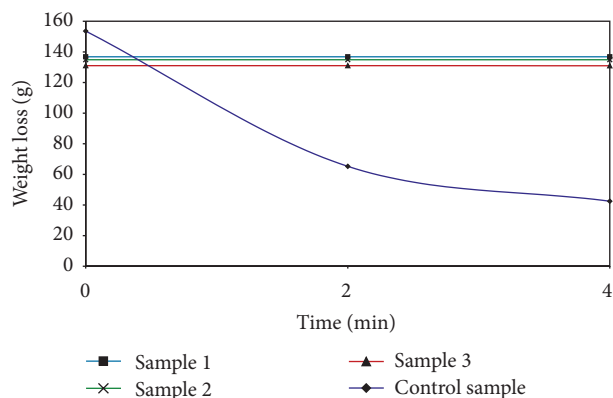


FIGURE 7: Weight loss versus time at 10 m/s wind speed.

at this speed is considered as fresh breeze, and yet it can blow off almost 75% of the sand within very short time. Wind blowing is a major agent in the weathering process, and wind erosion is common in the Gulf region where soils are generally unprotected and prevailing winds transport the exposed surface materials.

This movement of sand and soil, referred to as aeolian transport, is common throughout the United Arab Emirates. In addition, wind direction during sand storms often fluctuates, allowing the movement of sand which was previously deposited by wind from a slightly different direction. Blow-sand damage to both urban and agricultural uses can result in substantial economic losses. Damage to agriculture during a sand storm can result in deposition from an adjacent area or on-site erosion of the topsoil. Urban related damage is generally limited to equipment, buildings, and highways. It is, therefore, necessary to conduct large-scale or field experiment to verify the finding of these research results.

Figure 8 demonstrated a typical stress-strain diagram obtained from the MTS universal testing machine.

The average data for three successful test samples obtained from the MTS machine are given in Table 3.

The modulus and the tensile strength of the polymer-sand composite were directly obtained from the MTS machine for various polymer weight percentages. These mechanical properties are predominant for all composite materials and can be used to characterize them for various applications. Figure 9 shows the effect of increasing polymer weight % on the modulus of the prepared sample.

When polymer weight percent was 0.33%, the modulus obtained was very low reaching less than 10 MPa. When the polymer weight % in the composite was doubled, the Modulus increased by more than 15-fold reaching a value of 85 MPa. The substantial increase in modulus can be attributed to the binding strength of the polymeric material and also to the polymer having very high molecular weight represented by very long chain length where chain entanglement constitutes the prevailing forces. The trend in modulus was abrupt when the polymer weight percentage increased from

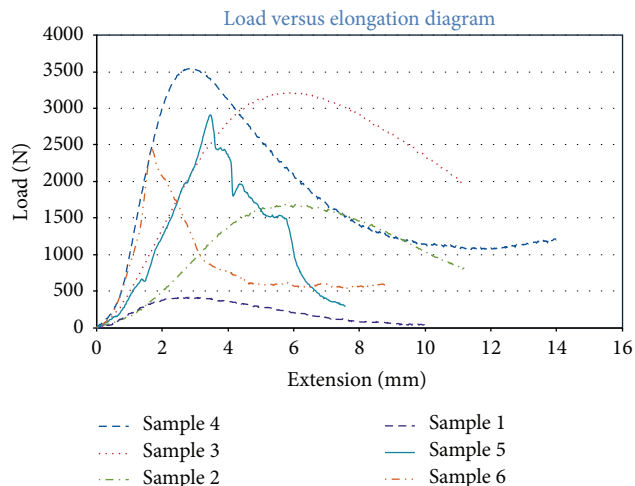


FIGURE 8: Typical load-deformation diagram obtained from the MTS universal testing machine for six test specimens with different polymer's weight percentage.

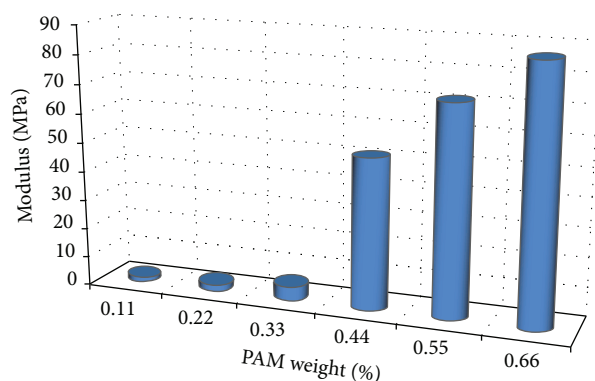


FIGURE 9: Modulus of elasticity of sand-polymer composites containing various polymer weight percent.

0.33% to 0.66% while the increase in the tensile strength was gradual as shown in Figure 10. It was also observed that the calculated value of the tensile strength was 0.6 MPa at 0.33% polymer weight and increased to 0.9 MPa when the polymer percentage was doubled.

4. Conclusions

Reverse-emulsion polymerization (water-in-oil) of acrylamide monomer was conducted under three different experimental conditions to produce polyacrylamide with high molecular weight. In contrast, solution polymerization was also used to prepare polyacrylamide, using three different experimental conditions. Characterizations of these polymers were performed using NMR, FT-IR, GPC, and Rheology and were typical for polyacrylamide. The aim of this research was to synthesize polyacrylamides using two different methods and exploiting their physical properties in binding the surface particles together with the soil or sand to

TABLE 3: Mechanical properties data obtained from the MTS universal testing machine (average of three samples).

Specimen number	Peak load (Newtons) N	Peak stress MPa	Modulus MPa	Cylindrical area (mm ²)	Elongation at peak (mm)	Tensile strength (σ) MPa
1	417.81	0.20	1.574	7857	1.293	0.11
2	1686.29	0.70	2.644	7857	2.875	0.43
3	2429.96	0.95	5.044	7857	2.983	0.62
4	2909.89	1.13	50.905	7857	2.868	0.74
5	3216.95	1.28	70.956	7857	1.725	0.82
6	3538.95	1.40	86.413	7857	1.710	0.90

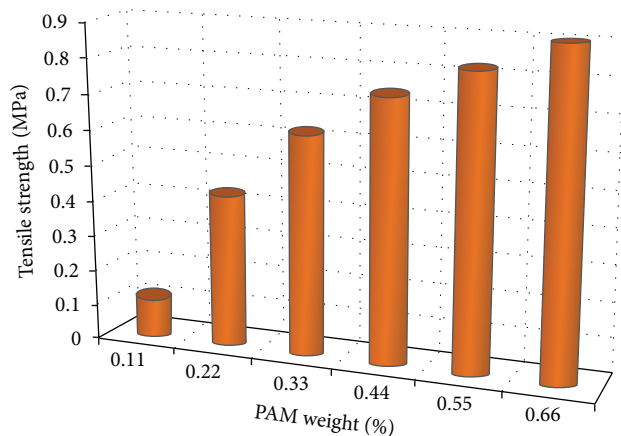


FIGURE 10: Tensile strength versus polymer weight percent in the sand-polymer composite.

form a solid crust protecting the sand from blowing away by the wind.

The surface crusts, formed from application of polyacrylamide solution, were anchored to the soil below the crust and penetrated easily, making the soil surface resistant to wind erosion. The flat surface held its integrity much better than the hill pattern and protected the sand surface from weathering effects and abrasion. Mechanical properties were used to study the wind erosion resistance and it was found that as the polymer weight percent increased the mechanical properties increased resulting in a stronger composite with high modulus and tensile strength.

It was obvious that there is a continuous and growing demand for sand dune stabilization in the UAE. It is required not only for practicing stable agriculture, but also for road construction and the development of urban and industrial areas. Agricultural land needs to be protected against dune encroachment, which can only be achieved by the application of chemical stabilizers, such as the one prepared in this study and which was successfully tested in the wind tunnel. These stabilizers are environmentally friendly, and they do not produce adverse effects of petroleum mulch. More experiments are required to examine the degradation rate and toxicity of these chemicals subjected to the UAE environment before any attempt to use them on the field.

Conflict of Interests

The authors declare that there is no conflict of interests regarding the publication of this paper.

Acknowledgment

The authors are thankful for the help and support that were received from the "Mechanical Engineering and Chemistry Departments" at the UAE University.

References

- [1] A. S. Alsharhan, K. W. Glennie, G. L. Whittle, and C. G. S. Kendall, *Quaternary Deserts and Climate Change*, A. A. Balkema, Rotterdam, The Netherlands, 1998.
- [2] D. J. Gallacher and J. P. Hill, "Effects of camel grazing on the ecology of small perennial plants in the Dubai (UAE) inland desert," *Journal of Arid Environments*, vol. 66, no. 4, pp. 738–750, 2006.
- [3] S. M. Lahalih and N. Ahmed, "Effect of new soil stabilizers on the compressive strength of dune sand," *Construction and Building Materials*, vol. 12, no. 6-7, pp. 321–328, 1998.
- [4] Z. Han, T. Wang, Z. Dong, Y. Hu, and Z. Yao, "Chemical stabilization of mobile dunefields along a highway in the Taklimakan Desert of China," *Journal of Arid Environments*, vol. 68, no. 2, pp. 260–270, 2007.
- [5] D. Y. Cheng, X. L. Zhao, and G. D. Kang, *Experiment and Research of Shifting sand Stabilization with Asphalt Emulsion. Research of Shifting Sand Control*, Ningxia People's Publishing House, Yinchuan, China, 1991.
- [6] T. H. Zhang, H. L. Zhao, S. G. Li et al., "A comparison of different measures for stabilizing moving sand dunes in the Horqin Sandy Land of Inner Mongolia, China," *Journal of Arid Environments*, vol. 58, no. 2, pp. 203–214, 2004.
- [7] Z. D. Zhu, X. L. Zhao, and Y. Q. Lin, *Sand Control Engineering*, China Environmental Science Press, Beijing, China, 2000.
- [8] Y. T. Gumaa, I. Haffar, and M. A. Al-Afifi, "Financial appraisal of date-frond mat fence systems for wind erosion control and sand dune stabilization in the arid region of the United Arab Emirates," *Journal of Arid Environments*, vol. 39, no. 4, pp. 549–557, 1998.
- [9] A. M. O. Mohamed, "The role of clay minerals in marly soils on its stability," *Engineering Geology*, vol. 57, no. 3-4, pp. 193–203, 2000.
- [10] H. I. Al-Abdul Wahhab and I. M. Asi, "Improvement of marl and dune sand for highway construction in arid areas," *Building and Environment*, vol. 32, no. 3, pp. 271–279, 1997.

- [11] S. M. Lahalih, "Development and evaluation of new multi-purpose soil additives," *Industrial & Engineering Chemistry Research*, vol. 37, no. 2, pp. 420–426, 1998.
- [12] M. M. El Banna, "Vulnerability and fate of a coastal sand dune complex, Rosetta-Idku, northwestern Nile Delta, Egypt," *Environmental Geology*, vol. 54, no. 6, pp. 1291–1299, 2007.
- [13] J. W. Vanderhoff, E. B. Bradford, H. L. Tarkowski, J. B. Shaffer, and R. M. Wiley, "Inverse emulsion polymerization," *Advances in Chemistry Series*, vol. 34, p. 32, 1962.
- [14] R. G. Gilbert, *Emulsion Polymerization: A Mechanistic Approach*, Academic Press, London, UK, 1995.
- [15] P. A. Clay and R. G. Gilbert, "Molecular weight distributions in free-radical polymerizations. 1. Model development and implications for data interpretation," *Macromolecules*, vol. 28, no. 2, pp. 552–569, 1995.
- [16] G. H. Alnuaimi, *Synthesis and solution characterization of water soluble polyacrylamides and its applications in oil industries [M.S. thesis]*, UAE University, 2005.
- [17] M. A. Mohsin and A. Farah, "Rheological properties of polyacrylamide in enhanced oil recovery applications," in *Proceedings of the 2nd Chancellor's Undergraduate Research Award (CURA '08)*, UAE University, Al-Ain, UAE, May 2008.

Research Article

Interface Bond Characterization between Fiber and Cementitious Matrix

Won-Chang Choi,¹ Seok-Joon Jang,² and Hyun-Do Yun²

¹Department of Architectural Engineering, Gachon University, Gyeonggi 13120, Republic of Korea

²Department of Architectural Engineering, Chungnam National University, Daejeon 34134, Republic of Korea

Correspondence should be addressed to Hyun-Do Yun; wiseroad@cnu.ac.kr

Received 5 June 2015; Revised 11 August 2015; Accepted 11 August 2015

Academic Editor: Osman Gencel

Copyright © 2015 Won-Chang Choi et al. This is an open access article distributed under the Creative Commons Attribution License, which permits unrestricted use, distribution, and reproduction in any medium, provided the original work is properly cited.

The use of high performance composite fibers allows for the improvement of the mechanical properties of cement composites. Previous research results indicate that the mechanical properties of such composites are determined predominantly by the interface properties between the fiber and cementitious matrix. Many researchers have conducted single-fiber pull-out tests using cementitious composites to quantify the interfacial properties between the fiber and cement matrix. This paper aims to establish a design methodology that employs coefficients to represent the design parameters for the interfacial properties for three types of fibers: carbon fiber, polypropylene fiber, and twisted wire strand steel cord. The parameters for each type of fiber include the water-to-binder ratio and fiber embedment length. The adopted equation used for the numerical analysis was calibrated using experimental data, and design coefficients are proposed accordingly. The developed models could be validated successfully, and the pull-out characteristics of each fiber type are presented.

1. Introduction

Fiber-reinforced cementitious composites (FRCCs) have unique tensile characteristics due to the fiber-bridging action that occurs across fine multiple cracks, which allows for the even distribution of the fibers. These mechanical characteristics result in tensile strain-hardening behavior with a high level of tensile deformation. The bridging action contributes to the composite's toughness by activating the fiber-matrix interface where energy is dissipated through the debonding of the interface and fiber pull-out [1]. The interfacial bond strength can be computed using the nonconstant interfacial shear strength that surrounds the fibers so that the fiber-matrix interfacial bond strength, which is a primary factor of the composite's behavior, can possibly be quantified by single-fiber pull-out testing of the cement composites. In the literature, results of single-fiber pull-out tests of cement composites, designed to examine the interfacial behavior of the fiber/cement composite matrix, have been reported [2].

The composite properties of the interface between the fiber and cement matrix have been examined in many studies found in the literature; these properties include composite strength, fatigue, ductility, energy absorption, and interface failure mode [3].

Li [2, 3] presented comprehensive research results in terms of the interface property characteristics of cement composites and developed numerical equations. One of Li's developed models is a strength-controlled model that is based on interface bond performance and is adopted in this study. The interface bond is characterized by frictional bonding and chemical bond strength. It is assumed that the debonding zone that incorporates the embedment length of the fiber is propagated when the shear stress overcomes a critical value at the tip of the debonding location [4].

A simplification of this phenomenon is that the pull-out load is resisted by a combination of the chemical bond strength and the frictional bond strength, which is not achieved on a robust physical basis but in a phenomenological

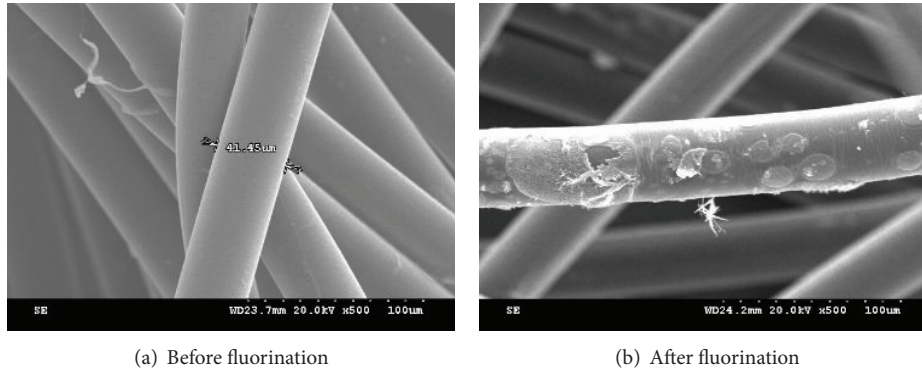


FIGURE 1: SEM images before and after fluorination of polypropylene fiber [9].

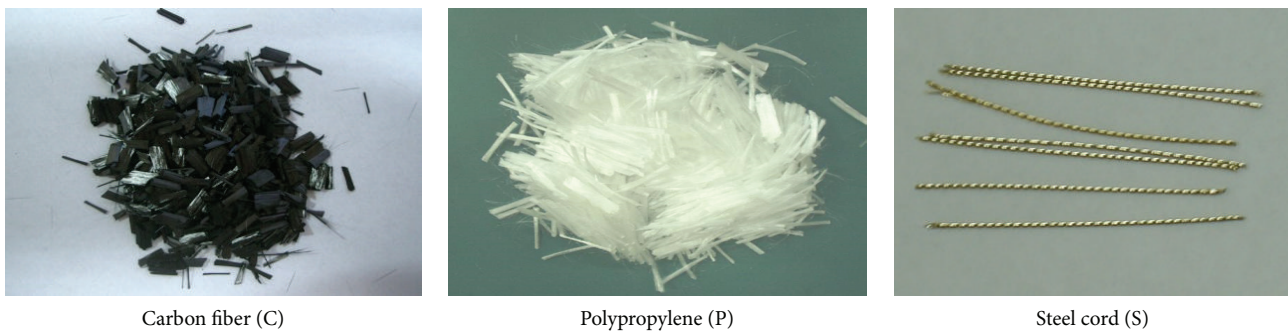


FIGURE 2: Images of composite fibers.

manner. After the transition from the debonding process to the pull-out process, the frictional bond is more dominant than the chemical bond in the pull-out process.

Therefore, in order to enhance the interfacial bond strength between the fiber and the cement composite matrix, various surface treatment techniques have been developed; these include plasma treatment, fiber fibrillation, fiber clamping, fiber twisting, and interface densification, the choice of which depends on the strength and strain capacity of the selected fiber [4]. Likely, many researches have been undertaken to enhance bond strength mechanically and chemically [5–8]. Among these possible surface enhancements, fluorination of carbon fiber and polypropylene fiber was used as a surface treatment in a previous study by the authors [9]. Figure 1 shows the difference in the polypropylene fiber before and after fluorination from scanning electron microscope (SEM) images. After fluorination, the abrupt discontinuity of the pull-out load was prevented after reaching the peak pull-out load.

This study is designed to assess the influential interface property characteristics with respect to the water-to-binder ratio of a composite mix, the embedment length of the fibers, and the type of fiber. These experimental results will allow the development of a rational analytical model to describe the bond behavior of FRCCs. For this purpose, an experimental program was carried out, and an adopted analytical model was implemented to obtain the design parameters.

2. Experimental Program

To investigate the pull-out mechanisms, both experimental research and theoretical research into single-fiber pull-out in a cementitious composite were undertaken in this study. Experimental testing was designed for three types of fiber (carbon fiber, polypropylene, and twisted strand steel cord), various embedment lengths (17% to 50% of the fiber length), and two water-to-binder ratios (0.4 and 0.5). The specimen designations are in the order of water/binder ratio, fiber type, and embedment length. For example, 0.4C7.5 indicates that the water-to-binder ratio is 0.4, the fiber type is carbon fiber, and the embedment length is 7.5 mm.

Figure 2 shows the different composite fiber types, and Table 1 presents the dimensions and mechanical properties of the composite fibers.

At least three specimens were prepared for each fiber type case and water-to-binder ratio and embedment length, as shown in Table 2. All specimens were cured in water for 14 days at $40^{\circ}\text{C} \pm 5^{\circ}\text{C}$ until testing. A cubic mold ($50 \times 50 \times 50$ mm) was used to determine the compressive strength of the cement composites. Tables 3 and 4 show the material properties and mix proportions used in the cement composites, respectively.

This study used a typical test set-up for the single-fiber pull-out testing of the specimens. The pull-out force and slippage displacement at the ends (tips) were recorded by

TABLE 1: Dimensions and mechanical properties of composite fibers.

Type	Diameter (μm)	Fiber length, L_f (mm)	Aspect ratio	Tensile strength (MPa)	Elastic modulus (GPa)
Carbon fiber (C)	7	6	857	3500	120
Polypropylene (P)	40	15	375	600	3.7
Steel cord (S)	405	32	79	2300	206

TABLE 2: Parameters for testing.

Fiber type	Water/binder (w/b)	Embedment length, L_e (mm)		Number of specimens
Carbon fiber (C)	0.4	1.0	17% of L_f	3
	0.5	1.5	25% of L_f	3
		3.0	50% of L_f	3
Polypropylene fiber (P)	0.4	3.75	25% of L_f	5
	0.5	5.0	33% of L_f	5
		7.5	50% of L_f	5
Steel cord (S)	0.4	7.5	24% of L_f	5
	0.5	15	47% of L_f	5

TABLE 3: Material properties for cement composites.

Cement	High early strength cement, density: 3.17 g/cm^3 , fineness: $3,230 \text{ cm}^2/\text{g}$
Sand	Silica sand, density: 2.64 g/cm^3 , grade: 0.1~0.3 mm
Fly-ash	Density: 2.13 g/cm^3 , fineness: $2,976 \text{ cm}^2/\text{g}$
High water-reducing agent	Polycarboxylate

a data acquisition system during the tests. The specimens were tested under increasing monotonic pull-out loading using 30-kN capacity universal testing machine (INSTRON) with displacement control at a rate of 0.2 mm/min until the fibers were pulled out. Figure 3 shows a schematic test set-up for the single-fiber pull-out test.

3. Results and Discussion

3.1. Pull-Out and Slippage Characteristics. Regardless of the fiber type, the pull-out load increased almost linearly at the beginning of the test, followed by abrupt discontinuity after reaching the peak pull-out load due to the loss of the friction-adhesive bond. Subsequently, nonlinear behavior was observed due to the reduction of the interfacial adhesion capacity between the fiber and the cement composite matrix. Figure 4(a) shows the interfacial surfaces of the cement composites after the polypropylene fiber was pulled out. The surface texture is smooth without voids, and no noticeable defects can be seen in the cement composite matrix and fibers as shown in Figures 4(b), 4(c), and 4(d).

3.2. Effect of Water-to-Binder Ratio and Embedment Length (L_e) for Carbon Fiber. The water-to-binder ratio may affect the interfacial bond strength between the fiber and the cement composite matrix. Figures 5(a) and 5(b) present the pull-out load versus pull-out slip results for the specimens with carbon fiber. Table 5 presents a summary of the test results from this study. The initial stiffness values were computed based on the slippage distance at the load that corresponds to 30% of the peak pull-out load.

As the water-to-binder ratio increased, the peak pull-out load was not affected significantly. However, the postpeak pull-out load values for the 0.5C1.5 and 0.5C1.0 specimens dropped rapidly after reaching the peak pull-out load. The 0.5C1.5 and 0.5C3.0 specimens tended to exhibit gradually decreasing pull-out loads after reaching the peak pull-out load, and specimen 0.5C3.0 showed better resistance to deformation and toughness until the carbon fiber was fully pulled out. However, the initial stiffness values of the specimens with the water-to-binder ratio of 0.4 were similar to those of the corresponding specimens with a water-to-binder ratio of 0.5.

As the embedment length of the fiber increased, the chemical bond strength also increased, whereas the frictional bond strength slightly decreased, even when the embedment length increased. These results may be due to the fact that the incremental increase in the interfacial bond surface area with the carbon fiber was compensated by the reduction in interfacial bond strength.

For the specimens with polypropylene fiber, the peak pull-out load was not affected significantly, as indicated by the increasing strength of the matrix, as seen in Figures 6(a) and 6(b). However, no sudden load drop occurred after the peak pull-out load, except for specimen 0.5P3.75. The specimens with polypropylene fiber tended to exhibit gradually increasing and decreasing pull-out loads due to

TABLE 4: Mix proportions for cement composites.

Fiber type	w/b (wt.)	FA/B (wt.)	Cement	Unit weight (kg/m ³)			f'_c (MPa)
				Water	Fly-ash	Sand	
C	0.40	0.20	762	381	191	627	54
	0.50	0.20	672	420	168	627	46
P	0.40	0.20	762	381	191	627	54
	0.50	0.20	672	420	168	627	44
S	0.40	0.20	762	381	191	627	54
	0.50	0.20	672	420	168	627	46

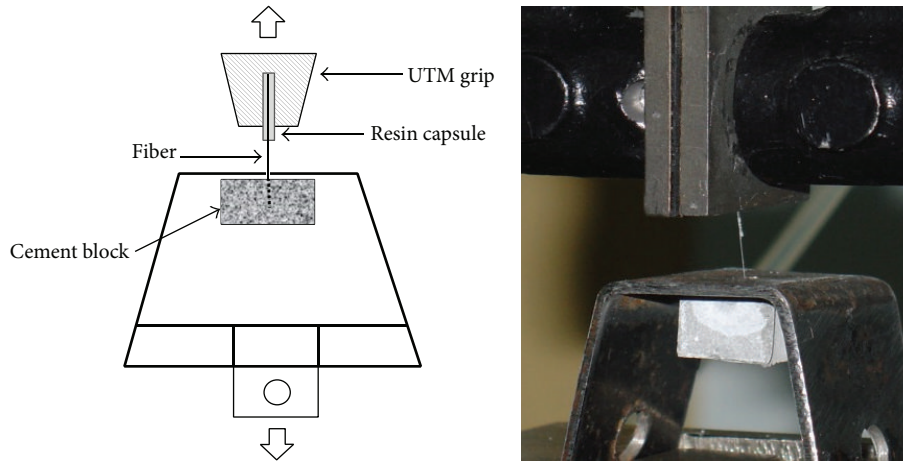


FIGURE 3: Schematic drawing for single-fiber pull-out test and photograph of test set-up.

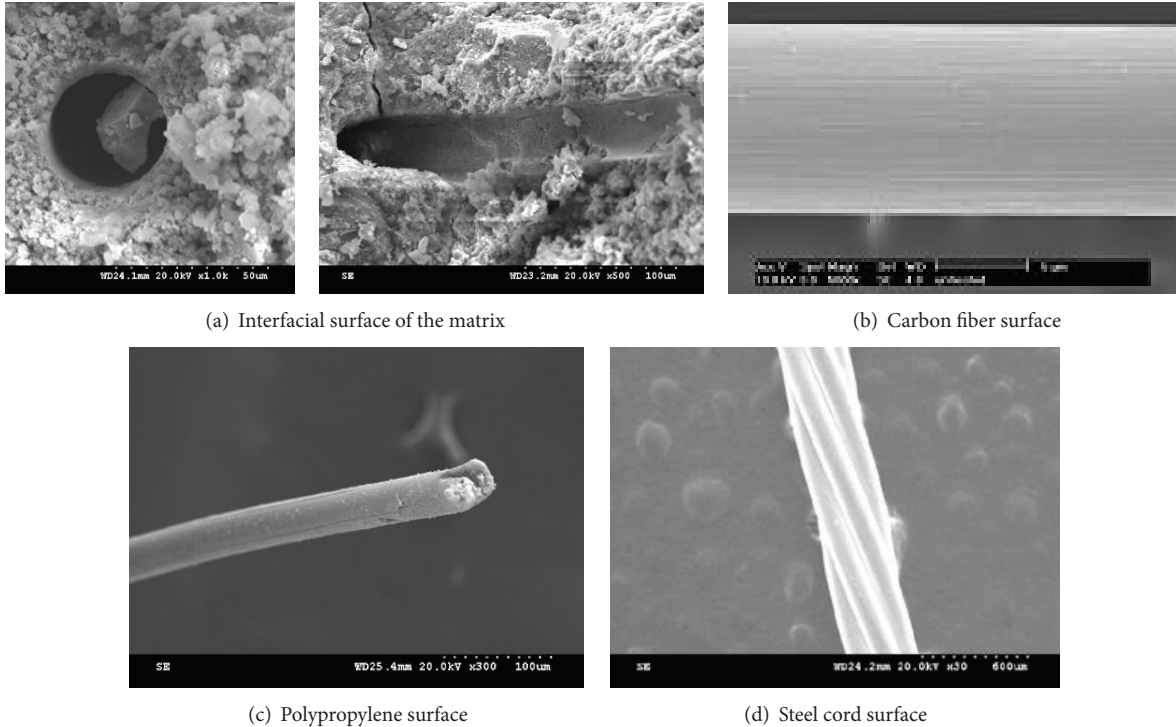


FIGURE 4: Interfacial surfaces of the cement composite matrix and fiber surfaces.

TABLE 5: Summary of test results.

I.D.	δ_0 (mm)	δ (mm)	Initial stiffness (N/mm)	Peak pull-out load (N)
0.4C3.0	0.098	0.150	3.940	0.616
0.4C1.5	0.088	0.143	3.700	0.460
0.4C1.0	0.093	0.137	2.380	0.340
0.5C3.0	0.110	0.222	3.613	0.603
0.5C1.5	0.109	0.150	2.756	0.503
0.5C1.0	0.100	0.155	2.241	0.309
0.4P7.5	0.276	1.316	2.252	0.405
0.4P5.0	0.310	0.918	0.777	0.306
0.4P3.75	0.277	0.735	0.870	0.228
0.5P7.5	0.323	1.763	2.346	0.374
0.5P5.0	0.386	1.288	0.711	0.298
0.5P3.75	0.279	0.703	1.096	0.199
0.4S15	0.226	0.443	845.1	207.4
0.4S7.5	0.302	0.465	391.6	171.85
0.5S15	0.250	0.408	510.0	170.44
0.5S7.5	0.284	0.552	349.3	135.76

Note: δ is the pull-out displacement; δ_0 corresponds to the displacement at which full debonding is completed.

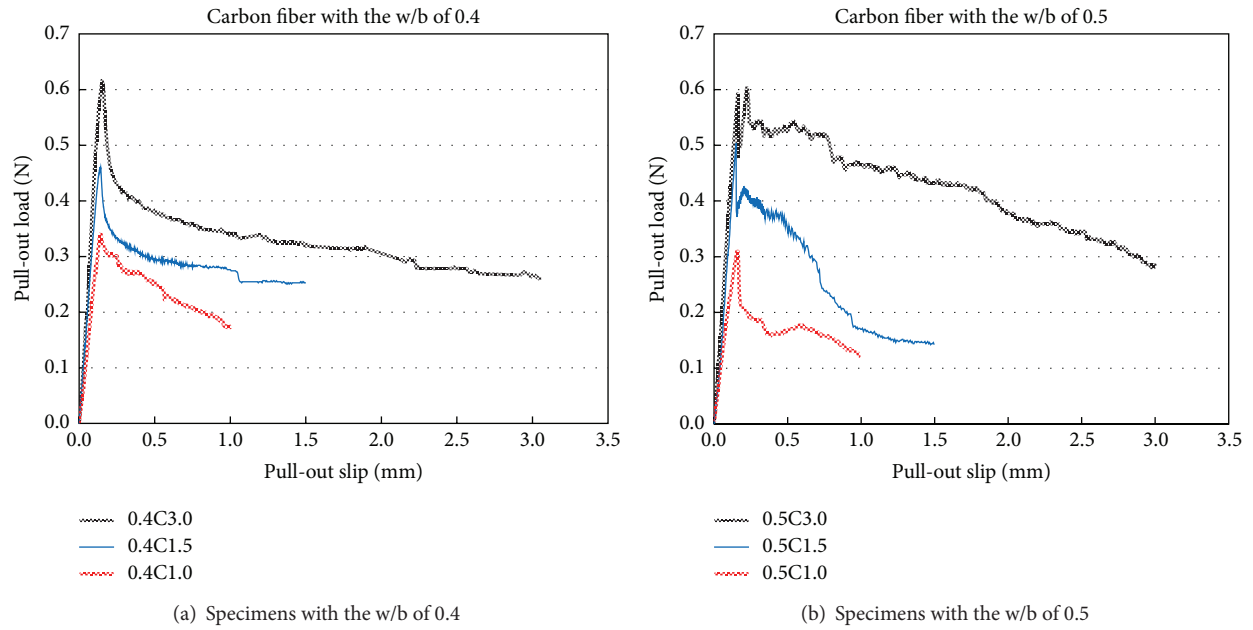


FIGURE 5: Pull-out load versus slip at the ends for specimens with carbon fiber.

the low elastic modulus value of the polypropylene fiber. For specimen 0.4P7.5, the postpeak behavior after reaching the maximum pull-out force was maintained at a plateau, which indicates its superior resistance to deformation and toughness, although the peak pull-out load was slightly low. On the other hand, the initial stiffness and bond strength values were similar regardless of the water-to-binder ratio.

In terms of water-to-binder ratio, for the specimens with an embedment length of 7.5 mm with water-to-binder ratios of 0.4 and 0.5, the maximum pull-out force increased as the water-to-binder ratio decreased. These results for the

interface friction and bond strength are due to the formation of a more condensed matrix. Similar results were observed for the specimens with the embedment length of 5 mm.

In short, a sufficient embedment length leads to mechanical bond strength and fiber plastic deformation. With a decrease in the embedment length, the maximum pull-out force is reduced.

Strain softening also was observed in this study. In general, the pull-out load increased as the embedment length increased for all three fibers regardless of the water-to-binder ratio. In particular, the pull-out response for

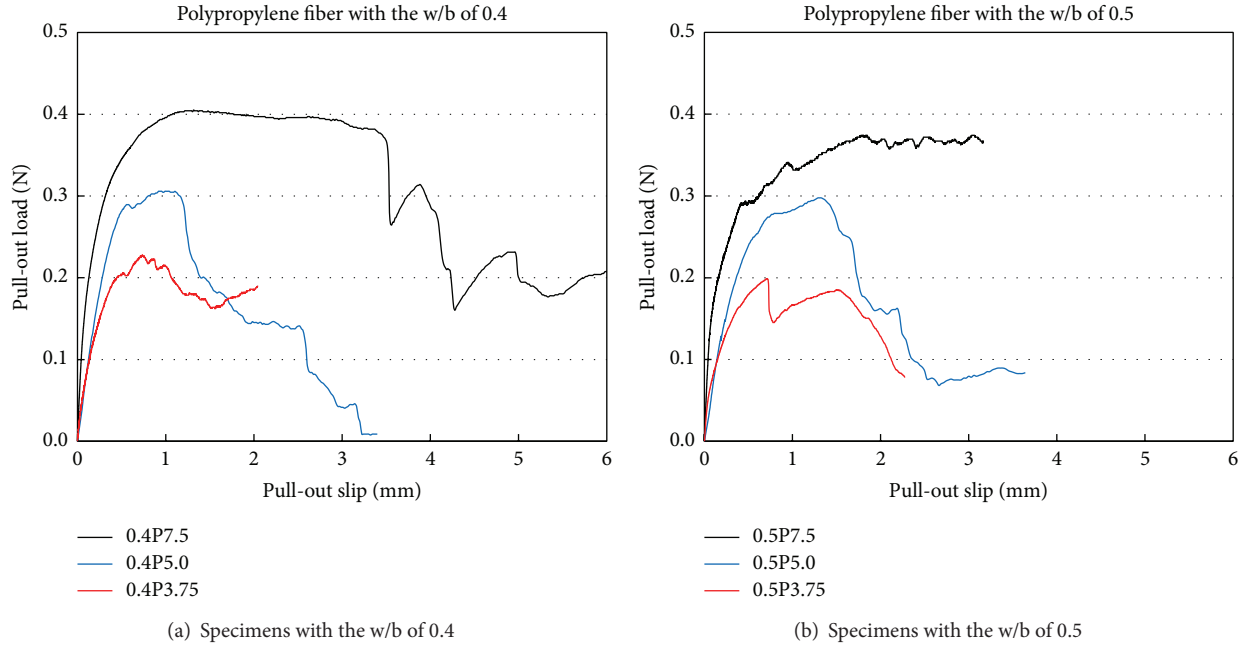


FIGURE 6: Pull-out load versus slip at the end for specimens with polypropylene fiber.

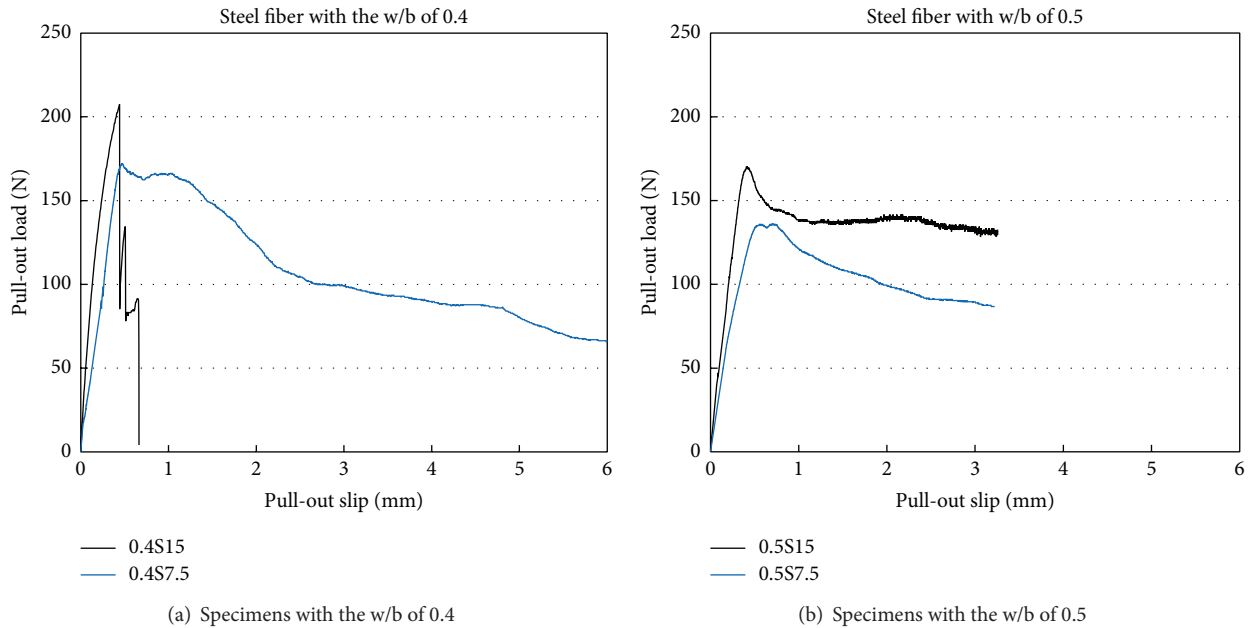


FIGURE 7: Pull-out load versus slip at the end for specimens with steel fiber.

the specimen with polypropylene fiber with 7.5 mm embedment length exhibited slip-hardening behavior without any surface treatment of the fibers.

For the specimens with steel fiber, Figures 7(a) and 7(b) show that the pull-out load increased linearly up to the peak pull-out load. The initial stiffness value of specimen 0.4S15 is high in comparison to the other specimens in that the fiber completely debonded without ductility. The slippage dropped rapidly after reaching the peak pull-out load due to the failure

of the fire breakage. For the remaining specimens, the pull-out force decreased gradually with slippage hardening effects.

Similarly, a sufficient embedment length was shown to enhance the mechanical bond strength and the fiber plastic deformation. As the embedment length decreased, the peak pull-out load also decreased. On the other hand, tensile rupture failure was observed for specimen 0.4S15 with steel fiber. Therefore, a shorter embedment length indicates expected slip-hardening effects for ductile behavior.

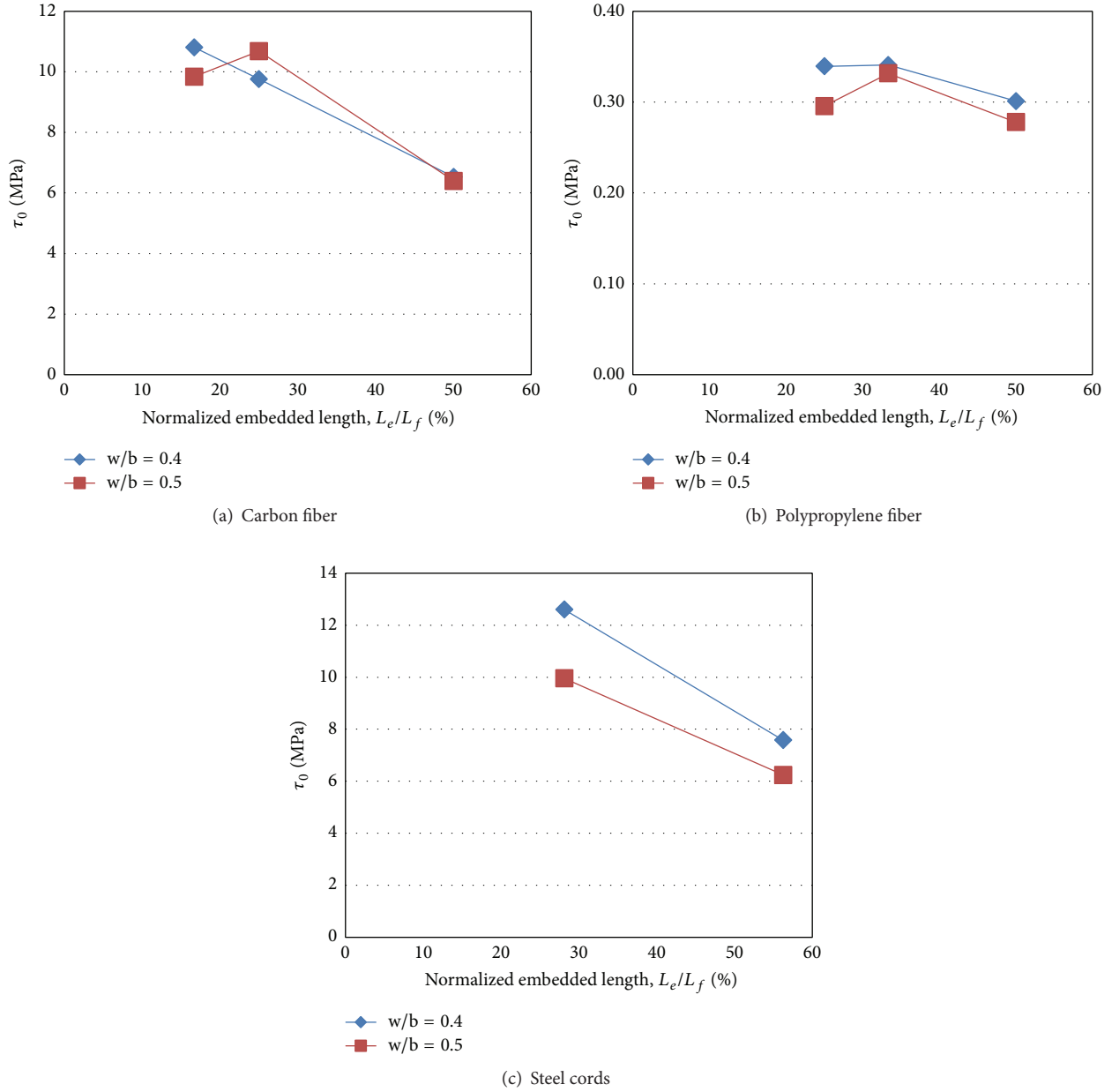


FIGURE 8: Frictional bond stress (τ_0) with respect to normalized embedment length (L_e/L_f).

4. Numerical Methods to Determine Interface Properties

Three typical descending behaviors were observed after the peak pull-out load: slip softening, constant friction, and slip-hardening in the fiber slippage phase [10]. Two numerical models can be found in the literature regarding these phenomena: a strength-controlled model and a fracture-controlled model. The fracture-controlled model that is adopted in this study is known to be capable of predicting fiber slippage. According to the literature [4, 11], because relative slippage between the fiber and the matrix in

the debonded portion is limited to a small area, the initial friction bond stress (τ_0) within the debonded zone remains at a constant so that the initial frictional bond stress can be expressed as

$$\tau_0 = \frac{P_b}{\pi d_f L_e}, \quad (1)$$

where P_b is the load after the sudden drop following the peak pull-out load (70% of P_a); L_e is the fiber embedment length; and d_f is the diameter of the fiber.

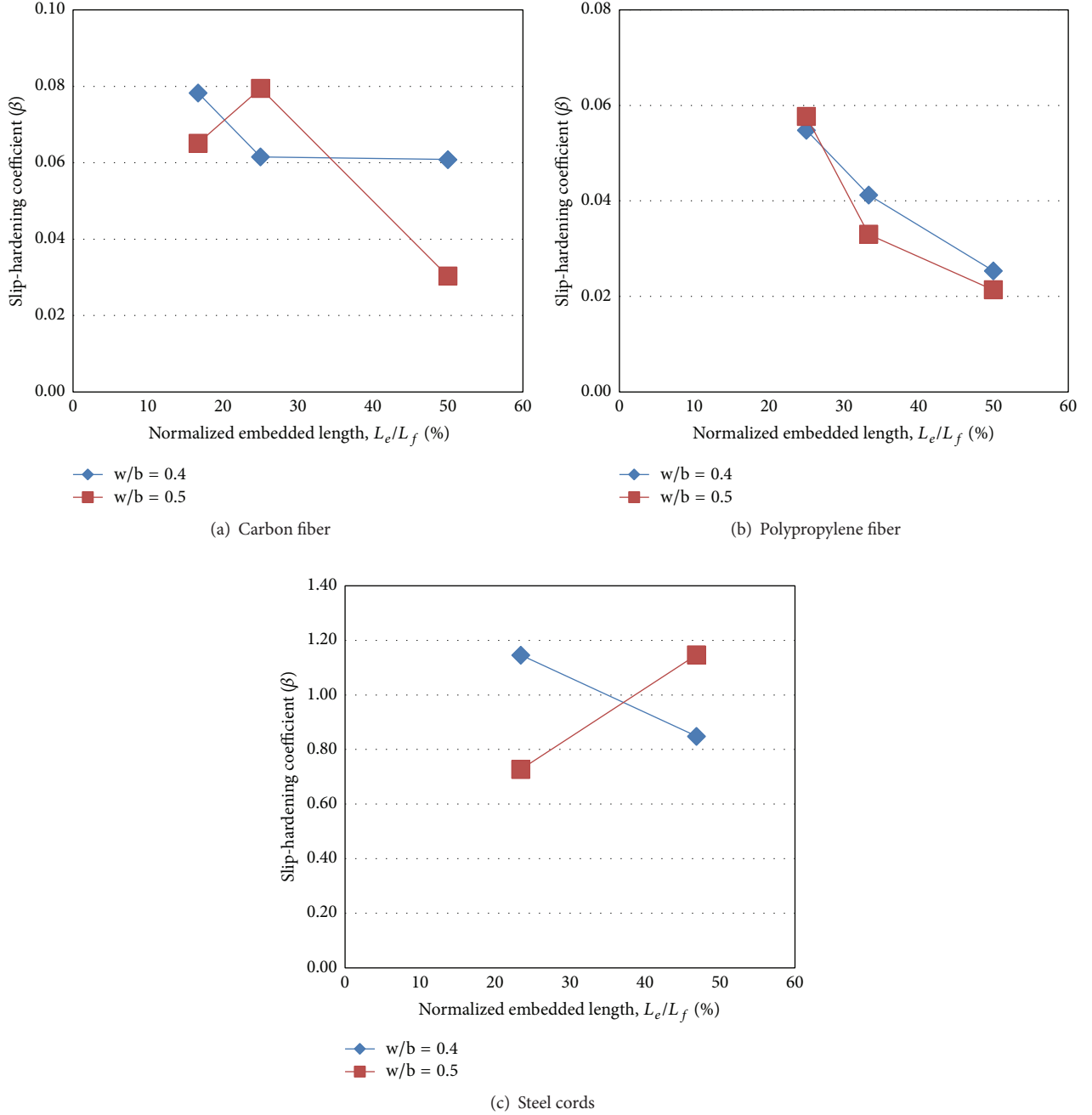


FIGURE 9: Slip-hardening coefficient (β) with respect to normalized embedment length (L_e/L_f).

After reaching the peak pull-out load (P_a), the interface shear stress cannot be determined solely using the friction stress that results from the pulling-out process of the fiber. So, the interface shear stress can be expressed using the slip-hardening coefficient (β) and slip distance (S):

$$\tau = \tau_0 \left(1 + \frac{\beta S}{d_f} \right). \quad (2)$$

The relationship between theoretical pull-out load P and pull-out slip δ can be expressed by [11]:

$$P = \begin{cases} \sqrt{\frac{\pi^2 \tau_0 E_f d_f^3 (1 + \eta)}{2} \delta + \frac{\pi G_d E_f d_f^3}{2}}, & 0 \leq \delta \leq \delta_0, \\ \pi d_f \tau_0 \left(1 + \frac{\beta (\delta - \delta_0)}{d_f} \right) (L_e - \delta + \delta_0), & \delta_0 \leq \delta \leq L_e, \end{cases} \quad (3)$$

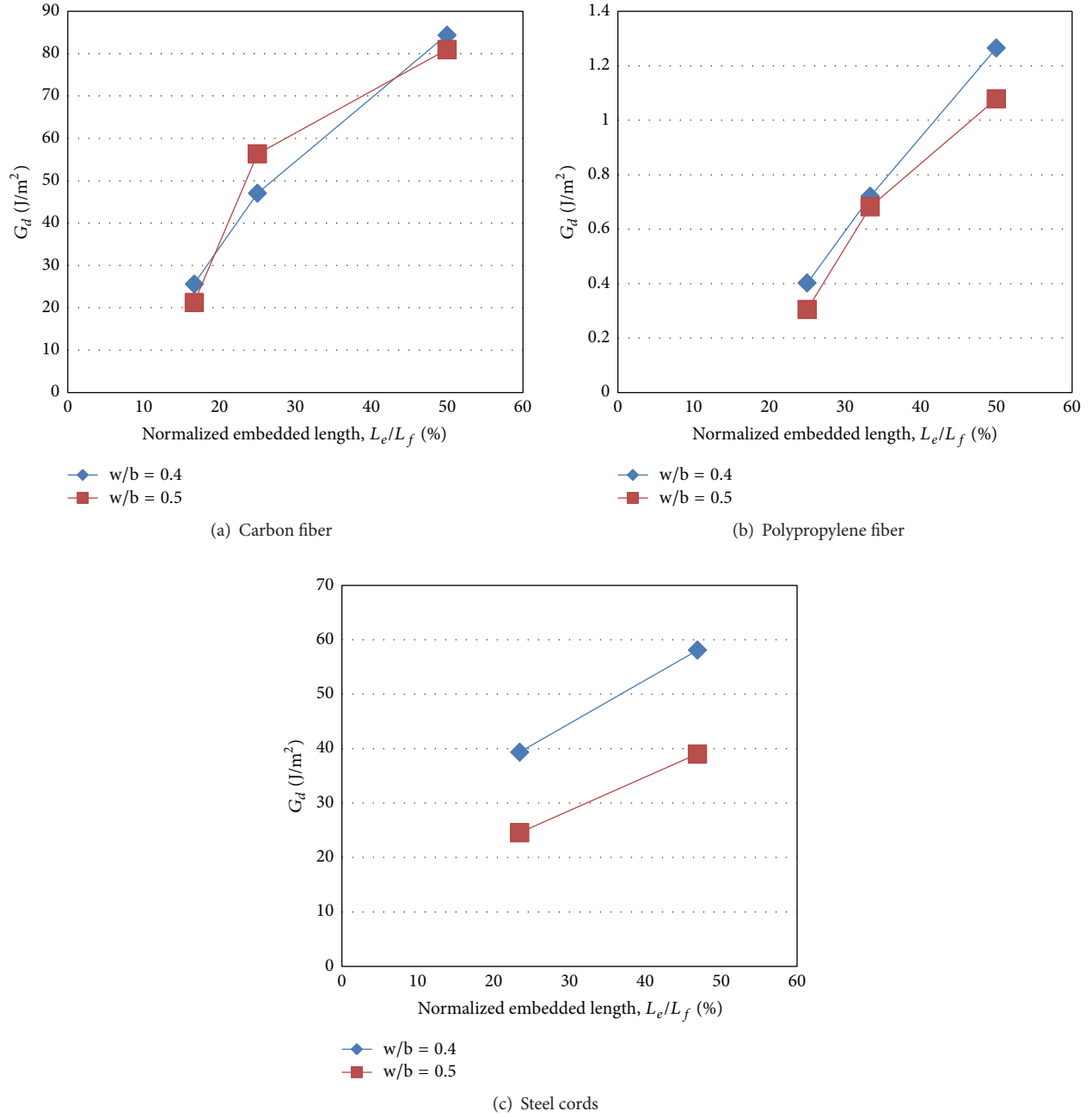


FIGURE 10: Chemical bond stress (G_d) with respect to normalized embedment length (L_e/L_f).

where δ is the pull-out displacement; δ_0 corresponds to the displacement at which full debonding is completed; G_d is the chemical bond strength (J/m^2); E_f is the elastic modulus of the fiber; $\eta = V_f E_f / V_m E_m$, E_m is the elastic modulus of the matrix; and V_f and V_m are the volume fractions of the fiber and matrix, respectively. η can be neglected in a single-fiber pull-out test.

These predictive equations have been validated in the literature [11] and adopted here to develop design parameters for various fibers associated with embedment length and water/binder ratio. The test results for each specimen were

used in this study to calculate the interfacial bond stress, slip-hardening coefficient (β), and chemical bond strength (G_d). G_d value implies the interfacial fracture energy and can be computed by

$$G_d = \frac{2(P_a - P_b)^2}{\pi^2 E_f d_f^3}. \quad (4)$$

This fracture energy indicates the energy that is absorbed by the bridging action of the fibers over the cracked plane. It can be used to determine the optimal fiber length. The chemical

bond stress tends to reduce the fracture energy because it leads to the rupture of the fiber.

The adopted model in this study allows the interface properties of fibers, such as carbon fiber, polypropylene fiber, and steel cord fiber, to be expressed quantitatively. Figure 8 indicates that low frictional bond stress levels (τ_0) were observed as the water-to-binder ratio increased, thereby resulting in a low elastic modulus value for mixtures with a high water-to-binder ratio. Moreover, the increasing porosity of the cement composite mixture in the interfacial zone that occurs as the water-to-binder ratio increases leads to a reduction of the fiber-matrix contact surface, which may result in lower frictional bond stress. Furthermore, in this study, low frictional bond stress (τ_0) was observed as the embedment length increased, which resulted in the lower elastic modulus value of the mixtures with a high water-to-binder ratio.

The slip-hardening coefficients (β) presented in Figure 9 were computed by best-fitting the curve for each specimen, as shown in Figures 5–7. For the polypropylene fiber, β values are in the range of 0.005 to 0.05 based on the literature and 0.02 to 0.06 based on this study. For the steel fiber, β value is around 1 from the literature and in the range of 0.65 to 1.18 from this study. The study results for both fibers match well with those found in the literature [12].

Figure 10 shows the chemical bond stress (G_d) results versus the normalized embedment lengths. For a short fiber with a low aspect ratio, the literature indicates that the pull-out force is controlled by the initial debonding stress, which is consequently governed by the chemical bond. For a specimen with steel fiber with a low aspect ratio (79 for the steel fiber), as the chemical bond strength increases, the pull-out load increases noticeably, as shown in Figure 10(c).

As the fiber lengthens, the subsequent pull-out process after the initial debonding process results in an active bridging action and stronger pull-out force. The pull-out force becomes almost independent of the fiber length when the fiber is excessively long and/or the chemical bond is excessively strong [11].

5. Conclusion

This research was undertaken to establish a design methodology for composites using single-fiber pull-out tests. For this purpose, the study presents the characteristics of both fiber-matrix interfacial properties and fiber rupture. The results of these tests allow specific design parameters to be evaluated quantitatively:

- (1) As the compressive strength of the cement composite and the embedment length of a single fiber increased incrementally, the pull-out force also increased.
- (2) The slip-hardening coefficients (β) for specimens with steel fiber ranged from 0.65 to 1.18 in this study. For specimens with polypropylene fiber, β value was in the range of 0.02 to 0.06. These results match well with the results found in the literature. In the same manner, β value for the carbon fiber was in the range of 0.03 to 0.08.

- (3) The chemical bond strength was relatively stable and was independent of the water-to-binder ratio of the matrix and fiber that had a high aspect ratio, which is contrary to the behavior that was resultant of the friction bond strength. The fracture-controlled theory adopted here was found to be capable of reasonably interpreting and reproducing the single-fiber pull-out test data.

Conflict of Interests

The authors declare that there is no conflict of interests regarding the publication of this paper.

Acknowledgment

The work reported here was financially supported by Gachon University research fund of 2014 (GCU-2014-0105).

References

- [1] J. M. Alwan, A. E. Naaman, and W. Hansen, "Pull-out work of steel fibers from cementitious composites: analytical investigation," *Cement and Concrete Composites*, vol. 13, no. 4, pp. 247–255, 1991.
- [2] V. C. Li, H. C. Wu, and Y. W. Chan, "Interface property tailoring for pseudo strain-hardening cementitious composites," in *Advanced Technology for Design and Fabrication of Composite Materials and Structures*, vol. 14 of *Engineering Applications of Fracture Mechanics*, pp. 261–268, Springer, Amsterdam, The Netherlands, 1995.
- [3] V. C. Li and H. Stang, "Interface property characterization and strengthening mechanisms in fiber reinforced cement based composites," *Advanced Cement Based Materials*, vol. 6, no. 1, pp. 1–20, 1997.
- [4] T. Kanda and V. C. Li, "Interface property and apparent strength of high-strength hydrophilic fiber in cement matrix," *Journal of Materials in Civil Engineering*, vol. 10, no. 1, pp. 5–13, 1998.
- [5] V. M. C. F. Cunha, J. A. O. Barros, and J. M. Sena-Cruz, "Pullout behavior of hooked-end steel fibres in self-compacting concrete," *Journal of Materials in Civil Engineering*, vol. 22, no. 1, pp. 1–9, 2010.
- [6] Y. Lee, S.-T. Kang, and J.-K. Kim, "Pullout behavior of inclined steel fiber in an ultra-high strength cementitious matrix," *Construction & Building Materials*, vol. 24, no. 10, pp. 2030–2041, 2010.
- [7] P. Di Maida, E. Radi, C. Sciancalepore, and F. Bondioli, "Pullout behavior of polypropylene macro-synthetic fibers treated with nano-silica," *Construction and Building Materials*, vol. 82, pp. 39–44, 2015.
- [8] Y.-W. Chan and S.-H. Chu, "Effect of silica fume on steel fiber bond characteristics in reactive powder concrete," *Cement and Concrete Research*, vol. 34, no. 7, pp. 1167–1172, 2004.
- [9] H. D. Yun, E. Jeon, W. S. Park, B. C. Han, I. S. Yang, and Y. S. Lee, "Pull-out response and surface treatment of carbon fiber with fluorination," *Journal of the Architectural Institute of Korea Structure & Construction*, vol. 21, no. 8, pp. 27–34, 2005 (Korean).

- [10] T. Nakajima, *Fluorine-Carbon and Fluoride-Carbon Materials*, CRC Press, 1995.
- [11] Z. Lin, T. Kanda, and V. C. Li, "On Interface property characterization and performance of fiber-reinforced cementitious composites," *Journal of Concrete Science and Engineering*, vol. 1, pp. 173–184, 1999.
- [12] F. Aslani and S. Nejadi, "Bond characteristics of steel fibre reinforced self-compacting concrete," *Canadian Journal of Civil Engineering*, vol. 39, no. 7, pp. 834–848, 2012.

Research Article

Behavior and Performance of GFRP Reinforced Concrete Columns with Various Types of Stirrups

**Woraphot Prachasaree,¹ Sitthichai Piriyaootorn,¹
Athawit Sangsrijun,² and Suchart Limkatanyu¹**

¹Department of Civil Engineering, Faculty of Engineering, Prince of Songkla University, Hat Yai, Songkhla 90112, Thailand

²Program in Landscape Technology, Faculty of Agricultural Technology, Rajamangala University of Technology Thanyaburi, Thanyaburi, Pathum Thani 12110, Thailand

Correspondence should be addressed to Woraphot Prachasaree; pworaphot@eng.psu.ac.th

Received 2 August 2015; Revised 5 September 2015; Accepted 9 September 2015

Academic Editor: João M. L. Dos Reis

Copyright © 2015 Woraphot Prachasaree et al. This is an open access article distributed under the Creative Commons Attribution License, which permits unrestricted use, distribution, and reproduction in any medium, provided the original work is properly cited.

Fiber reinforced polymer (FRP) composites are gaining acceptance in concrete structural applications due to their high ratio of strength/stiffness to self-weight and corrosion resistance. This study focused on the structural behavior and the performance of concrete columns internally reinforced with glass fiber reinforced plastic (GFRP) rebars. Twelve series of concrete columns with varied longitudinal reinforcement, cross section, concrete cover, and type of lateral reinforcement were tested under compression loading. The results show that the amount of GFRP longitudinal and lateral reinforcement slightly affects the column strength. The lateral reinforcement affects the confining pressure and inelastic deformation, and its contribution to the confined compressive strength increases with the GFRP reinforcement ratio. In addition, the confining pressure increases both concrete strength and deformability in the inelastic range. The confinement effectiveness coefficient varied from 3.0 to 7.0 with longitudinal reinforcement. The average deformability factors were 4.2 and 2.8 with spirals and ties, respectively. Lateral reinforcement had a more pronounced effect on deformability than on column strength.

1. Introduction

In general, concrete structures with conventional steel reinforcement have about 50 years of service life in an aggressive environment, such as in infrastructure highways and bridges with exposure to deicing salts, in marine structures, in waste water facilities, and in chemical treatment plants. In such conditions the corrosion of steel reinforcement leads to deterioration of the concrete structures and to loss of serviceability. This deterioration is one of the most serious problems in civil and infrastructural engineering. Such facilities incur tremendous repair costs annually. The replacement of steel with noncorroding materials, such as fiber reinforced plastics (FRPs), could be effective in alleviating these problems. The structural conditions of infrastructures would require long-term durability and a high degree of performance. In reinforced concrete columns, epoxy-coated steel rebars have

been used as a corrosion resistant alternative. However, this approach has its limitations because of the costs and the delayed but eventual susceptibility to corrosion. In the past decade, studies have been published on the performance and behavior of concrete structural members internally reinforced with FRPs. Fourteen concrete beam columns internally reinforced with glass fiber reinforced plastic (GFRP) rebars were experimentally investigated under compression and bending in [1]. The results showed that the maximum capacity of GFRP reinforcing rebars could only reach 70% of their tensile strength in pure flexure and 20–30% of ultimate compressive strength under axial compression. Twelve concrete columns reinforced with aramid fiber reinforced plastic (AFRP) rebars were tested under eccentric applied tension or compression [2]. It was concluded that the analysis methods for steel reinforced concrete columns were appropriate also for concrete columns reinforced with AFRP rebars.

Kobayashi and Fujisaki [3] studied the behavior of concrete columns with various types of longitudinal reinforcement using FRP rebars. The reinforced concrete columns were subjected to concentric loading, and the failure modes were reported as concrete crushing or compressive or tensile rupture of the FRP reinforcement. In addition, the ductile failures of columns were primarily influenced by the compressive strength of the FRP rebars. A comparative study between steel and FRP reinforced concrete columns was presented by Alsayed et al. [4]. Fifteen reinforced concrete columns with different combinations of steel and GFRP rebars were tested under concentric compression. The results showed about 10 percent strength reduction in the GFRP reinforced concrete cylinders with different spacings (10, 20, 35, and 50 mm) of aramid spiral stirrups were studied by Leung and Burgoyne [5]. The experimental results showed that the peak load capacity of test cylinders decreased with the spiral pitch. Eleven concrete cylinders internally reinforced with CFRP rebars were experimentally investigated under eccentric loads in [6] (Sharbatdar, 2003). The average concrete core strength with smaller stirrup spacing was slightly higher than with larger stirrup spacing. In 2005, Sharma et al. [7] studied the relation between the axial load capacity of a square concrete column and the GFRP reinforcement ratio. The ductility increased with the reinforcement ratio. The axial load and bending moment interaction curves for concrete columns reinforced with FRP rebars were generated by Choo et al. [8]. The FRP reinforcement contribution in the compression zone was ignored, and it was suggested that the reinforcement ratio must be at least 0.6 percent to avoid brittle failure. The performance and behavior of concrete columns, internally reinforced with GFRP rebars and CFRP spiral warps, were studied under concentric loads by Francis and Teng [9]. The experimental results showed that the load capacity of tested columns increased insignificantly when using higher elastic modulus GFRP rebars. Also, a small increase in the core confinement, strength, and stiffness of tested columns was achieved by decreasing the pitch of spiral warps. The structural performance of square concrete columns internally reinforced with GFRP rebars was evaluated under axial compressive load in [10]. The ductility increased with the main reinforcement ratios, rapidly with small ratios but the effects were quite low for large reinforcement ratios. The compression behavior of square concrete columns reinforced with FRP rebars and hoops stirrups was investigated by Tobbi et al. [11]. The nominal column capacity could be determined by using a 65 percent reduction in the tensile strength of FRP rebars. In a recent study, twelve circular concrete columns, reinforced with GFRP rebars and spirals, were tested under concentric axial loads [12]. The experimental results indicated that the concrete columns reinforced with GFRP rebars and steel reinforced concrete columns behaved in a similar manner. The average axial load capacity contributed by longitudinal GFRP rebars was from 5 to 10 percent of the maximum load capacity. For column design purposes, the FRP contribution to compressive strength could be neglected in the axial load capacity.

Moreover, performance and behavior of FRP confined concrete have widely interested many researchers over the last two decades. The compressive and confinement behavior of both concrete and reinforced concrete-filled fiber reinforced plastic tube were investigated through experiments. The results showed that the structural performance of test specimens was improved [13]. Numerous experimental and analytical studies have been conducted to understand and model the behavior of FRP confined concrete. Eighty-eight axial stress-strain models (published between 1991 and the end of 2011) of FRP confined concrete in circular sections were comprehensively reviewed by Ozbakkaloglu et al. [14]. All developed stress-strain models can be classified into two categories as follows: the design-orientated and analysis-orientated type. More than 700 experimental pieces of data of FRP confined concrete cylinders under monotonic axial compression were assessed through the previous stress-strain models. The assessment result showed that the stress-strain models developed by Lam and Teng [15] and Tamuzs et al. [16] provide the most accurate prediction of the ultimate strength and strain enhancement ratio, respectively. Recently, behavior of circular and rectangular high strength concrete-filled FRP tubes was experimentally studied under axial compression [17, 18]. The results showed that the specimen size did not significantly affect the compressive behavior of test specimens. The compressive behavior of test specimens was mainly influenced by fiber type and manufacturing method.

Many prior studies have assessed the performance and behavior of columns with GFRP rebars as longitudinal reinforcement and concrete-filled FRP tubes, as discussed above. However, at present most guidelines and standard codes of practice have no recommendations regarding FRP as longitudinal reinforcement in compression members. This might be due to the lack of rational design methodologies. The objective of this research was to experimentally evaluate the structural performance and investigate the behavior of GFRP reinforced concrete columns with various types of lateral reinforcement, to facilitate the future development of appropriate design principles.

2. Column Specimens

Twelve groups of concrete columns with different cross sections and reinforcement types were tested under concentric axial compressive load. For each group of concrete columns, three column specimens were cast and wet cured for 28 days before testing. The specimens were reinforced with ties, spirals or hoops, and longitudinal GFRP rebars. All specimens had the same 500 mm length. The height to diameter ratio was 3.3–4.0, depending on whether the column had a concrete cover or not. The concrete covers used were 15 mm thick. Thus, the ratio of the gross area to the concrete core area of the specimen section for both square and circular sections was equal to 1.44. For column specimens with longitudinal reinforcement, four GFRP rebars were used in this study. The main reinforcement ratio varied from 1.42 to 2.05 (from 1.91 to 2.63) for column specimens with square (circular) section. In addition, the area of lateral

TABLE 1: Characteristics of the test specimens.

Group number	Sample label	Cross section	Reinforcement	Stirrup	Cover (cm)	Dimension (cm)	ρ_{frp} (%)	ρ'_s (%)	f'_c (ksc)
C-1	SF-sc	Square (S)	FRP (F)	Spiral (s)	1.25 (c)	15.0 × 15.0	1.42	1.10	
C-2	SN-sc		—			15.0 × 15.0	—		
C-3	SF-sn		FRP (F)		— (n)	12.5 × 12.5	2.05		
C-4	SN-sn		—			12.5 × 12.5	—		
C-5	CF-sc	Circle (C)	FRP (F)	Spiral (s)	1.25 (c)	Ø 15.0	1.91	1.10	
C-6	CN-sc		—			Ø 15.0	—		
C-7	CF-sn		FRP (F)		— (n)	Ø 12.5	2.63		
C-8	CN-sn		—			Ø 12.5	—		
C-9	SF-tc	Square (S)	FRP (F)	Tied (t)	1.25 (c)	15.0 × 15.0	1.42		
C-10	SN-tc		—			15.0 × 15.0	—		
C-11	SF-tn		FRP (F)		— (n)	12.5 × 12.5	2.05		
C-12	SN-tn		—			12.5 × 12.5	—		

reinforcement was 0.011 times the concrete core area. To control failure region and prevent premature failure at the end zones of the test columns, the lateral reinforcement spacing in the end zones (~one-fourth of column height) was reduced to half the specific spacing in the middle zone. The details of the column specimens are summarized in Table 1 and Figure 1. In this study, we labeled the column specimens informatively with alphanumeric codes as follows. The initial “S” or “C” distinguishes between square and circular cross sections, and the next capital letter “F” or “N” indicates reinforcement with GFRP rebars or lack of main reinforcement. The second group in the labels starts with “s” or “t,” indicating spiral or tied reinforcement, and ends by indicating the concrete cover with a “c” or lack of it with an “n.”

3. Materials

The concrete used in this research was a Ready-mix, normal strength and weight concrete with 100 mm slump, obtained from a local supplier. Conventional steel round bars with diameter 6 mm and grade SR24 (yield strength of 240 MPa) were used for lateral steel reinforcement. Different types of lateral reinforcement, namely, circular spiral, rectangular spiral, and tied stirrups, were prepared with 50 mm spacing in the ~250 mm long middle zone of the column. The plain concrete columns were cast and tested after curing for 28 days. The unconfined plain concrete columns were prepared for dimensions identical with the GFRP reinforced columns that had different lateral reinforcement. Glass fiber reinforced polymer (GFRP) rods with 10 mm diameter were used for longitudinal reinforcement. The GFRP rebars provide excellent mechanical properties such as high tensile strength, absence of corrosion or good corrosion resistance, and light weight, in comparison to conventional steel rebars. These GFRP rebars had approximately 735 MPa tensile strength. However, the compressive strength of FRP rebars is significantly lower than their tensile strength [3, 19]. Due to the many different modes of failure (ACI 440.1R-06) that range from buckling of the entire rebars to local microbuckling of individual fibers, no standards exist yet for axial compression tests of FRP rebars. The anisotropy and inhomogeneity of

FRP rebar material are important factors that lead to complicated behavior under compressive loading and inaccurate test data. As reported in previous studies [3, 19], the compressive strength of FRP rebars must be reduced before estimating column load capacities. Deitz et al. [19] suggested a 50% reduction in the tensile strength of FRP rebars. In addition, the GFRP rebar compressive strength is 30 to 40 percent of its tensile strength, according to Kobayashi and Fujisaki [3]. It should be noted that the factor by which compressive strength is reduced depends on the fiber volume fraction, the type of polymer matrix, the manufacturing process, and the testing procedure, among other things.

4. Experimental Test Program

To investigate their structural performance and behavior, the concrete column specimens were tested under axial load. Cross section shape, use of concrete cover, and type of lateral reinforcement were varied to study their effects. Seven strain gages were mounted on each specimen at three positions on the column surface. To observe the reinforcement, two strain gages were attached to each surface of GFRP rebars and steel stirrups. To monitor the vertical displacement at the mid position lengthwise, linear variable differential transducers (LVDTs) with 150 mm gage length were used. The loads and vertical deformations were plotted for these effectively continuously recorded data. To conduct the monotonically compressive load test, the concrete column specimen was placed on a steel roller support, located on the steel base of a universal testing machine. Another steel roller support was placed on the top of the tested column. A concentrated compression load was applied to the thick steel plate over the top roller to distribute the compression load across the tested column specimen. A data acquisition system connected to all sensors as strain gages, LVDTs, and the load cell of the universal testing machine recorded the observational data. The test set-up is schematically presented in Figure 2.

5. Experimental Results and Discussion

The study investigated the performance and behavior of concrete columns with and without GFRP reinforcement,

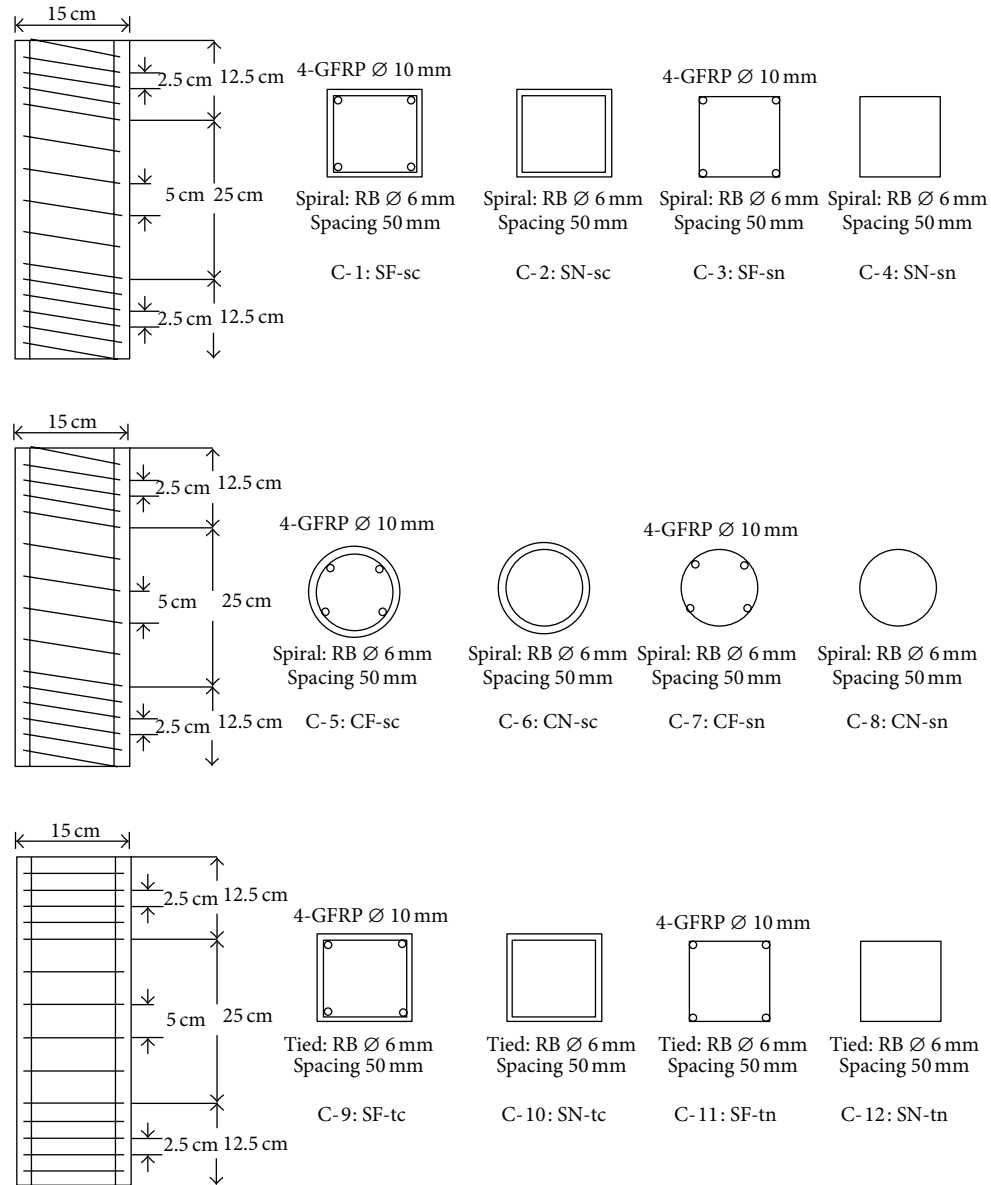


FIGURE 1: Geometry of the test specimens.

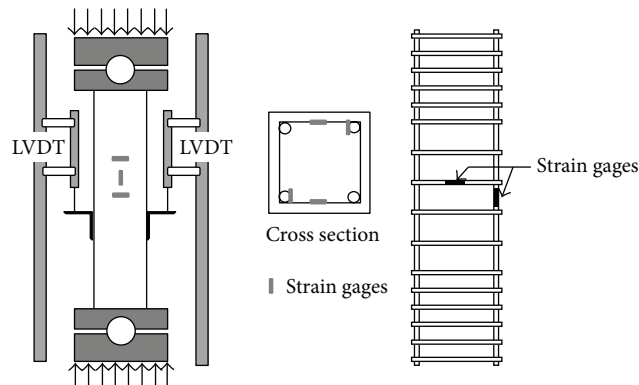


FIGURE 2: Schematic of the compression test set-up.

TABLE 2: Experimental test results.

Group sample	Number	ρ_{frp} (%)	Stirrup	@ Maximum compressive		Avg. ratio		@ Maximum compressive Column axial strain (mm/mm)
				Strength (kN)	Stress (MPa)	f'_{cc}/f'_c	% of difference	
C-1 SF-sc	1	1.42	Spiral (s)	380	16.9	1.643	0.218	0.005
	2			340	15.1			0.004
	3			390	17.3			0.007
C-2 SN-sc	1	—	Spiral (s)	—	—	1.425		—
	2			330	14.7			0.005
	3			310	13.8			0.005
C-3 SF-sn	1	2.05	Spiral (s)	360	23.0	2.085	0.454	0.004
	2			370	23.7			0.004
	3			—	—			—
C-4 SN-sn	1	—	Spiral (s)	240	15.4	1.631		0.005
	2			285	18.2			0.006
	3			285	18.2			0.006
C-5 CF-sc	1	1.91	Spiral (s)	320	18.1	1.892	0.429	0.006
	2			—	—			—
	3			370	21.5			0.007
C-6 CN-sc	1	—	Spiral (s)	280	15.8	1.440		0.003
	2			270	15.3			0.006
	3			250	14.1			0.007
C-7 CF-sn	1	2.63	Spiral (s)	310	25.3	2.427	0.463	0.004
	2			—	—			—
	3			320	26.1			0.004
C-8 CN-sn	1	—	Spiral (s)	—	—	1.964		—
	2			250	20.4			0.003
	3			260	21.2			0.005
C-9 SF-tc	1	1.42	Tied (t)	355	16.0	1.635	0.228	0.003
	2			375	16.7			0.004
	3			—	—			—
C-10 SN-tc	1	—	Tied (t)	320	14.2	1.407		0.006
	2			320	14.2			0.004
	3			310	13.8			0.005
C-11 SF-tn	1	2.05	Tied (t)	—	—	2.098	0.552	—
	2			375	24.0			0.007
	3			360	23.0			0.006
C-12 SN-tn	1	—	Tied (t)	277	17.7	1.515		0.003
	2			250	16.0			0.006
	3			270	17.2			0.007

with and without concrete cover, and with various types of lateral reinforcement. The experimental results in terms of maximum load capacity and column axial strain are shown in Table 2. In general, the load-deflection relation (illustrated in Figures 3–5) of a concrete column internally reinforced with FRP rebars was quite similar to that of conventionally reinforced concrete columns. It was found that deflections increased linearly with increases of load until the concrete columns reached the maximum load capacity. Vertical cracks and crushing were found on the concrete cover that also showed spalling depending on the type of lateral reinforcement. After the concrete cover spalled off, the longitudinal reinforcements were split by lateral displacement. Then the concrete core was crushed and the longitudinal reinforcements buckled outwards between the lateral reinforcements, as shown in Figure 6. In general, the axial load capacity of

a reinforced concrete column was determined both by the concrete and the longitudinal reinforcement and by their interactions. The contribution of concrete cover to the load capacity was assessed from the concrete cover strain in the transition range. From experiments as those shown in Figures 3–5 the concrete cover strain was determined from an initial spalling strain at 0.002 and the concrete cover strain at the end point of the transition range. The lateral strains (of concrete and lateral reinforcement) without concrete cover were higher than with cover when compared at a certain load, due to the confinement of the specimen core. For rectangular concrete columns reinforced with FRP, the axial load capacity with concrete covering was slightly higher than without it, by about 0.68–1.35% (C-1–C-3, C-9–C-11). However, the increase in axial load capacity of the circular columns caused by concrete covers was more significant at about 8.7%. Normally,

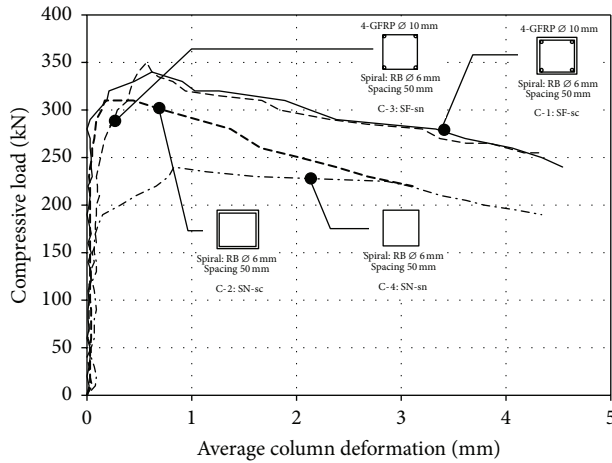


FIGURE 3: Load-deformation curves of rectangular specimens with spirals.

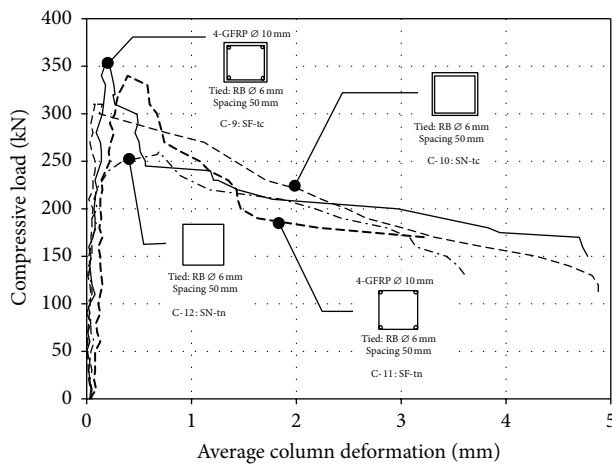


FIGURE 4: Load-deformation curves of rectangular specimens with ties.

a concrete cover affects the early effective confinement in a column, and its contribution to the column load capacity is smallish. On comparing reinforced specimens with and without GFRP reinforcement, as shown in Figures 3–5, the longitudinal GFRP reinforcement improved the load-deformation relation as long as buckling or rupture of this reinforcement occurred. Then, the reinforcement contribution at a certain deformation can be evaluated by subtracting the capacity of plain concrete confined columns from that of GFRP reinforced concrete columns. From this approach, the GFRP reinforcement increased the axial load capacity from 13% to 36%. For a rectangular cross section, the axial load capacity increase attributed to FRP with concrete covers (C-1-C-2, C-9-10) was lower by about half on comparing to cases without concrete cover (C-3-C-4, C-11-C-12). Also, the strain of GFRP related to its contribution to the load capacity. The GFRP strains with concrete cover were smaller than without cover, by about half. In addition, the axial load capacity increases of the circular columns (C-5-C-6, C-7-C-8) were approximately 26.5%, and the longitudinal strain

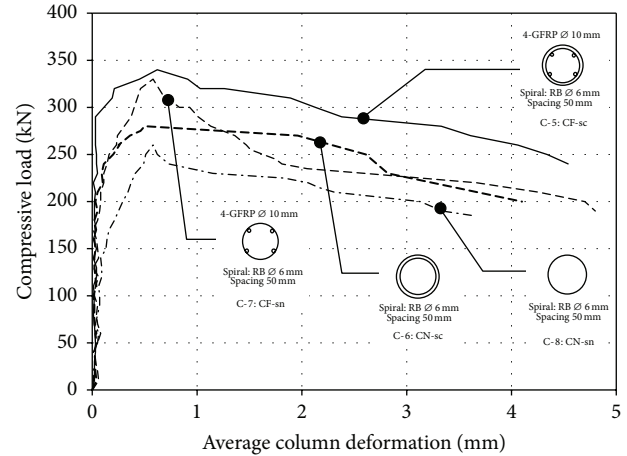


FIGURE 5: Load-deformation curves of circular specimens.

of GFRP reinforcement ranged from 0.015 to 0.02 at the maximum column capacity, as shown in Figure 7. However, the contribution of GFRP rebars under compression loading was much lower than under tension, in accordance with prior studies [3, 19]. In addition, the effect of longitudinal reinforcement on the concrete confinement is presented in terms of ratio f'_{cc}/f'_c . The difference of maximum compressive strength (f'_{cc}) to the unconfined compressive strength (f'_c) ratio is obtained from subtraction of this ratio between specimens with and without longitudinal reinforcement. From experimental results, the contribution to the confined compressive strength of specimens increases with an increase of GFRP reinforcement ratio as shown in Figure 8. The lateral reinforcement creates a confining pressure during the deformation of a specimen. This confining pressure increases both strength and inelastic range of deformations. The experimental results in Figure 9 indicate no differences in the maximum load capacity between the various types of lateral reinforcement, while differences were found in the descending region of load-deformation response. It should be noted that the maximum load capacity is not reached with intact concrete cover. At maximal load the concrete cover may spall off, which reduces the load capacity. After the maximum load, a sudden drop in the load capacity occurred in specimens with ties (both with and without concrete cover). The spiral lateral reinforcement proved to be the most effective in terms of confining pressure and inelastic deformation. The effect of the lateral reinforcement on deformability was more pronounced than on the maximum load capacity, in GFRP reinforced concrete columns.

To evaluate the confinement effectiveness of GFRP reinforced concrete columns, the basic approach from conventionally reinforced concrete was used. In general, the maximum confined strength was subtracted by the unconfined strength of test specimens. The ratio between the resultant and the confined pressure provided by the lateral reinforcement defines the coefficient of confinement effectiveness. The confined pressure determined from the yielding of lateral reinforcement depends on lateral reinforcement spacing, concrete core dimension, area of lateral reinforcement, and

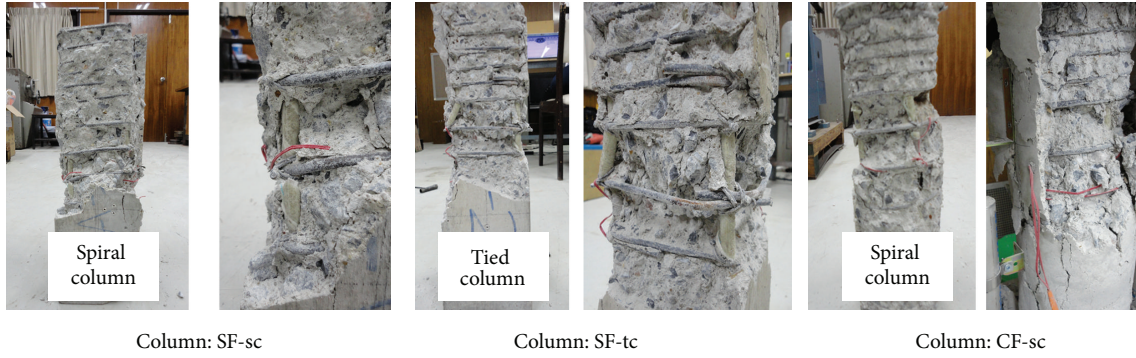


FIGURE 6: Failure modes of GFRP columns.

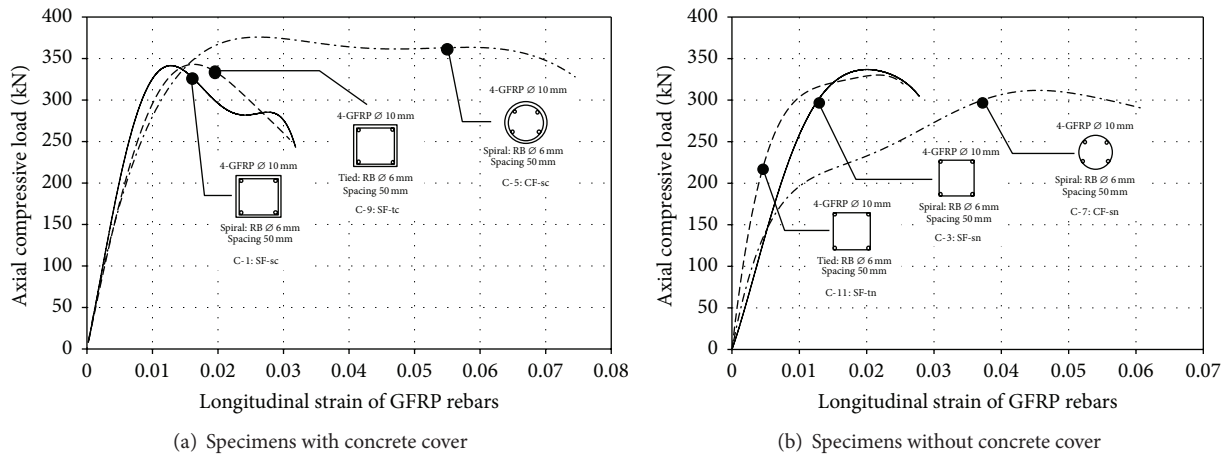
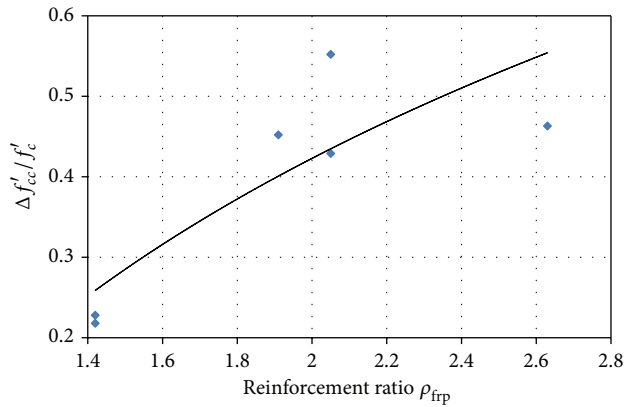


FIGURE 7: Load-strain curves of GFRP rebars.

FIGURE 8: Relation between the difference in f'_{cc}/f'_c and reinforcement ratio.

so forth. It was found that the confinement effectiveness coefficient varied from 3.0 to 7.0 for specimens with longitudinal reinforcement. The higher confinement effectiveness coefficient implied that the confined pressure is low and the unconfined concrete strength may be high. From experimental results, the specimens without concrete cover provided higher confinement effectiveness coefficients than those with

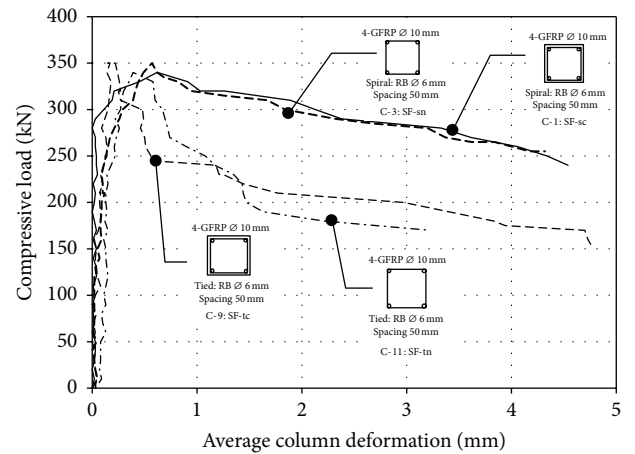


FIGURE 9: Comparison of load-strain curves with various types of lateral reinforcement.

concrete cover. This may be due to severe effects of early shrinkage and Poisson's ratio in cases without concrete cover, which delay confinement effects during specimen loading. The confinement will not be effective until large lateral deformations.

To establish relative performance of test specimens with the stress-strain models developed in recent studies [13, 15, 20, 21], the strength results of test specimens with circular cross section (C-6: CN-sc) were compared with the predicted strength results. The stress-strain models of FRP confined concrete with circular sections were considered as follows:

Park et al. [13]:

$$\frac{f'_{cc}}{f'_{co}} = 0.7 + 3.7 \left(\frac{f_{lu,a}}{f'_{co}} \right), \quad (1)$$

Lam and Teng [15]:

$$\frac{f'_{cc}}{f'_{co}} = 1 + 3.3 \left(\frac{f_{lu,a}}{f'_{co}} \right), \quad (2)$$

Wu and Wang [20]:

$$\frac{f'_{cc}}{f'_{co}} = 1 + 2.23 \left(\frac{f_{lu}}{f'_{co}} \right)^{0.96}, \quad (3)$$

and Realfonso and Napoli [21]:

$$\frac{f'_{cc}}{f'_{co}} = 1 + 3.57 \left(\frac{f_{lu,a}}{f'_{co}} \right), \quad (4)$$

where f'_{cc} is maximum axial compressive stress of FRP confined concrete, f'_{co} is maximum axial compressive stress of unconfined concrete, f_{lu} is nominal lateral confining pressure at ultimate, and $f_{lu,a}$ is actual lateral confining pressure at ultimate.

The predicted compressive strength obtained from the stress and strain models (Equations (1) to (4)) is equal to 291 kN, 291 kN, 272 kN, and 351 kN, respectively. Based on this study, the predicted stress and strain models provide higher strength results than the average experimental results (267 kN). The percentage difference between the predicted models and experimental results ranged from 9% to 31%. The most accurate prediction of ultimate strength can be obtained from using the stress and strain model by Lam and Teng [15] and Park et al. [13] with 9 percent difference. The findings on the strength comparison between the experimental data and predicted models are in agreement with the previous study [14]. In general, the postelastic behavior of conventional reinforced concrete members is indicated by ductility factor. The ductility of steel reinforced concrete members can be defined as the ratio of displacement or deformation at ultimate point to the corresponding values at yielding point of the steel reinforcement. However, the behavior of FRP reinforcement is quite different from that of steel, particularly under compression loading. Thus, the postelastic behavior is more appropriately characterized by energy absorption than by ductility factor. In this study, the deformability factor was defined as the ratio of energy absorption (area under load and deformation curve) at the ultimate point to the energy absorption at the limiting deformation in the ascending part of load versus deformation. The ultimate point was defined as the postelastic point at 85 percent of maximum load capacity in the descending part. The limiting deformation point was

defined as the deformation point at the maximum load capacity in the ascending part. From experimental results, the average deformability factors were 4.2 and 2.8 with spirals and ties, respectively.

6. Conclusions

Glass fiber reinforced plastic (GFRP) was used to reinforce concrete columns that were experimentally investigated under compression loading to assess structural behavior and performance. Specimens were prepared with varied longitudinal reinforcement, concrete cover, and lateral reinforcement. Based on this study, the amount of GFRP longitudinal and lateral reinforcement slightly affected the column strengths. While different types of lateral enforcement had little difference in strength, the spiral lateral reinforcement was the most effective in terms of the confining pressure and the inelastic deformation. The effect of the lateral reinforcement on deformability is more influenced than that on the column strength. The contribution to the confined compressive strength increased with the GFRP reinforcement ratio. The concrete cover mainly affected early confinement effects, not maximum load capacity or late stage deformation.

Conflict of Interests

The authors declare that there is no conflict of interests regarding the publication of this paper.

Acknowledgments

The authors would like to acknowledge Associate Professor Seppo Karrila, Ph.D., and Research and Development Office (RDO), Prince of Songkla University, for technical comments and corrections. This study was partially supported by Structural Engineering and Applied Mechanics (STREAM) Research Group under Grant ENG-51-2-7-11-022-S, Department of Civil Engineering, Faculty of Engineering, Prince of Songkla University, Hat Yai, Songkhla, Thailand.

References

- [1] N. S. Paramananthan, *Investigation of the behavior of concrete columns reinforced with fiber reinforced plastic rebars [M.S. thesis]*, Lamar University, Beaumont, Tex, USA, 1993.
- [2] N. Kawaguchi, "Ultimate strength and deformation characteristics of concrete members reinforced with AFRP rods under combined axial tension or compression and bending," in *Proceedings of the Interanational Symposium on Fiber Reinforced Plastic Reinforcement for Concrete Structures*, Special Publication 138, pp. 671–684, 1993.
- [3] K. Kobayashi and T. Fujisaki, "Compressive behavior of FRP reinforcement in non-prestressed concrete members," in *Non-Metallic (FRP) Reinforcement for Concrete Structures: Proceedings of the Second International RILEM*, CRC Press, 1995.
- [4] S. H. Alsayed, Y. A. Al-Salloum, T. H. Almusallam, and M. A. Amjad, "Concrete columns reinforced by glass fibre reinforced plastic rods," *International Concrete Abstracts Portal*, vol. 188, pp. 103–112, 1999.

- [5] H. Y. Leung and C. J. Burgoyne, "Compressive behavior of concrete confined by aramid fibre spirals," in *Proceedings of the International Conference on Structural Engineering Mechanics and Computation*, pp. 1357–1346, Cape Town, South Africa, June 2001.
- [6] M. K. Sharbatdar, *Concrete columns and beams reinforced with FRP bars and grids under monotonic and reversed cyclic loading [Ph.D. thesis]*, University of Ottawa, Ottawa, Canada, 2003.
- [7] U. K. Sharma, P. Bhargava, and S. K. Kaushik, "Behavior of confined high strength concrete columns under axial compression," *Journal of Advanced Concrete Technology*, vol. 3, no. 2, pp. 267–281, 2005.
- [8] C. C. Choo, I. E. Harik, and H. Gesund, "Strength of rectangular concrete columns reinforced with fiber-reinforced polymer bars," *ACI Structural Journal*, vol. 103, no. 3, pp. 452–459, 2006.
- [9] M. Francis and B. Teng, "Strength of short concrete columns reinforced with high modulus glass fibre reinforced polymer bars," in *Proceedings of the 2nd International Structures Specialty Conference*, pp. 45.1–45.8, Winnipeg, Canada, June 2010.
- [10] E. M. Lotfy, "Behavior of reinforced concrete short columns with fiber reinforced polymers bars," *International Journal of Civil and Structural Engineering*, vol. 1, no. 3, pp. 545–557, 2010.
- [11] H. Tobbi, A. S. Farghaly, and B. Benmokrane, "Concrete columns reinforced longitudinally and transversally with glass fiber-reinforced polymer bars," *ACI Structural Journal*, vol. 109, no. 4, pp. 1–8, 2012.
- [12] M. Z. Afifi, H. M. Mohamed, and B. Benmokrane, "Axial capacity of circular concrete columns reinforced with GFRP bars and spirals," *Journal of Composites for Construction*, vol. 18, no. 1, pp. 363–366, 2014.
- [13] J.-H. Park, B.-W. Jo, S.-J. Yoon, and S.-K. Park, "Experimental investigation on the structural behavior of concrete filled FRP tubes with/without steel re-bar," *KSCE Journal of Civil Engineering*, vol. 15, no. 2, pp. 337–345, 2011.
- [14] T. Ozbakkaloglu, J. C. Lim, and T. Vincent, "FRP-confined concrete in circular sections: review and assessment of stress-strain models," *Engineering Structures*, vol. 49, pp. 1068–1088, 2013.
- [15] L. Lam and J. G. Teng, "Design-oriented stress-strain model for FRP-confined concrete," *Construction and Building Materials*, vol. 17, no. 6-7, pp. 471–489, 2003.
- [16] V. Tamuzs, R. Tepfers, E. Zile, and O. Ladnova, "Behavior of concrete cylinders confined by a carbon composite 3. Deformability and the ultimate axial strain," *Mechanics of Composite Materials*, vol. 42, no. 4, pp. 303–314, 2006.
- [17] T. Ozbakkaloglu, "Axial compressive behavior of square and rectangular high-strength concrete filled FRP tubes," *Journal of Composites for Construction*, vol. 17, no. 1, pp. 151–161, 2013.
- [18] T. Ozbakkaloglu and T. Vincent, "Axial compressive behavior of circular high-strength concrete-filled FRP tubes," *Journal of Composites for Construction*, vol. 18, no. 2, Article ID 04013037, 2014.
- [19] D. H. Deitz, I. E. Harik, and H. Gesund, "Physical properties of glass fiber reinforced polymer rebars in compression," *Journal of Composites for Construction*, vol. 7, no. 4, pp. 363–366, 2003.
- [20] Y.-F. Wu and L.-M. Wang, "Unified strength model for square and circular concrete columns confined by external jacket," *Journal of Structural Engineering*, vol. 135, no. 3, pp. 253–261, 2009.
- [21] R. Realfonzo and A. Napoli, "Concrete confined by FRP systems: confinement efficiency and design strength models," *Composites Part B: Engineering*, vol. 42, no. 4, pp. 736–755, 2011.

Research Article

Effects of Elevated Temperatures on the Compressive Strength Capacity of Concrete Cylinders Confined with FRP Sheets: An Experimental Investigation

Sherif El-Gamal, Khalifa Al-Jabri, Ahmed Al-Mahri, and Saud Al-Mahrouqi

Civil Engineering Department, Sultan Qaboos University, Al-Khodh, P.O. Box 33, 123 Muscat, Oman

Correspondence should be addressed to Sherif El-Gamal; sherif@squ.edu.om

Received 8 August 2015; Revised 6 September 2015; Accepted 9 September 2015

Academic Editor: João M. L. Dos Reis

Copyright © 2015 Sherif El-Gamal et al. This is an open access article distributed under the Creative Commons Attribution License, which permits unrestricted use, distribution, and reproduction in any medium, provided the original work is properly cited.

Due to their high strength, corrosion resistance, and durability, fiber reinforced polymers (FRP) are very attractive for civil engineering applications. One of these applications is the strengthening of concrete columns with FRP sheets. The performance of this strengthening technique at elevated temperature is still questionable and needs more investigations. This research investigates the effects of exposure to high temperatures on the compressive strength of concrete cylinders wrapped with glass and carbon FRP sheets. Test specimens consisted of 30 unwrapped and 60 wrapped concrete cylinders. All specimens were exposed to temperatures of 100, 200, and 300°C for periods of 1, 2, and 3 hours. The compressive strengths of the unwrapped concrete cylinders were compared with their counterparts of the wrapped cylinders. For the unwrapped cylinders, test results showed that the elevated temperatures considered in this study had almost no effect on their compressive strength; however, the wrapped specimens were significantly affected, especially those wrapped with GFRP sheets. The compressive strength of the wrapped specimens decreased as the exposure period and the temperature level increased. After three hours of exposure to 300°C, a maximum compressive strength loss of about 25.3% and 37.9%, respectively, was recorded in the wrapped CFRP and GFRP specimens.

1. Introduction

Fibre reinforced polymers (FRPs) have been recognized as a reinforcing, strengthening, and repairing advanced material for civil engineering infrastructures worldwide [1–3]. They have been used as a replacement for conventional steel reinforcement in several new concrete structures such as bridges, parking garages, and concrete pavements [4–6]. One of the main applications of FRPs is the use of FRP jackets in building and bridge columns. Research initiatives around the world during the past two decades have documented the behaviour of externally bonded FRPs for strengthening reinforced concrete (RC) structures. In these applications, FRPs are bonded to the exterior of RC structures, typically using an epoxy resin saturant/adhesive, to provide additional tensile or confining reinforcement [7, 8]. FRP jackets are most effective at confining members with circular cross sections [9–13]. The FRP system provides a circumferentially

uniform confining pressure to the radial expansion of the compression member when the fibers are aligned transverse to the longitudinal axis of the member.

Sufficient research and implementations have been conducted for the development of various design codes and guidelines for the application of FRPs in conjunction with concrete structures. Numerous studies have shown that circumferential wraps of FRP on the exterior of reinforced concrete columns can significantly increase the strength and ductility of these members. Hence, FRP applications have been widespread in repair and restoration of reinforced concrete columns in existing bridges [14].

FRP sheets have been used for strengthening of columns, slabs, beams, and so forth. Some of the advantages of FRP sheets are that they can be applied easily and quickly, provide high resistance to the reinforced elements, and do not affect the shape of the structure. Although it was found that the behaviour of FRP-strengthened concrete structures at normal

temperature is satisfactory, little information regarding the behaviour of FRP-strengthened concrete members at high temperatures is available [15].

The objective of this research was to investigate the effect of elevated temperatures on the performance of concrete cylinders confined with glass FRP (GFRP) and carbon FRP (CFRP) sheets. To achieve this objective, an experimental investigation including the construction and testing of 90 standard 100 mm diameter \times 200 mm height concrete cylinders was made. Out of these specimens, 30 cylinders were unwrapped and the remaining 60 specimens were wrapped with one layer of GFRP or CFRP sheets. Some of the cylinders were exposed to room temperature, whereas other cylinders were exposed to heating regime of 100°C, 200°C, and 300°C for a period of 1, 2, and 3 hours. After high temperature exposure, specimens were tested under uniaxial compression until failure.

2. Literature Review

In a review study by Hollaway [16], it was concluded that temperature is one of the most physical parameters that affects the original state of FRP material. It changes or resets the arrangement of the monomer and consequently affects the whole properties of FRPs. The measurements demonstrate one critical temperature value called glass transition temperature (T_g). T_g is the midpoint of two different critical phases. Polymers below T_g are rigid and have both stiffness and strength, but above T_g , the polymers are viscous liquids and have much lower stiffness and strength. All physical properties of thermosetting polymers depend upon intermolecular cross-links and the temperature at which polymer will begin to soften (T_g). The temperature at which this happens depends upon the chemical structure building of the polymer [16].

The behaviour of FRP confined concrete cylinders after exposure to different temperatures has been investigated by Al-Salloum et al. [14]. The research included two phases; the first phase included the construction of concrete prisms while the second phase included the construction of standard concrete cylinders. In the first phase, the concrete prisms were wrapped by one layer of GFRP and CFRP laminates for conducting pull-off strength tests. In the second phase, concrete cylinders were wrapped with one layer of CFRP or GFRP sheets. Some of the wrapped and unwrapped specimens were exposed to room temperature. The other concrete cylinders were exposed to heating regime of 100°C and 200°C for different periods. The reduction of strength capacity of specimens was noticed for wrapped carbon and glass FRP specimens after being exposed to heating of 100°C for 2 hours because of epoxy melting. This reduction was significantly experienced at a temperature of 200°C.

Yaqub et al. [17, 18] studied the performance of postheated reinforced concrete square columns repaired with unidirectional FRPs. The test specimens were divided into three groups: unheated columns, postheated columns, and postheated columns wrapped with a single layer of unidirectional glass or carbon FRP jackets. The research investigated the

stiffness, ductility, ultimate strain, and ultimate strength of all specimens.

The ultimate strength of unstrengthened square columns was reduced significantly after heating to 500°C due to burning of cement, which reduced its capacity. On the other hand, some improvements were noticed after wrapping the specimens with one layer of CFRP or GFRP sheets. This improvement was due to confining of concrete dilation by the FRP sheet. However, the strength of postheated square columns could be restored to some extent but below the original level of undamaged concrete. This limitation of improvement was due to cross section of the columns where the distribution of lateral confining pressure of the GFRP or CFRP jackets varies from a maximum at the corners to a minimum between the corners due to arching action. The research recommended increasing the number of GFRP or CFRP layers and increasing corner radius to enhance the capacity of the columns.

Trapko [19] studied the effect of high temperature on the performance of CFRP and FRCM (Fiber Reinforced Cementitious Matrix) confined concrete elements. Concrete cylinders were wrapped with CFRP sheets and FRCM mesh and exposed to temperature of 40°C, 60°C, and 80°C over a period of 24 hours. The testing program was carried out on 24 concrete cylinders: 6 were unwrapped specimens, 9 were wrapped with two layers of CFRP, and the remaining 9 specimens were wrapped with two layers of FRCM mesh. The CFRP wrapped cylinders failed through a sudden rupture of fiber sheet. Failure of FRCM confined elements was initiated by debonding of mesh at the external pleat. In case of CFRP confined elements, higher temperature significantly reduced the compressive strength of the confined specimens. Load dropped by about 10% per each 20°C on average. For the FRCM confined specimens, temperature did not have that significant effect. Changes ranged between only 5 and 10%. Trapko developed an empirical equation to calculate the compressive strength of confined concrete cylinders. However, there was a large difference between experimental and empirical results. From literature, it can be concluded that more research is required to investigate the performance of FRP wrapped concrete columns after exposure to elevated temperatures.

3. Experimental Testing Program

3.1. Test Specimens. The experimental work in this study included the construction and testing of 90 concrete cylinders of 100 mm diameter \times 200 mm height. The specimens consisted of 30 unwrapped cylinders, 30 cylinders wrapped with one layer of CFRP sheets, and 30 cylinders wrapped with one layer of GFRP sheets. All specimens were exposed to 100°C, 200°C, and 300°C for a period of 1, 2, and 3 hours. After high temperature exposure, specimens were tested under uniaxial compression until failure according to ASTM C39 test method [20].

The test results included the ultimate capacity and failure mode. Table 1 summarizes the schedule of test specimens

TABLE 1: Schedule of test specimens.

Time of exposure (h)	Temperature (°C)	Unwrapped specimens	Wrapped with CFRP	Wrapped with GFRP
—	Room	3	3	3
1	100	3	3	3
	200	3	3	3
	300	3	3	3
	100	3	3	3
2	200	3	3	3
	300	3	3	3
	100	3	3	3
3	200	3	3	3
	300	3	3	3
Total number of specimens		30	30	30
			90	

TABLE 2: Required batch quantities for the 90 cylinders (in kg).

Aggregate		Cement	Water
20 mm	10 mm		
105.36	69.32	126.5	33.87

where a replicate of three specimens was used for each condition.

3.2. Used Materials

3.2.1. Concrete. Normal concrete with a target compressive strength of 30 MPa was prepared in the laboratory for concrete casting. The procedure of concrete mixing was carried out according to ASTM standards. Table 2 shows the mix quantities required for casting the 90 cylinders. Compressive and tensile strength tests were carried out using standard concrete cylinders and cubes that were cast and cured according to [21]. Test results show that the measured concrete compressive and tensile strengths were 21.5 and 2.35 MPa, respectively.

3.2.2. FRP Sheets and Resin. Uniaxial CFRP sheets and biaxial GFRP sheets were used for confining the concrete cylinders. The ultimate load of the CFRP sheets as given by the manufacturer is 350 kN/m and 180 kN/m width, respectively. Detailed mechanical properties of the FRP sheets used can be found in [22]. Figure 1 shows the CFRP sheet used. An epoxy resin was used for bonding the FRP sheets to concrete. According to manufacturers, the epoxy resin had a compressive strength greater than 60 MPa, bending strength greater than 50 MPa, and bond strength greater than 3 MPa. Figure 2 shows epoxy resin used for bonding FRP sheets. More details about the mechanical properties of the epoxy resin used can be found in [23].

3.3. Casting and Curing of Specimens. Ninety PVC pipes with an inside diameter of 100 mm and 200 mm height were used

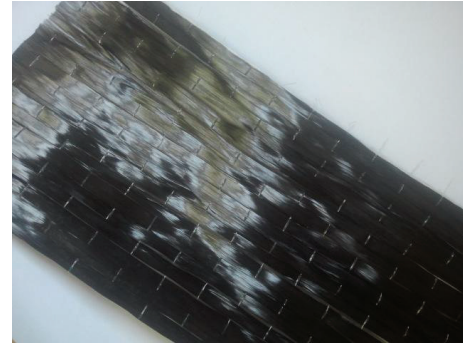


FIGURE 1: CFRP sheet sample.



FIGURE 2: Epoxy resin used for bonding of FRP sheets.

for concrete casting. Before casting, oil was added to the inner sides of the pipes to facilitate removing the concrete cylinder after casting. The pipes were put inside a vibration machine to compact concrete as shown in Figure 3. After concrete casting, the specimens were kept in the lab for one day. Then, the concrete specimens were removed from the moulds and were submerged in water for 28 days for curing as shown in Figure 4.

3.4. Application of FRP Sheets. The application of the FRP sheets was conducted according to ISIS manuals and ACI440-2R guidelines [24, 25]. Before confining the concrete with



FIGURE 3: Specimens on the vibration machine before casting.



FIGURE 4: Curing of concrete cylinders.

FRP sheets, the surface of the concrete specimens was polished to remove voids and deformities on it. The two-component epoxy system, consisting of resin and hardener, was thoroughly hand-mixed for at least 5 minutes before use. The FRP sheets were then applied directly onto the surface of the specimens providing unidirectional lateral confinement in the hoop direction. Figure 5 shows the steps of confining cylinder by the GFRP sheets.

After applying the FRP sheet, all specimens were stored at room temperature for at least 7 days to ensure enough time for curing of epoxy. Before testing, all specimens were exposed to heating regimes of 100°C, 200°C, and 300°C for a period of 1, 2, and 3 hours. After heating, the specimens were taken out from the oven and left to cool in the lab temperature before testing. This procedure was chosen to investigate any permanent deterioration caused by elevated temperatures in the fibres or in the resin. Another study is being carried out by the authors to test specimens directly after heating and its results will be included in another paper.

4. Test Results and Discussion

Tables 3–5 summarize the test results of unconfined and confined test specimens. It should be noted that the values

TABLE 3: Test results of the unconfined specimens.

Temperature	Average compressive strength (MPa)		
	Exposure time (h)		
	1 h	2 h	3 h
100°C	21.72 ± 0.8	20.41 ± 0.6	18.64 ± 0.5
200°C	23.03 ± 1.4	19.44 ± 1.2	18.62 ± 1.3
300°C	20.19 ± 0.5	18.90 ± 1.3	18.57 ± 0.9
Room	21.44 ± 0.7		

TABLE 4: Test results of CFRP confined specimens.

Temperature	Average compressive strength (MPa)		
	Exposure time (h)		
	1 h	2 h	3 h
100°C	56.1 ± 1.1	57.3 ± 0.9	54.7 ± 0.4
200°C	56.9 ± 1.3	56.4 ± 1.8	52.6 ± 0.7
300°C	55.4 ± 0.6	53.5 ± 1.5	41.0 ± 1.3
Room	54.9 ± 1.4		

TABLE 5: Test results of GFRP confined specimens.

Temperature	Average compressive strength (MPa)		
	Exposure time (h)		
	1 h	2 h	3 h
100°C	30.61 ± 0.7	30.01 ± 0.5	27.82 ± 1.1
200°C	27.14 ± 1.4	27.14 ± 0.8	23.07 ± 0.5
300°C	22.48 ± 0.4	22.48 ± 1.2	20.96 ± 0.8
Room	33.77 ± 1.2		

of compressive strength presented in Tables 3–5 are the average of three specimens. The test results of all specimens were consistent. The standard deviation ranged between 0.5 and 1.4 MPa for unconfined specimens with coefficients of variations between 2.7 and 6.1%. For the CFRP confined specimens, the standard deviations ranged between 0.4 and 1.8 MPa with coefficient of variation between about 1 and 3.2%. Similar observations were recorded in the GFRP confined specimens where the standard deviations ranged between 0.4 and 1.4 MPa with coefficients of variations between 1.8 and 5.2%.

4.1. Unconfined Specimens. Before testing, the unconfined specimens were exposed to room temperature and the heating regimes explained earlier. Thereafter, the specimens were tested in uniaxial compression. The performance of cylinders under axial load was found to be consistent. Table 3 reports the compressive strength of the unconfined specimens. The failure mode was characterized by shearing and splitting of concrete, as shown in Figure 6. It can be noticed that elevated temperatures considered in this study had very small effect on the compressive strength of the unconfined specimens.

4.2. CFRP Confined Specimens. Table 4 shows the compressive strength test results of the CFRP wrapped specimens



FIGURE 5: Steps of confining process.

after exposure to room temperature and heating regimes. It can be noticed that wrapping the concrete cylinders with CFRP sheets increased the compressive strength compared to the unconfined specimens. This increase ranged between 120 and 190%. All confined specimens show higher compressive strengths compared to unconfined specimens regardless of exposure period or temperature level. Table 4 also shows that one and two hours of exposure to 100°C, 200°C, and 300°C did not show a significant effect of the compressive strength compared to the confined specimens at room temperature. However, a significant decrease in the compressive strength (about 25%) was recorded after 3 hours of exposure to 300°C compared to the confined specimen at room temperature.

All the CFRP confined specimens failed by CFRP rupture in an explosive pattern with a huge energy dissipation regardless of temperature level or exposure period. Figure 7 shows photos of two CFRP wrapped specimens after failure.

4.3. GFRP Confined Specimens. Table 5 presents the compressive test results of the GFRP confined specimens. It can be noticed that wrapping the concrete cylinders with GFRP sheets slightly increased the compressive strength compared to the unconfined specimens (see Table 3). This increase ranged between only 11% after exposure to 300°C and 57% at room temperature. Table 5 also shows that the temperature level had a significant effect on the GFRP confined specimens. All specimens exposed to elevated temperatures showed lower compressive strength compared to the wrapped

specimens in room temperature. Increasing the temperature level significantly affected the compressive strength of the wrapped specimens as shown in Figure 8. The exposure period, however, had less influence on the compressive strength compared to the effect of temperature level.

All the GFRP confined specimens also failed by GFRP rupture regardless of temperature level or exposure period. Figure 9 shows typical failures of the GFRP wrapped specimens.

Figure 9 shows a colour change in the GFRP sheets after exposure to 200°C and 300°C. This is a sign of a permanent deterioration in the GFRP sheets, which explains the decrease in the compressive strength of the GFRP wrapped specimens after being exposed to elevated temperatures. This indicates that elevated temperatures had more harmful effect on the GFRP sheets than CFRP sheets.

4.4. Comparison of Test Results. Figure 10 shows the average compressive strength of all test specimens after exposure to different temperatures and exposure periods. The figure shows that the CFRP confined specimens had the maximum compressive strength followed by the GFRP confined specimens and then by the unconfined specimens.

For all test specimens, the exposure period had a minor effect on the compressive strength except for the CFRP confined specimen at 300°C where increasing the exposure period from 2 to 3 hours resulted in a significant decrease in the compressive strength. It can be also noticed that

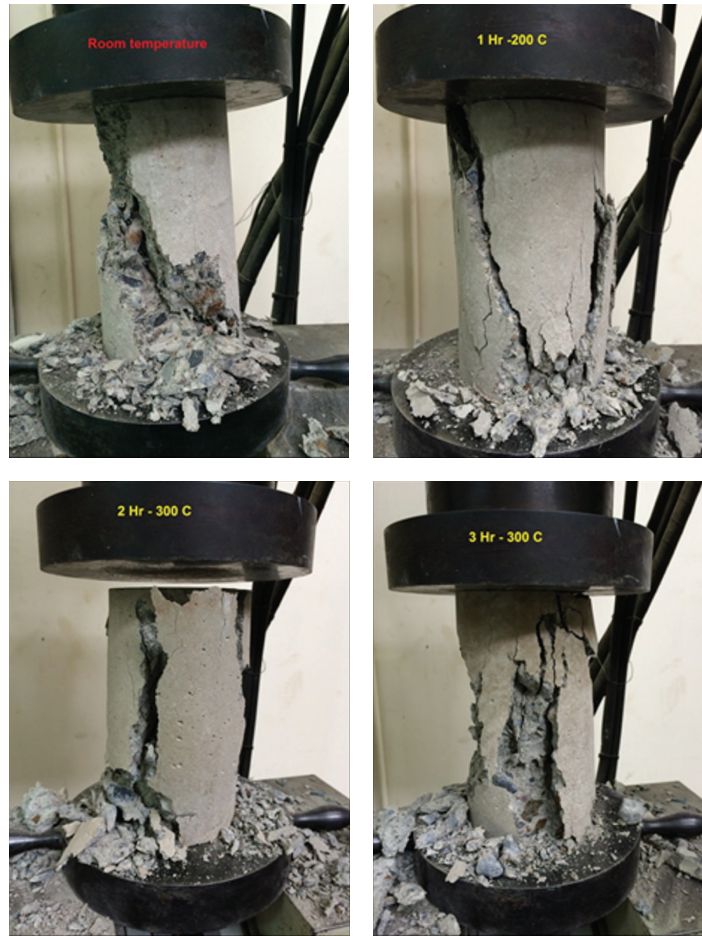


FIGURE 6: Failure of the unconfined specimens.

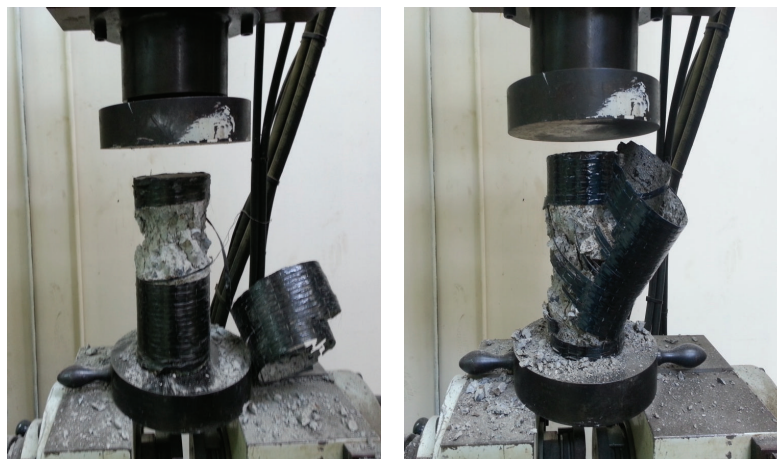


FIGURE 7: Failure of CFRP wrapped specimens.

increasing the temperature level had greater effect on the compressive strength than exposure period especially for the GFRP confined specimens.

Figure 11 shows the compressive strength loss of heated test specimens compared to the corresponding specimen at room temperature. For the unconfined specimens, it can

be noticed that the exposure period and temperature had insignificant effect on the compressive strength. A maximum strength loss of about 13.4% compared to specimen in room temperature was recorded after 3 hours of exposure to 300°C. A similar observation can be noticed for the CFRP confined specimens. Except for the specimens exposed to 300°C for

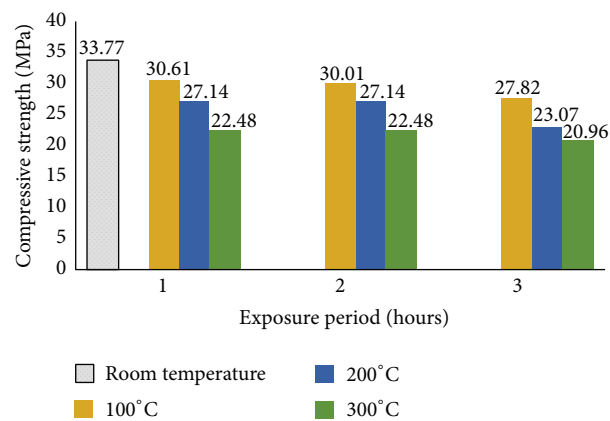


FIGURE 8: Average compressive strength of GFRP confined specimens after exposure to different temperatures.

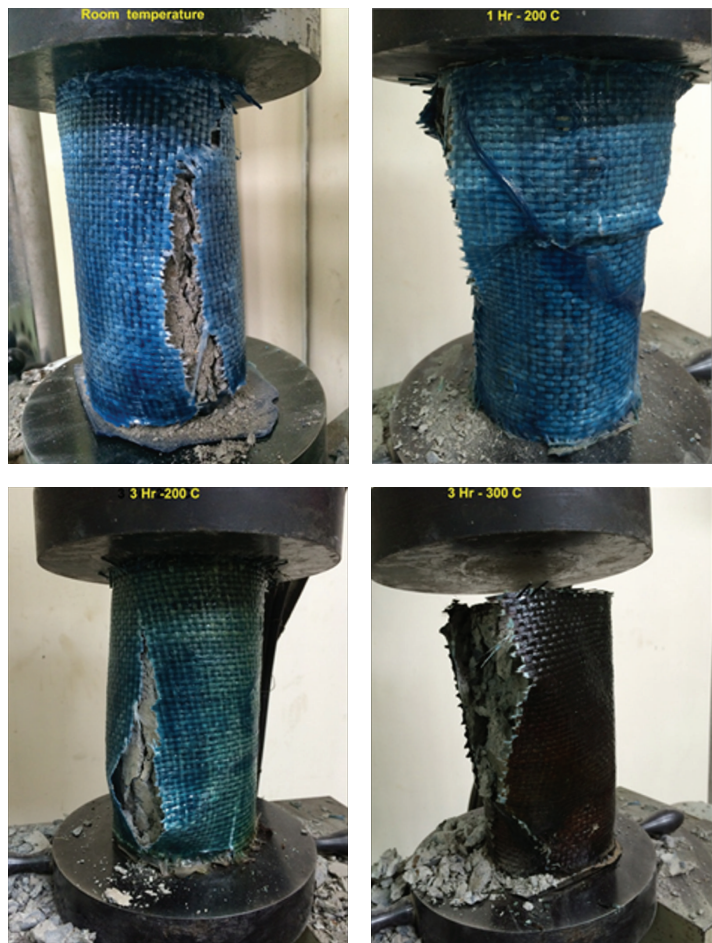


FIGURE 9: Failure of GFRP wrapped specimens.

3 hours that show a strength loss of about 25%, all other specimens, CFRP confined specimens, almost did not show any strength loss compared to the CFRP confined specimen at room temperature. For the GFRP confined specimens, Figure 11 shows that significant compressive strength losses were recorded. The strength losses increased as the temperature level or exposure period increased. The strength losses

ranged between 9.4 and 17.6 at 100°C, 19.6 and 31.7 at 200°C, and 33.4 and 37.9 at 300°C.

5. Conclusions

This study aimed to investigate the compressive strength of carbon and glass FRP confined concrete cylinders after

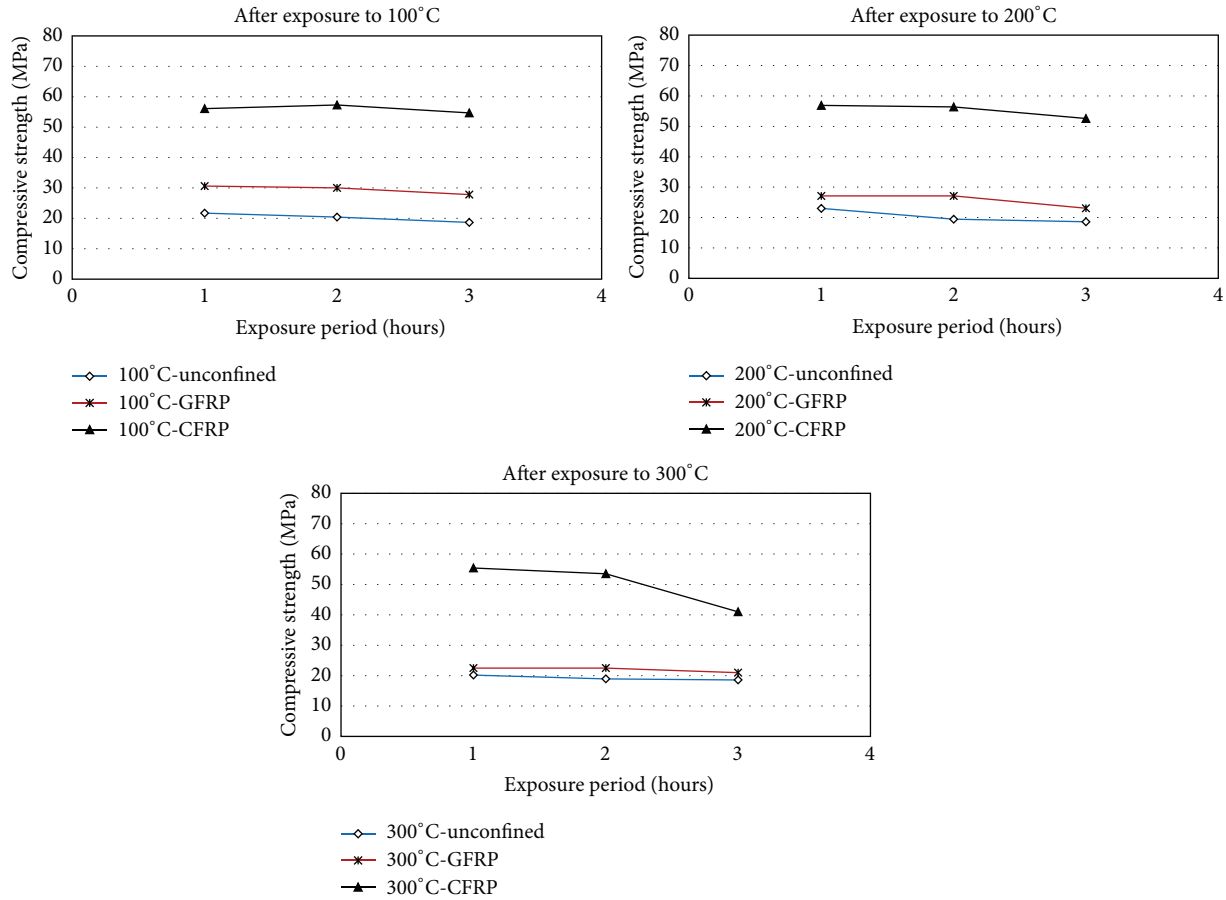


FIGURE 10: Comparison of test results.

exposure to elevated temperatures. The experimental program consisted of 90 concrete cylinders: 30 unwrapped, 30 wrapped with GFRP sheets, and 30 wrapped with CFRP sheets. All specimens were exposed to 100°C, 200°C, and 300°C for period of 1, 2, or 3 hours. The compressive strength of wrapped concrete cylinder with FRP sheets was compared with the unwrapped concrete cylinders under the same conditions. Based on test results, the following conclusions can be drawn:

- (i) All CFRP and GFRP wrapped specimens showed higher compressive strengths compared to unwrapped specimens. This increase ranged between 120 and 190% and 11 and 57% for CFRP and GFRP wrapped specimens, respectively. This indicates that the CFRP sheets were more effective in increasing the capacity of concrete cylinders.
- (ii) All wrapped specimens failed by rupture of the FRP sheets.
- (iii) The elevated temperatures considered in this study had a minor effect on the compressive strength of the unwrapped specimens. A maximum strength loss of about 13% was recorded after exposure to 300°C.
- (iv) For the CFRP wrapped specimens, the elevated temperatures considered in this study almost did not affect the compressive strength except for the specimens exposed to 300°C for 3 hours that showed a strength loss of about 25% compared to the CFRP wrapped specimens at room temperature.
- (v) For the GFRP wrapped specimens, significant compressive strength losses were recorded after exposure to elevated temperatures. The strength losses increased as the temperature level or exposure period increased. A maximum compressive strength loss of 37.9% was recorded after exposure to 300°C for 3 hours.
- (vi) The elevated temperatures considered in this study affected more the GFRP sheets than CFRP. This was recorded from the change in the colour of the sheets and high compressive strength losses recorded in those specimens.

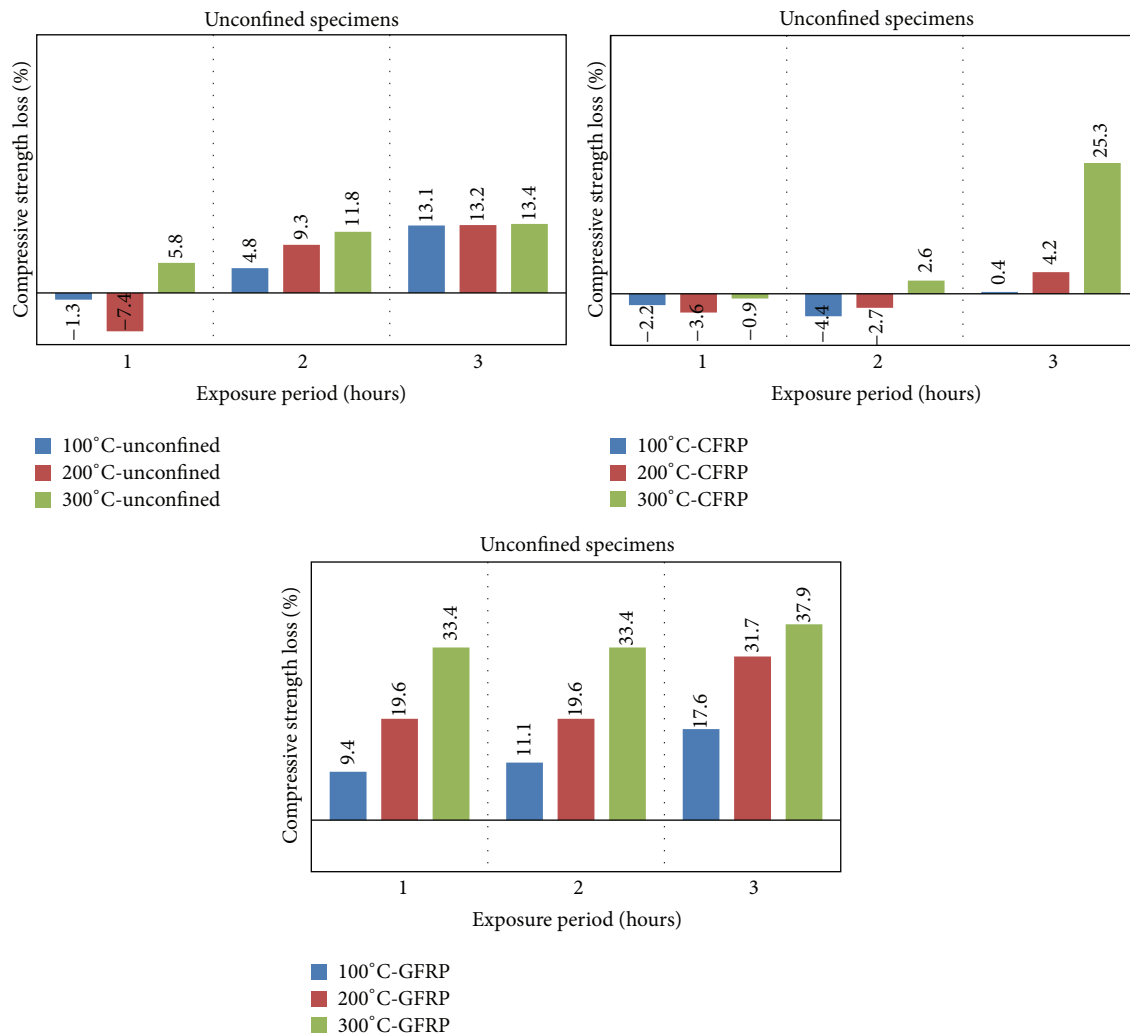


FIGURE 11: Compressive strength loss.

Conflict of Interests

The authors declare that there is no conflict of interests regarding the publication of this paper.

Acknowledgments

The authors would like to acknowledge Sultan Qaboos University and the Civil and Architectural Engineering Department for their support to conduct this research project. Thanks are also extended to the technicians at the structural laboratory of the Civil and Architectural Engineering Department for their help.

References

- [1] S. E. El-Gamal, *Behaviour of restrained concrete bridge deck slabs reinforced with FRP reinforcing bars under concentrated loads [Ph.D. thesis]*, Université de Sherbrooke, Québec, Canada, 2005.
- [2] S. E. El-Gamal, Y. Al-Salloum, S. Alsayed, and M. Aqel, "Performance of near surface mounted glass fiber reinforced polymer bars in concrete," *Journal of Reinforced Plastics and Composites*, vol. 31, no. 22, pp. 1501–1515, 2012.
- [3] Y. A. Al-Salloum, S. E. El-Gamal, T. H. Almusallam, S. H. Alsayed, and M. Aqel, "Effect of harsh environmental conditions on the tensile properties of GFRP bars," *Composites Part B: Engineering*, vol. 45, no. 1, pp. 835–844, 2013.
- [4] B. Benmokrane, E. El-Salakawy, A. El-Ragaby, and S. El-Gamal, "Performance evaluation of innovative concrete bridge deck slabs reinforced with fibre-reinforced-polymer bars," *Canadian Journal of Civil Engineering*, vol. 34, no. 3, pp. 298–310, 2007.
- [5] M. Eisa, S. E. El-Gamal, E. El-Salakawy, and B. Benmokrane, "Design and construction of first GFRP-CRC200P slabs implemented on highway 40 east (Montreal)," in *Proceedings of the 37th Annual Conference of the Canadian Society for Civil Engineering*, pp. 1–8, Québec City, Canada, 2008.
- [6] S. E. El-Gamal, B. Benmokrane, E. El-Salakawy, P. Cousin, and A. Wiseman, "Durability and structural performance of carbon fibre reinforced polymer—reinforced concrete parking garage slabs," *Canadian Journal of Civil Engineering*, vol. 36, no. 4, pp. 617–627, 2009.
- [7] ACI Committee 440, *440.2R-08 Guide for the Design and Construction of Externally Bonded FRP Systems for Strengthening*

- Concrete Structures*, ACI Committee, Farmington Hills, Mich, USA, 2008.
- [8] S. E. El-Gamal, A. Al-Nuaimi, A. Al-Saidy, and A. Al-Lawati, "Flexural strengthening of RC beams using near surface mounted fibre reinforced polymers," in *Proceedings of the 5th Brunei International Conference on Engineering and Technology (BICET '14)*, pp. 1–7, Institut Teknologi Brunei, Darussalam, Bandar Seri Begawan, Brunei, November 2014.
- [9] M. Demers and K. W. Neale, "Confinement of reinforced concrete columns with fibre-reinforced composite sheets—an experimental study," *Canadian Journal of Civil Engineering*, vol. 26, no. 2, pp. 226–241, 1999.
- [10] K. A. Harries and S. A. Carey, "Shape and 'gap' effects on the behavior of variably confined concrete," *Cement and Concrete Research*, vol. 33, no. 6, pp. 881–890, 2003.
- [11] M. N. Youssef, *Stress strain model for concrete confined by FRP composites [Ph.D. thesis]*, University of California, Irvine, Irvine, Calif, USA, 2003.
- [12] S. Matthys, H. Toutanji, K. Audenaert, and L. Taerwe, "Axial load behavior of large-scale columns confined with fiber-reinforced polymer composites," *ACI Structural Journal*, vol. 102, no. 2, pp. 258–267, 2005.
- [13] S. Rocca, N. Galati, and A. Nanni, "Experimental evaluation of FRP strengthening of large-size reinforced concrete columns," Report UTC-142, University of Missouri-Rolla, Rolla, Mo, USA, 2006.
- [14] Y. A. Al-Salloum, H. M. Elsanadedy, and A. A. Abadel, "Behavior of FRP-confined concrete after high temperature exposure," *Construction and Building Materials*, vol. 25, no. 2, pp. 838–850, 2011.
- [15] S. E. El-Gamal, "Bond strength of glass fiber-reinforced polymer bars in concrete after exposure to elevated temperatures," *Journal of Reinforced Plastics and Composites*, vol. 33, no. 23, pp. 2151–2163, 2014.
- [16] L. C. Hollaway, "A review of the present and future utilisation of FRP composites in the civil infrastructure with reference to their important in-service properties," *Construction and Building Materials*, vol. 24, no. 12, pp. 2419–2445, 2010.
- [17] M. Yaqub, C. G. Bailey, and P. Nedwell, "Axial capacity of post-heated square columns wrapped with FRP composites," *Cement & Concrete Composites*, vol. 33, no. 6, pp. 694–701, 2011.
- [18] M. Yaqub and C. G. Bailey, "Cross sectional shape effects on the performance of post-heated reinforced concrete columns wrapped with FRP composites," *Composite Structures*, vol. 93, no. 3, pp. 1103–1117, 2011.
- [19] T. Trapko, "The effect of high temperature on the performance of CFRP and FRCM confined concrete elements," *Composites Part B: Engineering*, vol. 54, no. 1, pp. 138–145, 2013.
- [20] ASTM International, "Standard test method for compressive strength of cylindrical concrete specimens," ASTM C39, ASTM International, West Conshohocken, Pa, USA, 2015, <http://www.astm.org/>.
- [21] British Standard BS 1881-111, *Method of Normal Curing of Test Specimens*, vol. 111, British Standards Institution, 1983.
- [22] SikaWrap-230, <http://gcc.sika.com/en/struct-bond-strength-redirect/sika-structural-strengthening-solutions/02a013/02a013sa06.html>.
- [23] <http://www.basf-cc.com.sg/en/products/ConcreteRepairandProtectionSystems/MBrace/MBraceSaturant/Pages/default.aspx>.
- [24] ISIS Design Manual, *Strengthening Reinforced Concrete Structures with Externally Bonded Fibre Reinforced Polymers*, The Canadian Network of Centers of Excellence on Intelligent Sensing for Innovative Structures, ISIS Canada, University of Winnipeg, Manitoba, Canada, 2001.
- [25] ACI 440.2R-08, *Guide for the Design and Construction of Externally Bonded FRP Systems for Strengthening Concrete Structures*, American Concrete Institute, Farmington Hills, Mich, USA, 2008.